

DISSERTATION

AMBIENT AND TELESEISMIC ELASTIC WAVEFIELDS OF THE ROSS ICE SHELF,
ANTARCTICA, AND THEIR APPLICATION TO CRUSTAL SCALE SEISMIC IMAGING

Submitted by

Michael G. Baker

Department of Geosciences

In partial fulfillment of the requirements

For the Degree of Doctor of Philosophy

Colorado State University

Fort Collins, Colorado

Spring 2020

Doctoral Committee:

Advisor: Richard C. Aster

Derek L. Schutt

David A. Krueger

Ken G. Dueker

Copyright by Michael G. Baker 2020

All Rights Reserved

ABSTRACT

AMBIENT AND TELESEISMIC ELASTIC WAVEFIELDS OF THE ROSS ICE SHELF, ANTARCTICA, AND THEIR APPLICATION TO CRUSTAL SCALE SEISMIC IMAGING

Laterally extensive floating tabular ice, such as the Ross Ice Shelf in Antarctica, is mechanically equivalent to a floating elastic plate and thus supports a variety of vibrational modes, including short-period (< 20 s) elastic waves, intermediate-to-long period (20–100 s) buoyancy-coupled elastic plate waves, and ultra long period (> 100 s) gravity waves. Vibrational energy may be excited by near-field sources such as intra-shelf crevassing or the impingement of ocean gravity waves at the shelf ice front, and also by far-field sources such as teleseismic earthquake waves incident at the sub-shelf seafloor and the shelf grounded margins. Broadband seismometers deployed on an ice shelf readily observe these signals and facilitate large scale studies of ice shelf properties (via, e.g., travel-time tomography or velocity dispersion analysis) and near-field environment processes (via remote signal detection and analysis). Using two years of continuous data from a 34-station broadband seismic array deployed to the Ross Ice Shelf, Antarctica, I analyzed spatial and temporal variations in the short-to-intermediate period (0.4–25 s) ambient and teleseismic vibrational wavefields. I show that the ambient, ocean-wave-coupled wavefields are strongly modulated by sea ice concentrations in the adjacent Ross Sea, and identify three separate source processes operating in distinct period bands. Next, I show that body wave and surface wave arrivals from teleseismic earthquakes (> 3000 km distant) are observed on the vertical components of ice shelf-sited seismometers with signal-to-noise ratios generally sufficient for crustal and mantle scale tomographic studies. I also show that teleseismic S-waves incident at the grounded margins routinely generate symmetric mode Lamb waves which propagate a minimum of 250 km into the ice shelf interior; this phenomenon occurs throughout the year, with broad azimuthal distribution, and may be exploited for travel-time tomography of the ice shelf. Finally, I present an algorithm for

processing vertical channel autocorrelations of teleseismic P-wave coda, as recorded by floating-ice-sited seismometers, to illuminate crustal-scale features such as the Mohorovičić discontinuity. I present Markov Chain Monte Carlo inversions of these autocorrelations which yield crustal thickness estimates that are compatible with previous studies of crustal thicknesses for the Ross Sea Embayment and West Antarctica.

ACKNOWLEDGEMENTS

This research was supported by NSF grants PLR-1142518, 1141916, 1142126, 1246151, and 1246416, and NSF grant OPP-1744856. The US Antarctic Program provided logistical support for all associated fieldwork. The seismic instruments were provided by the Incorporated Research Institutions for Seismology (IRIS) through the PASSCAL Instrument Center at New Mexico Tech. Data collected are available through the IRIS Data Management Center under RIS and DRIS network code XH (Wiens et al., 2015) (doi.org/10.7914/SN/XH_2014). The PSD-PDFs presented in this study were processed with the IRIS Noise Tool Kit (DMC, 2014). The facilities of the IRIS Consortium are supported by the National Science Foundation under Cooperative Agreement EAR-1851048 and the DOE National Nuclear Security Administration. The author appreciates the support of the University of Wisconsin-Madison Automatic Weather Station Program for the data set, data display, and information; funded under NSF grant number ANT-1543305. Ross Ice Shelf profiles were generated with the Antarctic Mapping Tools (Greene et al., 2017). Regional maps were generated with the Generic Mapping Tools (Wessel and Smith, 1998). Topography and bathymetry data for all maps in this study were sourced from the National Geophysical Data Center ETOPO1 Global Relief Model ([doi:10.7289/V5C8276M](https://doi.org/10.7289/V5C8276M)). Additional orthometric ice surface elevations for the RIS were provided by the Reference Elevation Model of Antarctica (REMA) (Howat et al., 2019). Code written for this research made extensive use of the Armadillo (Sanderson, 2010) and FFTW (Frigo and Johnson, 1999) C++ libraries.

TABLE OF CONTENTS

	ABSTRACT	ii
	ACKNOWLEDGEMENTS	iv
	LIST OF TABLES	vii
	LIST OF FIGURES	viii
Chapter 1	Introduction	1
1.1	Overview	1
1.2	Geologic Background and Motivation	4
Chapter 2	Seasonal and Spatial Variations in the Ocean- Coupled Ambient Wavefield of the Ross Ice Shelf	6
2.1	Introduction	6
2.2	Structure of the Ross Ice Shelf	8
2.3	Instrumentation and Data	9
2.4	Methods	11
2.4.1	Spectral Bands	11
2.4.2	Spectral Characterization	13
2.4.3	Temporal and Spatial Variation	13
2.5	Results and Discussion	15
2.5.1	Long to Very Long Period Band (>20 s)	15
2.5.2	Primary Band (10.0–20.0 s)	16
2.5.3	Secondary Band (5.0–10.0 s)	21
2.5.4	Tertiary Band (0.4–4.0 s)	23
2.6	Conclusions	26
2.7	Tables	29
2.8	Figures	33
Chapter 3	Teleseismic Earthquake Wavefields Observed on the Ross Ice Shelf	43
3.1	Introduction	43
3.2	Data and Methods	46
3.2.1	Instrumentation	46
3.2.2	Teleseismic Earthquake Signals on the RIS	47
3.2.3	Spectral Characterization of Teleseismic Signals	48
3.3	Elastic Waves in an Ice Shelf	49
3.3.1	Elastic Structure	50
3.3.2	Intralayer Resonances	51
3.3.3	Coupling of Seismic, Acoustic, and Gravity Waves	53
3.3.4	Coupling of Seismic and Plate Waves	54
3.4	Results	56
3.4.1	P-waves (0.5–2.0 s)	56
3.4.2	S-waves (10–15 s)	58

3.4.3	Surface waves (13–25 s)	61
3.5	Discussion	63
3.5.1	P-waves (0.5–2.0 s)	63
3.5.2	S-waves (10–15 s)	64
3.5.3	Surface waves (13–25 s)	65
3.6	Summary and Conclusions	68
3.7	Evidence for a Long Period Compressibility Limit	71
3.8	Tables	75
3.9	Figures	77
Chapter 4	Inversion of Teleseismic P-wave Autocorrelations for Crustal Velocity Structure Beneath the Ross Ice Shelf	89
4.1	Motivation	89
4.2	Data and Methods	91
4.2.1	Data and Preprocessing	91
4.2.2	Processing of Autocorrelations	92
4.2.3	Inverse Modeling	94
4.2.4	Forward Modeling	96
4.3	Results and Discussion	98
4.3.1	MPAT Validation Test	98
4.3.2	Ice Shelf Autocorrelations and Prior Model Selection	99
4.3.3	MCMC Results and Interpretation	100
4.4	Tables	103
4.5	Figures	104
Bibliography	112
Appendices	121
A1	Chapter 2	121
A2	Chapter 3	146

LIST OF TABLES

2.1	Ambient spectral bands.	29
2.2	Wave modes of the Ross Ice Shelf.	30
2.3	Mean band power annual statistics. DR stations	31
2.4	Mean band power annual statistics. RS stations	32
3.1	Parameters for teleseismic earthquake catalog.	75
3.2	Elastic parameters for the Ross Ice Shelf.	75
3.3	Comparative measurements of Ross Ice Shelf vertical structure.	76
4.1	RIS/DRIS array Moho depths.	103

LIST OF FIGURES

2.1	Map of Ross Ice Shelf stations used for the ambient noise study.	33
2.2	Annual sea ice coverage in the Ross Sea.	34
2.3	Floating versus grounded station power spectral density probability distributions functions.	35
2.4	Differential power spectral density curves.	36
2.5	Primary band sea ice correlation maps.	37
2.6	Primary band spatial and temporal variations.	38
2.7	Secondary band sea ice correlation maps.	39
2.8	Secondary band spatial and temporal variations.	40
2.9	Tertiary band sea ice correlation maps.	41
2.10	Tertiary band spatial and temporal variations.	42
3.1	Map of earthquakes used in signal-to-noise analysis.	77
3.2	Teleseismically induced wavefields of the Ross Ice Shelf.	78
3.3	Spectrogram of earthquake observed at a floating ice seismograph. Background subtracted.	79
3.4	Spectrogram of earthquake observed at a grounded ice seismograph. Background subtracted.	80
3.5	Teleseismic P-wave spatial and temporal variations.	81
3.6	Power spectral density plots of teleseismic P-waves observed at a floating ice seismograph.	82
3.7	Teleseismic S-wave spatial and temporal variations.	83
3.8	S_0 Lamb waves excited by teleseismic SV-waves.	84
3.9	Particle motions for S_0 Lamb waves.	85
3.10	Root-mean-square amplitudes for S_0 Lamb waves.	86
3.11	Teleseismic Rayleigh wave spatial and temporal variations.	87
3.12	Group velocities for teleseismic Rayleigh waves.	88
4.1	Map of earthquakes used in signal-to-noise analysis.	104
4.2	Effect of source function on autocorrelation stacking.	105
4.3	Example of COW tipping with synthetic autocorrelations.	106
4.4	Example of COW tipping with a floating station.	107
4.5	Schematic of reverberation wavefield.	107
4.6	Receiver function and autocorrelation inversions for MPAT.	108
4.7	Autocorrelation inversion for RS09.	109
4.8	Autocorrelation inversion for DR15.	109
4.9	Crustal P-wave velocity structure beneath the RIS.	110
4.10	Standard deviations for crustal P-wave velocity structure beneath the RIS.	111
4.11	Comparison of Moho depth estimates from previous studies	111

A-2.1	Map of Ross Ice Shelf ice front stations.	121
A-2.2	Bathymetry of the Ross Embayment.	122
A-2.3	Ocean-force wave modes of the Ross Ice Shelf.	123
A-2.4	Flexural-gravity band spatial and temporal variations.	124
A-2.5	Extensional band spatial and temporal variations.	125
A-2.6	Spatial variations in Tertiary band sea ice correlations. North channel.	126
A-2.7	Spatial variations in Tertiary band sea ice correlations. East channel.	127
A-3.1	Elastic energy coefficients for a water/ice interface.	146
A-3.2	Elastic energy coefficients for a sediment/water interface.	146
A-3.3	Spectrogram of earthquake observed at a floating ice seismograph. No background subtraction.	147
A-3.4	Spectrogram of earthquake observed at a grounded ice seismograph. No background subtraction.	147
A-3.5	Population metrics for teleseismic earthquake catalog.	148
A-3.6	Teleseismic P-wave spatial and temporal variations. No source normalization.	149
A-3.7	Teleseismic S-wave spatial and temporal variations. No source normalization.	150
A-3.8	S_0 Lamb waves excited by teleseismic SH-waves.	151
A-3.9	Teleseismic Rayleigh wave spatial and temporal variations. No source normalization.	152
A-3.10	Primary band spatial and temporal variations, extended to 13–25 s.	153

Chapter 1

Introduction

1.1 Overview

The ultimate goal of this research was to measure and characterize the vibrational excitation of a major ice shelf and to use this knowledge to estimate key aspects of the seismic velocity structure of the crust (i.e., the depth of the Mohorovičić discontinuity) beneath the Ross Ice Shelf, located within the greater West Antarctic Rift System. The novelty of this research stems from the uniqueness of the dataset and from the prevalence of exotic wave mechanics not typically encountered in solid Earth seismology. The data was collected by the RIS/DRIS project, a first-of-its-kind 34-station broadband network deployed across the Ross Ice Shelf (RIS) for a two-year study (2014–2016) of oceanic, cyospheric, and solid Earth processes (Wiens et al., 2014). Ice shelves in general are a frontier for seismological research due to: 1) a persistent, multi-mode ambient wavefield generated by direct coupling between ocean gravity waves and the ice front and sub-shelf cavity; 2) a stratified vertical structure with significant impedance contrasts at the ice/water, water/seafloor-sediment, and sediment /basement interfaces; and 3) specific to the RIS, vertical dimensions ($\sim 300\text{--}600$ m) such that intralayer resonances (e.g., SV-waves within the ice, or P-waves within the water column) and regime transitions between physical models of elastic behavior (e.g., the transition of the water column from compressible to incompressible behavior) occur at wave periods which overlap with local and teleseismic signals of interest.

The unified theme of this dissertation is, broadly, a decomposition of the ambient and teleseismic wavefields endemic to the RIS in order to establish the viability of utilizing teleseismic signals for passive crustal scale imaging.

Chapter 1 presents the geologic history of the West Antarctic Rift System and the Ross Ice Shelf and summarizes the importance of these provinces in the context of a changing global climate.

Chapter 2 analyzes spatial and temporal variations in the ocean-coupled ambient wavefield of the RIS and identifies the predominant wave modes and source mechanisms associated with three period bands typically relevant to solid Earth seismological studies. Vibrational energy at all periods is strongly modulated by the concentration of sea ice in the adjacent Ross Sea, resulting in a summer high power state during periods of negligible sea ice, and a winter low power state during periods of extensive and contiguous sea ice. In the 10–20 s "Primary" band, I show that the summer ambient field is dominated by a combination of symmetric and asymmetric mode Lamb waves generated by the interactions of ocean gravity waves with the ice front and sub-shelf cavity, respectively; during winter, extensive sea ice prevents the propagation of ocean waves into the Ross Sea and the RIS wavefield is instead driven by the passage (along the sub-shelf seafloor) of continental-scale primary microseism Rayleigh waves. In the 5–10 s "Secondary" band, I show that the ambient RIS wavefield is exclusively excited by the passage of secondary microseism Rayleigh waves. In the 0.4–4.0 s "Tertiary" band, I characterize a seasonal wavefield which is strongly correlated with the absence of sea ice above shallow, high relief bathymetric features. While I do not positively identify a source mechanism or propagation mode for this noise band, it is noticeably similar to short period microseisms observed by multiple prior studies and is likely explained by nonlinear wave-wave interactions within the Ross Sea between local wind sea and globally propagating ocean waves. The text of this chapter is presented as-published in the *Journal of Glaciology* (Baker et al., 2019).

Chapter 3 analyzes spatial and temporal variations in the signal-to-noise ratios (SNR) of P-wave, S-wave, and surface wave coda from teleseismic earthquakes. P-wave arrivals in the 0.5–2.0 s period band are generally well-observed on the vertical component of floating ice-stied seismometers and are accompanied by significant horizontal energy that is attributed to P-to-S-wave scattering within the ice shelf. Notably, teleseismic P-wave arrivals typically excite significant intralayer resonances within the ice (SV-wave) and water column (P-wave); the observed periods of these resonances are exploited (with assumptions of media velocities) to estimate the thicknesses of the ice and water layers to a high degree of fidelity with prior, satellite-based measurements. S-

wave arrivals in the 10–15 s period band are weakly observed on the vertical components of floating ice-sited seismometers via S-to-P-wave conversions at the sediment/basement and sediment/water interfaces. I also present novel observations of symmetric mode Lamb waves generated by teleseismic S-waves incident near the grounded margins of the RIS; these Lamb waves have the potential for long term, *in situ* seismic monitoring of ice shelf spatial and elastic properties. Vibrational energy observed by floating ice-sited seismometers in the 13–25 s period band coincident with teleseismic surface waves is attributed to passage of crustal Rayleigh waves along the sub-shelf seafloor. Additionally, I interpret observations across all three bands as consistent with a theoretical model for the transition of the water column from compressible to incompressible behavior in response to steeply incident solid Earth elastic waves, with a theoretically-determined delineating period of ~ 2.0 s. The text of this chapter is presented as-submitted for peer review to the *Journal of Glaciology*.

Chapter 4 presents depth estimates for the Mohorovičić discontinuity (the "Moho") obtained with Markov Chain Monte Carlo inversions of single-station vertical component autocorrelations of teleseismic P-wave first arrivals and their coda. Autocorrelations of teleseismic P-waves for single-station measurements of crustal scale velocity structure are a recently developed alternative (Sun and Kennett, 2016; Phạm and Tkalčić, 2017) to the traditional P-wave receiver function method. The latter method (Langston, 1979) has been well utilized under a variety of geologic conditions (e.g., over thick sedimentary basins or ice caps) but are fundamentally incompatible with an ice shelf environment due to their reliance on radial-component observations of P-to-S-wave conversions from crustal impedance contrasts (S-waves being unable to propagate through the water layer). Vertical component autocorrelations, in contrast, images crustal structure by detecting P-waves that are multiply-reflected between the surface and crustal impedance contrasts. To my knowledge, application of the autocorrelation method to an ice shelf environment has not been attempted. My autocorrelation results for the crustal velocity structure directly beneath the stations of the RIS/DRIS array indicate Moho depths of $21\text{--}25\pm 3$ km, which are generally in agreement with interpolated (Chaput et al., 2014) and surface wave-derived (Shen et al., 2018) estimates.

1.2 Geologic Background and Motivation

The West Antarctic Rift System (WARS) is the dominant feature of West Antarctica, and is one of the largest continental extension systems on the planet. Rifting generally is believed to have progressed in two stages: The first stage occurred from 105 to 80 Ma (Jurassic-Cretaceous) and resulted in widespread, uniform thinning of the West Antarctic crust [Siddoway et al., 2004]; The second stage occurred from 41 to 17 Ma (early Cenozoic to Miocene) and saw thinning concentrated in the Ross Sea region [Cande et al., 2000]. There is considerably less consensus on the amount of extension accommodated by the WARS crust, with studies finding evidence for as little as 120 km to up to 500 km.

Geologic surveys of the rift are hindered by the (up to) kilometers-thick icecaps that cover roughly 97% of the bedrock, as well as the general meteorologic and logistical hurdles inherent to Antarctic field work. As such, much of our knowledge of Antarctic geology is the result of numerous remote sensing campaigns. The BEDMAP2 project has developed a kilometer-scale subglacial topography model compiled from decades of terrestrial, aerial, and orbital surveys [Fretwell et al., 2013]. The semi-permanent POLENET and AGAP broadband seismic networks have mapped seismic velocity details of the crust and upper mantle using teleseismic earthquake and near-field noise sources [Chaput et al., 2014, Ramirez et al., 2016]. These data reveal a WARS crust that is relatively thin by continental standards (20 to 24 km, with the global continental Moho depth average being approximately 35 km (Reguzzoni et al., 2013)) and also predominantly below sea level as a result of icecap overburden. Geothermal studies at arguably disparate locations across West Antarctica have reported fluxes ranging from 100 to 285 mW m⁻², far in excess of the global continental average of 60 mW m⁻².

At regional scales, the combination of these factors indicate that the crustal geology of the WARS is a critical but largely unquantified variable in the long-term stability of the West Antarctic Ice Sheet. The high geothermal flux likely results from a combination of the thin, rifted crust and suspected underlying mantle plumes [Seroussi et al., 2017, Phillips et al., 2018]; geothermal flux is a major component of glacial heat budget and directly impacts basal melting and glacial flow

rates. Similarly, in the Ross Sea Embayment below the Ross Ice Shelf, suspected unusually thin crust and assumed elevated geothermal flux is an additional variable in the primarily seawater-driven basal melting rate of the RIS [Rignot and Jacobs, 2002]. Basal melt at ice shelf grounding zones decreases shelf thickness and buoyancy, thereby allowing warm sea water to penetrate deeper inland beneath grounded ice as it flows down the negative elevation bedrock. This can result in a positive feedback loop whereby mobilized grounded ice pushes the Ross Ice Shelf farther out to sea, where contact with the relatively warm Circumpolar Deep Water prompts an increase in melting and a further decrease in the RIS's buttressing of grounded ice [Dinniman et al., 2011].

Ice shelf sited seismometers have applications beyond tectonic studies. Because the ice shelf is directly coupled to the underlying Ross Sea, and thereby also to the Southern Ocean, these seismic stations are capable of second-order observations of global-scale oceanic events and regional-scale Ross Sea events. Seismic signatures for tsunami arrivals (100-1000 seconds) at the RIS have been reported for the 2004 Sumatra Okal and MacAyeal [2006] and the 2015 Chile earthquakes [Bromirski et al., 2017]. Ocean swell events (7-40 seconds) observed on the RIS have been individually traced to storms in the northern Pacific, Southern, and Indian oceans, with waves from the latter apparently diffracting around intervening land masses [Cathles et al., 2009]. Hydroacoustic phases traveling within the ocean's SOFAR zone (i.e., T phases) have also been identified for ocean-bottom teleseismic earthquakes [Okal and MacAyeal, 2006], suggesting that these stations might also have use for detecting T phases from underwater landslides or iceberg collisions. Sea ice concentrations in the Ross Sea dramatically modulate noise within a characteristic band (0.4-4.0 seconds), suggesting that annual changes within this band could be used to track sea ice trends. While several of these processes would arguably be more effectively observed with purpose-built, first-order devices, logistics and funding often do not permit deployment of a full suite of detectors. Refinement of these applications would therefore enable the use of a single seismic station as a multi-disciplinary observatory for future deployments to Earthly ice shelves or extraterrestrial (e.g., Europa, Titan) icy moons.

Chapter 2

Seasonal and Spatial Variations in the Ocean-Coupled Ambient Wavefield of the Ross Ice Shelf

¹The Ross Ice Shelf (RIS) is host to a broadband, multimode seismic wavefield that is excited in response to atmospheric, oceanic, and solid Earth source processes. A 34-station broadband seismographic network installed on the RIS from late 2014 through early 2017 produced continuous vibrational observations of Earth’s largest ice shelf at both floating and grounded locations. We characterize temporal and spatial variations in broadband ambient wavefield power, with a focus on period bands associated with primary (10–20 s) and secondary (5–10 s) microseism signals, and an oceanic source process near the ice front (0.4–4.0 s). Horizontal component signals on floating stations overwhelmingly reflect oceanic excitations year-round due to near-complete isolation from solid Earth shear waves. The spectrum at all periods is shown to be strongly modulated by the concentration of sea ice near the ice shelf front. Contiguous and extensive sea ice damps ocean wave coupling sufficiently so that wintertime background levels can approach or surpass those of land-sited stations in Antarctica.

2.1 Introduction

Scientific motivations and responsively evolving instrumentation have recently greatly expanded the collection and analysis of high-quality seismic data from Antarctica and other remote polar regions, and have driven significant developments in glacial seismology (Podolskiy and Walter, 2016; Aster and Winberry, 2017). An element of this is the deployment of floating seismographs atop tabular icebergs (Okal and MacAyeal, 2006; MacAyeal et al., 2008; Martin et al., 2010) and ice shelves (Bromirski and Stephen, 2012; Heeszel et al., 2014; Zhan et al., 2014).

¹This chapter originally published as: Baker, M. G., Aster, R. C., Anthony, R. E., Chaput, J., Wiens, D. A., Nyblade, A., ... and Stephen, R. A. (2019). Seasonal and spatial variations in the ocean-coupled ambient wavefield of the Ross Ice Shelf. *Journal of Glaciology*, 65(254), 912-925.

Floating seismograph deployments facilitate the study of a variety of physical and environmental phenomena, including: direct measurements of elastic and elastigravity wave propagation in ice (Sergienko, 2017; Chen et al., 2018); detection of hydroacoustic radiation from iceberg-iceberg collisions and iceberg shoaling (Talandier et al., 2006; Dowdeswell and Bamber, 2007; MacAyeal et al., 2008; Martin et al., 2010); and the monitoring and understanding of seismogenic fracture and other instability mechanisms that may lead to ice shelf weakening or collapse, particularly when preconditioned for failure by fracturing and englacial melt (e.g., MacAyeal et al., 2003; Bromirski and Stephen, 2012; Paolo et al., 2015; Furst et al., 2016; Massom et al., 2018; Olinger et al., 2019).

The ambient seismic wavefield of the Ross Ice Shelf (i.e., in the absence of local, regional, and teleseismic earthquake signals) is dominated by a broad spectrum of elastic and flexural-gravity waves that result from the coupling of the ice shelf with oceanic and atmospheric processes. At ultra-long periods (>100 s), flexural-gravity waves have been observed coincident with tsunami arrivals from the 2004 Sumatra earthquake (Okal and MacAyeal, 2006) and the 2015 Chile earthquake (Bromirski et al., 2017). At long periods (10–40 s), flexural-gravity waves and fundamental symmetric mode (S0) Lamb waves have been observed in response to ocean swell events traced to storms in the northern Pacific, Southern, and Indian oceans (Cathles et al., 2009; Chen et al., 2018). At short periods (<1 s), Rayleigh waves propagating within the near-surface firn/ice velocity gradient have been correlated to ocean waves interacting with the ice front (Diez et al., 2016) and to the coupling of wind into seismic energy via interactions with surface features such as sastrugi and snow drifts (Chaput et al., 2018).

Using two years of continuous data from the Ross Ice Shelf, we quantify the spatial and temporal variations in the seismic background state of the ice shelf in the context of oceanic excitation mechanisms. We focus on period bands that are typically associated with the global primary (10–20 s) and secondary (5–10 s) microseism signals (e.g., Hasselmann, 1966), and a short-to-intermediate period band (0.4–4.0 s) that we will show is strongly correlated to the absence of sea ice in the Ross Sea. Because the noise environment is strongly modulated by both oceanic forcing and ice shelf geometry, this study underpins background levels of seismic excitation that are

relevant to potential long-term seismic monitoring of the RIS in the context of climate-driven environmental changes. For example, dispersion curve analysis of short period Rayleigh waves can provide depth estimates for meteoric firn layers (Diez et al., 2016), while longer period flexural-gravity waves similarly sample the thickness of the entire ice column (Robinson, 1983). Strong spectral peaks are also associated with water column reverberations of P-waves (e.g., Diez et al., 2016) and ice layer reverberations of SV- and SH-waves (Crary, 1954); the peak periods of these signals also provide estimates of water and ice thicknesses, respectively. In the context of global seismology, the ambient spectral power within the 0.4–20 s period band additionally characterizes the background noise levels for observations of teleseismic earthquake P-waves (0.5–2.0 s), S-waves (10–15 s), and short-period surface waves (>17 s) that provide new constraints on the seismic structure of the Antarctic Plate in the Ross Embayment region (e.g., White-Gaynor et al., 2019). Quantification of teleseismic earthquake signal-to-noise ratios will be presented in a future study.

2.2 Structure of the Ross Ice Shelf

The Ross Ice Shelf (RIS) has an area of approximately 500,000 km² and a geographically-variable thickness generally in the range of 200–400 m. The RIS is structurally heterogeneous, being composed of varying proportions of advected onshore glacial, meteoritic, and bottom and peripheral marine ice. The RIS overlies an ocean column of variable but approximately comparable thickness. Where ice delivered from tributary glaciers abuts, prominent suture zones are formed that persist to the terminus as shelf ice is transported to the ice edge at velocities of up to approximately 1 km/yr. The location of the ice edge is controlled by the balance between advection and calving, commonly via large tabular icebergs (e.g., MacAyeal et al., 2008; Martin et al., 2010). Subglacial and surface crevasses and rifts on the RIS are commonly semi-aligned with the calving front, reflecting a generally tensional stress environment in the seaward flow direction (e.g., LeDoux et al., 2017). Shelf elastic structure is, on the largest scale, characterized by laterally extensive elastic components overlying the ocean and solid Earth that can produce strong

guided-wave phenomena. The principal components are: 1) a meteoritic snow-firn layer that transitions to glacial ice over tens of meters; 2) a glacial ice layer, which varies in thickness from 200 to 1400 m at RIS station sites (median 330 m for floating ice and 925 m for grounded ice), and which may incorporate a frozen ocean layer at its base; and 3) an ocean water layer that varies in thickness from 100 to 700 m for RIS station sites (median 440 m). Significant lateral variations within the ice shelf include tensional rifts, suture zones, grounding point perturbations, and shear zones associated with ice streams.

Nascent Iceberg (NIB) is a semi-detached spur at the RIS ice front partially bounded by a 46 km long rift. Expansion of the rift—and eventual calving of NIB—has apparently been arrested by propagation of the rift into a suture zone with a higher fracture toughness than the surrounding ice shelf (Borstad et al., 2017; LeDoux et al., 2017; Lipovsky, 2018) and has been in near-steady-state since at least 2004 (Okal and MacAyeal, 2006; Lipovsky, 2018). By design, three stations located at the northern terminus of the array transected NIB for the purpose of studying ice front mechanics and cryoseismic signals. Our preliminary observations from these stations indicate that the RIS ice front experiences broadband, nonlinear, ocean-forced excitation during periods of especially energetic swell activity. These ambient processes are apparently closely bound to the ice front as they are not significantly observed even at the closest interior station located 50 km landward. Due to the complexities of the ice front spectra, we will focus this current work on the interior stations and will address the ice front signals in a future study.

2.3 Instrumentation and Data

34 polar-engineered Incorporated Research Institutions for Seismology (IRIS) Polar Programs broadband seismic stations were installed during late 2014 for an approximately two-year continuous deployment during the coordinated RIS (Mantle Structure and Dynamics of the Ross Sea from a Passive Seismic Deployment on the Ross Ice Shelf) and DRIS (Dynamic Response of the Ross Ice Shelf to Wave-Induced Vibrations) projects (Figure 2.1, Figure A-2.1) (Bromirski et al., 2015) (doi:10.7914/SN/XH_2014).

Seismographs were deployed in an \sim 1100 km-long ice-front-parallel transect bisected by a \sim 425 km long ice-front-perpendicular transect. The network consisted of 1) a shelf-spanning large aperture array (RS01 to RS18) with an average spacing of 100 km; and 2) a central medium aperture array (DR01 to DR16) with stations spaced at 20–50 km. All stations were sited on floating ice with the exceptions of RS08 and RS09 on Roosevelt Island, RS11–RS14 in Marie Byrd Land, and RS17 on an unnamed grounded region of the southern RIS.

All RS and DR stations utilized Nanometrics Trillium 120PH posthole sensors buried at depths of 2–3 m below the snow surface at the time of installation, with the exception of RS09, RS11–RS14, and RS17, which were Nanometrics Trillium 120PA sensors installed on phenolic resin pads within shallow vaults. All DR stations and RS04 sampled at 200 Hz; all other RS stations sampled at 100 Hz. Stations ran on solar power during the Antarctic summer and lithium batteries during the winter. Due to Iridium satellite power and bandwidth constraints, only state of health information was telemetered, necessitating annual service visits to recover data. The noise analysis presented here incorporates data from the full two-year deployment (approximately November 2014–November 2016). A subset of stations (RS10–RS14) remained deployed in Marie Byrd Land until early February 2017.

We also make use of the following supplemental datasets: 1) daily sea ice concentration measurements from the National Snow and Ice Data Center (NSIDC) for a region of the Ross Sea between longitudes 139°W and 155°E, and south of latitude 65°S (Cavalieri et al., 1996); 2) wind speed measured at weather station Whitlock (WTL) on Franklin Island, from the University of Wisconsin-Madison Automatic Weather Station Program (AWS); 3) seismic data recorded by permanent stations VNDA (40 Hz) in the McMurdo Dry Valleys (Global Telemetered Seismograph Network, doi:10.7914/SN/GT) and QSPA (40 Hz, Location Code 70) at South Pole Station (Global Seismograph Network, doi:10.7914/SN/IU); 4) glacial ice thicknesses and water column depths for the RIS and Marie Byrd Land, from the BEDMAP2 survey (Fretwell et al., 2013); and 5) bathymetry and topography data from the National Geophysical Data Center ETOPO1 Global Relief Model (doi:10.7289/V5C8276M).

We use data from supplemental sources 1–3 for a date range between 1 November 2014 through 31 March 2017. We note that features of the RIS from BEDMAP2 may be outdated as the model is based on data collected in 1996. However, based on observations of P- and S-wave reverberations in the water and ice layers, respectively, the BEDMAP2 thicknesses remain usefully accurate for our purposes as of 2016 (Diez et al., 2016; Chaput et al., 2018). The northward extent of the RIS ice front, however, has advanced several kilometers since 1996 and is presently located ~ 3 km north of the ice front stations DR01–DR03. For the large-scale maps presented in this study, we have manually shifted the coordinates of the ice front stations south by ~ 23 km; profiles of the North-South transect show the unaltered positions.

Sea ice concentrations are based on surface brightness temperatures amalgamated from satellite-based microwave imagers (Cavalieri et al., 1996). Data are provided in 25×25 km grids at daily resolution. Sea ice concentration for each grid is specified by a fractional value ranging from 0.0 (open sea) to 1.0 (complete ice coverage). Accuracy is estimated to be ± 0.05 during the winter and ± 0.15 during the summer, with the latter being adversely affected by surficial melt ponds. Figure 2.2 maps the variations in the sea ice concentration data used in this study. We also define an open water concentration, O , as the complement of ice sea concentration, I (i.e., $O = 1 - I$); this is for clarity on plots where spectral power would otherwise be anticorrelated with sea ice concentration.

2.4 Methods

2.4.1 Spectral Bands

We address three spectral bands defined by time-varying phenomenology observed by the RIS network (Table 2.1).

We define the Primary (10–20 s) and Secondary (5–10 s) bands to coincide with the period bounds typically associated with the global primary and secondary microseism wavefields, respectively. For land-sited stations (i.e., not deployed on an ice shelf or iceberg), the Primary band is dominated by globally-observed, principally crustal, Rayleigh waves generated by wind-

driven deep ocean waves shoaling on shallow continental shelves (e.g., Hasselmann, 1966). The Secondary band records Rayleigh waves generated by wave-wave interferences of ocean swells reflecting from coastlines or ice edges, or from wind and storm scenarios that otherwise create standing wave components (Longuet-Higgins, 1950). Both microseism wavefields are principally sourced in shallow coastal waters but are easily observed at land-based stations hundreds or thousands of kilometers inland via Rayleigh wave propagation.

High-latitude extratropical cyclonic storm activity increases during winter, accompanied by an increase in primary and secondary microseism power observed globally at mid- to high-latitude seismic stations (Aster et al., 2008). However, primary and secondary microseism power observed at land-sited seismographs in polar regions is broadly anticorrelated with sea ice density and attendant near-continent ocean swell attenuation (Aster et al., 2008; Bromirski et al., 2010; Tsai and McNamara, 2011; Anthony et al., 2017), so that late-winter background levels in Antarctica, in particular, have been previously noted to be typically less than late summer levels in these bands (e.g., Aster et al., 2008, 2010).

We define the Tertiary band (0.4–4.0 s) based on a summertime "high-power state" which we will show is strongly correlated with the seasonal break-up and formation of sea ice in the Ross Sea. Environmentally-forced excitation of this band has previously been identified by land-sited seismometers in proximity to coastlines (Kibblewhite and Ewans, 1985; Tsai and McNamara, 2011) and lake shores (Xu et al., 2017; Anthony et al., 2018; Smalls et al., 2019). These studies have found that the amplitude of this signal is strongly correlated with regional wind-sea and regional swell, and is strongly attenuated by the formation of sea or lake ice. Also common among these studies is a spectral peak of ~ 1 s, regardless of lake or ocean dimensions. The source mechanism for this spectral band has not been conclusively identified, though it is generally hypothesized to relate the same linear wave-seafloor interactions or nonlinear wave-wave interactions responsible for the primary and secondary microseism wavefields, respectively, operating at higher frequencies.

We emphasize a notational difference between the primary and secondary microseism wavefields, which consist solely of Rayleigh waves, and the Primary and Secondary bands defined for

this study, which may include additional wave modes. We choose the name "Tertiary band" as a logical progression of this naming scheme, in keeping with the aforementioned studies that have suggested that the attendant wavefield is a common component of the microseism spectrum. As with the Primary and Secondary bands, observations of the Tertiary band on an ice shelf may include wave modes other than Rayleigh waves.

2.4.2 Spectral Characterization

We visualize and quantify the background seismic noise environment using probability density function representations of the power spectral density (e.g., Figure 2.3). These so-called PSD-PDFs (McNamara and Buland, 2004) were constructed using the IRIS Noise Toolkit (DMC, 2014). For PSD-PDF analysis, velocity time series data were segmented into hour-long time segments with 50% overlap. For each segment, acceleration PSDs were generated using Welch's subsection averaging method (Welch, 1967) incorporating fifteen Hanning-tapered subsegments. PSDs are smoothed by averaging over 1/8 octave intervals and rounded to the nearest dB. The resultant PSD-PDF is a two-dimensional histogram of observed power and period. We do not remove teleseismic earthquake or local icequake signals from the PSD data, as these events are sufficiently transitory so as to not significantly impact median PSD-PDF statistics for these windowing parameters, except in unusual circumstances (Aster et al., 2008; Anthony et al., 2015).

2.4.3 Temporal and Spatial Variation

The vibrational excitation of the Ross Ice Shelf by ocean waves is highly seasonally variable. Two critical seasonal factors affecting the interacting between ocean waves and the RIS are the presence or absence of the wind- and salinity-controlled polynya directly offshore of the ice front (Nakata et al., 2015), and the waxing and waning of circum-continental sea ice (Aster et al., 2008; Anthony et al., 2015). We categorize noise spectra here in terms of "seasons" that are dictated by annually periodic sea ice variations. "Summer" or "SMR" denote the generally open-water ice front periods between 1 December and 31 March, while "Winter" or "WTR" denote the remainder of the year, during which sea ice is historically contiguous across the ice shelf front (e.g., Cavalieri

et al., 1996). To create inter-seasonal metrics for the two years of observation, distinct PSD-PDFs were computed for the Summer and Winter seasons.

We assess the spatial contributions of sea ice variability in the Ross Sea to the seismic power observed in each spectral band by calculating the time series correlations between the spectral band powers and the open water concentrations for each 25 x 25 km grid cell of NSIDC data.

We quantify spatial variations across the RIS by plotting the mean band powers at each station along the North-South and West-East network transects. We calculate the mean band power as the mean value of the median PSD curves (i.e., the average of the Winter and Summer median curves; Figure 2.3) for the period bounds specified in Table 2.1. The North-South transect includes, in order, stations DR02, DR04–DR06, DR10, DR12–DR15, RS16, DR16, and RS18. The West-East transect includes, in order, stations RS01–RS03, DR07–DR10, RS04, DR11, RS05–14. Stations RS15 and RS17 do not align with either transect and are omitted from this spatial analysis. We qualitatively identify the predominant wavefield modes observed along each transect based on bandpass filtering (as detailed in the next section) and the mean band power horizontal-over-vertical ratios (HOV); because we report the mean band powers in decibels, the HOV values (also in dB) are calculated as the differences between the horizontal (HHN, HHE) powers and the vertical (HHZ) power (Figure 2.4).

For this study, we will assume that the interior of the RIS is isotropic and steady-state; that is, we will ignore any potential effects associated with large-scale structural heterogeneities (e.g., crevasses, internal stress fields) or short-term variabilities in physical dimensions (e.g., calving, basal freezing and melting). We also limit our discussion to the interior stations of the RIS/DRIS array (i.e., excluding DR01-DR03), where we assume that the Ross Ice Shelf uniformly behaves as a linear elastic plate floating on an isotropic water column. The unusual spectral properties arising from the nonlinear and other mechanics endemic to the ice front will be addressed in a future study. For this study, it should be noted that DR02 will often appear as a significant outlier as a result of these edge effects.

For comparative purposes, we will generally use RS04 as a proxy for all floating stations as it is located at the intersection of the array transects and displays spectral characteristics similar to most other floating stations (Figure A-2.27). RS08 on Roosevelt Island similarly exemplifies the grounded ice stations of the RIS array (Figure A-2.31). Other stations will be presented as necessary to highlight features of interest.

2.5 Results and Discussion

Figure 2.4 presents the differential PSDs for a subset of stations chosen to highlight spectral details that will be of importance to this discussion. Table 2.2 in the Supplemental Materials provides a summary of the elastic- and gravity-driven flexural modes found on a floating ice platform, and Figure A-2.3 illustrates the most relevant of these wavemodes. Other Supplemental Materials include three-channel PSD-PDFs and differential PSDs for all RIS stations, as well as equivalent plots for regional land-sited stations VNDA and QSPA for comparison (Figures A-2.8–A-2.43). 2.3 and 2.4 tally the number of days per year that each station recorded mean spectral band powers above or below the global New High and Low Noise Models.

2.5.1 Long to Very Long Period Band (>20 s)

Long to very long period signals observed with floating seismometers have previously been extensively studied for the RIS array (Bromirski et al., 2017; Chen et al., 2018) and for semi-detached and free floating icebergs (MacAyeal et al., 2006; Cathles et al., 2009). Our own measurements of spatial and temporal distributions in this band are consistent with these sources and are included in the supplemental material for completeness (Figures A-2.4, A-2.5). We otherwise direct the reader to these detailed works.

2.5.2 Primary Band (10.0–20.0 s)

All floating and grounded stations recorded higher three-channel Primary power during the summer months (e.g., Figure 2.5a). The temporal and spatial characteristics of this high-power state, however, vary substantially between grounded and floating stations.

Grounded stations at Roosevelt Island and in Marie Byrd Land throughout the study period observed Primary band powers that were similar in amplitude, component distribution (i.e., HOV = 0 dB), and rates of change. For both summers, onset of the high-power state began when median open water concentration for the entire Ross Sea exceeded $\sim 50\%$ (Figure 2.5a; SEA). A maximum of ~ 10 dB above winter background levels was reached and maintained coincident with a 100% open sea state. Notably, the high-power state persisted into early winter, unabated by the return of sea ice until open water concentrations had dropped to $\sim 25\%$, at which time Primary band power returned to winter levels; this suggests that early-season thin sea ice does not substantially attenuate the ocean swell responsible for the primary microseism wavefield. For grounded stations, the Primary band high-power state was in effect for 5 January 2015 through 7 April 2015 and again for 21 December 2015 through 15 April 2016.

Floating ice shelf stations recorded Primary band powers with generally similar temporal variations, but with spatially-varying amplitudes and HOV distributions. For both summers, the high-power state was observed only while median open water concentrations were above $\sim 50\%$. During the 2014–2015 summer, Primary band power at all floating stations reached a plateau coincident with a 100% open sea state. In contrast, the 2015–2016 summer continued to trend upward during 100% open waters and experienced several high-power excursions in the months following an unusual El Niño-linked RIS melt event from 10–21 January 2016 (Nicolas et al., 2017; Chaput et al., 2018). The available data is insufficient to determine if the behavior of the Primary band during either of these summers could be classified as "normal" for previous or successive summers. The high-power state was in effect from 5 January 2015 through 23 March 2015 and again from 21 December 2015 through 10 April 2016. We note that these dates are poorly aligned with our nominal "Summer" start and end dates; this phase delay causes an ~ 5 dB discrepancy between

the calculated summertime median PSD and the high-probability, high-power path evident on the floating station PSD-PDFs (e.g., Figure 2.3; RS04, Box A).

Winter Primary band powers at all stations were generally highest in April and May and gradually trended to a minimum in November as sea ice continued to thicken throughout the winter and increasingly attenuated the ocean swell activity responsible for primary microseism generation.

Temporospatial correlations for grounded and floating stations (Figure 2.5b–d) indicate that Primary band power was strongly reduced (correlations >0.85) by high sea ice density beyond the continental shelf break (north of 72°S). This portion of the Ross Sea is dominated by the Ross Gyre, a cyclonic ocean current responsible for thermal and salinity exchange between the circumpolar deep water and the Ross Embayment. Accelerated melting of the West Antarctic Ice Sheet—due to contact with the warm circumpolar deep water—has resulted in significant freshening of the Ross Gyre over recent decades (Jacobs et al., 2002). This decreased salinity likely explains the longevity of summertime sea ice within the Ross Gyre region (Figure 2.2, Figure 2.5a; ROI). We therefore attribute the high correlation between Primary band power reduction and the freshening Ross Gyre to the modulation of ocean swell by melt-resistant sea ice.

High temporospatial correlations between Primary power reduction and sea ice concentration are also evident in the western Ross Sea along the coast of Victoria Land. This feature is most prominent on floating-station north-channel correlations and is strikingly similar to the underlying bathymetric highs (e.g., the Mawson and Crary Banks, Figure A-2.2). It is unclear at this time if this region is a) spuriously correlated with the causative regions associated with the Ross Gyre; b) actively influences the Primary band through modulation of the sea ice; or c) if the relatively shallow depths (~ 400 m below sea level for the Mawson Bank, versus ~ 650 m for the adjacent Drygalski Trough) directly enhance Primary band powers, e.g., through the focusing or refracting of ocean swell. Notably, open water concentrations above the much larger Pennell Bank exhibit much lower correlations (0.6–0.8) with high Primary power, suggesting that the dynamics of sea ice melt are the controlling factors, rather than coupling between ocean swell and the sea floor.

Wind velocities recorded at Franklin Island (Figure 2.5a, WTL) were inconsistently associated with Primary band power; that is, peaks in wind velocity were not always coincident with peaks in Primary band power, and vice versa. This is to be expected, as ocean swells are commonly driven by distant storm centers and are thus only weakly affected by local wind (Kibblewhite and Ewans, 1985; Apel, 1987). Therefore, coherencies between Primary band power and wind velocity at WTL are likely indicative of the arrivals of swell-generating ocean storms.

Spatial variations in Primary band power across the West-East and North-South transects are shown in Figure 2.6. As previously mentioned, grounded stations generally observed a ~ 5 dB increase in Primary band power across all channels during Summer. This appears to be independent of distance from the Ross Sea—to the extent of the available data—with similar increases observed at, for example, VNDA (~ 47 km), RS08 (~ 110 km), and QSPA (~ 1300 km) (Figure 2.4). Stations RS11, RS13, and RS14 display notable variations in HOV values (Figure 2.6a), which is also observed at longer periods (e.g., Figure A-2.4a, Figure A-2.5a). Long period, horizontal-dominant noise is often a hallmark of sensor tilt, which can result from thermal or barometric fluctuations, or other factors (e.g., Wilson et al., 2002; McNamara and Buland, 2004; Aderhold et al., 2015; Anthony et al., 2015). A qualitative examination of PSD-PDFs for periods longer than 20 s suggests that RS09, RS11–RS14, and RS17 suffered from seasonally modulated sensor tilt, with symptoms worsening during the winter months (Figure A-2.32, Figure A-2.34–Figure A-2.37, Figure A-2.40). Notably, this is the complete subset of stations deployed with vault-buried Trillium 120PAs, rather than the direct-buried Trillium 120PHs deployed for the rest of the array. The sensor tilt at RS13 and RS14 extends to periods below 20 s and thus contaminates measurements of environmental noise in the Primary band at these stations. In the absence of transient sensor artifacts (e.g., at stations RS08, RS09, RS12, RS17) grounded station signal within this band is consistent with previous observations of the primary microseism wavefield for Antarctic stations (Anthony et al., 2015).

Floating stations showed more nuance in their spatial and seasonal variations relative to grounded stations, but were generally systemically consistent. Along the North-South transect (ice front per-

pendicular, Figure 2.6b), Primary band power for both seasons and all three channels decreased nearly monotonically with distance from the ice front, with the greatest decreases observed within the first 100 km, between DR02 to DR05. During Winter, three-channel Primary band power dropped by a remarkable 30 dB for DR02 through DR05; vertical power remained approximately consistent along the rest of the transect, while horizontal power continued to decrease at a rate of 0.03 dB/km. Summer power levels for all components dropped by 42 dB (vertical) and 30 dB (horizontals) over the same initial 100 km; vertical power decayed to Winter levels within 260 km (RS16), while the horizontals remained elevated by 14 dB (HHN) and 8 dB (HHE) over Winter values at the transect terminus.

Notably, Summer HOV values underwent two sign changes along the North-South transect, in contrast to Winter HOV values which remained negative for the entire transect. These Summer HOV sign changes indicate that signals recorded by the vertical (HHZ) and horizontal (HHN and HHE) channels have independent rates of change and are therefore the result of different excitation processes. Winter HOV values also decrease with distance from the ice front (i.e., horizontal power decreases more quickly than vertical power), again indicating that vertical and horizontal motions are decoupled during the winter.

Interpretation of Primary Band Energy

A qualitative analysis of these HOV distributions, in conjunction with a knowledge of the ocean-forced wave modes endemic to a floating ice platform (e.g., Table 2.2, Figure A-2.3), provides a consistent hypothesis for the composition of the Primary band ambient wavefield.

The vertical channel recorded flexural-gravity waves (i.e., buoyancy-coupled asymmetric mode (A0) Lamb waves, Figure A-2.3a) that are induced through a combination of two mechanisms: wind-driven ocean waves penetrating into the water column beneath the ice shelf (Chen et al., 2018); and primary microseism Rayleigh waves which propagate in the crust and displace the water column via seismic-to-acoustic-gravity wave coupling (Yamamoto, 1982; Okal and MacAyeal, 2006). During open-water months, ocean-excited flexural-gravity waves are responsible for most of the vertical power at distances less than 100 km from the ice front (DR02–DR05); farther

landward (i.e., RS16 and beyond), the RIS attenuates Primary band flexural-gravity waves, as evidenced by Summer vertical power dropping to Winter values. Consequentially, RS16 through RS18 were likely recording vertical motion generated solely by the aforementioned crustal Rayleigh waves; this is substantiated by the similarities between the Summer vertical channel (HHZ) powers observed at RS08 (grounded) and RS18 (floating) on Figure 2.5a. That these stations, and RS10, lack the +5 dB summertime differential observed at grounded stations may indicate that the Rayleigh-to-flexural-gravity wave conversion is inefficient. By this interpretation, the intermediate stations (i.e., between DR05 and RS16) observed a transitional wavefield resulting from both processes.

North channel power during Summer recorded fundamental, symmetric mode (S0) Lamb waves (Figure A-2.3b) generated by the transfer of energy from ocean waves against the RIS front. This is consistent with Figure 2.6b in that, beyond DR02, the north (HHN) channel recorded a greater increase in Summer Primary band power than the east (HHE) channel, relative to Winter levels. The positive HOV (beyond 100 km landward, where flexural-gravity amplitudes are sufficiently attenuated) and northward-polarized oscillations are consistent with S0 Lamb waves originating at the ice front. Consistent with this interpretation, Chen et al. (2018) have previously derived and beamformed the generation of coherent S0 Lamb waves from discrete ocean swell events which arrived, on average, for 20 days out of each month during the summer. Our observations show that daily mean power within the Primary band remains elevated throughout the summer, with the only deviations of note being high-power spikes that presumably correspond to specific storm swells (e.g., Figure 2.5a; RS18, HHN, HHE). We thus suggest that the Summer ambient wavefield of the RIS includes a persistent (and likely incoherent) S0 Lamb wave component, independent of ocean storm conditions.

East component power during Summer is consistent with a combination of scattered S0 Lamb waves (from their general N-S propagation direction) and shear-horizontal plate waves of converted-wave or other origin. Scattering is also inferred from the homogenization of north and east powers near the Roosevelt Island grounding zones (Figure 2.6a), though this could also be influenced by

the thinning water layer. Shear-horizontal waves are suggested from the apparent deviation in spectral content between the north and east channels. For example, the non-parallel track of Traces 5 and 6 within Box A for station RS18 in Figure 2.4 indicates that waves recorded on the north versus east channels have different dispersion relationships; if power measured on the east component were due entirely to the scattering of S0 Lamb waves, the east HOV curve (Trace 6) would be expected to be lower than, but still parallel to, that of the north HOV (Trace 5). Admittedly, this hypothesis is based on rather tenuous evidence and would require a more in-depth evaluation for substantiation.

Along the West-East transect (ice front parallel, ~ 130 km landward; Figure 2.6a), three-channel powers during both seasons generally decrease with increasing ice thicknesses. For an elastic plate such as an ice shelf, the flexural rigidity is directly proportional to the cube of the plate thickness (e.g. Sergienko, 2017), consistent with the observation of weaker plate mode powers as ice thickness increases between RS01 (222 m) and RS07 (404 m). Additionally, because flexural-gravity waves are generated by the coupling of ocean gravity wave energy with the base of the RIS (Figure A-2.3a), and because ocean gravity wave energy decreases exponentially with depth, the vertical channel power associated with flexural gravity waves is further reduced with increasing ice thickness (Chen et al., 2018). A rigorous mechanical treatment of how three-dimensional RIS geometry affects the propagation of plate modes is, however, beyond the scope of this study. Alternatively, these geographic power distributions may also (or instead) be caused by unidentified oceanographic processes that modulate the propagation of ocean swell within the Ross Sea.

2.5.3 Secondary Band (5.0–10.0 s)

The Summer high-power state recorded by the Secondary band was generally similar across the array and notably less extreme than the Primary band. Secondary band powers increased coincident with increasing open water concentrations in the Ross Sea (Figure 2.7a; SEA), and continued to climb approximately linearly throughout the summer, even after the development of 100% open waters. Similarly, the high-power state decreased coincident with the development of minimal sea

ice densities and continued to drop linearly throughout Winter. For both years, Secondary band power generally increased between 1 December and 15 March, and decreased throughout the rest of the year.

Temporospatial correlations for grounded and floating stations (Figure 2.7b–d) were similar to those for the Primary band, reflective of their common source mechanism: i.e., ocean storm-generated swell that enters the Ross Sea and shoals on the continental seafloor (primary microseisms) or rebounds from the coasts and—possibly—the ice front of the RIS (secondary microseisms).

Variations in observed Secondary band power for the West-East and North-South transects are shown in Figure 2.8. Mean powers were generally equivalent for Winter and Summer due to the strongly linear seasonal trends (Figure 2.7a). Exceptions to this are stations RS01–RS05 and DR04–DR10, which recorded higher horizontal powers during Summer (Figure 2.8). HOV values at grounded stations were slightly negative (>-5 dB), reflective of the crustal secondary microseism Rayleigh wavefield that is expected to dominate this band. Floating station HOV values were strongly negative (>-15 dB) and dependent on ice thickness and distance from the ice front.

Interpretation of Secondary Band Energy

Based on these observations, we suggest that the composition of the Secondary band wavefield is mechanically similar to the Primary band wavefield, but is more strongly attenuated by distance from the ice front and ice thickness (i.e., compare Figure 2.6b, Figure 2.8b).

The vertical component of the RIS wavefield is dominated by strong flexural-gravity modes (Figure A-2.3a) near the ice front, but transitions to a secondary microseism crustal Rayleigh wave regime at landward distances greater than 50 km (Figure 2.8b). At this time, we have not evaluated the physical dependencies of this regime transition for this period band.

The horizontal wavefield has a significant S0 Lamb wave component (Figure A-2.3b) that is attenuated by some combination of distance from the ice front and ice thickness (Figure 2.8a and b, respectively); we do not at this time propose an exact mechanical description of this dependency.

As noted in the discussion for the Primary band, the relatively thinner ice below the western RIS results in a lower flexural rigidity, which in turn allows for the excitation of shorter period S0 Lamb waves (Viktorov, 1967) in response to the impact of shorter period ocean gravity waves at the RIS ice front. A comparison of the differential PSDs for the horizontal channels at, for example, RS01 and RS04 illustrates this "spectral leakage" of the Primary band into the Secondary period range (Figure A-2.24, Figure A-2.27; Traces 2 and 3). This is also evident in the daily Secondary band powers at, for example, RS04 (Figure 2.7a), for which the horizontal channels recorded a dramatic, late-Summer decrease coincident with a similar power drop in the Primary band (Figure 2.5a). In the absence of S0 Lamb wave energy, the horizontal channels at floating stations also appear to record secondary microseism Rayleigh energy, as inferred from the similarities between the daily power plots at, for example, RS08 and RS18 during Summer (Figure 2.7a).

2.5.4 Tertiary Band (0.4–4.0 s)

Summer excitation of the Tertiary band was strongly observed at all floating stations on the Ross Ice Shelf (e.g., Figure 2.9a). The Tertiary band is also well-observed at grounded stations in adjacent provinces: for example, at VNDA, located in the Dry Valleys of Victoria Land, 122 km west of Ross island (see also, Figure 2.4), and at RS14, located approximately 300 km east of the RIS in Marie Byrd Land (Figure A-2.37). The temporal behavior of the high-power state was generally similar for floating and grounded stations, with onset, termination, and time spent at peak being generally correlated to open water concentrations for a region of the Ross Sea directly north of the eastern RIS (Figure 2.9a–c). The 10–21 January 2016 melt event (Nicolas et al., 2017; Chaput et al., 2018) contemporaneously depressed Tertiary band power at all study locations but otherwise did not strongly influence season-long trends for 2015–2016. For both years and at all stations, this high-power state was generally active between 1 December and 31 March.

Temporospatial correlations at all stations suggest that the Tertiary band is sensitive to bathymetric features (Figure 2.9b–d, Figure A-2.2). Correlations were highest (>0.8) for open waters above the continental shelf break (with depths <1000 m). In particular, the region-of-interest out-

lined in the eastern Ross Sea (Figure 2.9a–c) overlies the Hayes and Houtz Banks, which range from ~ 400 to ~ 500 m below sea level, compared to the ~ 600 m for the adjacent basins (Figure A-2.2). High correlations in the western Ross Sea also display features reminiscent of the underlying Crary, Mawson, and Pennell banks and the intervening troughs. The area corresponding to the Ross Sea Polynya (RSP) is surprisingly well-defined by relatively lower correlations. A high-correlation zone in the northeast Ross Sea—above the apparent continental rise at a depth of 4000 m below sea level—is not associated with any geophysical feature or process that we can identify, though it is adjacent to a region of anomalously melt-resistant sea ice (Figure 2.2). VNDA, installed in a solid-rock borehole in the ice-free McMurdo Dry Valleys, recorded qualitatively dissimilar temporospatial correlations to the RIS array; for example, RS01 was highly similar to RS04, despite an interstation distance of 250 km, versus a distance of only 200 km to VNDA (Figure A-2.6, Figure A-2.7).

Spatial power trends across the RIS for the Tertiary band are presented in Figure 2.10. Floating station HOV values were generally uniform for both horizontal channels, independent of distance from the ice front, water column thickness, or ice thickness. Compared seasonally, HOV values were slightly lower in Winter (-12 dB) than Summer (-10 dB), indicating a larger increase in horizontal channel power during the Summer high-power state. Along the West-East transect (Figure 2.10a), the Summer band power increase was ~ 12 dB for vertical channels and ~ 14 dB for horizontal channels for all floating stations except for RS10, which observed an 8 dB increase for the vertical channel. For the North-South transect (Figure 2.10b), the Summer high-power state again decreased monotonically with distance from the ice front.

Grounded stations near the ice shelf margins (Figure 2.10a; RS08, RS09, RS11) recorded a summertime vertical channel increase of 10 dB, compared to < 6 dB for interior stations (RS12–RS14). As with the floating stations, all grounded stations observed a comparatively larger increase in horizontal powers during the summer, with HOV values increasing from -2 dB (Winter) to +2 dB (Summer). VNDA was again an outlier, with slightly negative HOV values all year (Figure 2.4; Traces 5, 6, 8, 9. Figure 2.9a).

Interpretation of Tertiary Band Energy

The spectral peak for the Summer high-power state was at ~ 1.2 s for both grounded and floating stations (Figure 2.4; Traces 1–3). At floating stations, local maxima were observed at periods consistent with P- and S-wave reverberations within the water and ice layers, respectively (Press and Ewing, 1951; Crary, 1954) (e.g., Figure 2.4; RS04. Figure A-2.3c), but only during the Summer (e.g., Figure A-2.27), indicating a strong excitation of ice and water layer reverberations by the high-power state wavefield. Other spectral features within this band may relate to flexural mode resonances between the RIS and the seafloor (e.g., Chen et al., 2018) or to the long-period compressibility limit for a thin, hydrostatic water column (Yamamoto, 1982; Ardhuin and Herbers, 2013).

High wind speeds measured at Franklin Island (Figure 2.9a; WTL) were inconsistently associated with spikes in Summer Tertiary band power, as was also observed for the Primary band (Figure 2.5a; WTL). Prior studies of smaller waterbodies have found evidence for a causal relationship between local wind velocities and wave heights and Tertiary band power (e.g., Kibblewhite and Ewans, 1985; Xu et al., 2017; Anthony et al., 2018). These studies had access to more spatially comprehensive data for wind velocities and wave heights; similar data are unfortunately not available for the Ross Sea for the deployment period of the RIS array. Nonetheless, we do observe a suggestive link between Tertiary band power and wind speeds (e.g., coincident peaks observed at RS04 and RS13 during the 2014–2015 summer, Figure 2.9a) to motivate future investigations.

The scope of our current analysis cannot positively identify the source mechanism or propagation modes for the Summer high-power state. We do, however, make two key qualitative interpretations: 1.) The excitation source is to the north of the RIS, either immediately at the ice front or in the continental shelf waters of the Ross Sea, and is longitudinally homogenous when averaged over the entire summer. These points are evident from, respectively, the landward decay of Tertiary band power along the North-South transect (Figure 2.10b), and the lack of azimuthal polarization on the horizontal channels (Figure 2.10a). 2.) The Summer high-power state is clearly recording an open water process, rather than fractional sea ice processes such as thermal or mechanical frac-

turing or inter-ice collisions. If the latter were responsible, we would expect a dramatic decrease in daily Tertiary band power as sea ice concentrations approached zero. Instead we find that Tertiary band power was at a maximum during prolonged periods of 100% open water concentrations (Figure 2.9a). Furthermore, fractional ice processes are typically observed in the 0.1–0.2 s (5–10 Hz) band (MacAyeal et al., 2003; Talandier et al., 2006; Dziak et al., 2015) and would therefore be expected to contribute only minimal energy to the 0.4–4.0 s Tertiary band.

2.6 Conclusions

We characterize the seasonal and spatial trends of the 0.4–20 s seismic wavefield observed on the Ross Ice Shelf (RIS) and at nearby terrestrial seismic stations. We show that the ambient spectral power recorded across this period band is very strongly modulated by the annual growth and breakup of sea ice in the adjacent Ross Sea, and quantify this variability on a seasonal time scale. Coupling between the RIS and oceanic processes during the sea ice-free summer months results in the excitation of a persistent, multimode wavefield that may increase ambient seismic noise by up to 30 dB above wintertime background levels, dependent on local RIS geometry and distance from the ice front.

In the 10–20 s Primary band, we used spatial and temporal changes in horizontal-over-vertical (HOV) ratios to infer that ocean gravity waves in this period range excite multiple vibrational modes within the RIS and that the vertical and horizontal wavefields are the results of separate processes. Within 100 km of the ice front, Summer power is predominantly vertical, consistent with flexural-gravity waves (i.e., buoyancy-coupled asymmetric Lamb waves); this wavefield attenuates rapidly (0.42 dB km^{-1}) with landward distance due to an unknown combination of intrinsic and scattering attenuations. Farther landward, vertical power is attributed to incompressible displacement of the sub-shelf water column by primary microseism crustal Rayleigh waves traveling along the sub-shelf seafloor. This primary microseism-induced signal is minor in comparison to the flexural-gravity modes and can only be easily observed once the latter has decayed to the Winter (sea ice-attenuated) background levels; our stations observe this to occur beyond 260 km

from the ice front. Beyond 100 km from the ice front, north and east HOV values are strongly and persistently positive throughout the summer. This horizontal ambient wavefield is polarized to the north, consistent with symmetric mode Lamb waves generated at the ice front. East HOV values suggest some scattering of symmetric Lamb waves from grounding zones and the possible generation of shear-horizontal plate modes. Onset and termination of the high-power state within this band are strongly correlated with open water concentrations in the (low-salinity) Ross Gyre, suggesting that melt-resistant sea ice in this region is a particularly strong modulator of ocean swell in the Ross Sea.

In the 5–10 s Secondary band, spatial and seasonal variations in spectral power indicate a Summer wavefield similar in composition to the Primary band. Flexural-gravity waves again dominate near the ice front but attenuate (0.35 dB km^{-1}) to shelf-interior background levels within 50 km. S0 Lamb waves are evident at stations within 150 km of the ice front and are additionally attenuated in regions of increased ice thicknesses. We conclude that these flexural-gravity waves and S0 Lamb waves are merely a short-period extension of the same excitation processes identified in the Primary band. In the absence of these plate wave modes, floating stations indicate three-dimensional elastic coupling between the RIS and secondary microseism Rayleigh waves propagating in the sub-shelf crust. In comparison to nearby grounded stations, vertical channel power at floating stations is actually elevated by +5 dB, while horizontal channel powers are depressed by -10 dB.

In the 0.4–4.0 s Tertiary band, we make initial observations of a seasonal ambient signal that is strongly observed across the RIS and up to 250 km to the east in Marie Byrd Land. At all floating stations, Summer power in this band is predominantly vertical (HOV < -10 dB), azimuthally symmetric (horizontal channel powers are equivalent), and decreases monotonically with landward distance from the RIS ice front; these observations indicate that the signal source is broadly distributed along the RIS ice front or across the Ross Sea. Onset and termination of the high-power state within this band are anticorrelated with sea ice densities in the waters above the continental shelf, particularly above local bathymetric highs (<400 m below sea level). Peak power is reached and maintained only during periods of minimal sea ice, indicating that the source mechanism is an

open sea process, possibly related to the same linear and nonlinear ocean wave interactions that generate the primary and secondary microseisms, respectively.

For all three bands, we find that wintertime ambient noise levels recorded on vertical channels at floating stations were generally less than 10 dB higher than those recorded at the nearby grounded stations. Wintertime ambient noise levels recorded on horizontal channels at floating stations, however, were as much as 10 dB lower than those recorded at the grounded stations, reflective of the isolation of floating stations from solid-Earth shear motions. Tertiary band powers for floating station horizontal channels, in particular, were equal to or less than the Global Seismic Network New Low Noise Model.

2.7 Tables

Table 2.1: Ambient spectral bands referred to in this study. The lettered bands are specifically addressed in this study. The Flexural-Gravity and Extensional bands are covered in other sources (see Section 2.5) and are listed here only for completeness.

Band Name	Box	Bandpass
Flexural-Gravity	—	50 – 100s
Extensional	—	20 – 50 s
Primary	A	10 – 20 s
Secondary	B	5 – 10 s
Tertiary	C	0.4 – 4.0 s

Table 2.2: Wave modes of the Ross Ice Shelf. Velocities and periods, unless otherwise noted, are calculated with ice thickness $h = 330$ m, water thickness $H = 440$ m, P-wave velocity $\alpha_i = 3.87$ km s⁻¹, S-wave velocity $\beta_i = 1.875$ km s⁻¹ ^a, and acoustic velocity $\alpha_w = 1.50$ km s⁻¹.

Wave Type	Wavelength Limits	Bandpass (s)	Velocity (km s ⁻¹)	HOV (dB)	Notes
Flexural-Gravity	< 11 km ^f	$\sim 1 - 150$	$< 0.07^{b,d}$	(-)	Transitions to pure gravity modes at very long periods. Transitions to water-coupled A0 Lamb at short periods.
Lamb, A_0	$\frac{h}{2} - 2(h+H)$	$0.1 - 1.0$	$\leq \alpha_w^d$	(-)	Transitions to Rayleigh wave at short periods.
Lamb, S_0	$\frac{h}{2} - \infty$	$0.1 - \infty$	$3.2^{b,c}$	(+)	Insensitive to ice/water interface. ^b Transitions to Rayleigh wave at short periods.
Rayleigh	$\frac{1}{\infty} - \frac{h}{2}$	$\frac{1}{\infty} - 0.1$	1.75^c	(-)	Couples with both plate surfaces at long periods. Dispersive for periods < 0.02 s; i.e., confined to firn layer. ^a
Love, $n = 1$	$\approx 5.0h$	0.33	5.0^c	(+)	For $p = 0.2$ s km ⁻¹ .
Crary, $n = 1$	$\approx 0.97h$	0.15	2.1^e	(+)	For $\theta_c = 29^\circ$.

^a Empirical value from Diez et al. (2016).

^b Empirical value from Chen et al. (2018).

^c Theoretical value from Viktorov (1967).

^d Theoretical value from Robinson (1983).

^e Theoretical value from Crary (1954).

^f Flexural-gravity wavelength from Lipovsky (2018).

Table 2.3: Number of days per year for which DRxx station mean band power (M) (based on the daily median power) approached the band-averages for the New Low and New High Noise Models (NLNM and NHNM, respectively) (Peterson, 1993). The left column tallies the number of days such that $M \leq \text{NLNM} + 2$ dB; the right column tallies the number of days such that $M \geq \text{NHNM} - 2$ dB. Lo/Hi days were counted across the full deployment and scaled to 365 days.

Station		Tertiary (0.4–4.0 s)	Secondary (5–10 s)	Primary (10–20 s)	Extensional (20–50 s)	Flex-Grav (50–100 s)
DR01	HHZ	0 10	0 124	0 49	0 365	0 365
	HHN	35 5	0 94	1 39	0 365	0 365
	HHE	50 2	0 90	1 22	0 365	0 365
DR02	HHZ	0 19	0 352	0 67	0 365	0 365
	HHN	0 14	0 136	0 53	0 365	0 365
	HHE	1 9	0 141	0 51	0 365	0 365
DR03	HHZ	0 21	0 109	0 27	0 365	0 365
	HHN	14 6	0 71	3 21	0 365	0 365
	HHE	19 5	0 71	0 16	0 365	0 365
DR04	HHZ	0 0	0 66	0 2	0 344	0 344
	HHN	194 0	0 57	2 0	0 344	0 344
	HHE	192 0	2 52	2 0	0 344	0 344
DR05	HHZ	0 0	0 41	0 0	0 365	0 365
	HHN	232 0	3 44	3 0	0 365	0 365
	HHE	222 0	7 36	2 0	0 360	0 365
DR06	HHZ	0 0	0 8	0 0	0 275	0 365
	HHN	226 0	4 42	2 0	0 360	0 365
	HHE	224 0	6 27	4 0	0 336	0 365
DR07	HHZ	0 0	0 2	0 0	0 150	0 365
	HHN	223 0	5 42	1 0	0 352	0 365
	HHE	210 0	4 37	3 0	0 290	0 365
DR08	HHZ	0 0	0 1	0 0	0 116	0 365
	HHN	224 0	8 37	2 0	0 351	0 365
	HHE	205 0	9 28	4 0	0 286	0 365
DR09	HHZ	0 0	0 1	0 0	0 100	0 365
	HHN	227 0	10 35	5 0	0 350	0 365
	HHE	227 0	10 24	5 0	0 289	0 365
DR10	HHZ	0 0	0 1	0 0	0 110	0 365
	HHN	228 0	7 35	4 0	0 351	0 365
	HHE	227 0	10 20	5 0	0 294	0 365
DR11	HHZ	0 0	0 1	0 0	0 157	0 365
	HHN	224 0	12 31	5 0	0 354	0 365
	HHE	207 0	13 18	6 0	0 301	0 365
DR12	HHZ	0 0	0 1	0 0	0 88	0 365
	HHN	219 0	5 29	4 0	0 351	0 365
	HHE	214 0	9 17	4 0	0 296	0 365
DR13	HHZ	0 0	0 0	0 0	0 69	0 365
	HHN	222 0	5 36	4 0	0 353	0 365
	HHE	219 0	10 13	5 0	0 291	0 365
DR14	HHZ	0 0	0 0	0 0	0 49	0 365
	HHN	213 0	11 21	0 0	0 289	0 365
	HHE	192 0	19 6	5 0	0 212	0 365
DR15	HHZ	0 0	0 0	0 0	0 0	0 353
	HHN	209 0	15 6	5 0	0 248	0 365
	HHE	202 0	30 1	8 0	0 134	0 352
DR16	HHZ	0 0	0 0	0 0	0 0	0 0
	HHN	250 0	118 0	23 0	0 19	0 24
	HHE	242 0	141 0	24 0	0 1	0 2

Table 2.4: Continuation of Table 2.3 for RSxx stations.

Station		Tertiary (0.4–4.0 s)	Secondary (5–10 s)	Primary (10–20 s)	Extensional (20–50 s)	Flex-Grav (50–100 s)
RS01	HHZ	0 0	0 44	0 1	0 365	0 365
	HHN	189 0	0 60	0 0	0 365	0 365
	HHE	193 0	0 56	0 0	0 360	0 365
RS02	HHZ	0 0	0 27	0 5	0 359	0 365
	HHN	208 0	0 56	1 0	0 364	0 365
	HHE	180 0	2 44	0 0	0 328	0 365
RS03	HHZ	0 0	0 7	0 7	0 215	0 365
	HHN	212 0	3 52	2 0	0 352	0 365
	HHE	118 0	7 41	1 0	0 319	0 365
RS04	HHZ	0 0	0 2	0 0	0 168	0 365
	HHN	210 0	8 34	3 0	0 353	0 365
	HHE	185 0	11 16	6 0	0 295	0 365
RS05	HHZ	0 0	0 4	0 0	0 205	0 365
	HHN	234 0	27 13	11 0	0 356	0 365
	HHE	229 0	34 7	7 0	0 305	0 365
RS06	HHZ	0 0	0 0	0 0	0 56	0 365
	HHN	229 0	62 3	31 0	0 272	0 365
	HHE	232 0	40 2	15 0	0 265	0 365
RS07	HHZ	0 0	0 1	0 0	0 19	0 365
	HHN	185 0	29 0	17 0	0 116	0 365
	HHE	87 0	19 0	4 0	0 76	0 365
RS08	HHZ	0 0	0 0	0 0	0 0	0 0
	HHN	1 0	0 0	0 0	0 0	0 0
	HHE	1 0	0 0	0 0	0 0	0 0
RS09	HHZ	17 0	17 0	17 0	17 0	17 0
	HHN	17 0	17 0	17 0	17 0	17 47
	HHE	17 0	17 0	17 0	17 0	17 0
RS10	HHZ	0 0	0 0	0 0	0 0	0 0
	HHN	5 0	0 3	0 0	0 116	0 236
	HHE	108 0	0 3	0 0	0 133	0 82
RS11	HHZ	0 0	0 0	0 0	0 0	0 0
	HHN	0 0	0 0	0 0	0 70	0 158
	HHE	0 0	0 0	0 0	0 56	0 141
RS12	HHZ	0 0	0 0	0 0	0 0	0 0
	HHN	0 0	0 0	0 0	0 0	0 1
	HHE	0 0	0 0	0 0	0 0	0 0
RS13	HHZ	0 0	0 0	0 0	0 0	0 0
	HHN	0 0	0 0	0 0	0 46	0 116
	HHE	0 0	0 0	0 0	0 59	0 116
RS14	HHZ	0 0	0 0	0 0	0 0	0 0
	HHN	0 0	0 0	0 0	0 73	0 142
	HHE	0 0	0 0	0 0	0 69	0 112
RS15	HHZ	0 0	0 0	0 0	0 0	0 0
	HHN	239 0	169 0	25 0	0 23	0 258
	HHE	250 0	131 0	9 0	0 2	0 120
RS16	HHZ	0 0	0 0	0 0	0 0	0 0
	HHN	234 0	48 0	11 0	0 61	0 282
	HHE	228 0	72 0	9 0	0 27	0 17
RS17	HHZ	0 0	0 0	0 0	0 0	0 0
	HHN	0 0	0 0	0 3	0 0	0 0
	HHE	0 0	0 0	0 2	0 0	0 0
RS18	HHZ	0 0	0 0	0 5	0 0	0 0
	HHN	260 0	162 0	7 0	0 4	0 15
	HHE	259 0	170 0	8 0	0 0	0 6

2.8 Figures

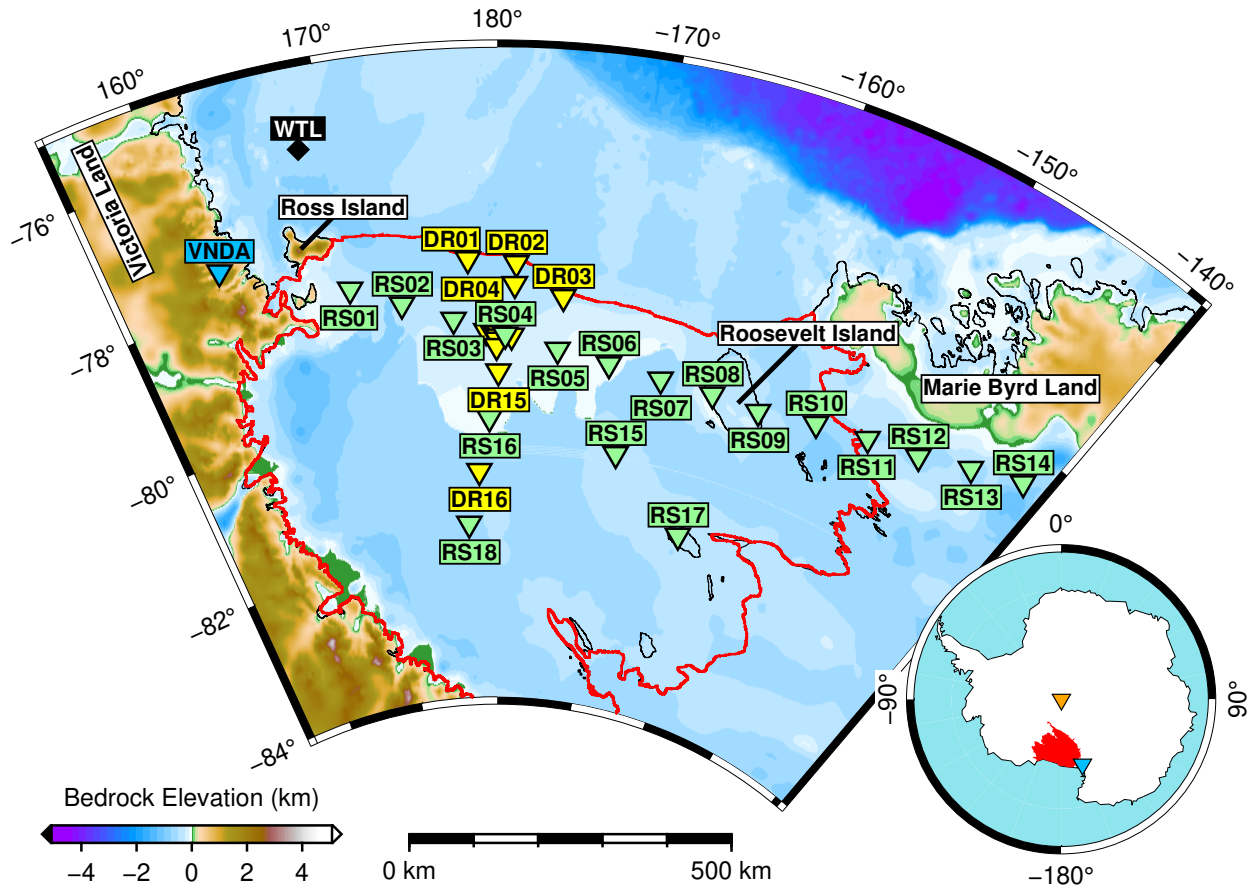


Figure 2.1: RIS array station locations. DR stations not explicitly labeled here (DR05–DR14; unlabeled yellow triangles) were deployed in the vicinity of central station RS04, as shown in Figure A-2.1. High-resolution bathymetry is shown in Figure A-2.2. All RS and DR stations were deployed on ice and all were on the floating ice shelf with the exception of: RS08 and RS09 on Roosevelt Island; RS11–RS14 on the West Antarctic Ice Sheet in Marie Byrd Land; and RS17 on an unnamed subglacial island within the RIS. Also shown is the bare-rock station VNDA (blue) in the Dry Valleys region, and Automatic Weather Station (AWS) WTL on Franklin Island. The Ross Ice Shelf is outlined in red. Inset: Map of Antarctica at the standard Grid-North orientation, with the Ross Ice Shelf highlighted in red. QSPA (orange) and VNDA (blue) are shown for reference.

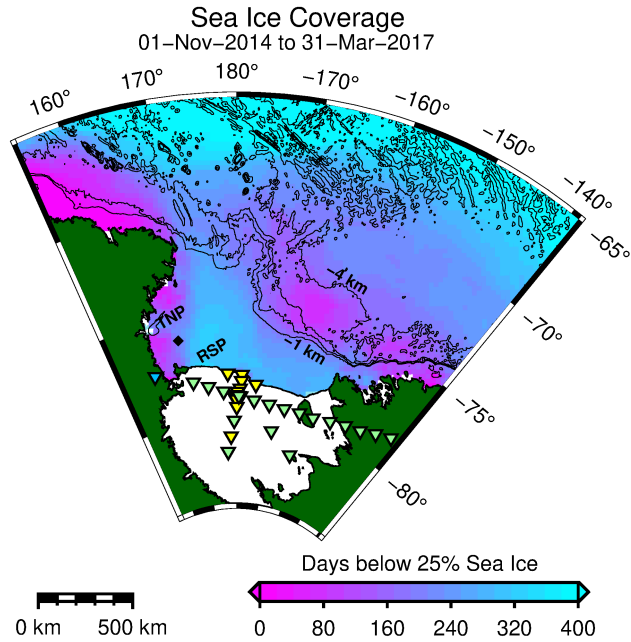


Figure 2.2: Sea ice concentrations in the Ross Sea (Cavalieri et al., 1996), presented as the number of days that each 25 x 25 km cell recorded a concentration below 25%. Blue indicates portions of the Ross Sea where the sea ice is minimal during the summer, while fuchsia indicates areas of near-perennial sea ice coverage. Bathymetry contour lines are presented at 1 km intervals. RSP and TNP mark the approximate locations of the annual Ross Sea and Terra Nova Polynyas, respectively.

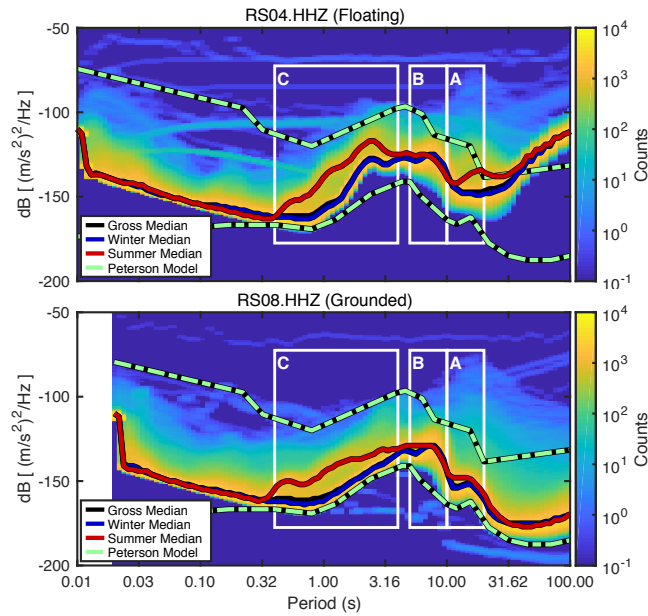


Figure 2.3: Vertical channel Power Spectral Density Probability Distributions Functions (PSD-PDFs) from representative floating and grounded stations. RS04 is situated near the intersection of the array transects and has the array-wide median ice thickness of 330 m. RS08 is on grounded ice at Roosevelt Island. Labeled boxes (A, B, C) outline the signal bands listed in Table 2.1 and discussed throughout the text. Green contours denote the Global Seismographic Network-derived New High and New Low Noise Models (Peterson, 1993). The high-power, low-probability broadband artifacts apparent on both stations are caused by transient sensor processes (e.g., McNamara and Buland, 2004).

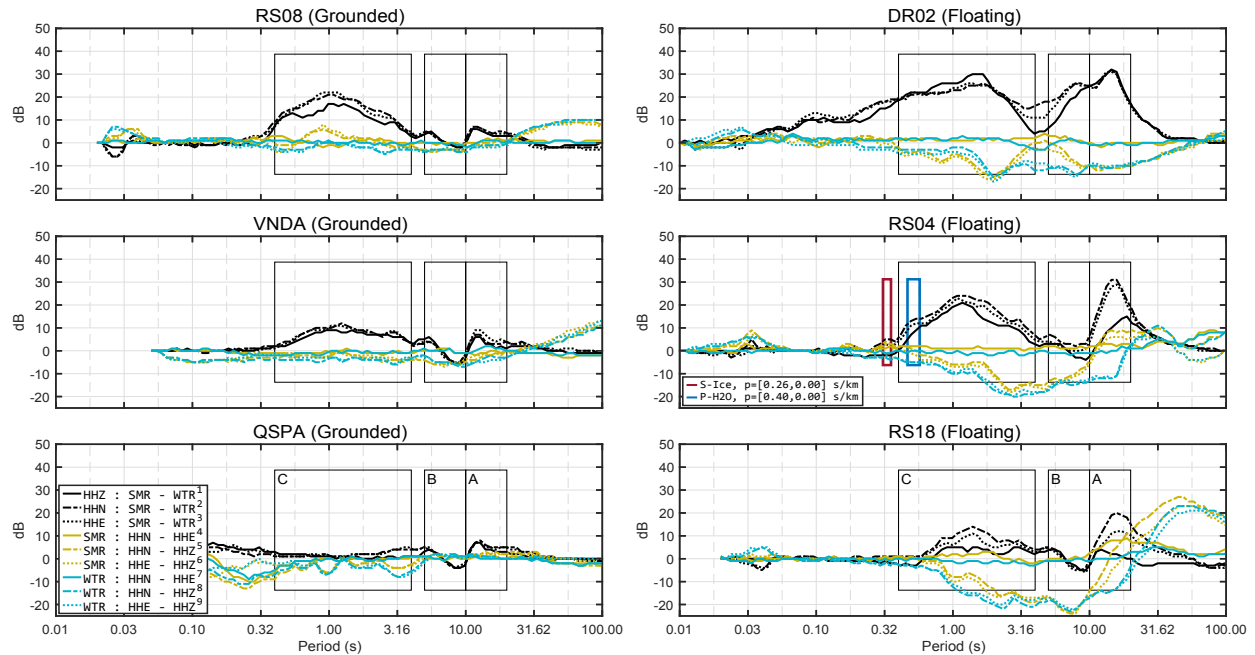


Figure 2.4: Differential PSDs for representative stations, showcasing the variations in seismic power for the disparate near-surface geometries. Traces are produced by subtracting the seasonal median PSD-PDF dB values. Black traces (1,2,3) show seasonal changes between for each component, with positive values indicating higher power during the Summer. Solid yellow (4) and teal (7) traces show power differences in north versus east components for Summer and Winter, respectively, with positive values indicating higher power observed on the north component. Chain-dashed yellow (5) and teal (8) traces indicate north versus vertical HOV values; dotted yellow (6) and teal (9) traces indicate east versus vertical HOV values.

RS08 is on grounded ice on the western shore of Roosevelt Island, ~ 7 km from the nearest grounding line and ~ 110 km from the RIS ice front. VNDA is a borehole sensor located in the ice-free McMurdo Dry Valleys, ~ 120 km from the RIS. QSPA is an ice-borehole sensor located 8 km from the Amundsen-Scott South Pole Station, ~ 600 km from the RIS, and is presented as a baseline for the Primary (A), Secondary (B), and Tertiary (C) bands. DR02 is ~ 3 km from the ice front and provides a reference near the ice front. RS04 is located at the intersection of the array transects (~ 135 km from the ice front) and is representative of RIS-interior floating stations. S-Ice and P-H₂O in the RS04 panel highlight spectral peaks caused by reverberations of S-waves in the shelf ice and P-waves in the water column, respectively.

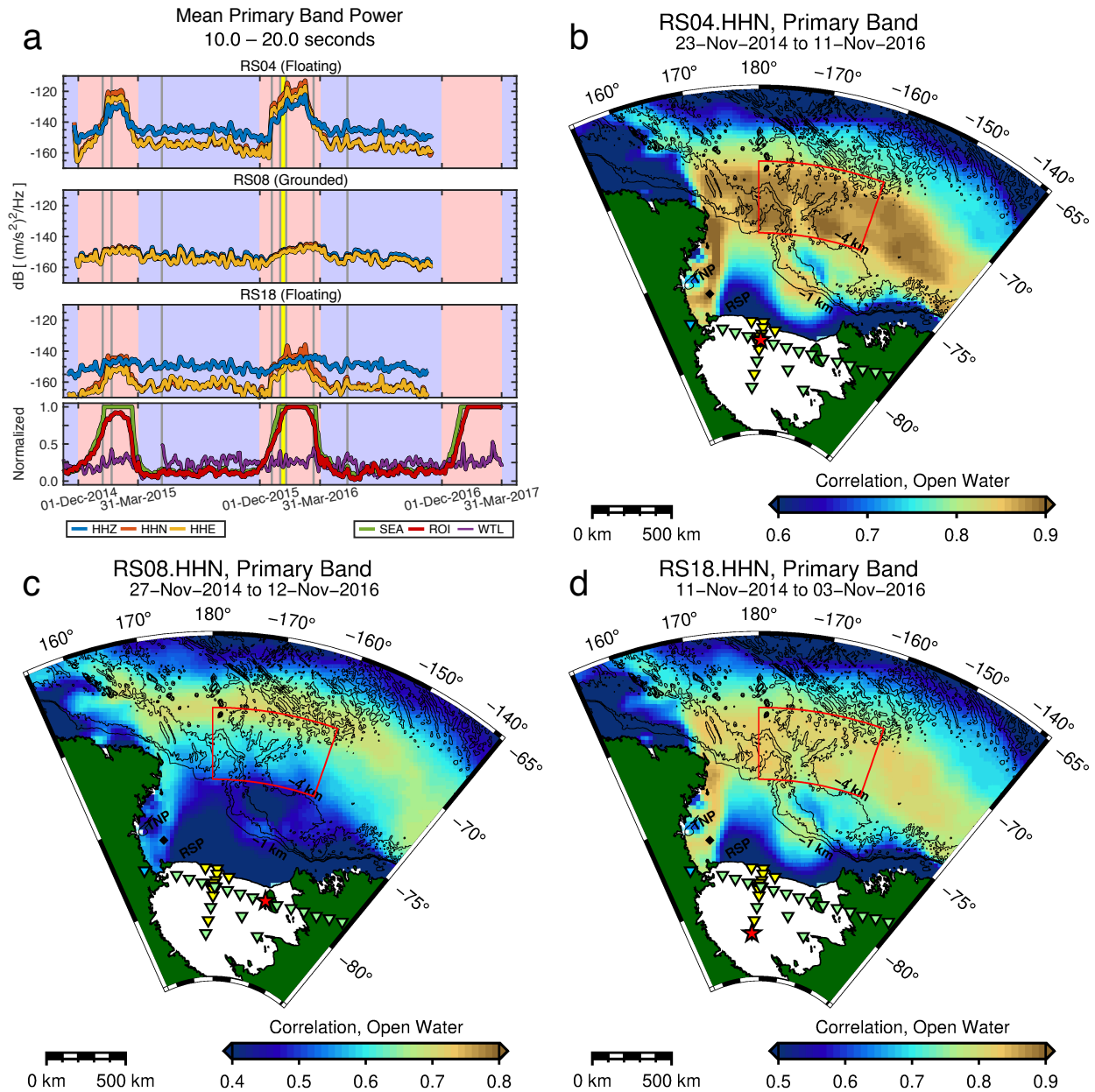


Figure 2.5: **a**) Daily average Primary band powers for vertical (HHZ), north (HHN), and east (HHE) seismometer channels, compared to median open water concentrations for the entire mapped region (SEA), the mean open water concentration for the red-bounded region-of-interest (ROI), and the mean daily wind speed measured at Franklin Island (WTL). Wind velocity has been normalized to 20 m s^{-1} . Primary band powers and wind velocity were smoothed with a ± 5 day moving average; open water concentrations were not smoothed. The vertical yellow band marks the 10 January to 21 January 2016 RIS melt event; the gray vertical bars mark wind events that correlate with elevated spectral band powers. Red and blue backgrounds indicate Summer and Winter months, respectively. **b–d**) Pearson correlation coefficients for daily mean Primary band north component power and daily open water concentration at each cell. Both time series were smoothed with a ± 1 day moving average before correlation. Spatial distributions for vertical and east channels are similar. The red region-of-interest overlaps a near-central portion of the Ross Gyre.

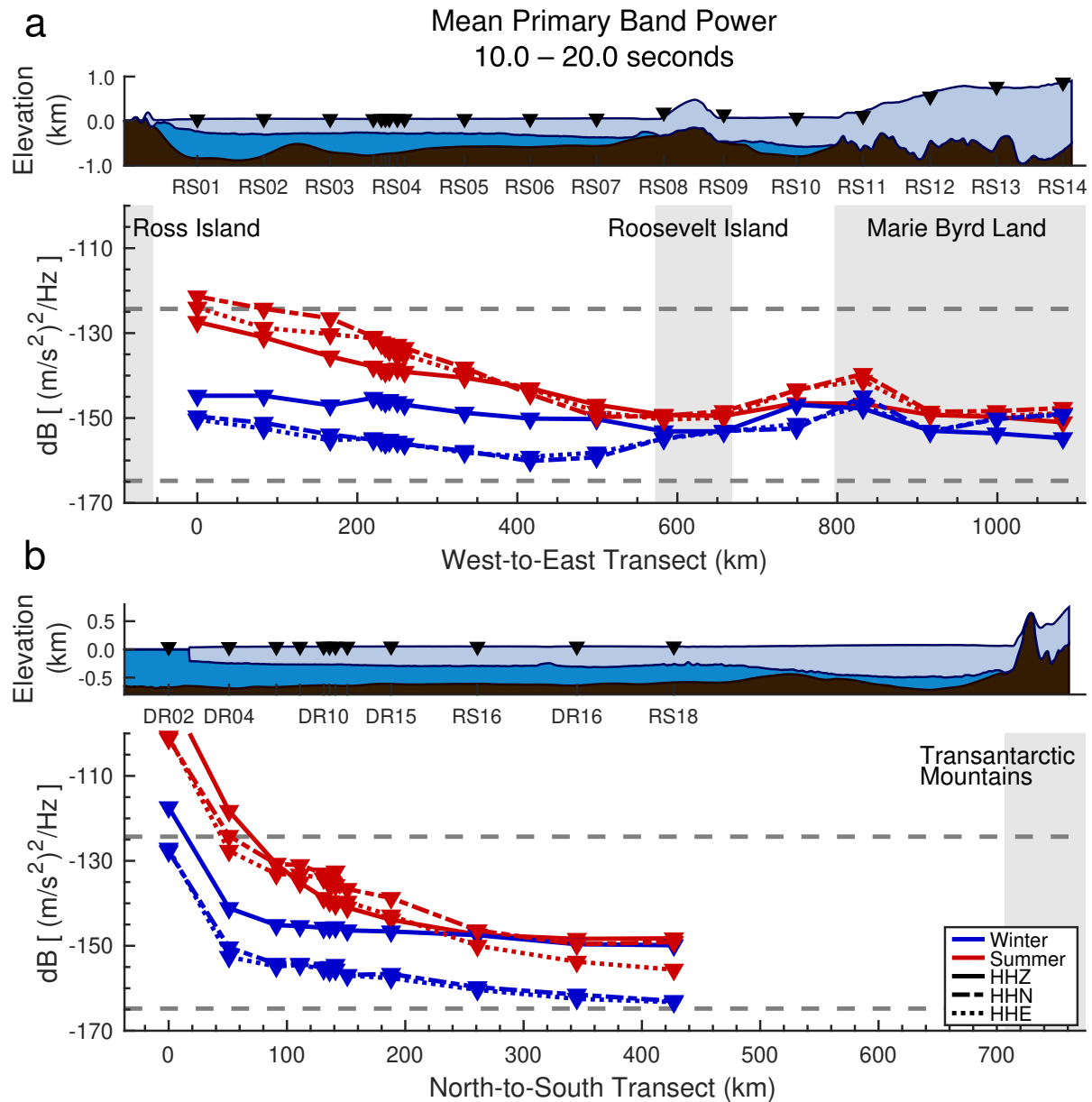


Figure 2.6: Seasonal and geographic variations in average seismic acceleration power in the Primary band, for the indicated seasonal PSD-PDF medians. DR02.HHZ summertime mean power was -90 dB. The dashed gray lines indicate the mean Global Seismic Network high- and low-noise model limits for the same band. Ice and water thickness profiles are based on outdated BEDMAP2 data. The RIS ice front currently sits ~3 km north of DR02. Gray backgrounds indicate approximate areas of grounded ice.

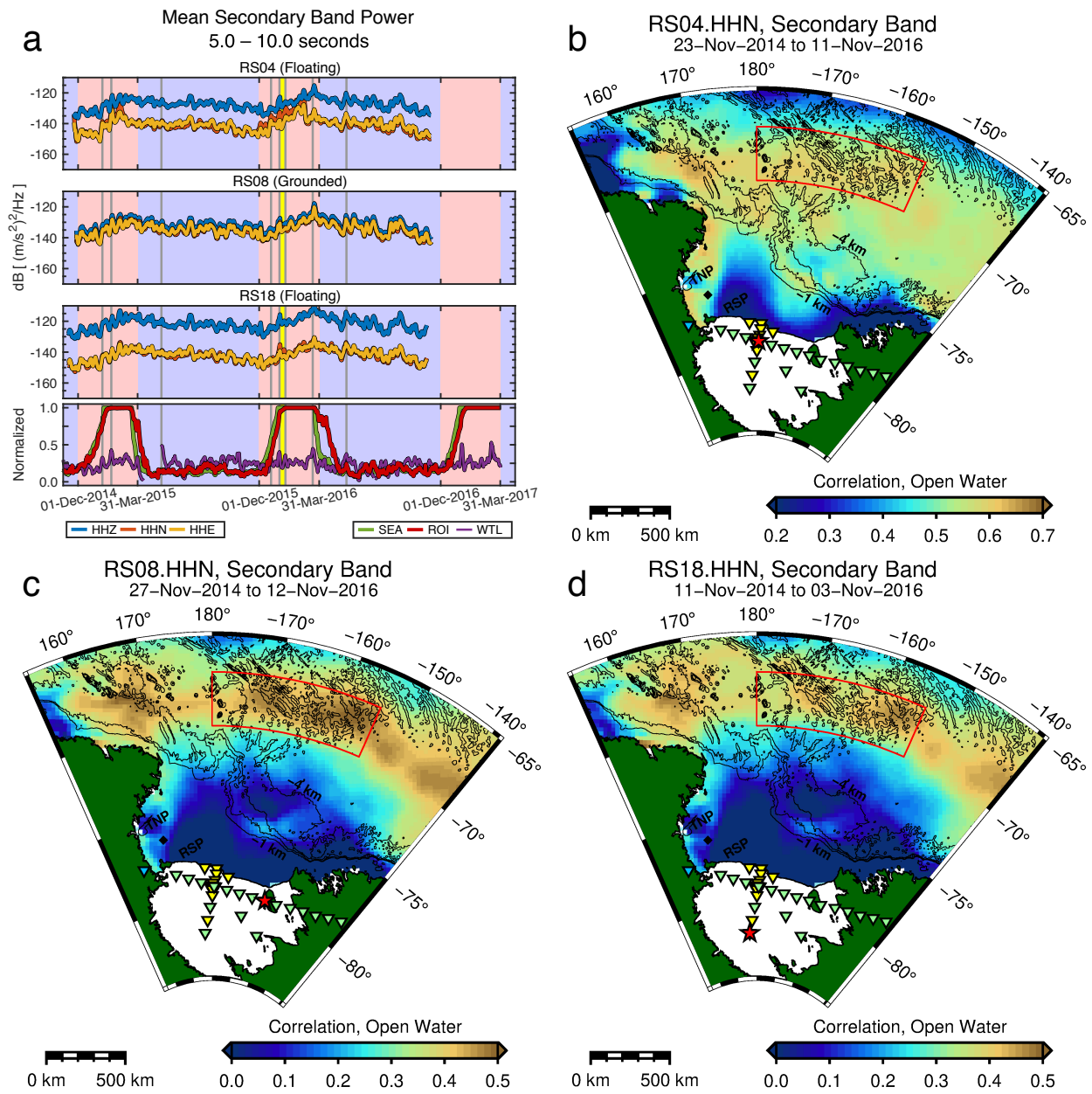


Figure 2.7: Temporal variations and temporospatial correlations for the Secondary band. See Figure 2.5 for details.

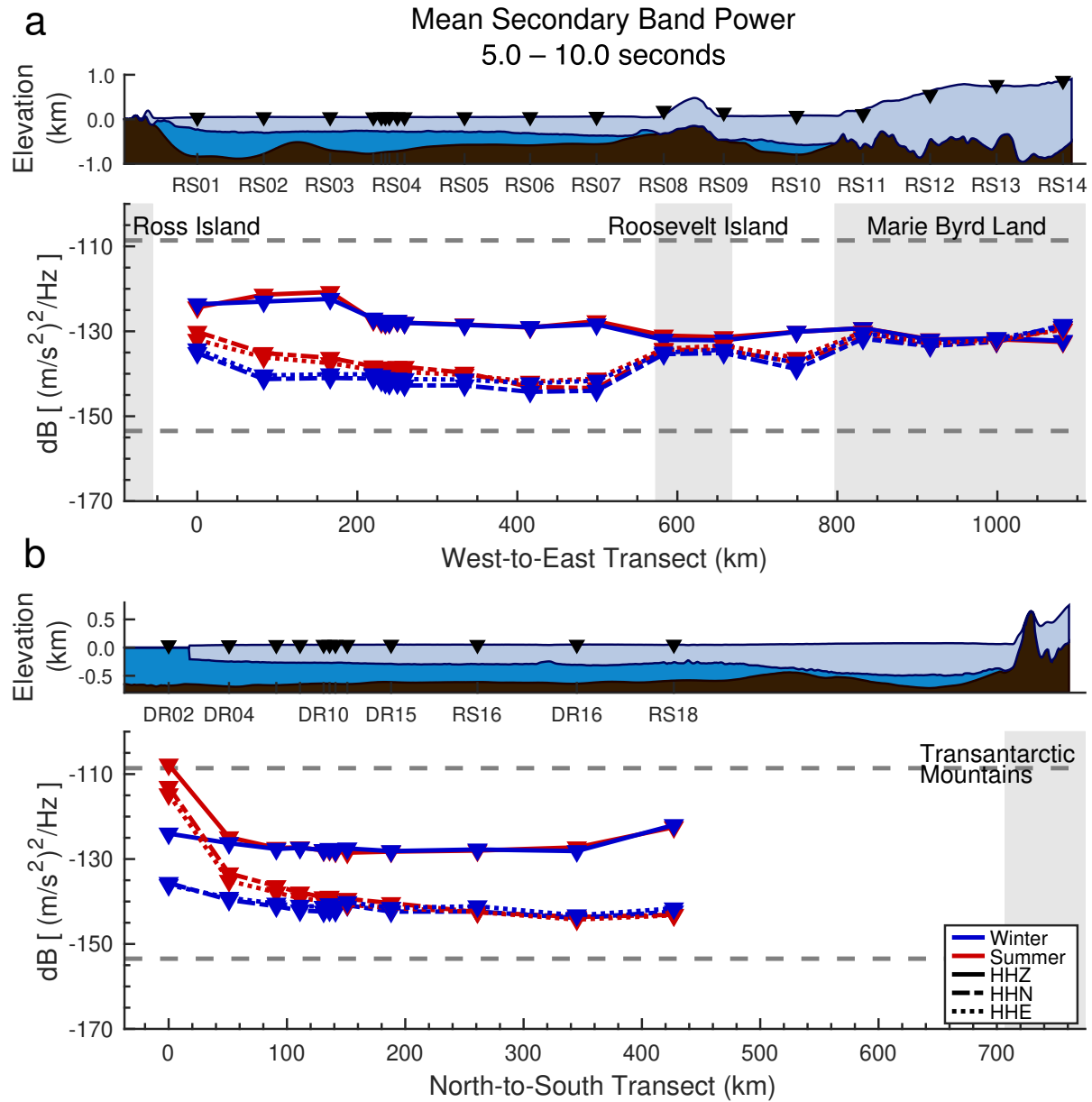


Figure 2.8: Seasonal and geographic variations of the Secondary band mean acceleration power. DR02 may be observing nonlinear mechanical excitation of the RIS ice front; these edge effects are beyond the scope of this study. See Figure 2.6 for details.

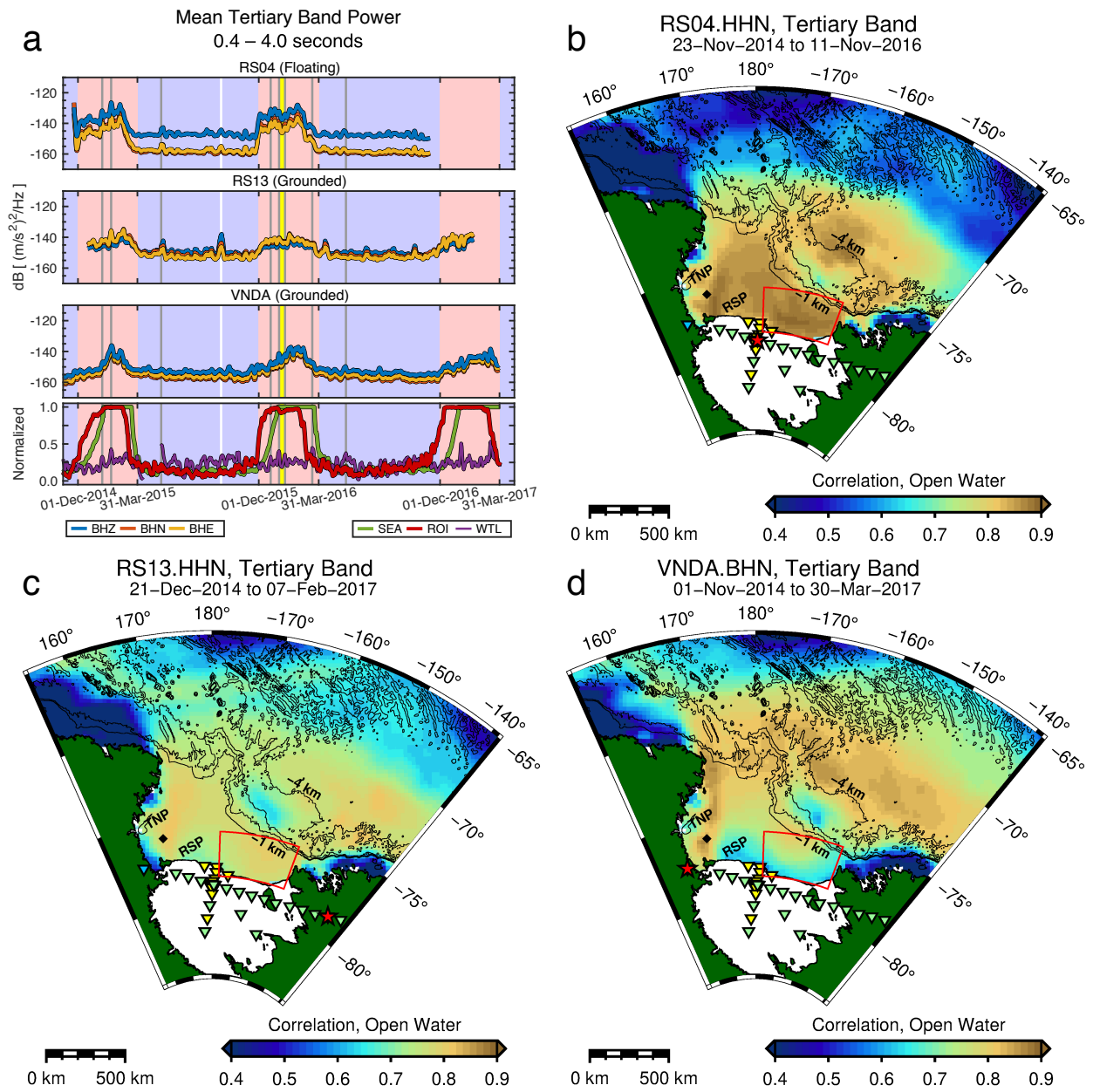


Figure 2.9: Temporal variations and temporospatial correlations for the Tertiary band. See Figure 2.5 for details. **a)** White vertical line marks the 16 September 2015 Mw 8.3 Illapel, Chile earthquake. **b–d)** The red-bounded region-of-interest encompasses the Hayes and Houtz Banks (Figure A-2.2).

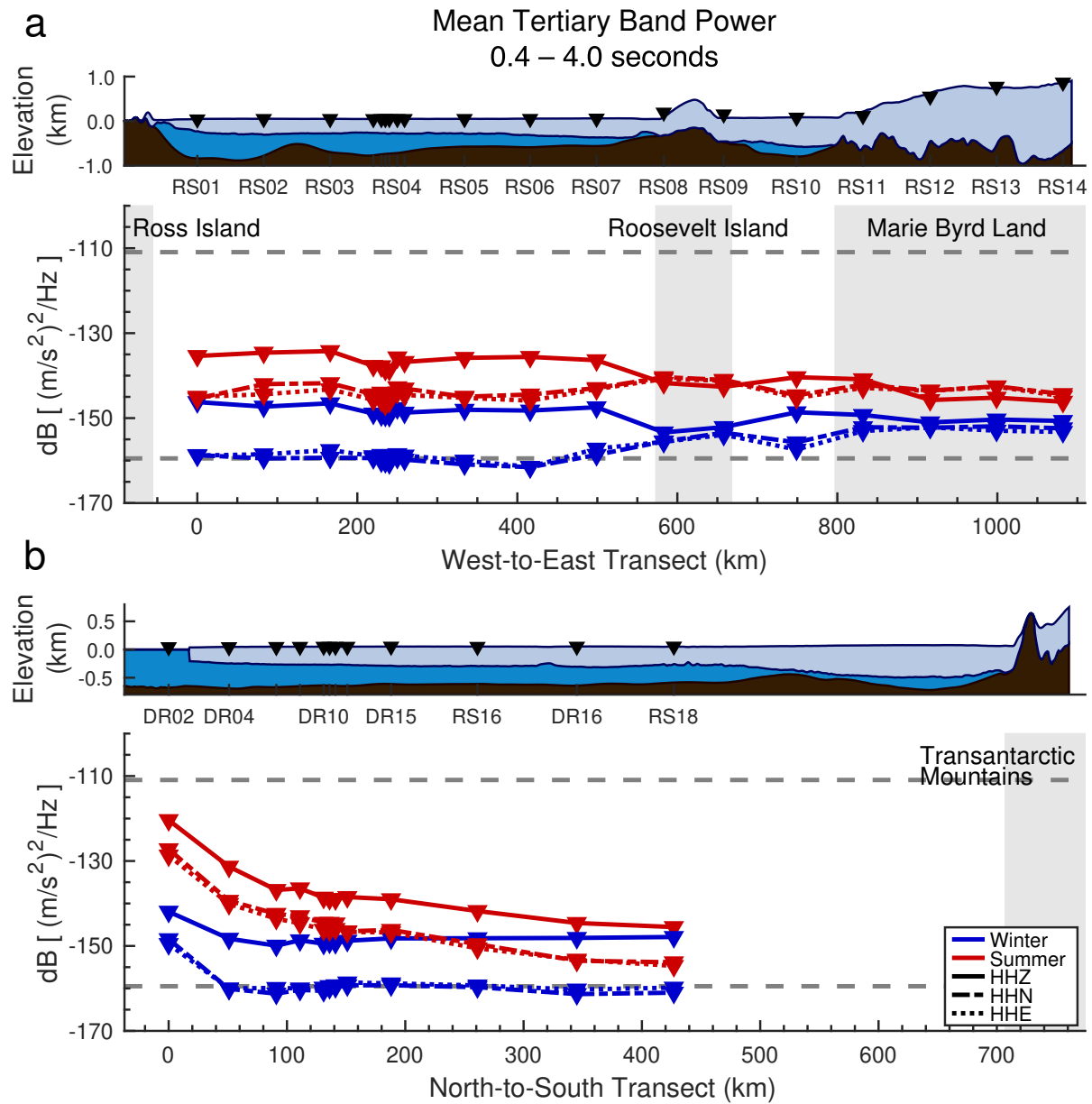


Figure 2.10: Seasonal and geographic variations of the Tertiary band mean acceleration power. See Figure 2.6 for details.

Chapter 3

Teleseismic Earthquake Wavefields Observed on the Ross Ice Shelf

²Observations of teleseismic earthquake signals with broadband seismometers on the Ross Ice Shelf (RIS) must contend with several environmental and structural processes that do not exist for land-sited seismometers. Important considerations are: 1) A broadband, multi-mode, elastic and flexural-gravity ambient wavefield excited by ocean gravity wave interactions with the ice shelf; 2) Strong body wave reverberations produced by high seismic impedance contrasts at the ice/water and water/seafloor interfaces; and 3) Decoupling of the solid Earth horizontal wavefield by the sub-shelf water column. We analyze seasonal and geographic variations in signal-to-noise ratios for teleseismic P-wave (0.5–2.0 s), S-wave (10–15 s), and surface wave (13–25 s) arrivals in the presence of the RIS background noise field. We show that ice and water layer reverberations generated by teleseismic P-waves may be used to accurately estimate the sub-station thicknesses of these layers. Finally, we present evidence for the generation of fundamental, symmetric-mode Lamb waves by teleseismic S-waves incident on the grounding zones of the RIS. Despite these complicating factors, we conclude that teleseismic signals can be readily utilized for passive imaging of Earth structure below ice shelves, although longer deployment durations—relative to conventional land-sited seismic stations—may be necessary to acquire adequate teleseismic data volumes.

3.1 Introduction

Multi-year seismic instrumentation of Antarctica has been historically sparse for regions not immediately accessible from the established science bases. This largely reflects the engineering

²This chapter has been submitted to the Journal of Glaciology as: Baker, M. G., Aster, R. C., Wiens, D. A., Nyblade, A., Bromirski, P. D., Gerstoft, P., and Stephen, R. A. Teleseismic Earthquake Wavefields Observed on the Ross Ice Shelf.

and logistical challenges of year-round seismograph operation in extreme environmental conditions and limited opportunities for maintenance and data recovery. Scientific motivations (e.g. Podolskiy and Walter, 2016; Aster and Winberry, 2017) and instrumentation advancements across the past two decades have resulted in a dramatic increase in available seismic data, driven by numerous deployments of long-term or permanent broadband seismic instruments in both West and East Antarctica (Anthony et al., 2015).

In the past decade, two key developments in particular have removed the scientific and technical barriers to long-term, broadband ice shelf seismology. First, multiple studies utilizing local and teleseismic data from grounded-ice networks have established new analytical methods for stations sited on thick glacial ice (e.g., Barklage et al., 2009; Chaput et al., 2014) and the baseline models of seismic activity (Anthony et al., 2015, 2017) necessary to contextualize broadband observations collected from an ice shelf-sited array. Second, community advancements in power and other technologies have produced lightweight broadband seismographs that are capable of continuous operation throughout multiple Antarctic winters.

Pioneering studies in ice shelf seismology have consisted of short-term deployments (less than three months) of single stations or small aperture arrays. High frequency experiments have focused on cyroseismic sources (Zhan et al., 2014) and active source imaging of ice shelf and seafloor structure (Kirchner and Bentley, 1979; Beaudoin et al., 1992). Other short-term studies placed broadband sensors at the RIS ice front and a free-floating iceberg and showed the viability of floating-ice-sited broadband seismometers as observatories of oceanic processes (Okal and MacAyeal, 2006; Cathles et al., 2009), and even teleseismic earthquakes (MacAyeal et al., 2009).

The RIS/DRIS 34-station broadband network (Figure 3.1) was installed in late 2014 across the Ross Ice Shelf (RIS) for a two-year study of oceanic, cyrospheric, and solid Earth processes (Wiens et al., 2015) by recording elastic and flexural-gravity waves on the ice shelf (Bromirski and Stephen, 2012). Ocean signals recorded atop large tabular floating ice bodies include tsunamis and infragravity waves (Bromirski et al., 2017); ocean swell (Okal and MacAyeal, 2006; Cathles et al., 2009; Baker et al., 2019); waves from remote calving events (MacAyeal et al., 2009);

and ice-ice and ice-seafloor interactions and their seismic and acoustic radiation (Talandier et al., 2006; Dowdeswell and Bamber, 2007; MacAyeal et al., 2008; Martin et al., 2010). The large-scale RIS/DRIS deployment additionally greatly expanded opportunities for teleseismic tomography in the sparsely-sampled Ross Embayment sector of the Antarctic plate (Shen et al., 2018; White-Gaynor et al., 2019), with scientific motivations that include tectonic province boundaries, possible plumes (Seroussi et al., 2017; Phillips et al., 2018) and the activity and origins of Antarctica's intraplate volcanism (e.g. Kyle et al., 1992; Hole and LeMasurier, 1994; Reusch et al., 2008; Lough et al., 2013). Heat flow, elastic lithosphere thickness, and mantle viscosity constrained by geodesy and seismic proxies (Ramirez et al., 2016; O'Donnell et al., 2017) have important implications for West Antarctic Ice Sheet dynamics and stability (Rignot and Jacobs, 2002; Joughin and Alley, 2011; Barletta et al., 2018).

The ambient seismic environment of the RIS during the RIS/DRIS project has been previously documented at short periods (<1 s) by Diez et al. (2016) and Chaput et al. (2018), and for longer periods (>30 s) by MacAyeal et al. (2006); Cathles et al. (2009); Bromirski et al. (2017) and Chen et al. (2018). For intermediate periods (0.5–20 s), Baker et al. (2019) presents seasonal and geographic variations in the RIS noise field and discusses potential source mechanisms. Our current signal-noise analysis makes extensive use of that work.

We present a signal-to-noise analysis of teleseismic P-wave (0.5–2.0 s period), S-wave (10–15 s), and surface wave (17–23 s) arrivals and their immediate coda. We show that these signals may be readily observed at floating-ice-sited seismographs, but are strongly modulated by seasonal changes in ocean wave-generated noise. We quantify how teleseismic observations are affected by station proximity to the RIS ice front and grounding zones and note secondary wavefields that are excited within the RIS by teleseismic wavefields. We utilize acoustic and Crary (i.e., SV-waves trapped in floating ice) reverberations to estimate water column and ice thicknesses, respectively. We document the conversion of teleseismic S-wave energy at grounding zones into fundamental mode, symmetric (S_0) Lamb waves (e.g., Figure 3.2) which may propagate as much as 250 km into

the ice shelf interior. Finally, we document teleseismic surface wave dispersion on the ice shelf and present representative group velocity curves for Rayleigh waves.

3.2 Data and Methods

3.2.1 Instrumentation

The coordinated RIS (Mantle Structure and Dynamics of the Ross Sea from a Passive Seismic Deployment on the Ross Ice Shelf) and DRIS (Dynamic Response of the Ross Ice Shelf to Wave-Induced Vibrations) projects (Figures 3.1, A-2.1) consisted of 34 polar-engineered broadband seismic stations provided by the Incorporated Research Institutions for Seismology (IRIS) Polar Programs. The stations were installed in late 2014 and recorded approximately two years of continuous data.

Seismographs were deployed in along two main transects: an 1100 km-long ice-front-parallel transect (W-E) and a 425 km long ice-front-perpendicular transect (N-S). The network consisted of 1) a shelf-spanning large aperture array (RS01 to RS18) with a median spacing of 83 km; and 2) a central medium aperture array (DR01 to DR16) with stations spaced at 20–50 km. RS04 is located at the intersection of the two main transects. All stations were sited on floating ice with the exceptions of RS08 and RS09 on Roosevelt Island, RS11–RS14 in Marie Byrd Land, and RS17 on an unnamed grounded region of the southern RIS.

Most RIS (RS) and DRIS (DR) stations utilized Nanometrics Trillium 120PH posthole sensors direct-buried at depths of 2–3 m below the snow surface; exceptions were RS09, RS11–RS14, and RS17, which were Nanometrics Trillium 120PA sensors installed on phenolic resin pads within shallow vaults. All DR stations and RS04 had a sampling rate of 200 Hz; all other RS stations had a sampling rate of 100 Hz. Stations used solar power during the Antarctic summer and single-use lithium thionyl batteries during the winter. Due to Iridium satellite power and bandwidth constraints, only state of health information was telemetered, and the network was therefore serviced in 2015 for intermediate data recovery and any other necessary servicing. The signal-to-noise analysis presented here incorporates data from the full deployment period of approximately November

2014 through November 2016. Stations RS10–RS14 remained deployed in Marie Byrd Land until early February 2017 due to logistical issues.

3.2.2 Teleseismic Earthquake Signals on the RIS

We perform a signal-to-noise ratio (SNR) analysis for teleseismic earthquake signals (M_w of 5.5 or greater) observed by RIS/DRIS stations at epicentral distances $>30^\circ$, selecting P-wave, S-wave, and surface wave arrivals and their immediate coda, with spectral bandpass filtering and signal times shown in Table 3.1. Predicted arrival times for individual phases for all earthquakes are based on *ak135* travel time curves (Kennett et al., 1995). Bandpass filtering was determined based on the peak periods of the median modified SNR curves.

To characterize teleseismic P-wave signals, we examine events at epicentral distances between 30° (slowness 0.08 s km^{-1}) and 95° (0.04 s km^{-1}) from each station. The teleseismic S-wave catalog is limited to events between 60° and 95° to prevent interference from surface wave arrivals near 5 km s^{-1} . Conversely, the surface wave catalog is restricted to 4 km s^{-1} to 2 km s^{-1} arrivals from earthquakes with epicentral distances between 45° and 100° to prevent interference from body waves.

The ambient noise field of the RIS in the 0.4–30 s period band has seasonal variations of approximately 5 to 20 dB (Baker et al., 2019). This seasonal amplitude dependence reflects the reduced excitation and attenuation of ocean gravity waves due to the appearance of spatially continuous winter Ross Sea sea ice (Anthony et al., 2015, 2017). A lack of extensive continuous ice determines the onset and termination dates of the “Summer” (1 December–31 March) high-noise state analyzed in Baker et al. (2019). We similarly subdivide our catalog into “Summer” earthquakes occurring during the approximate open-water interval between 1 December and 31 March, and “Winter” earthquakes occurring during the remainder of the year during which sea ice is broadly contiguous at the ice shelf front. Note that we henceforth refer to “winter” and “summer” noise conditions as indicating these annual sea ice-determined time periods following Baker et al. (2019), and not to the formal austral seasons.

3.2.3 Spectral Characterization of Teleseismic Signals

The signal-to-noise (SNR) ratios of individual events generally depend on a variety of source and propagation factors that include moment, radiation pattern, depth, and distance. Here, we focus on general reverberative teleseismic excitation of the ice shelf beyond that of initial phase arrivals (White-Gaynor et al., 2019). For body wave arrivals, the phase arrival and its subsequent coda are extracted in fixed duration time segments (Table 3.1) regardless of epicentral distances, back azimuths, and magnitudes. For surface wave trains, we analyze 4 to 2 km s⁻¹ surface waves, with a total signal length that is dependent on epicentral distance. Data segments for all three arrival types include 10 s of pre-arrival noise. For all segment types, the “noise” time series is drawn from immediate pre-arrival data using an equal number of seconds as the “signal” analysis. For example, for a P-wave arriving at $t_0 = 0$ s, the noise data is comprised of $T_n = [t_0 - 110 \dots t_0]$ s, while the signal data spans $T_s = [t_0 - 10 \dots t_0 + 100]$ s. All data are de-meaned, de-trended, cosine-tapered by 5 s, decimated to 10 Hz, and rotated to (Z,R,T) (vertical, radial, transverse) coordinates using USGS NEIC Comcat parameters.

SNR spectra are calculated as the ratios of the signal and noise power spectral densities (PSD). PSDs are estimated using Welch’s method (Welch, 1967), with the number of (Hann-tapered) sub-segments determined by requiring 80% overlap and sub-segment lengths approximately equal to ten times the upper period limits indicated in Table 3.1. PSD estimates are subsequently smoothed by averaging over 1/8 octave bins in 1/16 octave increments.

Due to the geographic extent of the RIS array and the nonuniform distribution of earthquake sources (Figure 3.1), not all stations observed the same population of earthquakes given the event selection process. These disparities are especially exaggerated during our defined high-noise, low-sea-ice summer (1 December –31 March) months, which include roughly a quarter of the number of events as the winter (1 April–30 November). For the goals of this study, we require an idealized teleseismic source that is uniformly observed by all stations, such that interstation variations in SNR are predominantly controlled by receiver-side phenomena. To approximate such a source, we apply a correction analogous to the relative radiometric normalization used in remote sensing, but

operating on the source rather than the receiver. We normalize individual earthquake SNRs to a theoretical earthquake model, with the scaling factor based on USGS seismic moment and losses from geometric spreading. For P- and S-waves, the corrected signal-to-noise ratio (SNR') is

$$SNR' = SNR \frac{M_{0ref}}{M_0} \left(\frac{D}{D_{ref}} \right)^2, \quad (3.1)$$

where SNR is the uncorrected signal-to-noise ratio, M_0 and M_{0ref} are the respective event and reference seismic moments, and D and D_{ref} are the depth-dependent, source-to-receiver ray path distances through a spherical *ak135* Earth model. For surface waves, the correction is

$$SNR' = SNR \frac{M_{0ref}}{M_0} \left(\frac{\sin(\Delta)}{\sin(\Delta_{ref})} \right), \quad (3.2)$$

where Δ and Δ_{ref} are the great arc distances, and the sine function corrects for two dimensional spreading (Stein and Wysession, 2009). We use a reference event with a magnitude of M_w 6.0 (the approximate mean of all observed events), band-specific great arc distances as listed in Table 3.1, and a depth of 10 km. We note that this algorithm adds an ~ 2.5 dB offset to the temporospatial SNR estimates presented.

We make no attempt to correct for source function beyond median stacking, nor do we eliminate overlapping events.

To evaluate seasonal variations in SNR, we calculate the seasonal median SNR from all appropriate summer and winter events, as defined above and in Baker et al. (2019). We evaluate spatial variations across the RIS array with respect to the mean of station-specific median seasonal PSDs for the arrival bandpasses listed in Table 3.1.

3.3 Elastic Waves in an Ice Shelf

Floating tabular ice bodies support elastic-gravity wavefields that are generally not encountered elsewhere in seismology (e.g., Viktorov, 1967; Sergienko, 2017; Chen et al., 2018; Baker et al.,

2019). Here, we overview short-intermediate period (<20 s) wave phenomena for floating elastic plates that are relevant to this study.

3.3.1 Elastic Structure

The Ross Ice Shelf spans an area of $487,000 \text{ km}^2$ and floats on the relatively shallow continental shelf waters of the Ross Sea embayment with only sparse internal pinning points. RIS/DRIS station sites have ice thicknesses of 200–400 m (median 325 m; \tilde{h}) and water column thicknesses of 100–700 m (median 464 m; \tilde{H}) in BEDMAP2 (Fretwell et al., 2013) (Table 3).

Laterally varying structures in ice shelves are introduced by the convergence of source glaciers near the grounding line and by the subsequent advection of shelf ice towards the RIS calving front (at up to 1 km yr^{-1} for the RIS). Internal structures include suture zones between tributary glaciers that persist to the terminus of the RIS ice front. Also present are subglacial and surface crevasses and rifts that are generally parallel with the calving front, reflecting a broadly tensional stress state in the seaward flow direction. This tensional stress field is magnified near the free-floating terminus (LeDoux et al., 2017) and is cyclically influenced by tidal tilt (e.g., Olinger et al., 2019). Significant vertical structure include a meteoritic snow-firn layer that transitions to glacial ice over tens of meters (e.g., Diez et al., 2016), and for some shelves, a seasonally modulated basal freeze layer. The sub-shelf seafloor may be comprised of up to several kilometers of low velocity lithified sediment overlying a high velocity basement (e.g., Beaudoin et al., 1992).

We assume bulk elastic properties for the RIS system as listed in Table 3.2. We also assume that the RIS is laterally and vertically homogeneous and isotropic, with ice/water and water/seafloor interfaces that vary smoothly at scales much longer than the ice thickness. We justify this simplification by noting that RIS/DRIS stations were deliberately sited in regions of solid glacial ice several kilometers or more distant from crevassed or rifted areas as a matter of safety. For teleseismic body wave arrivals (i.e., Table 3.1) with near-normal angles of incidence, the maximum ice shelf basal piercing distance would be 230 m for a P-wave with a ray parameter of 0.08 s km^{-1} , assuming a 700 m thick shelf with a P wave velocity of 3.87 km s^{-1} . For vertical features, our

simplification is justified by the resolution limit of the teleseismic waves of interest. Assuming a quarter-wavelength limit, the highest resolving wave would be an SV-wave generated by a teleseismic P-wave at the ice/water interface, with a period of 0.5 s and a seismic velocity of 2.0 km s^{-1} , and a minimum resolution of 250 m. For contrast, the low-velocity firn layer becomes important only in the uppermost 60 m (Kirchner and Bentley, 1979; Beaudoin et al., 1992; Diez et al., 2016).

3.3.2 Intralayer Resonances

High seismic impedance contrasts in the vertical structure of an ice shelf system—specifically at the ice/water, water/seafloor, and sediment/basement interfaces—create strong reverberatory wavefields by multiply reflecting incident body waves. A similar but less severe effect is common to geologic basins where low velocity sediment overlies high velocity basement rock. The amplitude of this effect is maximized when the wavefield constructively interferes with itself. For any individual layer, the resonance periods, P_R are

$$P_R = \frac{2\mathcal{Z}\eta}{n+m} \quad \text{for } n = 1, 2, 3, \dots, \quad (3.3)$$

where \mathcal{Z} is the layer thickness, η is the vertical slowness of the incident primary wavefield, the integers n are harmonic mode orders, and m accounts for phase reversals at reflective interfaces (modified from Press and Ewing, 1951; Crary, 1954). For resonances spanning multiple layers (e.g., compacted ice and firn), the period is simply the series summation of all layers. For the ice shelf system, strong resonance wavefields may be generated for S-waves within the ice shelf and P-waves within the water column.

The layered structure of an ice shelf creates a highly efficient waveguide for plane-media polarizations of shear waves. SH waves within an ideal ice shelf with perfectly horizontal boundaries undergo lossless, in-phase reflections ($m = 0$) at the free surface and the ice/water interface; at any resonance period, P_R , an SH-polarized shear wavefield will propagate laterally along the ice shelf as a shear horizontal plate wave (Press and Ewing, 1951; Rose, 1999). SV-waves will experience lossless, out-of-phase reflections ($m = 1$) from either boundary only at the critical angle

$\theta_c = \sin^{-1}(\beta_i \alpha_i^{-1})$; a critically reflected SV-wavefield ($m = 1$) at any P_R will propagate laterally along the ice shelf as a Crary wave (Crary, 1954). SV-waves incident on the ice/water interface at all angles other than θ_c will lose energy via SV-to-P conversions within the ice and water (Figure A-3.1).

For the structure specified in Table 3.2, $\theta_c = 29.6^\circ$, equivalent to a ray parameter of $p = 0.263$ s km⁻¹. Therefore, we do not expect to observe excitation of Crary waves by teleseismic body waves, for which $p = 0.04$ – 0.12 s km⁻¹. However, the steeply incident ray parameters typical of teleseismic P-waves result in non-negligible P-to-SV conversion coefficients (10–20%) for both the free surface and the ice/water interface, with strong SV reflection coefficients (>80%), and no phase shift ($m = 0$) (Figure A-3.1). Furthermore, for the ice shelf values listed in Table 3.2, and a ray parameter of $p = 0.06$ s km⁻¹, Equation (3.3) yields $P_R = 0.328$ s, which is generally within the spectral content of the P-wave teleseismic signal. We therefore expect to observe significant SV-resonant energy associated with these arrivals. We will refer to these as Crary resonances to differentiate them from true, lossless Crary waves.

SH-wave energy may potentially be observed coincident with teleseismic P-wave arrivals as a result of scattering from sloping interfaces or due to ice anisotropy. We do not expect to observe Crary resonances associated with teleseismic S-waves, due in part to their longer periods which are incompatible with the RIS resonant periods, and for additional reasons to be discussed later in this section.

Extending the previous resonance analysis to the water column, we expect teleseismic P-wave codas to excite acoustic resonances ($m = 0$) with periods near $P_R = 0.61$ s. This resonance is markedly less efficient than the Crary resonance and will leak P- and SV-wave energy into the ice and seafloor. In the Results section we show that the spectral signatures of these Crary and acoustic resonances may be exploited to accurately estimate the thicknesses of the RIS and the sub-shelf water column.

3.3.3 Coupling of Seismic, Acoustic, and Gravity Waves

For elastic waves within an open water column of finite depth H (i.e., bounded by a free surface and a solid elastic Earth), there exists an acoustic cutoff period, $P_c = 4H\alpha_w^{-1}$, above which any vertical component of displacement ceases to propagate and becomes evanescent (i.e., decays exponentially in the vertical direction) (Ewing et al., 1957, pp. 174–189). For oscillations at periods greater than P_c , gravity becomes increasingly relevant to the vertical restoring force, and completely dominates for periods greater than the Brunt-Väisälä period (Apel, 1987, pp. 349–356). For the period band bounded by the acoustic cutoff period and the Brunt-Väisälä period, the propagation of oscillatory energy through the water column lies in the acoustic-gravity wave domain. Traer and Gerstoft (2014) and Ardhuin and Herbers (2013) provide derivations of this wave type as an extension of the nonlinear wave-wave interaction model first proposed by Hasselmann (1966). In the language of continuum mechanics, this acoustic-gravity regime may be understood as a transition between compressible and incompressible fluid behavior with increasing period. Useful analytical representations for the response of an ocean above vertically displaced ocean floor are given by Yamamoto (1982). Literature on acoustic-gravity waves is extensive but has focused on wave mechanics confined to the water layer. Recent studies have begun to address acoustic-gravity waves in the presence of an ice layer, but have thus far been restricted to inelastic ice caps (Kadri, 2016) or thin ($h \ll H$) elastic sea ice (Abdolali et al., 2018) and thus do not address coupling between acoustic-gravity and seismic waves.

To obtain an estimate for the cutoff period for the combined ice shelf and water column at the RIS, we use the derivation for the similar case of a three-layered liquid half space (Ewing et al., 1957, pp. 151–156). We justify this simplification by noting that teleseismic P-waves propagate within the water column at an angle of incidence of 3.3° – 6.6° (0.04 – 0.08 s km $^{-1}$) and therefore lose less than 5% energy at any interface via conversion to SV-waves (Figures A-3.1, A-3.2). This approximation does not account for the flexural rigidity of the ice shelf, or the overlying firn layer. The cutoff period, P_c , may in this case be determined with

$$\tan m_i h = \frac{m_i}{m_w \delta_1} \left(\frac{\delta_2 m_s \tan m_w H - m_w}{\delta_2 m_s + m_w \tan m_w H} \right), \quad (3.4)$$

where $m_{i,w,s}$ are vertical wave numbers within the ice, water, and sediment layers, respectively, and $\delta_1 = \rho_i/\rho_w$, $\delta_2 = \rho_w/\rho_s$ (Ewing et al., 1957). For the values listed in Table 3.2, $P_c \approx 2.25$ s, and varies within ± 0.6 s for the range of sub-station ice and water layer thicknesses.

Short period teleseismic arrivals associated with the P-wave coda (0.5–2.0 s) are therefore predicted to be observable on all three channels at floating stations. However, longer-period (e.g., 10–15 s) teleseismic compressional energy (e.g., S-to-P converted phases originating at the sediment/basement interface) should be observable solely on the vertical channel, reflecting the water column’s predominately incompressible response to longer-period vertical seafloor displacement (e.g., Ewing et al., 1957, pp. 174–189). Observations of Rayleigh waves (>15 s) are similarly expected to be vertically dominant (as previously noted by Okal and MacAyeal (2006)). Love wave arrivals should not be observable by floating stations above a planar seafloor due to the zero traction horizontal boundary condition.

3.3.4 Coupling of Seismic and Plate Waves

A floating ice layer is an elastic plate system and therefore supports a variety of elastic modes that are not observed in solid-Earth or ocean-bottom seismology. On an ice shelf, plate modes are expected to be excited by tractions imposed upon the ice by ocean gravity waves at the ice front and within the sub-shelf water cavity. At ultra-long periods (>3 hours), ocean waves may generate normal modes across the entirety of the RIS, which may in turn couple into acoustic-gravity waves within the atmosphere (Godin and Zabolotn, 2016). At periods of 50–100 s, infragravity and tsunami waves originating up to thousands of kilometers away generate flexural-gravity waves (i.e., buoyancy-coupled asymmetric mode (A_0) Lamb waves) which propagate several hundred kilometers into the RIS interior (Bromirski et al., 2017). In the 1–50 s period band, ocean swell impacts at the ice front generate zeroth order, symmetric mode (S_0) Lamb waves, in addition to flexural-gravity modes (Chen et al., 2018; Aster et al., 2019). On the RIS, flexural-gravity wave motion dominates the ambient wavefield at distances less than 120 km from the ice front. At greater dis-

tances, extensional wave motion (i.e., S_0 Lamb) dominates and is observable at least 450 km from the ice front (Chen et al., 2018; Baker et al., 2019).

Of interest to the present study are the symmetric mode Lamb waves. Particle motion for these waves is retrograde elliptical in the vertical/radial plane, with a high eccentricity oriented parallel to the radial axis (Figure 3.2). Lamb waves may be generated within a plate by compressional forces applied normal to the plate end face, or by shear forces applied in traction parallel to the basal plate surface. The theory and application of these methods have been rigorously documented in a number of publications on ultrasonics, where Lamb waves are often used in nondestructive testing (e.g., Viktorov, 1967; Rose, 1999) For this study, we are concerned only with Lamb wave generation via normal end face tractions, such that

$$E_L \propto A^2 \cos^2 \phi , \quad (3.5)$$

where E_L is the energy of the resulting Lamb wave, A is the amplitude of the source signal, and ϕ is the angle between the source traction and the normal to the plate face (Figure 3.2) (Rose, 1999). For simplicity, we have restricted the source signal to oscillating within the same plane as the plate surface (i.e., horizontal). For the generation of ocean-coupled Lamb waves, the RIS is oriented such that ocean gravity waves propagating across the Ross Sea generally impact the ice shelf face at oblique-to-normal angles of incidence, maximizing the transfer of horizontal impulse between the incoming waves and the shelf.

The grounding lines of ice shelves are also plate boundaries at which Lamb wave energy may be generated. A relevant situation for this study is the case of teleseismic S-waves arriving near the grounding lines at nearly vertical angles of incidence (Figure 3.2). Both SV- and SH-waves have the potential to generate Lamb wave energy, E_L , according to the general relationships

$$E_L \propto A_{sv}^2 \cos^2 \varphi , \quad (3.6)$$

$$E_L \propto A_{sh}^2 \sin^2 \varphi , \quad (3.7)$$

$$\varphi = 90^\circ - \theta_{gl} - \theta_{eq}, \quad (3.8)$$

where A_{sv} and A_{sh} are the amplitudes of the SV- and SH-waves, respectively, θ_{gl} is the strike of the grounding line (with the RIS defined as down-dip using the right-hand-rule convention), and θ_{eq} is the back azimuth to the source earthquake.

3.4 Results

Figure 3.3 shows representative component spectrograms for an M_w 6.4 earthquake recorded by floating station RS16. This spectrogram shows multiple features that are relevant to our discussion of the various arrival bands. Spectrograms for the same event recorded at grounded station RS08 are shown in Figure 3.4.

3.4.1 P-waves (0.5–2.0 s)

Teleseismic P-wave wavetrains in the 0.5–2.0 s period band are generally well-observed on the vertical and horizontal components of floating stations during both winter and summer noise conditions. In the 5–10 s band, secondary microseism noise overwhelms both vertical and horizontal component signal (Figure A-3.3). Notably, energy in the 10–20 s band is well-observed on the vertical component, but is very poorly observed on the horizontal components; for example, compare Figures 3.3 and 3.4. This relative lack of horizontal signal may reflect the transition of the water column from compressible to incompressible beyond the acoustic cutoff period (Equation (3.4)); this behavior is addressed in detail in the Supplemental Material.

Figure 3.5 shows spatial and seasonal variations in the mean SNR for teleseismic P-wave arrivals in the 0.5–2.0 s period band.

During the winter low-noise state, mean vertical component SNR at nearly all floating ice stations for the P wave and its immediate coda was 25 dB, similar to the grounded ice stations on Roosevelt Island and Marie Byrd Land (Figure 3.5a, HHZ). Winter vertical SNR did not appear to be significantly affected by ice or water layer thicknesses or distance from the ice front (Figure 3.5a,b, respectively). The notable exceptions were the ice front stations (DR01–DR03), for

which the vertical SNR dropped to 15 dB. The radial (HHR) and transverse (HHT) component SNRs showed greater spatial variations; along the West-East (W-E) transect, SNR generally increased from 19 dB at RS01 (West end) to 23 dB at RS07 (East end), suggesting a dependence on increasing ice or decreasing water layer thicknesses. Along the North-South (N-S) transect, horizontal SNR increases from 5 dB at DR02 to 23 dB for all stations farther than 120 km from the ice front. Surprisingly, the radial and transverse components show approximately equivalent SNR at most stations except for the those with the thickest ice and thinnest water columns (RS05–RS07), or those farthest from the ice front (DR16, RS18). In contrast, at grounded stations the radial SNRs were 2–3 dB higher than the transverse.

The summer high-noise state, predictably, resulted in generally lower P-wave SNR at all stations. Along the W-E transect, SNR dropped by 8–12 dB across all three components for all floating stations and the grounded stations closest to the grounding zones (RS08, RS09, RS11) (Figure 3.5a). Stations RS12–RS14, located more than 110 km inland from the grounding zone, observed only a 5 dB decrease in vertical SNR, and an 8 dB decrease in horizontal SNRs. Along the N-S transect, vertical SNR was reduced to 5 dB at DR02, but increased exponentially with distance from the ice front, to 26 dB at RS18 (0.05 dB km^{-1}), nearly equivalent to the winter SNR observed at the same station. The horizontal SNRs showed similar exponential increases, from 3 dB at the ice front, to 21 dB (HHR) and 18 dB (HHT) at RS18, only 5 dB less than the winter values.

Estimates of Layer Thicknesses from Resonance Periods

Figure 3.6 shows the median PSDs for all P-wave arrivals observed by RS04 and identifies the local maximums associated with the acoustic and Crary resonances (Figure 3.2). The peak periods of these resonances may be used in conjunction with Equation (3.3) and Table 3.2 to estimate the vertical dimensions of the RIS proximal to each floating station. The orthometric elevation of the RIS may be estimated with Archimedes' principle.

To account for the low velocity meteoric firn layer, the resonance period P_r (Equation (3.3)) may be solved for as the summation of a glacial ice layer of unknown thickness h' and a firn layer

of assumed known thickness F . The firm layer should also be accounted for in the calculation for orthometric elevation, e :

$$e = h - h' \frac{\rho_i}{\rho_w} - F \frac{\rho_f}{\rho_w}, \quad (3.9)$$

where $h = h' + F$ is the total ice shelf thickness.

Table 3.3 presents these results for all RIS floating stations and compares them to BEDMAP2 and REMA (Reference Elevation Modal of Antarctica; Howat et al. (2019)) values. BEDMAP2 water column depths were derived from satellite-based gravimetric mapping of sub-RIS bathymetry. BEDMAP2 ice shelf thicknesses were inferred from satellite radar altimetry of orthometric elevation using Archimedes' principle and accounted for a meteoric firm layer of geographically variable thickness (Griggs and Bamber, 2011). REMA measurements of RIS orthometric elevations were compiled from multiple sources of airborne and satellite altimetry.

Admittedly, our method is vulnerable to error from a number of sources, including incorrect elastic parameters, nonplanar ice/water and water/seafloor interfaces, seasonal variations in ice thickness due to basal freezing and thawing, and possible changes in near-station bathymetry as the stations move up to 1 km yr^{-1} with the flow of the ice shelf. Our assumed firm layer thickness of 75 m is based on empirical measurements from the center of the RIS (Diez et al., 2016) and may not be appropriate for all stations; RS01, for example, was sited on thinner ice than all other stations and also yielded the largest deviation in ice thickness from BEDMAP2. The BEDMAP2 values also have unspecified errors stemming from their age (originally collected in 1996) and grid resolution (50 km). Nonetheless, our estimates are in agreement with the interpolated BEDMAP2 and REMA values, and confirm our interpretations of these spectral peaks.

3.4.2 S-waves (10–15 s)

Theoretically, floating ice-sited seismometers are incapable of directly observing teleseismic S-wave arrivals due to the inability of the underlying water column to propagate shear stresses. Nonetheless, the floating stations of the RIS array did record signals in the 10–15 s period band, co-

incident with *ak135*-predicted arrival times for teleseismic S-waves. These signals were recorded most reliably for moderate magnitude ($M_w > 6.0$), low-noise (winter) events such as shown in Figure 3.3. These S-wave-associated arrivals exhibited strong vertical polarization, similar to the 10–20 s period P-wave arrivals.

A lack of horizontal signal coincident with vertical signal is consistent with a transition of the water column from compressible to incompressible behavior (see Electronic Supplement). Horizontal energy, when observed, was delayed by up to tens of seconds from the predicted S-wave arrivals, increasing with station distance from the RIS grounding zones (e.g., Figure 3.3, red arrows). For comparison, signals from the same event at a grounded RIS station are shown in Figure 3.4.

Figure 3.7 shows spatial and seasonal variations in the mean SNR for teleseismic S-wave arrivals in the 10–15 s period band. As detailed in the “Spectral Characterization” section, the noise component for this figure is comprised of 200 seconds of pre-S-wave arrival time data. The S-wave SNR is therefore referenced against the extended P-wave coda, rather than pre-event noise as in Figures 3.3 and 3.4.

Vertical component SNRs along the W-E transect were nearly uniform at 5–6 dB for most floating and grounded stations during summer and winter (Figure 3.7a). For the N-S transect (Figure 3.7b), winter vertical SNR was 5–6 dB and was generally insensitive to distance from the ice front, while summer SNR was a more variable 4–6 dB and showed slight increases with distance from the ice front. The ice front stations DR01–DR03 (represented by DR02 on Figure 3.3b) recorded vertical SNRs of only 2 dB during winter and summer.

Horizontal component floating station SNRs along the W-E transect decreased with station distance from the grounding line. Radial component (HHR) SNR during winter reached a maximum of 10 dB for floating stations <100 km from the grounding lines (Figure 3.7a, RS01, RS07, RS10), similar to SNR values observed for the grounded stations on Roosevelt Island and in Marie Byrd Land. Floating station radial component SNR decreased at a rate of 0.04 dB km^{-1} towards the RIS interior, reaching a minimum of 2.5 dB at RS04. Summer radial SNR followed similar trends, peaking at 7.5 dB near the shelf margins (somewhat lower than the grounded station values of 9.5

dB) and decreasing at a rate of 0.03 dB km^{-1} to a minimum of 2.5 dB at RS04. Transverse component (HHT) SNRs showed similar spatial distributions as the radial component for floating and grounded stations during winter and summer, although at some stations the transverse SNR was up to 2 dB greater than the radial. Along the N-S transect, floating station radial and transverse component SNRs were generally equivalent and showed less than 1 dB of change between summer and winter (Figure 3.7b). Horizontal SNRs increased with distance from the ice front at a rate of 0.017 dB km^{-1} .

Coupling Between Teleseismic S-waves and Lamb Waves

Longitudinal stresses applied to an ice shelf margin have the potential to generate symmetric Lamb wave modes (e.g., Viktorov, 1967; Rose, 1999). Chen et al. (2018) showed that ocean gravity waves impacting the RIS ice front generate fundamental mode symmetric (S_0) Lamb waves with a propagation velocity of 3.2 km s^{-1} , in agreement with theoretical predictions for RIS thickness, density, and elastic properties.

Figure 3.8 shows a representative record section for S-wave arrivals from an M_w 6.6 earthquake in the Java Sea. Serendipitously, the epicenter of this event and the W-E transect were within 1° of a common great circle arc. The grounding lines at Ross Island and Roosevelt Island are nearly perpendicular to this great circle, yielding a favorable polarization alignment between the teleseismic SV-waves and RIS-propagating S_0 Lamb waves (Equation (3.6), $\varphi \approx 0^\circ$). Arrival times of the Lamb waves shown in Figure 3.8 show a propagation velocity of 3.2 km s^{-1} for waves radial from Ross Island, and 3.3 km s^{-1} for waves anti-radial from Roosevelt Island. Particle motions (Figure 3.9) are retrograde in the vertical/radial plane and highly elliptical in the radial direction, consistent with theoretical descriptions of symmetric Lamb waves (Viktorov, 1967). Figure 3.10 shows the attenuation of Lamb wave amplitude with distance from the grounding lines and is notably similar to the horizontal SNRs in Figure 3.7. Figure A-3.8 shows a similar record section for an inferred SH-Lamb conversion from the grounding line of Roosevelt Island.

3.4.3 Surface waves (13–25 s)

Surface wave arrivals at floating stations with periods longer than the acoustic cutoff period are most strongly observed on the vertical channel; again, see Figures 3.3 and 3.4 for a representative comparison of floating and grounded stations, respectively. Velocity dispersion is measurable on vertical component spectrograms even for moderate magnitude ($M_w > 6.0$) earthquakes, particularly during winter (Figure 3.3).

Figure 3.11 shows spatial and seasonal variations in the mean SNR for teleseismic surface wave arrivals in the 13–25 s period band. The “signal” for this figure incorporates 4–2 km s⁻¹ arrivals. The “noise” uses an equal length of pre-4 km s⁻¹ noise, which includes the P- and S-wave codas, and some amount of pre-event background noise.

Surface wave SNRs saw significant seasonal variations in absolute and relative component magnitudes. For floating stations along the W-E transect (Figure 3.11a), winter vertical SNRs were improved by 3–6 dB over summer values, with the greatest increases observed over stations with the thinnest ices and thickest water columns. At grounded stations, winter vertical SNRs were <2 dB greater than summer values. The radial component SNR at floating stations was 2 dB greater than the transverse component. Summer radial and transverse SNRs at floating stations were nearly equivalent. At grounded stations, during both winter and summer, radial SNRs were consistently 3.5 dB higher than transverse SNRs. Both radial and transverse SNRs improved by <1 dB during winter. For the N-S transect (Figure 3.11b), seasonal variations were generally similar to the W-E transect.

Surface wave SNRs also displayed systematic geographic variations. Along the W-E transect (Figure 3.11a), floating station vertical SNR was highest in the east at RS07 and lowest in the west at RS01, decreasing by 0.009 dB km⁻¹ during winter and 0.012 dB km⁻¹ during summer. In contrast, horizontal SNRs were highest near the grounding lines (i.e., RS01 and RS07) and lowest at the centerline of the RIS (i.e., RS04). During winter, both radial and transverse decreased most rapidly with distance from Roosevelt Island (0.017 dB km⁻¹, RS07–RS04) than from Ross Island (0.006 dB km⁻¹, RS01–RS04). During summer, horizontal SNRs were uniformly 2.5 dB at most

floating stations; accounting for the linear offset introduced by Equation (3.2), these values were actually 0 dB (Figure A-3.9). Exceptions were RS07 and RS10, which both recorded SNRs that were 1.5 dB higher than RS01–RS06.

Along the the N-S transect (Figure 3.11b), floating station SNRs generally increased with distance from the ice front. For all seasons and all components, SNR at ice front station DR02 was effectively 0 dB. During winter, vertical SNR increased by 0.076 dB km^{-1} between DR02 and DR10, and by only 0.004 dB km^{-1} between DR10 and RS18. Summer vertical SNR increased by 0.042 dB km^{-1} between DR02 and RS16, and was equal to winter SNRs for RS16 through RS18. Horizontal SNRs increased uniformly between DR02 and RS18: during winter, the radial and transverse components increased at $0.0148 \text{ dB km}^{-1}$ and 0.011 dB km^{-1} , respectively; during summer, both horizontal components increased at 0.006 dB km^{-1} .

Rayleigh Wave Group Velocities

Figure 3.12 shows Rayleigh group velocities for the sub-RIS crust along portions of both transects, following the multiple filter methods of Dziewonski et al. (1969) and Meier et al. (2004). For the W-E transect, we use a station pair of SBA on Ross Island and RS08 on Roosevelt Island; this limits the dispersion analysis to the portion of the West Antarctic Rift System directly beneath the RIS and excludes any influence from the thicker crustal province in Marie Byrd Land (i.e., RS11–RS14). For the N-S transect, we use a station pair of RS04 and RS18, restricted by the degradation of surface wave SNR at stations $<130 \text{ km}$ from the ice front. We limited source earthquakes to back azimuths within $\pm 5^\circ$ of their respective transect great circles and manually selected events for high signal to noise. The W-E analysis used four events from the Nazca subduction zone; the N-S analysis used seven events from the New Zealand subduction zone. Unsurprisingly, the floating stations of the N-S transect yielded a considerably higher median absolute deviation than the grounded stations of the W-E transect. Nonetheless, both transects yielded similar dispersion curves in the low-error 17–23 s period band.

3.5 Discussion

3.5.1 P-waves (0.5–2.0 s)

For the teleseismic P and immediate coda wave field, differences between the summer and winter SNR values could technically reflect selection biases in our earthquake catalog (i.e., the signal) or actual variations in the ambient noise field of the RIS. However, since our winter and summer event populations are generally reflective of global earthquake rates (Figure A-3.5), and given previously documented seasonal background variations (below), we exclude selection bias as a significant contributor to the seasonal SNR variation. Baker et al. (2019) examined temporal-spatial variations in ambient noise on the RIS in the 0.4–4.0 s period band and found that onset and termination of the summer high-noise state were strongly correlated with the breakup and redevelopment of contiguous sea ice in the Ross Sea. They suggest that this “Tertiary” noise band, which overlaps with the teleseismic P-wave band, is recording short-period microseisms generated by nonlinear wave-wave interactions (e.g., Ardhuin and Herbers, 2013), consistent with similar short period peaks studied elsewhere in Antarctica (Anthony et al., 2015, 2017).

Winter SNR values are generally equivalent between floating and grounded stations (excluding ice front stations DR01–DR03). Summer SNR may be improved by increasing the minimum event magnitude threshold, at the expense of the corresponding decrease in available events (Figure A-3.5). In either case, SNR values at floating-ice-sited seismographs are generally adequate for passive imaging methodologies, with the significant caveat that only the vertical component conveys information about structural velocities of the crust or mantle. Teleseismically-derived energy in this band observed on horizontal components is the result of P-to-S conversions at the water/ice interface, scattering from internal shelf structure, or is conveyed to the ice shelf waveguide through excitation at the grounding line (see below). Consequently, receiver function or similar converted wave analyses would be useful only for estimating velocity structures within the ice shelf. Vertical component autocorrelation analysis (e.g., Sun and Kennett, 2016; Phạm and Tkalčić, 2018), however, may prove useful for constraining deeper structure.

3.5.2 S-waves (10–15 s)

We interpret signals observed at floating stations during the S-wave arrival window as a combination of secondary wavefield effects resulting from interactions of teleseismic S-waves with the sub-shelf seafloor and the shelf grounded margins.

Signal recorded on the vertical component is explicable as S-to-P conversions at impedance contrasts within the crust or sub-shelf sediments (e.g., Beaudoin et al., 1992; Diez et al., 2016). The lack of horizontal signal coincident with these S to P vertical arrivals (Figure 3.3) implies that the S-to-P converted waves couple into the water column as acoustic-gravity waves, as expected for steeply incident waves with periods longer than the acoustic cutoff (Equation (3.4)). As previously noted, vertical motions associated with the propagation of acoustic-gravity waves are predominantly incompressible and therefore would not generate significant S-wave modes in the ice. The relatively uniform vertical SNR along the W-E transect may indicate that the S-to-P conversion for floating and grounded stations occurs at the same impedance contrast (e.g., the sediment/basement interface); this is, however, entirely speculative and we acknowledge that the uniformity may instead be an artifact.

The composition of post-S arrival signals on the horizontal components varies with proximity to the grounding lines, as is evident from the changing ratios between radial and transverse SNRs. In the RIS interior, such horizontal energy is interpreted to be dominated by plate waves generated by teleseismic S-waves coupling at the grounding zones, with additional signal perhaps arising from acoustic-gravity modes. Figure 3.3, for example, shows two discrete and delayed arrivals on the horizontal components (red arrows) consistent with a symmetric S_0 Lamb wave generated the arrival of the teleseismic SV wave at the southeastern margin of the RIS (HHR) and by SH-waves incident along the southwestern margin (HHT). Horizontal power in these signals is found to increase systematically with proximity to the grounded margins, indicating that these plate waves undergo significant attenuation and/or geometrical spreading in the ice shelf. The stations closest to the grounding lines may also observe elastic wave energy scattered into the ice shelf as incoherent, subcritical reverberations (i.e., highly lossy). The discrepancy in HHT SNR between the western

and eastern ends of the transect (Figure 3.7a) may reflect the greater ice thicknesses in the east, which would allow a greater spectrum of periods and ray parameters to couple into the shelf as resonance modes.

Baker et al. (2019) showed that the annual formation of sea ice in the Ross Sea during the winter months depresses noise in the 10–15 s period range by as much as 30 dB across all seismic components. In contrast, our present analysis found no significant seasonal variation in vertical SNR for energy associated with teleseismic S-wave arrivals, indicating that the long period P-wave coda is the most significant noise source for vertical component observations of teleseismic S-waves. Similarly, we found that the significant reductions (relative to summer) in horizontal noise during winter sea ice conditions were not accompanied by a proportionate increase in horizontal SNR.

3.5.3 Surface waves (13–25 s)

Signals observed by floating stations during the surface wave arrival window are often overwhelmingly on the vertical channel and have dispersion relations comparable to those of nearby grounded ice stations (e.g., Figures 3.3, 3.4). This behavior is consistent with the general model we have established for the interactions of solid Earth elastic waves with the Ross Ice Shelf and the sub-shelf water column. That is, we expect that long period (>13 s) teleseismic Rayleigh waves propagating beneath the RIS should couple with the water column and the ice shelf as, predominately, incompressible vertical displacements; horizontal signals at the seafloor should not be observed above the water column. Semblance between the vertical component dispersion curves at floating and grounded stations further indicates that the RIS floating stations directly observed teleseismic Rayleigh wave arrivals. Similar observations of teleseismic Rayleigh waves on a free-floating tabular iceberg were presented in Okal and MacAyeal (2006) for the 2004 and 2005 Sumatra earthquakes (M_w 9.1 and 8.6, respectively).

Signals coincident with surface wave arrivals are weakly observed on the horizontal components during the winter low-noise state, with generally higher SNRs on the radial component than

the transverse (Figures 3.3, 3.11). We suggest two non-exclusive mechanisms. The perhaps more obvious explanation is the propagation of plate wave modes from the grounding line via the same excitation processes as observed for S-wave arrivals. This would account for both radial (Lamb) and transverse (shear horizontal plate) signals. The decreasing horizontal SNRs with increasing distances from the grounding lines (Figure 3.11a) would also be consistent with attenuation of these plate wave modes. For the radial component, S_0 Lamb waves propagate across the RIS at 3.2 km s^{-1} (Figure 3.8), in comparison to 3.5 km s^{-1} for crustal Rayleigh waves (Figure 3.12), allowing for roughly similar arrival times between vertically polarized Rayleigh waves and radially polarized Lamb waves (Figure 3.3). Shear horizontal plate waves would be restricted to the fundamental mode at these long periods and would propagate at the S-wave velocity of the RIS, β_i (Rose, 1999). An alternate explanation is that the radial signal is the result of acoustic Rayleigh leakage into the water column. A Rayleigh wave traveling along a solid/liquid interface will lose energy to the liquid medium at a rate of e^{-1} per 10 wavelengths if the acoustic velocity of the liquid, α_w , is less than the phase velocity of the Rayleigh wave, V_R (Viktorov, 1967). These so-called “leaky” Rayleigh waves emit acoustic waves at angles of incidence greater than the Rayleigh angle, $\theta_R = \sin^{-1}(\alpha_w/V_R)$ (Glorieux et al., 2002). For $V_R = 3.5 \text{ km s}^{-1}$, $\theta_R = 24.5^\circ$. Acoustic waves are post-critical at the water/ice interface for this angle and convert $>80\%$ of their energy into SV-waves within the ice (Figure A-3.1). It is beyond the scope of this study as to how leaky Rayleigh wave energy would interact in detail with acoustic-gravity wave phenomena, but we expect that the elastic energy of such a mode would be increasingly favored with increasing angle of incidence. However, the strength of the apparent relation between horizontal SNR and distance from the grounding line (Figure 3.11a) suggests that any effect of sub-shelf Rayleigh wave leakage is secondary to the plate modes.

Generally, we do not expect to observe sub-shelf crustal Love waves at floating stations. Steeply sloping bathymetry may, in theory, cause leakage of Love wave energy into the water column. However, we have observed no clear evidence of such signals.

Ambient noise in the 13–25 s period band is a multi-mode wavefield driven by the impacts of ocean swell with the RIS ice front, as described by Baker et al. (2019). For their analysis, Baker *et al.* restricted their so-called Primary band to periods of 10–20 s, keeping with the traditional bandpass of the primary microseism wavefield. However, the PSDs included there indicate that the summertime high-power state for this wavefield is actually observed at periods as long as 30 s. As such, we have adjusted the noise calculations from that study to the 13–25 s period band and have included the results in Figure A-3.10; we stress that this updated figure merely adjusts the quantitative distributions and does not otherwise change the qualitative interpretations.

We note some similarities between the spatial and seasonal distributions of vertical component surface wave SNR and Primary band noise. As noted by Baker et al. (2019), the predominant source of noise for the RIS throughout the year in this general period band is ocean gravity waves. During the summer open water months of the Ross Sea, ocean gravity waves generate ambient noise via direct interaction with the ice front and penetration into the sub-shelf water cavity; these forcings remain observable throughout winter, even in the presence of extensive sea ice. Along the N-S transect, both summer and winter vertical component SNRs (Figure 3.11b) are generally inverted from the adjusted Primary band noise powers (Figure A-3.10b). This indicates that, consistent with Baker et al. (2019), the vertical noise wavefield in the 13–25 s period band is driven by a combination of ocean gravity waves and primary microseism Rayleigh waves. Ocean gravity waves are the predominant forcing within 130 km of the ice front during winter and within 250 km during summer, while primary microseism Rayleigh waves are responsible for the wavefield at greater distances. Variations in vertical SNR along the W-E transect (Figure 3.11a) are similarly inverted with respect to the Primary microseism noise band trend (Figure A-3.10a); this is explained by the decreased flexural rigidity of the thinner ice near Ross Island, which in turn allows for larger amplitude flexural-gravity waves.

3.6 Summary and Conclusions

We present a signal-to-noise and phenomenological analysis of two years of teleseismic earthquake signals recorded by a 34-station broadband seismic array deployed across the Ross Ice Shelf (RIS), Antarctica. Teleseismic observations in this environment must contend with a complex elastic and gravity wave displacement wavefield consisting of: 1) Short period (0.4 to 4.0 s) ocean noise associated with shorter period microseism generation and/or direct ice front excitation; 2) Primary and secondary microseisms; 3) Flexural-gravity waves excited by infragravity and ocean swell waves; 4) Water layer-decoupled P- and S-wave arrivals; 5) High frequency (1–10 Hz) reverberations from the strong ice shelf basal and surface impedance contrasts; and 6) Intermediate to long period (10–50 s) plate waves induced by oceanic and teleseismic forcings. The ocean-forced components of this ambient wavefield have a strong dependence on sea ice extent in the Ross Sea, resulting in bimodal noise distributions between “winter” (1 April to 30 November) and “summer” (1 December to 31 March) sea ice periods.

We use 300–400 teleseismic earthquakes to generate band-averaged signal-to-noise ratios (SNR) for P-wave (0.5–2.0 s), S-wave (10–15 s), and surface wave (13–25 s) arrivals and codas, as recorded at floating- and grounded-ice-sited seismometers. We also address secondary wavefield effects such as P-wave-derived intralayer resonances, S-wave-derived symmetric mode Lamb waves, and the effects of incompressible displacement of the sub-shelf water column by long period/long wavelength solid Earth elastic waves.

Teleseismic P-wave arrivals were well-observed at RIS floating stations throughout the year. During the winter low-noise state, three-component P-wave SNR at floating stations was uniformly equivalent to observations at nearby grounded stations (20–25 dB); an exception were stations within 3 km of the RIS ice front, where three component SNRs were up to 10 dB lower. During the summer high-noise state, three-component SNR was effectively 0 dB at the ice front and increased by 0.05 dB km^{-1} landward; extrapolating from these trends suggests that summer SNR values would reach winter SNR values at 460 km from the RIS ice front. Given the similarity between floating and grounded station SNR values, we conclude that teleseismic P-waves may be useful to

passive imaging methods for the determination of structural velocity within the ice shelf (vertical and horizontal components) and the sub-shelf crust and mantle (vertical component, only).

Teleseismic P-wave codas contain elastic wave frequencies that are optimal for generating fundamental mode resonances within the ice shelf and the sub-shelf water column. We used the peak periods of these resonances—which are readily apparent on power spectral density plots of earthquake arrivals—in conjunction with the mean ray parameter to estimate ice shelf and water column thicknesses. Our results agree with interpolated BEDMAP2 estimates of ice and water thicknesses (based on buoyancy and gravimetry, respectively, from 1996) (Fretwell et al., 2013) to within 4%. This demonstrates that long-term deployments of seismometers to terrestrial or extra-terrestrial (e.g., Europa) ice shelves have potential for year-round monitoring of ice shelf thicknesses and possibly even initial estimates of unknown vertical geometries.

Teleseismic S-wave codas were generally very poorly recorded (<5 dB SNR) at all floating stations throughout the year. However, we do show that these arrivals, when incident near the RIS grounding lines, generate symmetric mode Lamb waves which may be observed at least 250 km into the interior the ice shelf. Significantly, the travel times and attenuation of these Lamb waves may be exploited for large scale, wide angle measurements of ice shelf properties using the same techniques already perfected by the field of ultrasonic non-destructive testing.

Teleseismic Rayleigh wave arrivals were generally well-observed (>10 dB SNR) on the vertical components of floating stations, particularly during the winter, but were poorly observed (<5 dB) on the radial components. A similar deficit, relative to grounded stations, between vertical and radial power was also observed for long period P-wave arrivals (>20 s). This phenomena we attribute to the shallow-water acoustic cutoff period (~ 2.0 s), above which solid Earth elastic waves are expected to couple into the water column as incompressible vertical displacements. Such a displacement of the water column would not generate a P-to-S converted phase at the water/ice interface. Notably, these vertical displacements do preserve the Rayleigh dispersion values and may be exploited to determine the sub-shelf crustal Rayleigh wave group velocity curves. Our initial attempt at calculating group velocities between a pair of floating stations yielded similar

values in the 17–23 s band as also determined for a pair of grounded stations. Unfortunately, the floating station analysis developed significant errors at periods longer than 25 s and diverged from the grounded station fit.

In addition to quantifying teleseism metrics and characteristics on the RIS and implications for other ice shelves using this unusually extensive data set, we note widely observed wave phenomena that can be applied for spatial and temporal studies of the elastic state of ice shelves. In particular, the presence of spectral resonances that can be utilized to estimate local layer thicknesses, and the new, and common, observation of shelf-spanning teleseismically-induced Lamb waves generated at grounded zones by teleseismic S-waves. With a suitably dense network, observations of these vertical and horizontal wavefields might allow for time lapse seismic tomography at the ice shelf scale.

3.7 Evidence for a Long Period Compressibility Limit

As noted in the main text, Yamamoto (1982) presents a detailed derivation of the compressibility limit for a hydrostatic water column. In simplified physical terms, the water/seafloor interface is an unwelded contact, such that the vertical stress boundary conditions within the water column are supplied solely by the hydrostatic weight of the water column. As the strain rate applied to the base of the water column decreases (with increasing period), the resistive force required for transient compression of the water column increases. Acoustic cutoff therefore occurs when the hydrostatic weight of the water column is less than the (strain-rate-dependent) resistive force needed for compression. (As a rough analogy, consider the case of quickly and loudly striking the end of a table with a hammer, as opposed to the case of slowly and quietly pushing the same table; in this example, the resistive force for compression is provided by the friction between the table and the floor.) Note that the cutoff effect is not directionally symmetric: that is, for a downward-directed acoustic source near the surface of the water column, the resistive force is supplied by the structural rigidity of the Earth and is therefore functionally infinite.

We define an incompressible medium as having constant density ($\frac{\delta\rho}{\delta t} = 0$) at all volumetric scales. The velocity of longitudinal stress fields, $c_L = \sqrt{\frac{\lambda+2\mu}{\rho}}$, is infinite for an incompressible medium, where λ is the first Lamé parameter and μ is the shear modulus. The velocity of compressional waves, $\alpha = \lambda f$, is undefined as a direct consequence of the time-invariant density: the amplitude of a compressional wave in an incompressible medium is zero, so the wave equation is also zero at all times.

We present observations which we interpret as evidence for acoustic cutoff behavior. We will use floating station RS16 (Figures 3.3, A-3.3) and grounded station RS08 (Figures 3.4, A-3.4) as references; however, these observations are valid for any floating or grounded station from the RIS/DRIS experiment.

1. For the event shown in Figure 3.3, at RS16:

- (a) P-waves arrive with a ray parameter of 0.0555 s/km, or angles of incidence of 4.5° in the water and 12.4° in the ice.
 - (b) S-waves arrive with a ray parameter of 0.1084 s/km. Scattered P-waves would have angles of incidence of 9.0° in the water and 24.8° in the ice.
 - (c) Both ray parameters are well below the water/ice critical angle of 22.4° (0.263 s/km) (Figure A-3.1).
 - (d) The acoustic cutoff period, as estimated with Equation 3.4, is $P_c \approx 2.0$ s.
2. P-wave arrivals with periods less than 3 s are observed strongly on all three channels at both floating and grounded stations. Notably the SNR across all three channels is generally self-similar at RS16 and RS08.
- (a) Because there are no S-waves in the water, all horizontal power observed at RS16 must be the result of P-to-S conversions at the ice/water and ice/free surface boundaries.
 - (b) The wintertime horizontal background noise is generally at the NLNM in the 0.4–4.0 s band (Baker et al., 2019). This helps the SNR of the horizontal scattered signal, considering that scattering coefficients are on the order of only 5% (Figure A-3.1).
 - (c) Horizontal component signal with periods of 2–3 s (i.e., greater than the estimated acoustic cutoff) may be the result of evanescent tunneling.
3. P-wave arrivals with periods greater than 10 s are observed on all three channels at RS08; Z and R are stronger than T, as expected for P-waves. In contrast, at RS16, these same long period P-waves are observed only on the vertical channel.
- (a) Teleseismic P-waves generate significant scattered S-waves in the ice, as shown by the horizontal signal at periods less than 3 s. For a fully elastic ice shelf, P-waves incident on the water/ice interface should generate S-waves in the ice for all angles of incidence greater than normal.

- (b) By the working theory, 10–20 s P-wave arrivals are above the acoustic cutoff period and therefore would not excite acoustic waves in the water column. In other words, in response to the displacement of the seafloor by the solid Earth P-wave, the water column responds as an incompressible mass and all physics governing elastic wave propagation are irrelevant. Such incompressible displacement of the water/ice column would only register on the seismometer as a vertical displacement (since again, there are no elastic waves in the water column at these periods to scatter into horizontal power). This is consistent with what we observe at floating stations.
 - (c) Wintertime horizontal noise in the 10–20 s band is also very nearly at the NLNM. Coincidentally, the absolute power of the NLNM is similar in the 0.4–4.0 s and 10–20 s bands. Stronger noise can therefore be ruled out as the cause of the lack of horizontal power coincident with the 10–20 s P-wave arrivals.
4. Teleseismic S-wave arrivals (10–15 s) are strongly observed on all three channels at RS08 (grounded), consistent with basic theory.
- (a) S-to-P wave conversions can occur at the Moho, the sediment/basement interface, and the seafloor/water interface. Following classical elastic theory, at RS16, we would predict to observe vertical signal resulting from teleseismic S-to-P conversions at the aforementioned interfaces, as well as horizontal signal resulting from P-to-S scattering at the ice/water interface and the ice free surface. Additionally, due to the steeper angles of incidence for teleseismic S-waves, these conversions should produce $\sim 2x$ more scattered energy in the ice layer relative to the teleseismic P-waves.
 - (b) Seafloor sediments would create strong S-wave resonances which would continually leak additional acoustic wave energy into the water column, to be scattered into P- and S-waves in the ice layer. For a fully elastic water/ice column, the observed P- and S-wave budget would be substantial. In reality, we see only vertical signal at periods

longer than 10 s (with the exception of horizontal signal that can be attributed to Lamb waves, as described in the main text).

- (c) Vertical SNR in the 10–15 s band at RS16 is ~ 30 dB. For P-wave arrivals with periods shorter than 3.0, 30 dB of SNR on the vertical channel resulted in observable signal on the horizontal channels. Noise levels between the two bands are similar, so a direct comparison of SNR is valid. The conclusion, again, is that short period displacement of the seafloor generates elastic waves in the water/ice column, while long period displacement generates incompressible waves governed by gravity.
- (d) Horizontal noise at periods greater than 20 s is at the NHHM. At these long periods, the lack of horizontal signal could be attributed to high noise. However, by the presented logic, we do not expect to see any signal anyway.

5. Rayleigh waves again follow a similar pattern.

- (a) Rayleigh waves should be leaky for the seafloor/water interface and would radiate P-wave energy at a characteristic angle (26.5°). These water column P-waves would be post-critical at the water/ice interface and would convert 80% of their energy into SV-waves in the ice. Consistent with this, we do observe some radial power at RS16 coincident with the peak (> 50 dB) Rayleigh wave power, beginning around 2500 s. This may also be evanescent tunneling of elastic energy across the water column, which may scatter into S-wave energy in the ice. Whether this radial power is the entirety of the expected power, or is actually due to evanescent tunneling, is unclear at this time.

3.8 Tables

Table 3.1: Parameters for teleseismic signals used in this study. \bar{N} indicates the mean number of events across all stations for each season. Summer includes all events between December 1 and March 31. Winter includes all events between 1 April and 30 November. “Mean Dist.” indicates the mean arc distance across all stations and all events. The mean magnitude for all bands across all stations and all events was M_w 6.0.

Arrival	Bandpass	Distance	Ray Prm. (s/km)	Signal Length	\bar{N}_{Winter}	\bar{N}_{Summer}	Mean Dist.
P-wave	0.5 – 2.0 s	30 – 95°	0.080 – 0.041	100 s	314	125	66.5°
S-wave	10 – 15 s	60 – 95°	0.116 – 0.078	200 s	215	94	74.0°
Surface	13 – 25 s	45 – 95°	N/A	1250 – 2650 s	280	113	69.7°

Table 3.2: Elastic parameters for the Ross Ice Shelf used in this study. Firm values are the averages of empirical results published in the listed references.

Property	Symbol	Value	Reference
P-wave, Firm	α_f	3.10 km s ⁻¹	<i>ad</i>
P-wave, Ice	α_i	3.84 km s ⁻¹	<i>ac</i>
P-wave, Water	α_w	1.45 km s ⁻¹	<i>b</i>
P-wave, Sediment	α_s	3.75 km s ⁻¹	<i>cg</i>
S-wave, Firm	β_f	1.56 km s ⁻¹	<i>adg</i>
S-wave, Ice	β_i	1.94 km s ⁻¹	<i>g</i>
S-wave, Sediment	β_s	2.25 km s ⁻¹	<i>g</i>
Density, Firm	ρ_f	726 kg m ⁻³	<i>adg</i>
Density, Ice	ρ_i	917 kg m ⁻³	<i>e</i>
Density, Water	ρ_w	1029 kg m ⁻³	<i>b</i>
Density, Sediment	ρ_s	2450 kg m ⁻³	<i>g</i>
Est. Thickness, Firm	F	0.075 km	<i>adg</i>
Med. Thickness, Ice	\tilde{h}	0.325 km	<i>f</i>
Med. Thickness, Water	\tilde{H}	0.464 km	<i>f</i>

^a (Kirchner and Bentley, 1979)

^b (Fofonoff and Millard Jr, 1983)

^c (Beaudoin et al., 1992)

^d (King and Jarvis, 2007)

^e (Griggs and Bamber, 2011)

^f (Fretwell et al., 2013)

^g (Diez et al., 2016)

Table 3.3: Comparative measurements of Ross Ice Shelf total ice thickness (“Ice”), subshelf cavity thickness (“H₂O”), and orthometric elevation (“Elv”) for all floating stations. The GPS column lists the averaged coordinates for the entire deployment period, derived from twice-daily telemetered state-of-health reports. Data for the BEDMAP2 (50 km² resolution) and REMA (8 m² resolution) columns were interpolated to the twice-daily state-of-health coordinates and then averaged. The PSD-Estimated column shows ice and water layer thicknesses as derived with Equation (3.3), Table 3.2, and resonance periods manually selected from the median P-wave arrival PSDs (e.g., Figure 3.6). Residuals are the differences of the BEDMAP2 or REMA values from the PSD-Estimated values. All values are in kilometers, for consistency with Tables 2.1 and 3.2. BEDMAP2 H₂O values for DR01–DR03 show the depth of the entire water column, as the RIS ice front did not extend to these locations when those data were collected; REMA also does not report elevations for these locations.

Station	GPS		PSD-Estimated			BEDMAP2			REMA	Residuals			
	Lat	Lon	Ice	H ₂ O	Elv	Ice	H ₂ O	Elv	Elv	Ice	H ₂ O	Elv _{BEM2}	Elv _{REMA}
DR01	-77.767	178.346	0.215	0.489	0.037		0.744				-0.255		
DR02	-77.824	-178.424	0.326	0.542	0.049		0.691				-0.149		
DR03	-78.262	-175.115	0.224	0.489	0.038		0.598				-0.109		
DR04	-78.280	-178.794	0.296	0.481	0.046	0.272	0.498	0.044	0.045	0.024	-0.017	0.002	0.001
DR05	-78.632	-179.093	0.309	0.420	0.048	0.295	0.471	0.047	0.048	0.014	-0.051	0.001	0.000
DR06	-78.788	-179.715	0.323	0.458	0.049	0.317	0.470	0.049	0.051	0.006	-0.012	0.000	-0.002
DR07	-78.931	179.198	0.304	0.523	0.047	0.307	0.508	0.048	0.048	-0.003	0.015	-0.001	-0.001
DR08	-78.949	179.658	0.335	0.481	0.050	0.312	0.504	0.049	0.050	0.023	-0.023	0.001	0.000
DR09	-78.957	179.889	0.315	0.426	0.048	0.322	0.489	0.050	0.051	-0.007	-0.063	-0.002	-0.003
DR10	-78.965	-179.880	0.326	0.458	0.049	0.329	0.473	0.051	0.051	-0.003	-0.015	-0.002	-0.002
DR11	-78.996	-178.953	0.329	0.359	0.050	0.324	0.423	0.050	0.052	0.005	-0.064	0.000	-0.002
DR12	-79.009	-179.922	0.332	0.497	0.050	0.327	0.479	0.050	0.050	0.005	0.018	0.000	0.000
DR13	-79.054	-179.965	0.323	0.458	0.049	0.329	0.478	0.051	0.049	-0.006	-0.020	-0.002	0.000
DR14	-79.142	179.948	0.329	0.466	0.050	0.326	0.469	0.051	0.048	0.003	-0.003	-0.001	0.002
DR15	-79.492	-179.920	0.323	0.432	0.049	0.350	0.427	0.053	0.048	-0.027	0.005	-0.004	0.001
DR16	-80.869	178.431	0.352	0.317	0.052	0.351	0.286	0.052	0.052	0.001	0.031	0.000	0.000
RS01	-78.184	169.965	0.289	0.685†	0.045	0.222	0.703	0.041	0.041	0.067	-0.018	0.004	0.004
RS02	-78.493	173.346	0.335	0.523	0.050	0.326	0.544	0.050	0.051	0.009	-0.021	0.000	-0.001
RS03	-78.760	176.878	0.318	0.426	0.048	0.326	0.379	0.050	0.051	-0.008	0.047	-0.002	-0.003
RS04	-78.981	-179.418	0.323	0.414	0.049	0.320	0.459	0.050	0.048	0.003	-0.045	-0.001	0.001
RS05	-79.160	-175.533	0.320	0.286	0.049	0.330	0.293	0.051	0.052	-0.010	-0.007	-0.002	-0.003
RS06	-79.283	-171.620	0.335	0.335	0.050	0.342	0.344	0.052	0.053	-0.007	-0.009	-0.002	-0.003
RS07	-79.365	-167.605	0.390	0.226	0.056	0.405	0.221	0.059	0.060	-0.015	0.005	-0.003	-0.004
RS10	-79.279	-155.469	0.597†	0.187	0.079	0.616	0.179	0.081	0.082	-0.019	0.008	-0.002	-0.003
RS15	-80.496	-169.979	0.381	0.177	0.055	0.375	0.099	0.055	0.056	0.006	0.078	0.000	-0.001
RS16	-80.133	179.368	0.315	0.397	0.048	0.312	0.420	0.049	0.049	0.003	-0.023	-0.001	-0.001
RS18	-81.594	177.335	0.362	0.221	0.053	0.369	0.238	0.054	0.051	-0.007	-0.017	-0.001	0.003
Median			0.326	0.458	0.049	0.326	0.471	0.050	0.051	0.003	-0.015	-0.001	-0.001
MAD			0.011	0.061	0.001	0.015	0.073	0.002	0.002	0.010	0.023	0.001	0.001

† Both the $n = 1$ and $n = 2$ resonance harmonics were identified for these layers at these locations. For all other locations, only the $n = 1$ harmonic could be identified.

3.9 Figures

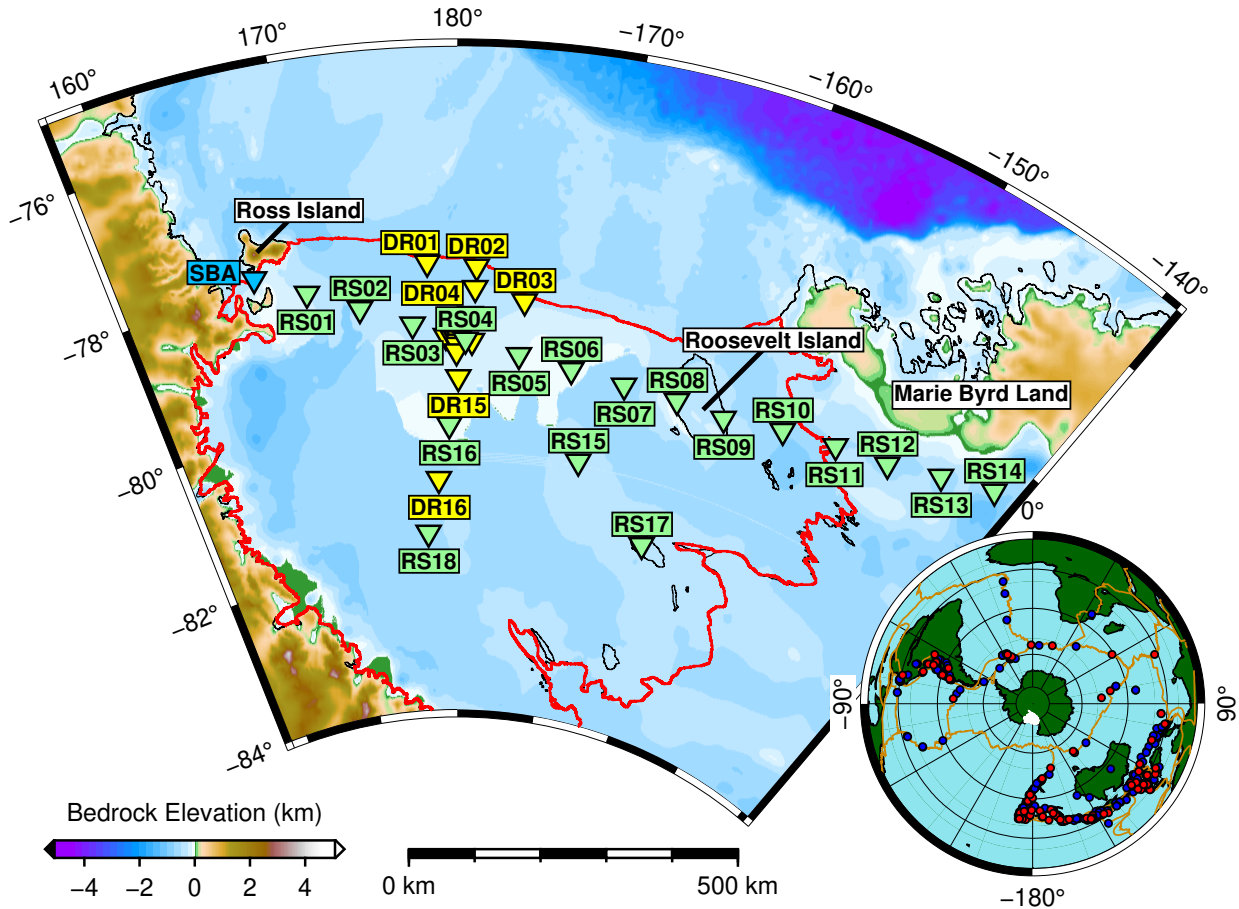


Figure 3.1: RIS array station locations. DR stations not explicitly labeled here (DR05–DR14; unlabeled yellow triangles) were deployed in the vicinity of central station RS04 (Figure A-2.10). All RS and DR stations were deployed on ice and all were on the floating ice shelf with the exception of: RS08 and RS09 on Roosevelt Island; RS11–RS14 on the West Antarctic Ice Sheet in Marie Byrd Land; and RS17 on an unnamed grounded location within the RIS. Also shown is the Global Seismographic Network (Butler et al., 2004) land station SBA on Ross Island (blue). The Ross Ice Shelf is outlined in red. A few features of the RIS in BEDMAP2 (Fretwell et al., 2013) are outdated since that model is based on data collected by 1996. In particular, the northward extent of the RIS ice front has advanced several kilometers since 1996 and in 2017 was located ~ 3 km north of the ice front stations DR01–DR03. For Figures 3.1 and A-2.1, we shifted the coordinates of the ice front stations south by 23 km to avoid confusingly plotting stations in the ocean, but our profiles of the North-South transect utilized the unaltered positions. **Inset:** Map of Summer (red) and Winter (blue) earthquake-signal sources used in this study. Antarctica is displayed with the traditional Grid-North orientation.

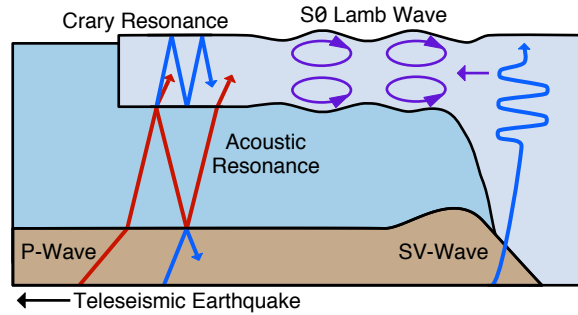


Figure 3.2: Schematic of the secondary wavefields generated within a floating plate by teleseismic body wave arrivals (“P-wave”, “SV-wave”). “Crary Resonance” refers to an SV-wave resonance within the ice layer; this resonance may occur at non-critical angles for the ice/water layer interface and is therefore akin to a leaky Crary wave. An “Acoustic Resonance” is simply P-waves reverberating within the water column. “ S_0 Lamb Wave” shows the fundamental-mode symmetric Lamb wave generated by a teleseismic SV-wave incident at the grounding zone, with SV particle displacement perpendicular to the grounding line. Other plate modes are possible (e.g., P-to-SV resonances within the ice, or shear-horizontal plate waves generated by SH-waves incident at the grounding zone) but are not illustrated here.

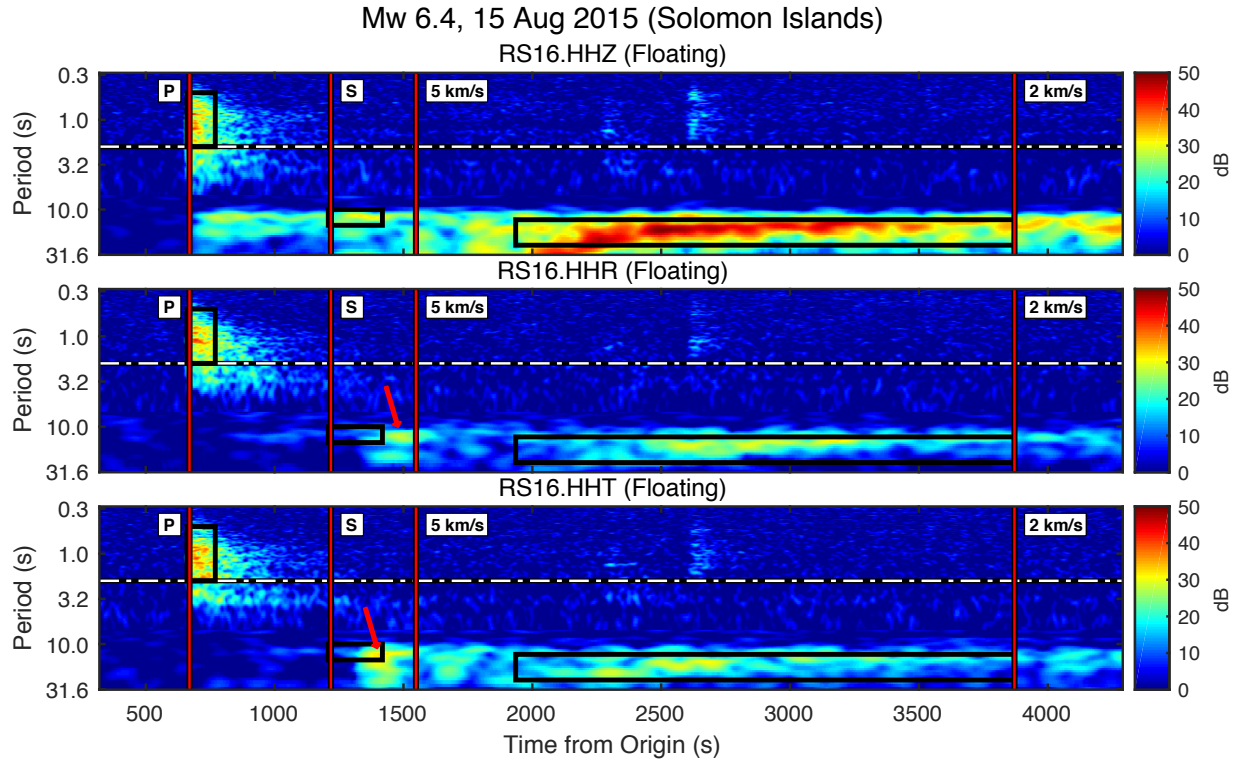


Figure 3.3: Pre-P background-normalized spectrogram from floating station RS16 of an M_w 6.4 earthquake east of the Solomon Islands, with an epicentral distance of 7740 km, a hypocenter depth of 8 km, and a back-azimuth of 345° . For periods less than 7.0 s, PSDs were calculated using 50 s segments in 0.5 s moving increments. For periods greater than 7.0 s, PSDs were calculated for 200 s intervals in 2.0 s moving increments. Red vertical lines mark *ak135*-predicted arrival times. Black rectangles mark the spectral and temporal integration bounds used for signal analysis. White and black line marks the acoustic cutoff period as estimated by Equation (3.4). Red arrows indicate probable Lamb waves generated by S-wave arrivals at RIS grounding lines to the southeast (HHR, Equation (3.6)) and to the southwest (HHT, Equation (3.7)). This event is illustrative in that it has a high SNR 2.1), being recorded during winter low-noise conditions when contiguous sea-ice in the Ross Sea strongly attenuates ocean gravity waves before they can excite the RIS (Baker et al., 2019) or generate strong microseisms (Anthony et al., 2015). Figure A-3.3 shows the unnormalized spectrogram.

Mw 6.4, 15 Aug 2015 (Solomon Islands)
RS08.HHZ (Grounded)

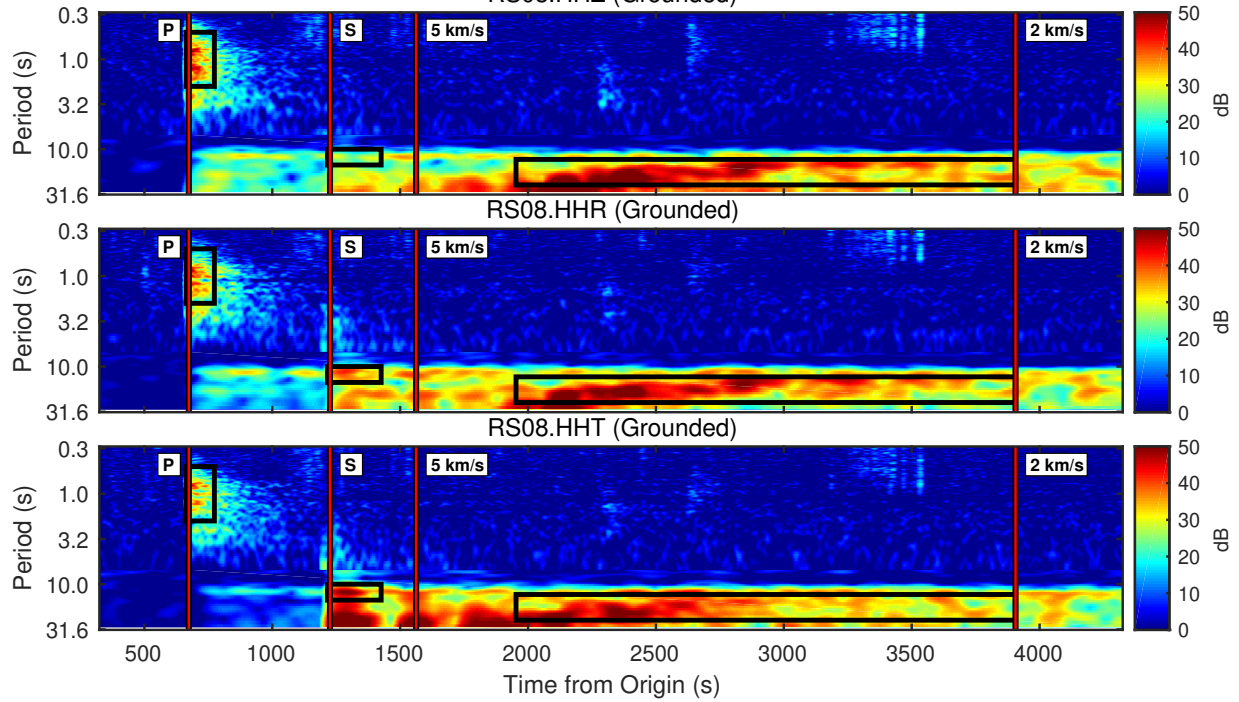


Figure 3.4: Pre-P background-normalized spectrogram from grounded station RS08 for the same earthquake presented in Figure 3.3. Epicentral distance was 7800 km with a back-azimuth of 325°. Figure A-3.4 shows the unnormalized spectrogram.

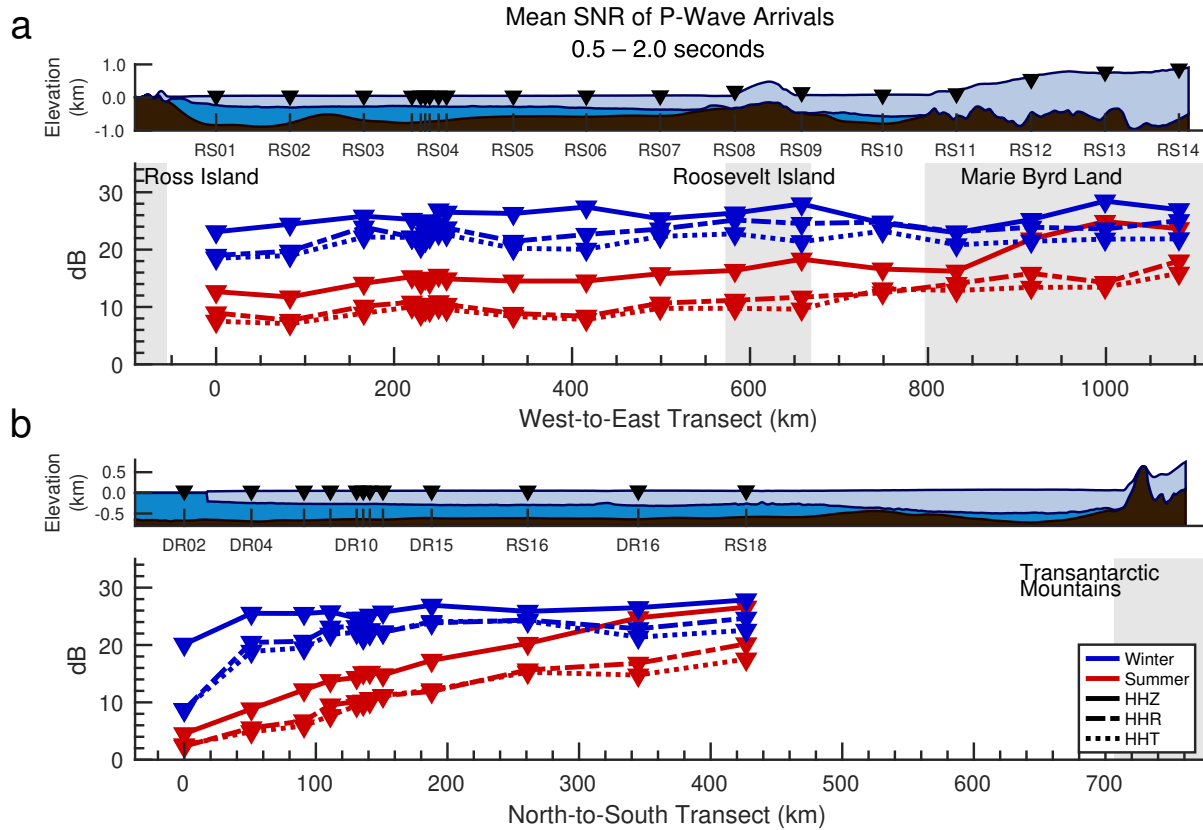


Figure 3.5: Seasonal and geographic variations in average acceleration power for teleseismic P-wave arrivals, for the indicated seasonal SNR-PSD medians. Ice and water thickness profiles are based on outdated BEDMAP2 data. The RIS ice front currently sits ~ 3 km north of DR02. Gray backgrounds indicate approximate areas of grounded ice. Data have been corrected using Equation (3.1); Figure A-3.6 plots the uncorrected data.

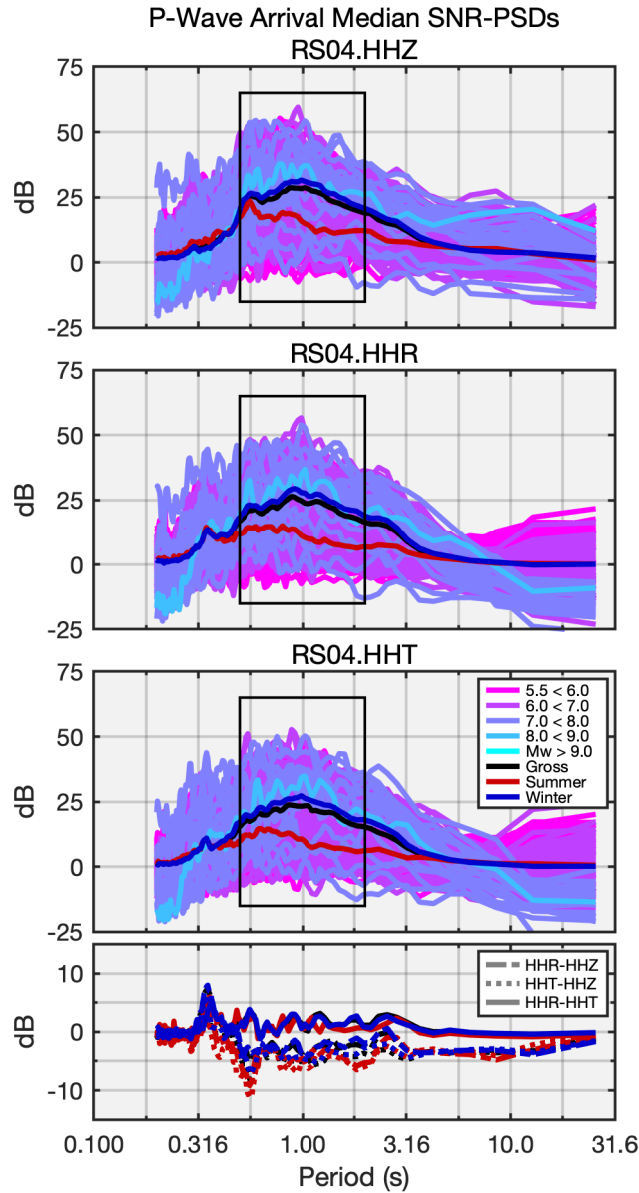


Figure 3.6: Median SNR-PSDs for all teleseismic P-wave arrivals recorded at floating station RS04. Acoustic resonances are apparent on the vertical (HHZ) and radial (HHR) components. Cray resonances are observed on the radial (HHR) and transverse (HHT) components. The bottom panel shows the differential PSDs. The periods of these peaks (manually selected) at each floating station were used with Equation (3.3) and Table 3.2 to estimate the ice and water thicknesses shown in Table 3.3. SNR-PSDs were not smoothed for this process (to maintain spectral resolution) but were scaled by distance and magnitude using Equation (3.1).

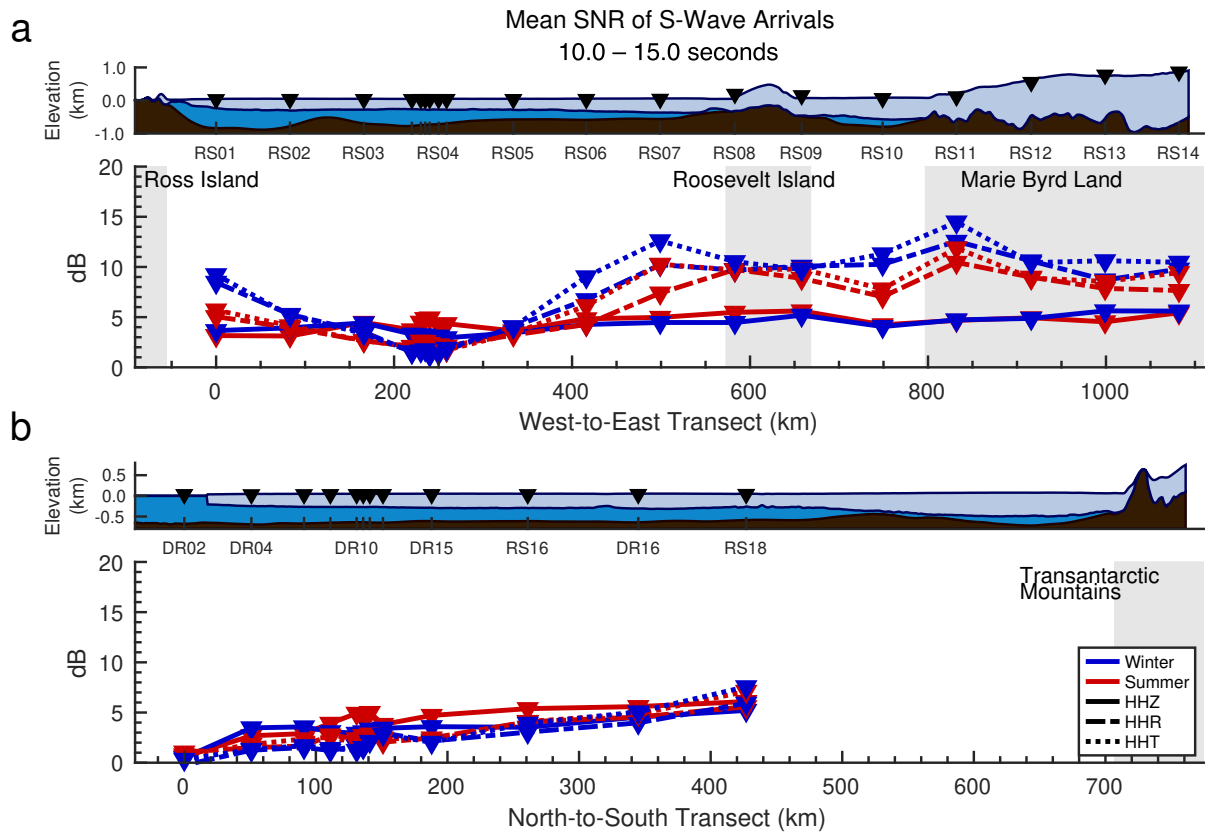


Figure 3.7: Seasonal and geographic variations in average acceleration power for teleseismic S-wave arrivals, for the indicated seasonal median SNR-PSDs. See Figure 3.5 for other details. See Figure A-3.7 for the plot of the uncorrected data.

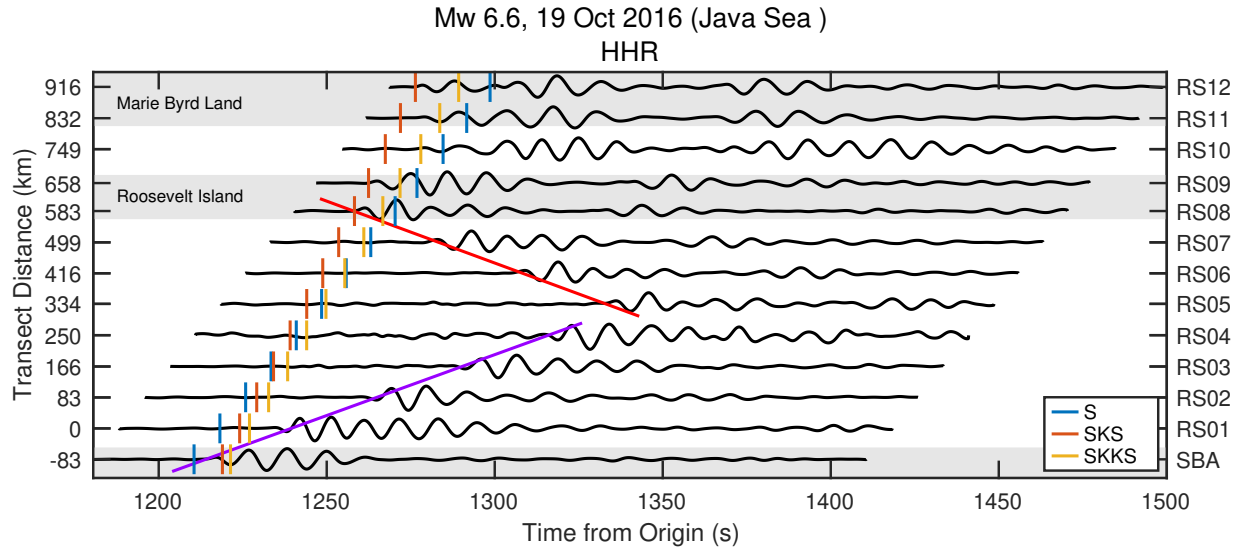


Figure 3.8: Radial component ground velocity record section for teleseismic S-waves arriving from the 19 October, 2016, M_w 6.6 Java Sea earthquake (hypocenter depth: 614 km). Stations and event epicenter are within 1° of a common great circle arc. The purple and red lines mark the (manually fit) travel time curves for S_0 Lamb waves generated by SV-wave incident at the grounding lines at Ross (3.25 km s^{-1}) and Roosevelt (3.32 km s^{-1}) Islands, respectively. Ground velocity data were bandpass filtered at 10–15 s and were self-normalized for clarity. Body wave arrival times were predicted with *ak135*.

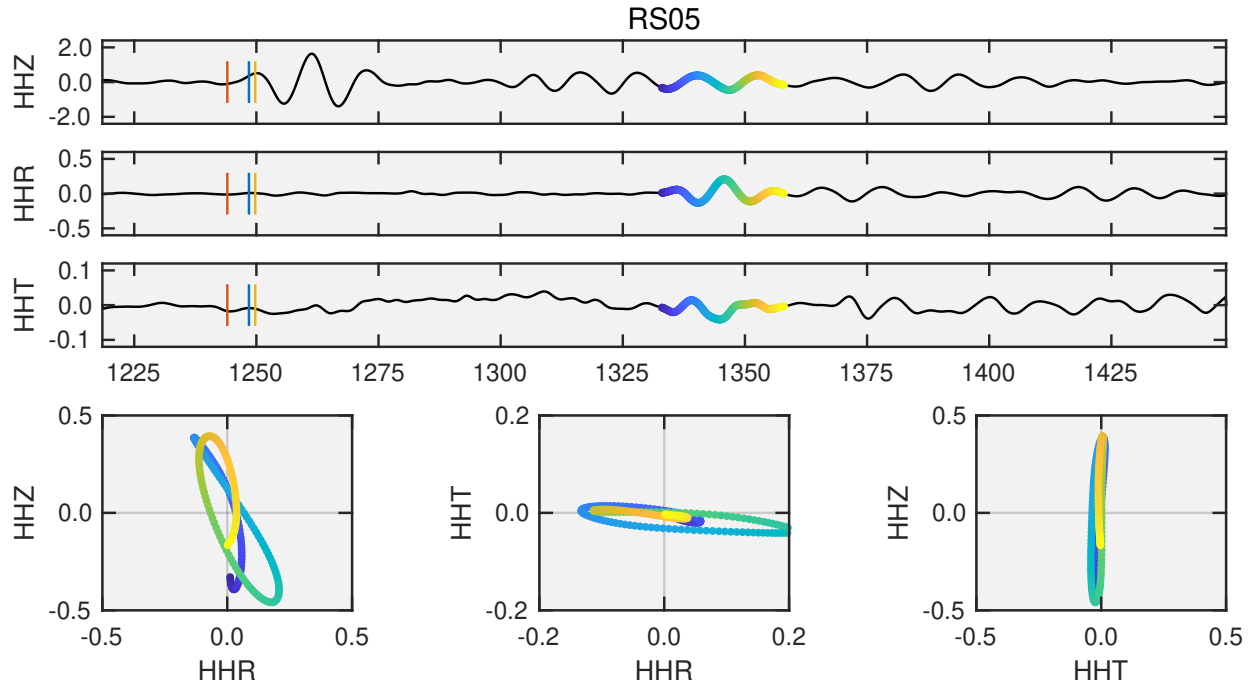


Figure 3.9: Three-component ground velocities and particle motions ($\mu\text{m s}^{-1}$) at floating station RS05 for the earthquake described in Figure 3.8. The identified Lamb wave arrival and associated particle motions are highlighted by the 25 s of multi-colored trace. Clockwise particle motions in the radial/vertical (HHR/HHZ) plane are consistent with an S_0 Lamb wave with expected retrograde particle motions (Viktorov, 1967; Rose, 1999) propagating in the anti-radial direction from the grounding line at Roosevelt Island (Figure 3.8, red travel time curve). Motion on the vertical component is dominated by the solid-Earth S-wave coda; S_0 Lamb waves are otherwise expected to be radially polarized.

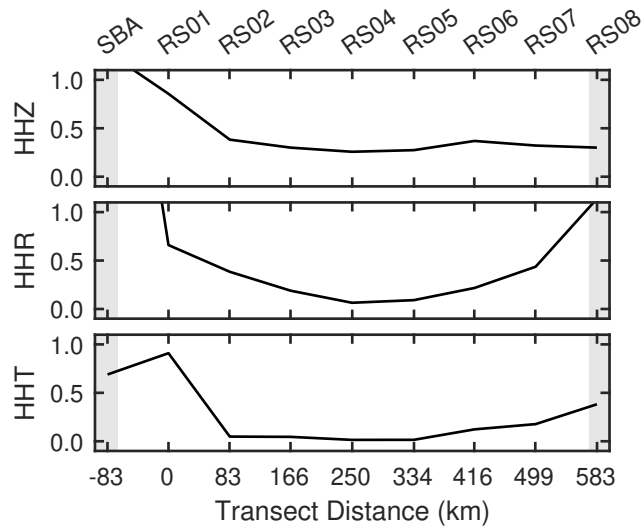


Figure 3.10: Root-mean-squared (RMS) ground velocity amplitudes ($\mu\text{m s}^{-1}$) for the Lamb waves identified in Figure 3.8. RMS values are based on 25 s of Lamb wave arrival, similar to Figure 3.9. Radial component RMS at SBA was $4.7 \mu\text{m s}^{-1}$; RS08 was $1.14 \mu\text{m s}^{-1}$. Gray backgrounds indicate approximate areas of grounded ice.

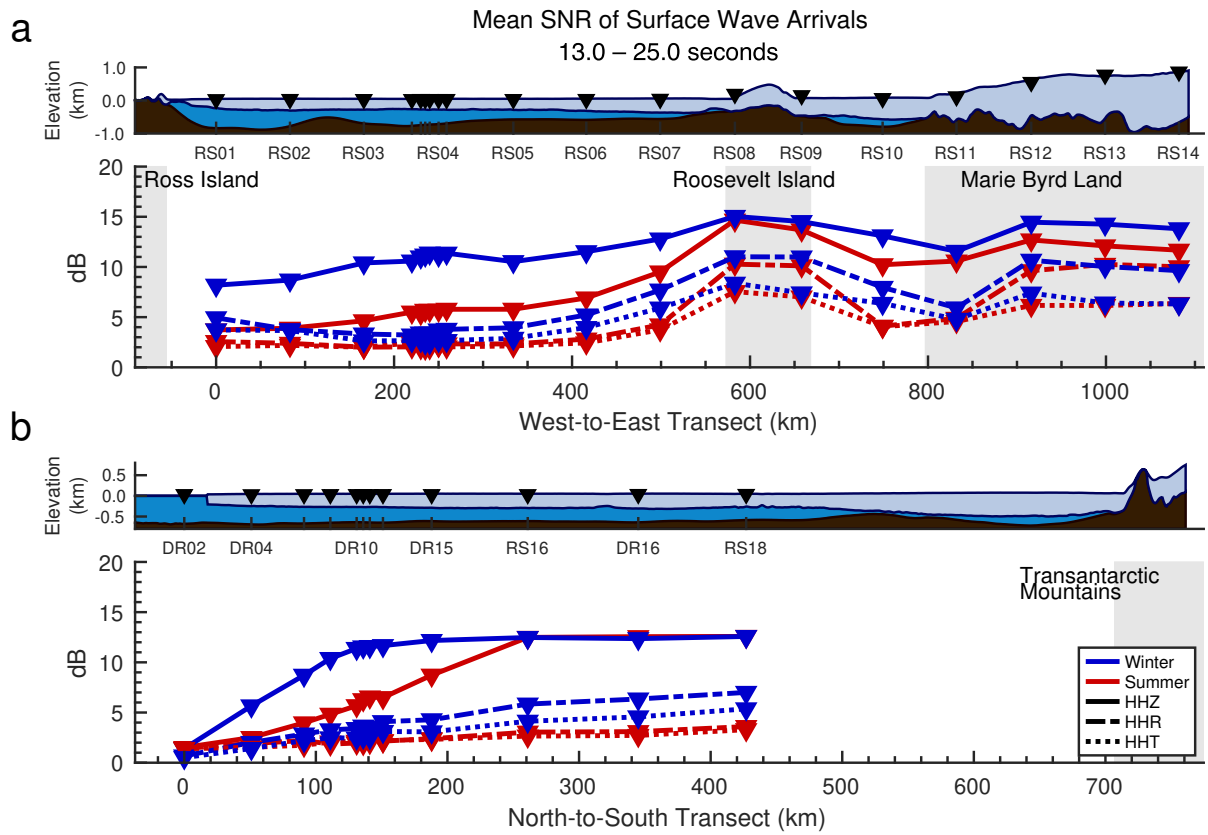


Figure 3.11: Seasonal and geographic variations in average acceleration power for teleseismic surface wave arrivals, for the indicated seasonal median SNR-PSDs. See Figure 3.5 for details. Data have been corrected using Equation (3.2); Figure A-3.9 plots the uncorrected data.

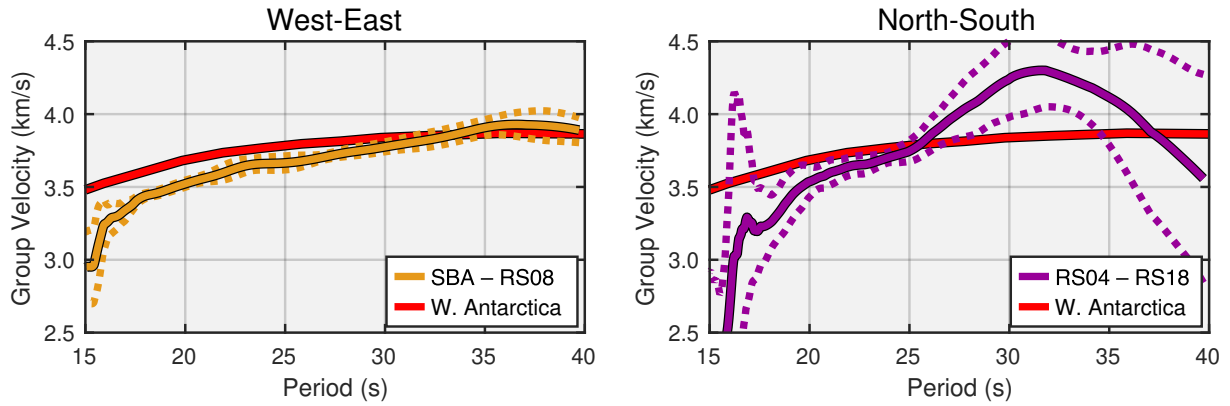


Figure 3.12: Representative regional Rayleigh wave group velocities along the RIS transects, determined from cross-correlation of multiple filter analyses for the indicated station pairs (Dziewonski et al., 1969; Meier et al., 2004). The W-E curve is the median of four events from the Nazca subduction zone; the N-S curve is the median of seven events from the New Zealand subduction zone. Dashed lines indicate the Median Absolute Deviations. Data have been smoothed with a 21-point rolling average filter. Red curves are representative group velocities for West Antarctica from Shen et al. (2017).

Chapter 4

Inversion of Teleseismic P-wave Autocorrelations for Crustal Velocity Structure Beneath the Ross Ice Shelf

4.1 Motivation

Passive seismic imaging of crustal scale velocity discontinuities using data from a single seismograph station has traditionally utilized the receiver function method, wherein strong impedance contrasts are detected by comparison of the vertical and horizontal wavefields. Receiver functions may be calculated with first arrival teleseismic P-waves or S-waves, though the longer periods of teleseismic S-waves yields resolutions more appropriate for mantle scale studies. For P-wave receiver function analysis (PRF), the vertical seismograph component is assumed to record only steeply incident first arrival teleseismic P-waves, while the horizontal components record the P-to-S converted wavefield excited by P-wave scattering from crustal impedance contrasts (i.e., the coda).

The PRF, $h(t)$, is an approximation of the radial impulse of the substation crust which can be recovered from the radial and vertical seismograms, $r(t)$ and $z(t)$, respectively, by assuming that

$$r(t) = I(t) * h(t) * e(t) , \quad (4.1)$$

$$z(t) = I(t) * \delta(t) * e(t) , \quad (4.2)$$

where the instrument response, $I(t)$, and the earthquake source function, $e(t)$, are assumed the same for both components; the vertical impulse response of the crust is assumed to be the delta function $\delta(t)$; and $*$ indicates convolution (Langston, 1979). The PRF equation, $h(t) * z(t) = r(t)$, may be solved for through application of the convolution theorem, such that

$$h(t) = \mathcal{F}^{-1} \left[\frac{R(\omega)}{Z(\omega)} \right], \quad (4.3)$$

where \mathcal{F}^{-1} is the inverse Fourier transform, and $R(\omega)$ and $Z(\omega)$ are the frequency domain radial and vertical seismograms. In practice, deconvolution through spectral division may become numerically unstable near frequencies at which $Z(\omega)$ approaches zero, so Equation (4.3) is typically solved via a regularized or filtered deconvolution in the frequency or time domain.

Because the shear modulus of water is zero, S-waves originating in the solid Earth below an ice shelf cannot propagate into the water column, effectively decoupling the horizontal tractions of the ice shelf and the solid Earth. For seismographs sited on an ice shelf, any observed horizontal wavefield is the result of ambient (e.g., oceanic or atmospheric forcing) or internal transient (e.g., ice shelf icequakes) processes, or P-to-S-wave scattering at the water/ice interface, the free surface of the ice, or plate wave energy propagating from the grounding lines (e.g, Chapter 3). Consequently, receiver functions collected on an ice shelf can only provide information on impedance contrasts within the ice itself.

Autocorrelation of teleseismic P-wave coda is recently developed method for single station, passive imaging of crustal scale features (Sun and Kennett, 2016; Phạm and Tkalčić, 2017). Autocorrelations interrogate velocity structure by emphasizing single-phase wavefields that are multiply-reflected between impedance contrasts (e.g., the PpPp phase reflected between the free surface and the Moho).

In this chapter, I will show that vertical component autocorrelation of teleseismic P-wave coda is a viable method for single station, passive imaging of crustal scale features beneath an ice shelf. First, I will test the autocorrelation method against a PRF inversion of land-sited seismic station MPAT, located at Mount Patterson, Antarctica; this station is an ideal benchmark due to its historically unambiguous inversions (Chaput et al., 2014). I will present autocorrelation-derived Moho depth estimates for all RIS/DRIS stations, and will test the consistency of these results relative to PRF-interpolated (Chaput et al., 2014) and surface wave-derived (Shen et al., 2018) estimates of Moho depths across the Ross Embayment.

4.2 Data and Methods

4.2.1 Data and Preprocessing

Event selection was similar to that used in Chapter 3 (Figure 3.1). Earthquake magnitude was limited to M_w 5.5 or greater to guarantee usable signal-to-noise ratios (SNR). Earthquake location was restricted to epicentral distances of 30° to 95° from each station, as dictated by P-wave shadows within the Earth (Stein and Wysession, 2009). Autocorrelations were ultimately calculated from 100 s of post-P-wave arrival, as predicted by *ak135* travel time curves (Kennett et al., 1995). For matched-noise filtering, I additionally collected 100 s of pre-P-wave arrival time series.

I do not discriminate against overlapping events or the summer high noise state. Due to the large number of earthquakes (approximately 420 earthquakes per station) and stations (34), I also do not manually cull low signal-to-noise events. As shown in Chapter 3, the low noise environment of the RIS in the 0.5–2.0 s band provides upwards of 10 dB of SNR for teleseismic P-wave arrivals even during the summer high noise state. Furthermore, impedance contrasts within the ice shelf system and the presumed seafloor sediments (Beaudoin et al., 1992) result in extensive reverberatory codas (in comparison to grounded stations) which hinder automated SNR checks (e.g., STA/LTA).

All time series data are corrected for instrument response, and then downsampled to 10 Hz to reduce processing times. Seismograms are rotated to "vertical-radial-transverse" (ZRT) coordinates.

Matched-noise filters are constructed from 100 s of pre-event noise and convolved with the associated signal time series. The frequency domain noise filter, $N_f(\omega)$ is:

$$N_f(\omega) = 1 - \frac{|N(\omega)|}{\max|N(\omega)|}, \quad (4.4)$$

where $N(\omega)$ is the frequency domain noise data.

In addition to the spectral whitening recommended by Phạm and Tkalčić (2017), floating station seismograms generally require two rounds of bandpass filtering—one before and one after the spectral flattening—to properly emphasize Moho-reflected phases on the autocorrelations. Both applications of filtering uses a 2-pole Butterworth filter with corners periods nominally at 0.5 and 2.0 s, as suggested by the P-wave arrival PSDs (Figure 3.6).

The spectral whitening operation is:

$$Z(\omega)'_q = \frac{Z(\omega)_q}{\frac{1}{2^{\mu+1}} \sum_{m=q-\mu}^{q+\mu} |Z(\omega)_m|} G_k(\omega), \quad (4.5)$$

where q indexes the frequency domain elements of the signal, $Z(\omega)$, μ is the width of the smoothing operation, and $G_k(\omega)$ is a Gaussian filter. This study uses an empirically derived value of $\mu = 5$ and a Gaussian filter width of 2 Hz.

4.2.2 Processing of Autocorrelations

The vertical component autocorrelations, $zz(t)$, are computed in the frequency domain with the entire 100 s of preprocessed signal, $z(t)$:

$$zz(t) = \mathcal{F}^{-1} \left[Z(\omega) Z^*(\omega) \right], \quad (4.6)$$

where $Z^*(\omega)$ is the complex conjugate of $Z(\omega)$.

Because the autocorrelation is simply the time domain counterpart of the power spectral density, the same techniques for enhancing PSD SNR may be applied to autocorrelations. For the current application, Welch segment averaging (Welch, 1967) and multitaper segment averaging (Helffrich, 2006) were tested but yielded insignificant (or even ambiguous) gains for greater computational expense, and therefore were not utilized for the final processing. A 1.5 s cosine taper was applied to all autocorrelations to decimate the central correlation peak.

Complex source functions (i.e., non-impulsive) have the potential to obscure receiver-side crustal reflections. This is typically not a concern for the traditional receiver function method, con-

tingent on the assumption that the source function is equally represented within the radial and vertical seismograms (Equation (4.3)). Autocorrelation inherently retains the source function, which may be problematic for the analysis of individual seismograms. For such cases, deconvolution of an estimated source kernel derived from cross correlating adjacent network stations may improve the SNR of crustal reflections (Langston, 2011).

For robust datasets comprised of hundreds of seismograms, simple linear stacking of autocorrelations is sufficient for mitigating variations in source functions (Figure 4.2). By the definition, the constituent Fourier sinusoids of an autocorrelation all have zero phase; as a consequence, spectral components that are coherent across multiple seismograms (e.g., surface to Moho reflections) will stack constructively regardless of contamination by incoherent source functions or noise.

Slowness correction can be applied to autocorrelations in a similar manner as to receiver functions, potentially boosting the SNR of Moho phases that would otherwise be obscured by the direct stacking of waveforms with variable ray parameters (e.g., Figure 4.2). For this study, I employ a correlation optimized warping (COW) algorithm (Nielsen et al., 1998; Tomasi et al., 2004). Similar to dynamic time warping, COW corrects for misalignments or shifts in discrete data through piecewise linear warping of a sample signal, as required to match a supplied signal kernel. The sample signal is partitioned into segments of predetermined length and each segment, in sequence, is contracted (linearly decimated) or expanded (linearly interpolated) through a range of warping factors (e.g., $0.8N$ to $1.2N$). At each stage of warping, the correlation coefficient is determined for the warped segment and an equal length segment of the kernel signal. The warped segment with the highest correlation coefficient is used to rebuild the sample signal.

For slowness correction, the COW segment length and warping factor may be determined based on estimated Moho depth. For example, assuming an *ak135*-like crust with a Moho depth of 24 km, the PpPp phase should appear on the autocorrelation at between 8.61 s and 9.27 s relative to the initial P-wave, for epicentral distances of 30° and 95° , respectively. For a kernel autocorrelation representative of an epicentral distance of 60° , the PpPp phase should appear at 9.0 s. Prescribing a COW segment length of 10 s and a warping range of ± 0.5 s should align the PpPp phase for

a given sample autocorrelation with the kernel, effectively applying a slowness correction to 60° . Figures 4.3 and 4.4 present demonstrations of this method.

After the COW slowness correction has been applied to each individual autocorrelation, a station-representative autocorrelation is produced with a phase-weighted stacking (Schimmel and Paulssen, 1997; Phạm and Tkalčić, 2018) of all individual autocorrelations collected by that station. The phase-weighted autocorrelation stack, $\tilde{z}z(t)$, is:

$$\tilde{z}z(t) = \frac{1}{N_E} \sum_{j=1}^{N_E} zz_j(t) \left| \frac{1}{N_E} \sum_{k=1}^{N_E} \exp[i\Phi_k(t)] \right|, \quad (4.7)$$

where N_E is the number events, and $\Phi_k(t)$ is the instantaneous phase of the analytic signal of the autocorrelation $zz_k(t)$.

4.2.3 Inverse Modeling

Inverse modeling of crustal velocity structure using the vertical component P-wave autocorrelations is accomplished with Markov Chain Monte Carlo (MCMC) sampling (Mosegaard and Tarantola, 1995; Chaput et al., 2014; Aster et al., 2018). The Monte Carlo method uses randomly generated parameters (e.g., body wave velocity and layer thickness for a vertically stratified crustal model) to explore a theoretical model space (the *posterior distribution*) with the goal of extracting a forward model that best fits the observed data. Markov Chain parameter generation specifies that, for a random walk through a parameter space, the value of each successive value is dependent only on the immediately previous value; in other words, the probability distribution of the random walk is time invariant.

The MCMC algorithm starts from a predefined *prior model* and is set to randomly perturb the model parameters within a chosen *proposal distribution*. To ensure that the posterior space contains only physically plausible models, a *prior distribution* is also defined to discard any candidate models that diverge too far from the prior model. For each accepted candidate model (e.g., a crustal velocity model that lies within the prescribed prior distribution), a forward model is constructed (e.g., the synthetic autocorrelation for the impulse response of the velocity model) and is quantita-

tively compared to the observed data. Forward models that result in a smaller misfit than previous models are added to the posterior distribution. Model steps that increase the misfit may also be allowed (and thus seed greater exploration of posterior models), but are subject to a Metropolis-Hastings proposal function selection criterion (e.g., Aster et al., 2018). When a sufficient number of posterior models have been sampled, the best-fit model is extracted as the mean of the posterior model.

Because the initial model of the MCMC is often in a poorly-fit region of the posterior space, a *burn-in* period (here empirically set to 3000 iterations) is imposed on the MCMC algorithm. Posterior models sampled during the burn-in period are not added to the posterior distribution, reducing the number of poorly-fit and initially biased outliers incorporated into the posterior mean and other marginal statistical metrics.

Selection of the prior model will be discussed in Section 4.3.2, pursuant to interpretation of the recovered ice shelf autocorrelations.

The presence of low velocity ice and sediment layers, and their associated strong impedance contrasts, may result in strong amplitude resonances (e.g., Chaput et al., 2014; Walter et al., 2014). MCMC sampling may incorrectly fit these resonances with physically-improbable models with alternating high and low velocity layers. Total Variation (TV) regularization is therefore used to penalize wildly alternating models during the calculation of the objective function for each iteration. The TV regularization term, T_m , is

$$T_m = \sum_{l=1}^L |m_{l+1} - m_l| , \quad (4.8)$$

where m is the candidate model, and L is the number of layers to regularize (here, restricted to crustal layer models). For each MCMC iteration, the objective function, M_i , is then

$$M_i = \left[\sum_{n=1}^N z z(n)^2 - \hat{z} \hat{z}(n)^2 \right]^{1/2} + \alpha T_m , \quad (4.9)$$

where N is the number of points in the time series, $zz(n)$ is the observed autocorrelation, $\widehat{zz}(n)$ is the forward-modeled autocorrelation, and α is an inversely proportional weighting term that penalizes negative velocity jumps, at the expense of data fit. The weighting term is empirically determined on a per-station basis.

As noted above, a Metropolis-Hastings sampler (Aster et al., 2018) was implemented to dissuade the MCMC algorithm from excessive convergence in the vicinity of local objective function minima of the objective function. Specifically, for each candidate model the change in the objective function, $\log_{10}(\Delta M_{j-i})$, must be less than a uniformly distributed random variable, $\log_{10}(U[0,1])$, or else the candidate model is discarded and the MCMC iterates again from the previously accepted candidate model; logarithms are used to avoid floating-point precision errors.

4.2.4 Forward Modeling

Impulse responses for the crustal models used in this study were calculated with the reflectively method detailed in Kennett (2013). For a crustal model with L layers and interfaces, the free surface displacement vector, $u_{z,r}^0$, resulting from an impulsive source located in the semi-infinite halfspace is

$$\begin{bmatrix} u_z^0 \\ u_r^0 \end{bmatrix} = W_0 Q_U^{0,L} \begin{bmatrix} \Phi_U^L \\ \Psi_U^L \end{bmatrix} \quad (4.10)$$

where W_0 is the free surface operator that converts P- and S-wave vectors into vertical and radial displacements, respectively, $Q_U^{0,L}$ is the wavefield transfer map for layer interfaces 0 through L , and Φ_U^L and Ψ_U^L are the source P- and S-wave vectors located in the halfspace layer L , just below interface L .

The transfer map, $Q_U^{0,L}$, represents a superposition of all upward and downward propagating wavefields, including resonance wavefields arising from reflections at each interface. As an example, the transfer map for the first three layers, $Q_U^{0,2}$, is

$$Q_U^{0,2} = \left\{ \mathbf{1} + \sum_{m=1}^M \left\{ \left[P^0 T_U^1 P^1 R_D^2 P^1 T_D^1 P^0 R_U^0 \right]^m + \left[P^0 R_D^1 P^0 R_U^0 \right]^m \right\} \right\} \left[P^0 T_U^1 P^1 T_U^2 \right] \\ + \left[P^0 T_U^1 \right] \left\{ \sum_{m=1}^M \left[P^1 R_D^2 P^1 R_U^1 \right]^m \right\} \left[P^1 T_U^2 \right] \quad (4.11)$$

where P is the wave vector phase advance across the superscripted layer, $R_{U,D}$ and $T_{U,D}$ are the upward and downward reflection and transmission coefficients for the superscripted interfaces, and M indicates the highest order of reverberation to be calculated.

The color highlighted raypaths are illustrated in Figure 4.5. These matrix terms include both compressive and (in solid media only) shear wavefields and correspond to: Purple) the initial, direct arrival; Green) a resonance between the free surface and the water/seafloor interface, with crustal and ice layer wavefield consisting of both P- and SV-waves; Blue) a resonance within the ice layer that includes SV-wave Crary resonances, pure P-wave resonances, and mixed mode P- and-SV-wave resonances; and Red) an acoustic resonance within the water column which leaks into the ice layer as both P- and SV-waves.

For $M = \infty$, the reverberation terms may be condensed into a more convenient (and computationally efficient) form by power series summation (Kennett, 2013). For example, using the red-highlighted term above for the water layer reverberation:

$$\sum_{m=1}^{M=\infty} \left[P^1 R_D^2 P^1 R_U^1 \right]^m = \left[I - P^1 R_D^2 P^1 R_U^1 \right]^+ \quad (4.12)$$

where I is the identity matrix, and the superscript $+$ indicates the Moore-Penrose pseudoinverse, which becomes necessary in the presence of solid/liquid interfaces.

The reflection and transmission matrices (R and T , respectively) are calculated with the Zoeppritz equations (Aki and Richards, 2002). Though derived for elastic wave scattering at a solid/solid interface, the matrix form of the Zoeppritz equations is easily modified—through deletion of the rows and columns governing S-wave scattering within the water layer—to satisfy the boundary conditions for a solid/liquid interface.

For elastic waves initially in a liquid and propagating upward into a solid:

$$RT = \begin{bmatrix} R_D^{PP} & R_D^{SP} & T_U^{PP} \\ R_D^{PS} & R_D^{SS} & T_U^{PS} \\ T_D^{PP} & T_D^{SP} & R_U^{PP} \end{bmatrix}. \quad (4.13)$$

For elastic waves initially in a solid and propagating upward into a liquid:

$$RT = \begin{bmatrix} R_D^{PP} & T_U^{PP} & T_U^{SP} \\ T_D^{PP} & R_U^{PP} & R_U^{SP} \\ T_D^{PS} & R_U^{PS} & R_U^{SS} \end{bmatrix}. \quad (4.14)$$

Similar to Figures A-3.1 and A-3.2, the superscripts read left to right; e.g., T_D^{PS} denotes the transmission coefficient for the downward propagating P-to-S-wave conversion.

4.3 Results and Discussion

4.3.1 MPAT Validation Test

Figure 4.6 shows the results of MCMC inversions for crustal velocity structure using P-wave receiver functions (PRF), vertical and radial component autocorrelations (ZZRR), and only vertical component autocorrelations (ZZ). The PRF inversion yielded a Moho depth of 28.5 ± 1 km versus 27.1 ± 3.65 km and 27.1 ± 1.68 km from the ZZRR and ZZ inversions, respectively. Chaput et al. (2014) reported a Moho depth of 27.5 ± 1 km, also based on PRF inversion.

MPAT was chosen as a benchmark for its unusually clear Moho-converted phases (e.g., Ps, PpPs, PpSs), its lack of both ice and water layers, and its repeatable inversion results.

Notably, the uncertainty of the ZZRR posterior mean model (Figure 4.6b) is more than twice that of the PRF and ZZ models. This may indicate that the chosen proposal distribution is inappropriate for joint inversion of P-wave and S-wave structure. Regardless, the success of the ZZ inversion relative to the PRF inversion demonstrates the viability of the vertical-only method for estimating Moho depths. The radial component can be safely ignored.

4.3.2 Ice Shelf Autocorrelations and Prior Model Selection

The preprocessing method described above yielded generally clean autocorrelations for all floating and grounded autocorrelations. Figure 4.4 is generally representative of autocorrelations obtained for floating and grounded stations in this study. Prominent and coherent reflection phases are observed at all stations at 8 to 10 s, consistent with an expected PpPp phase. An additional phase is observed at >16 s for most stations. This phase could not be replicated by synthetic models with only a single basal discontinuity, suggesting that it related to an additional, deeper impedance contrast rather than recording, for example, a second order PpPp reflection. For the sake of reduced inversion times, observed and forward modeled autocorrelations were truncated at 16 s, with the additional benefit of precluding the need to model the later arrival.

The vertical autocorrelations are also generally devoid of strong arrivals prior to 8 s. Teleseismically induced acoustic resonances occur at periods of ~ 1.0 s or shorter (Chapter 3, but are considerably attenuated by the spectral whitening process and long integration times (100 s); calculation of PSDs for teleseismic P-wave SNR used shorter Welch-averaged segments which emphasize shorter period signals. Assuming the sediment parameters listed in Table 3.2 and a thickness of 3 km, S-wave resonances in the seafloor sediment would leak acoustic energy into the water column at periods of ~ 2.4 s (Equation (3.3)). Strong resonance peaks at such periods are not observed on autocorrelations; this is again likely due to the processing parameters chosen for emphasizing the deeper Moho phase at the expense of shallower phases (Phạm and Tkalčić, 2018). During initial testing, incorporation of a sediment layer in the MCMC inversion typically resulted in poorly matched forward models and unstable or physically implausible posterior distributions.

Informed by these observations, a simplified prior model was chosen for MCMC inversion, consisting only of an *ak135*-like crust (Kennett et al., 1995; Chaput et al., 2014; Shen et al., 2018) overlaid by a station-specific water column and ice shelf. The crust is modeled as eight layers with Moho located at 25 km depth. Ice shelf values are as determined in Chapter 3, while grounded ice stations use Fretwell et al. (2013) values for ice cap thickness.

The parameter random walk is allowed to perturb crust layer thickness, P-wave velocity, and Poisson’s ratio within a prior distribution of ± 2 km, ± 1 km s⁻¹, and 0.01, respectively. Ice and water parameters are held constant. Candidate models are pulled from a uniform probability distribution with limits of 2 times the prior distribution bounds; this yields a prior distribution *acceptance ratio* of $\sim 50\%$, which is generally sufficient for exploring the entire posterior space (Mosegaard and Tarantola, 1995). Only a single model parameter—chosen randomly from all layer thicknesses and velocities—is perturbed each iteration.

The TV regularization coefficient, α , was set to 0.01 for all stations (Equation (4.9)).

4.3.3 MCMC Results and Interpretation

In general, the MCMC algorithm needed $\sim 50,000$ iterations and ~ 50 posterior samples to converge to the global minimum of the objective function within the prior distribution. Beyond ~ 100 posterior samples, the acceptance rate for posterior models decreased significantly, with the MCMC generally requiring 10,000 or more iterations to find new, marginally better-fit models. For the sake of statistical rigor, I imposed a soft limit of 100 accepted posterior models, after which the MCMC was reset to the prior model and—after another burn-in period—was allowed to again randomly sample the posterior space. These resets continued until a cumulative total of 300 posterior samples was collected.

The observed data was well-fit by the MCMC algorithm and the forward model: Pearson correlation coefficients (ρ) between the observed data and the posterior distribution mean exceeded 0.80 for all stations. Grounded ice stations (e.g., Figure 4.7) generally yielded higher-fidelity solutions ($\bar{\rho} = 0.89$) than floating ice stations ($\bar{\rho} = 0.85$) (e.g., Figure 4.8).

Figure 4.9 shows interpolated velocity structure for both transects of the RIS/DRIS array; P-wave velocity standard deviations are shown in Figure 4.10. The contour lines in Figure 4.9 indicate where the P-wave velocity of the posterior distribution crosses above 7.0, 7.5, and 8.00 km s⁻¹, from top to bottom, respectively. At most stations, the transition from 7.0 to 7.5 km s⁻¹ occurs within 2 km of depth, whereas the transition from 7.5 to 8.0 km s⁻¹ occurs over ~ 6 km of depth;

RS10, RS14, RS16, and DR16 are exceptions at which both transitions each occur over 6 km of depth. Also notable is that Figure 4.10 indicates considerably greater uncertainty in the 7.0–7.5 km s⁻¹ transition zone, in comparison to the rest of the model. The mean depths to the 7.5 km s⁻¹ contours are collected in Table 4.1 for all RIS/DRIS stations; Figure 4.11 plots these values in comparison to Chaput et al. (2014).

The noted velocity transitions are depressed by ~5 km in the region underlying the transects intersection (i.e., at RS04 and DR10 on Figure 4.9a and b, respectively). Perhaps coincidentally, Tertiary band power shown in Figure 2.10 and P-wave SNR shown in Figure 3.5 also are also slightly depressed in this region.

Interpretation

The *ak135* standard model of global average seismic velocities (Kennett et al., 1995) defines the Moho transition as an instantaneous (with depth) increase in P-wave velocity from 6.5 to 8.0 km s⁻¹. This transition occurs at ~35 km depth for continental crust, and 12 km for oceanic crust. Continental crust includes a second, shallower velocity contrast (the Conrad transition) from 5.8 to 6.5 s⁻¹, at depth of 20 km.

Seismic wave scattering (i.e., reflection and P-to-S conversion) is strongest at rapid impedance contrasts. The aforementioned 7.0–7.5 km s⁻¹ is the strongest contrast apparent in Figure 4.9 and is the likely source of the assumed PpPp phases matched by the MCMC inversions. Assuming this transition is analogous to the Moho (i.e., the base of the geologic crust), my results indicate an abbreviated crust/mantle boundary that is intermediate in depth between continental and oceanic crust. As noted in Chapter 1, the Ross Ice Shelf is located above the West Antarctic Rift System, a (debatably) inactive rifted province with extant volcanism and suspected mantle plumes. Rifted regions, by definition, are characterized by substantially thinned crust. Thermally driven geochemical processes are also expected in rifted regions with decompression melting and mantle plumes, which may explain the more gradual (i.e., poorly defined) increase in P-wave velocity for the 7.5–8.0 km s⁻¹ range.

The Conrad transition is interpreted to lie at 10–15 km depth, indicated by the gradient from blue to cyan, also consistent with thin, rifted continental crust.

Shen et al. (2018) and Chaput et al. (2014) both reported Ross Embayment crustal thicknesses of 20–24 km, the former based on Rayleigh wave dispersion curve tomography recorded by the RIS/DRIS stations, and the latter on interpolated PRF inversions from seismographs sited throughout West Antarctica and the Transantarctic Mountains. For Marie Byrd Land, both studies reported Moho depths of 28 km, both based on MCMC inversion of PRF data.

My study finds similarly shallow Moho depths beneath the floating ice RIS/DRIS stations. I additionally find a localized increase in Moho depth from 22 km to 28 km beneath the array intersection (with the exception of outliers RS04 and DR08). In Marie Byrd Land, I find Moho depths of 25 km at RS11, RS13, and RS14, and 28 km at RS12. The reference studies are based on PRF studies, which utilize S-waves to constrain Moho depths, as opposed to the current study which relies entirely on P-waves. As noted for Figure 4.6, joint inversion of P-wave and S-wave autocorrelation data resulted in a doubling of the uncertainty in Moho depth. The discrepancy between my results and the reference studies may therefore be indicative of poorly modeled P-to-S ratios. Further study of P- and S-wave autocorrelations with the Marie Byrd Land stations is warranted.

4.4 Tables

Table 4.1: Crustal thickness estimates from MCMC inversions of vertical autocorrelations for all RIS/DRIS array stations, defined as the mean depth at which the interpolated posterior distribution samples exceed a P-wave velocity of 7.5 km s^{-1} (Figure 4.9). Note that the standard deviations shown here are for the depth of the 7.5 km s^{-1} horizon, as opposed to the P-wave velocity at depth shown in Figure 4.10.

Station	Moho (km)	Stddev (km)	Station	Moho (km)	Stddev (km)
RS01	22.9	2.1	DR01	22.0	3.4
RS02	23.4	3.0	DR02	24.4	1.7
RS03	26.6	2.0	DR03	22.3	0.6
RS04	24.1	1.7	DR04	23.3	1.8
RS05	23.5	2.3	DR05	23.9	3.3
RS06	22.9	1.1	DR06	26.6	3.0
RS07	23.0	1.1	DR07	27.2	2.7
RS08*	23.5	2.9	DR08	26.1	3.7
RS09*	26.3	2.2	DR09	26.8	2.2
RS10	26.3	0.9	DR10	29.5	2.4
RS11*	25.1	2.3	DR11	27.0	4.2
RS12*	28.3	1.4	DR12	28.4	2.9
RS13*	25.9	1.8	DR13	26.8	2.9
RS14*	24.3	3.2	DR14	25.3	1.8
RS15	27.2	2.8	DR15	24.0	3.7
RS16	27.0	2.9	DR16	27.6	2.9
RS17*	26.2	2.0			
RS18	25.2	2.8			

* Grounded ice station.

4.5 Figures

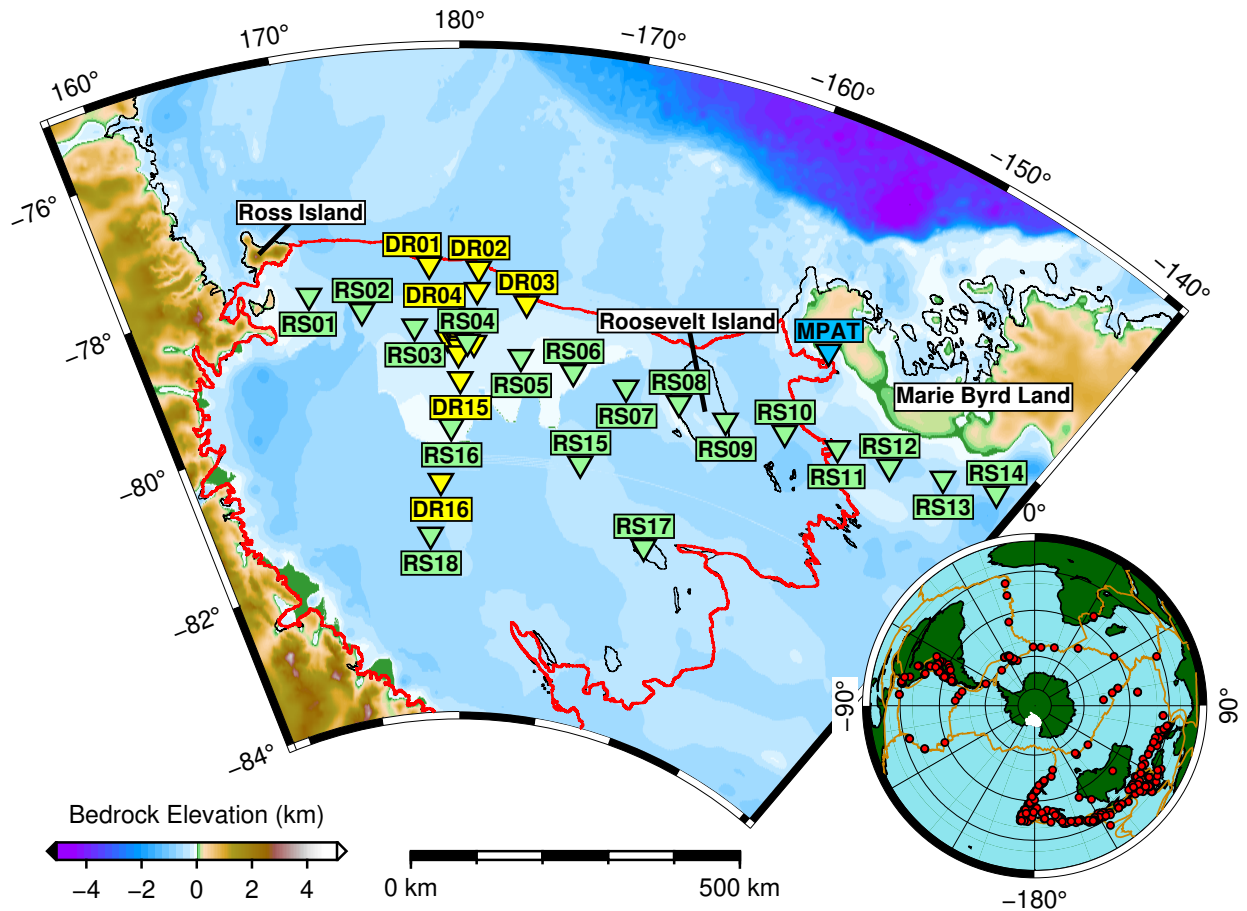


Figure 4.1: RIS/DRIS array station locations. Two years of earthquake data observed by station MPAT (blue) are also used in this study. **Inset:** Map of earthquake signal sources used in this study. Antarctica is displayed with the traditional Grid-North orientation.

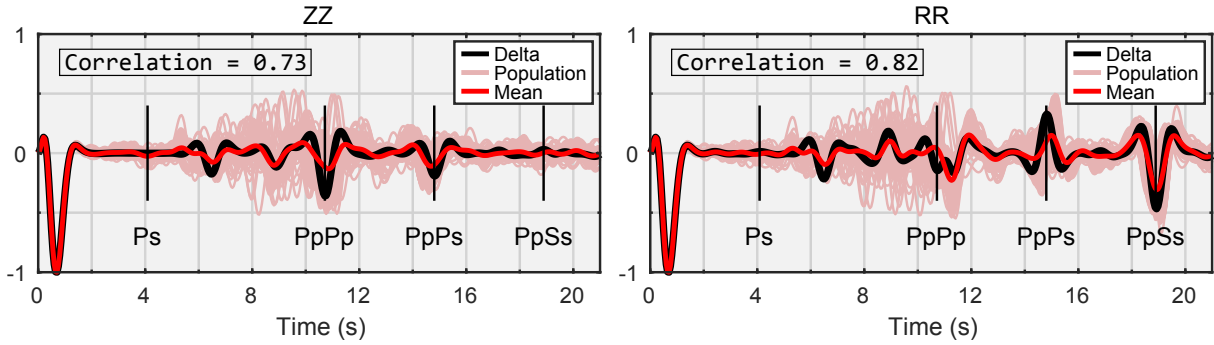


Figure 4.2: Synthetic test of the influence of source functions on autocorrelation stacking. 200 source functions were generated with randomly picked source wavelets (Ricker, Meyer, or Poisson), ray parameters ($0.04\text{--}0.08\text{ s km}^{-1}$, corresponding to epicentral distances of $95^\circ\text{--}30^\circ$), peak frequencies ($0.1\text{--}2.0\text{ Hz}$), and phase lags ($0.0\text{--}4.0\text{ s}$). Synthetic seismograms were then produced from the convolutions of the source functions with the seismic plane wave response of an *ak135* velocity model. The resulting autocorrelations (“Population”) are linearly stacked (“Mean”) and compared to an ideal autocorrelation produced from the impulse response of the velocity model (“Delta”). The autocorrelation in the $0\text{--}2\text{ s}$ range is dominated by filtering artifacts; the Pearson correlation coefficient is therefore calculated only for time series data greater than 2 s . The randomized ray parameter has the strongest impact on the misfit of the stacked autocorrelations; the same bootstrapping performed with fixed, uniform ray parameters yields correlation coefficients of >0.99 for ZZ and RR.

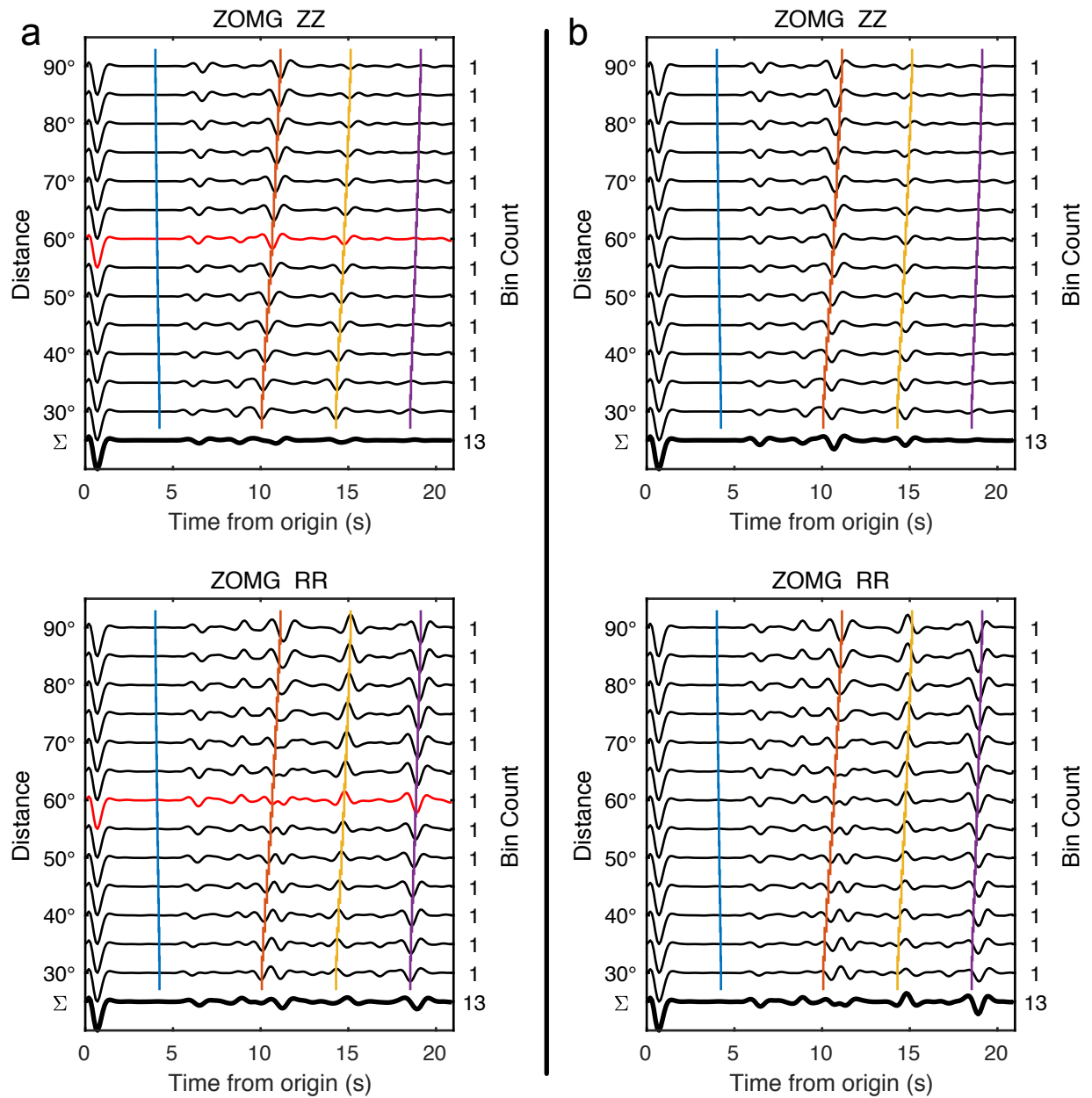


Figure 4.3: a) Synthetic autocorrelations for an *ak135* crustal model. Moho phases are, from left to right: Ps (blue), PpPp (orange), PpPs (yellow), and PpSs (purple). The initial Ps arrival (blue) is not a reflection and is therefore not detected by autocorrelations.

b) Slowness corrected autocorrelations produced by correlation optimized warping, using the 60° autocorrelation (red) as a kernel, a segment length of 10 s, and a warping factor of ± 0.5 s. Phase arrival times were not recalculated for the adjusted slownesses.

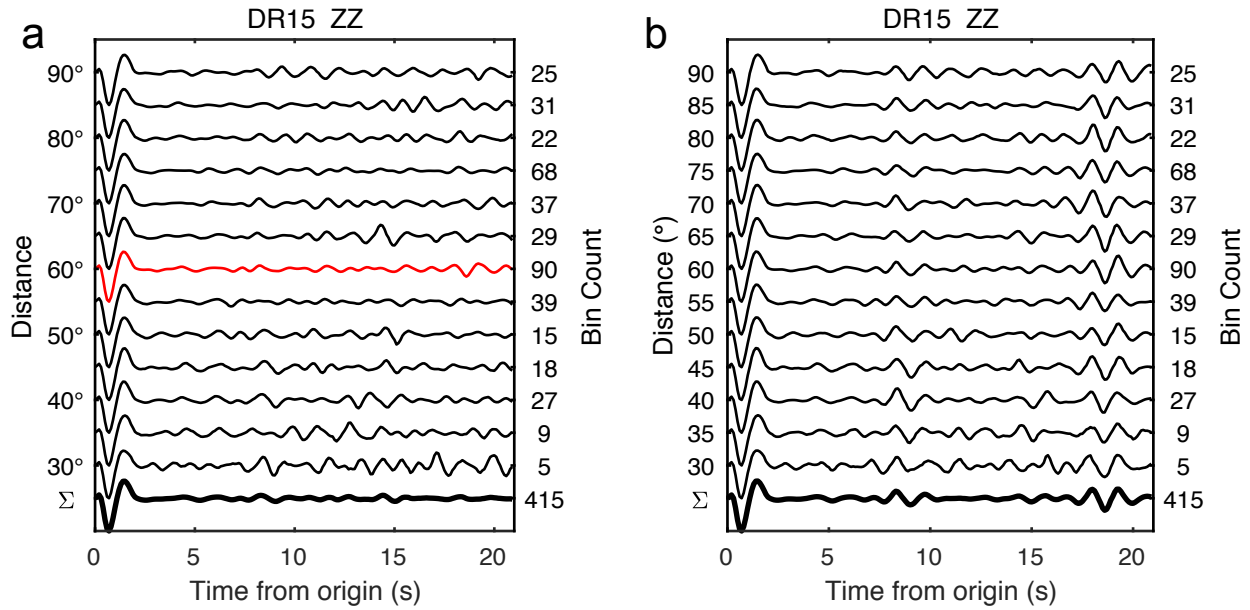


Figure 4.4: **a)** Uncorrected ZZ stacks from floating station DR15 (ice thickness = 0.323 km, water layer thickness = 0.432 km, Table 3.3), binned by epicentral distance in 5° intervals. The PpPp phase is visible near 9 s on the 60° stack (red) and on the aggregate stack (Σ).

b) Slowness corrected ZZ stacks produced with correlation optimized warping of individual autocorrelations, using the red uncorrected trace as a kernel.

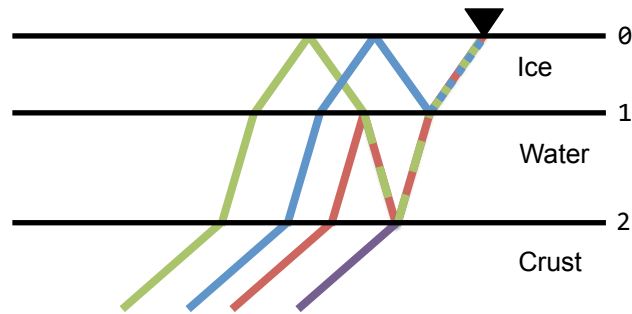


Figure 4.5: Schematic of the reverberation wavefield for the topmost three layers of the forward model. Colored ray traces correspond to the highlighted parts of Equation (4.11).

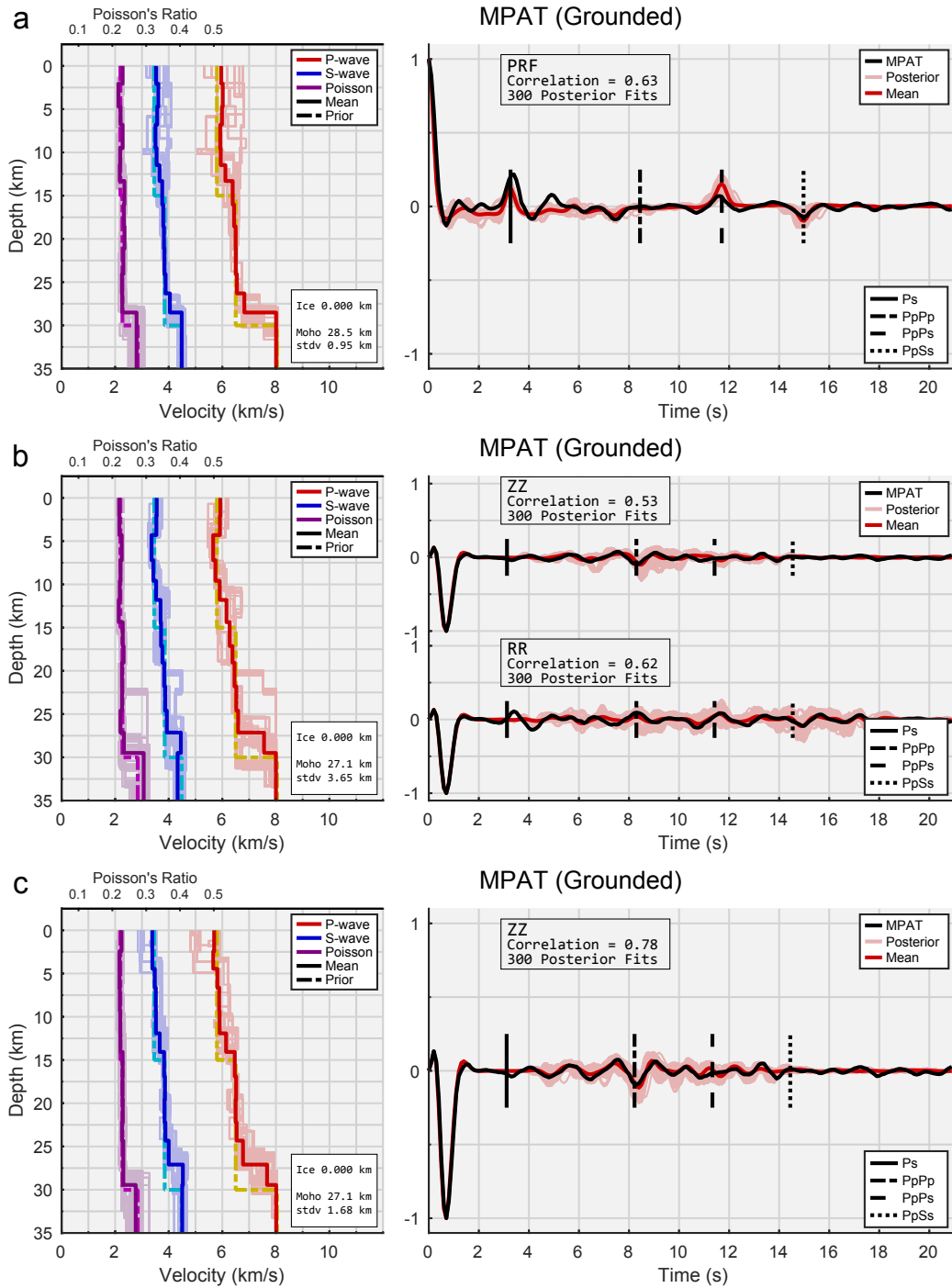


Figure 4.6: Comparison of velocity structures for station MPAT, sited on exposed bedrock at Mt. Patterson, Antarctica. **a)** Solo inversion of P-wave receiver functions. **b)** Jointly inverted vertical and radial component autocorrelations. **c)** Solo inversion of vertical component autocorrelations. Moho-converted phase arrivals are based on travel times calculated for the mean model (dark red and blue) of the posterior distribution (light red and blue).

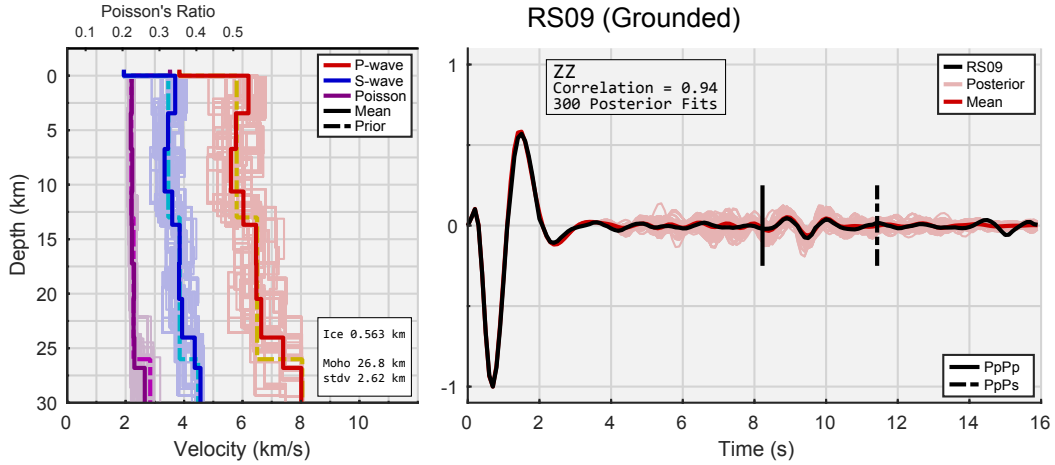


Figure 4.7: Vertical autocorrelation MCMC inversion results for grounded ice station RS09. The posterior distribution velocity models and mean model are shown in the left panel. The black trace in the right panel is the observed autocorrelation. Phase arrivals are calculated for the mean model and provide a qualitative metric for gauging the accuracy of the posterior distribution.

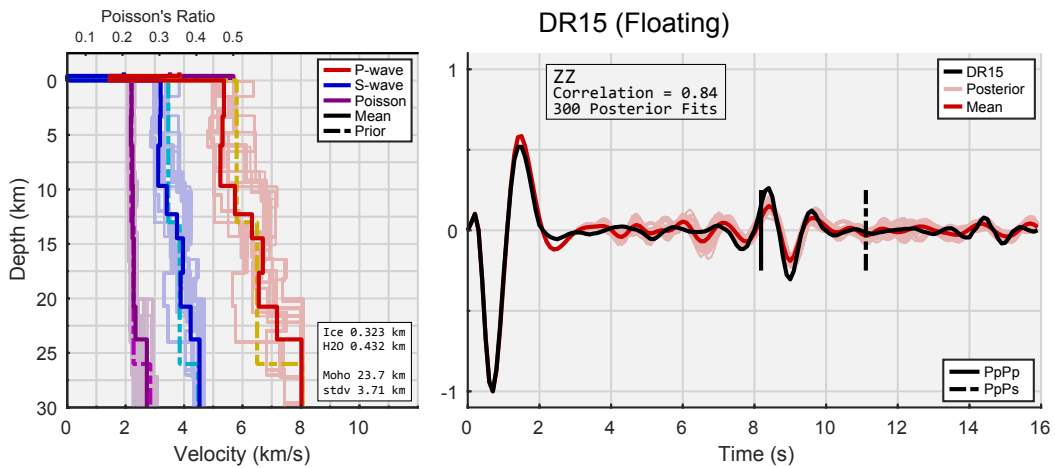


Figure 4.8: Vertical autocorrelation MCMC inversion results for floating ice station DR15.

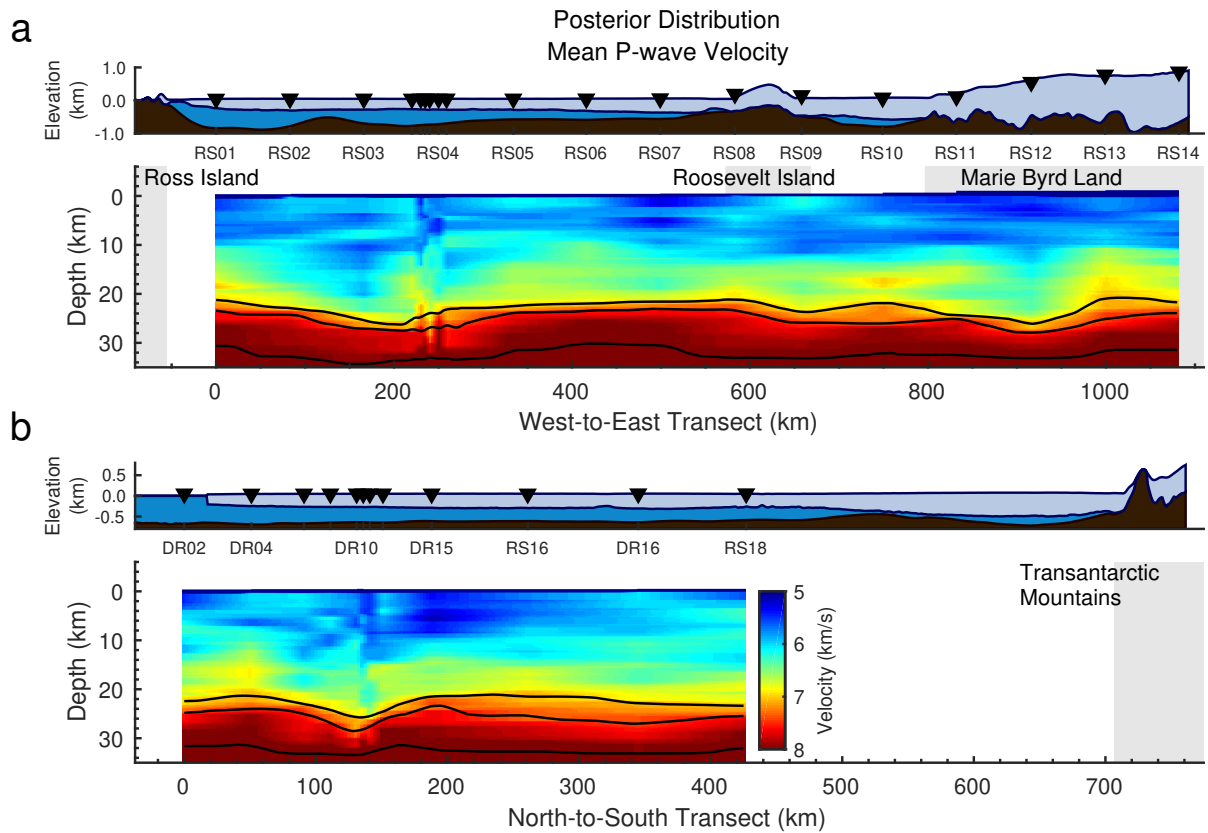


Figure 4.9: Vertical autocorrelation-constrained crustal P-wave structure beneath the main RIS/DRIS transects, constructed by linearly interpolating the station probability distributions (e.g., Figures 4.7 and 4.8) to vertical resolutions of 0.01 km and 0.01 km s⁻¹, and then linearly interpolating the mean vertical model to lateral, inter-station resolutions of 2.5 km. The black lines mark the 7.0, 7.5, and 8.0 km s⁻¹ contours, smoothed via moving average to a lateral resolution of ±0.5 km. Gray backgrounds indicate approximate areas of grounded ice.

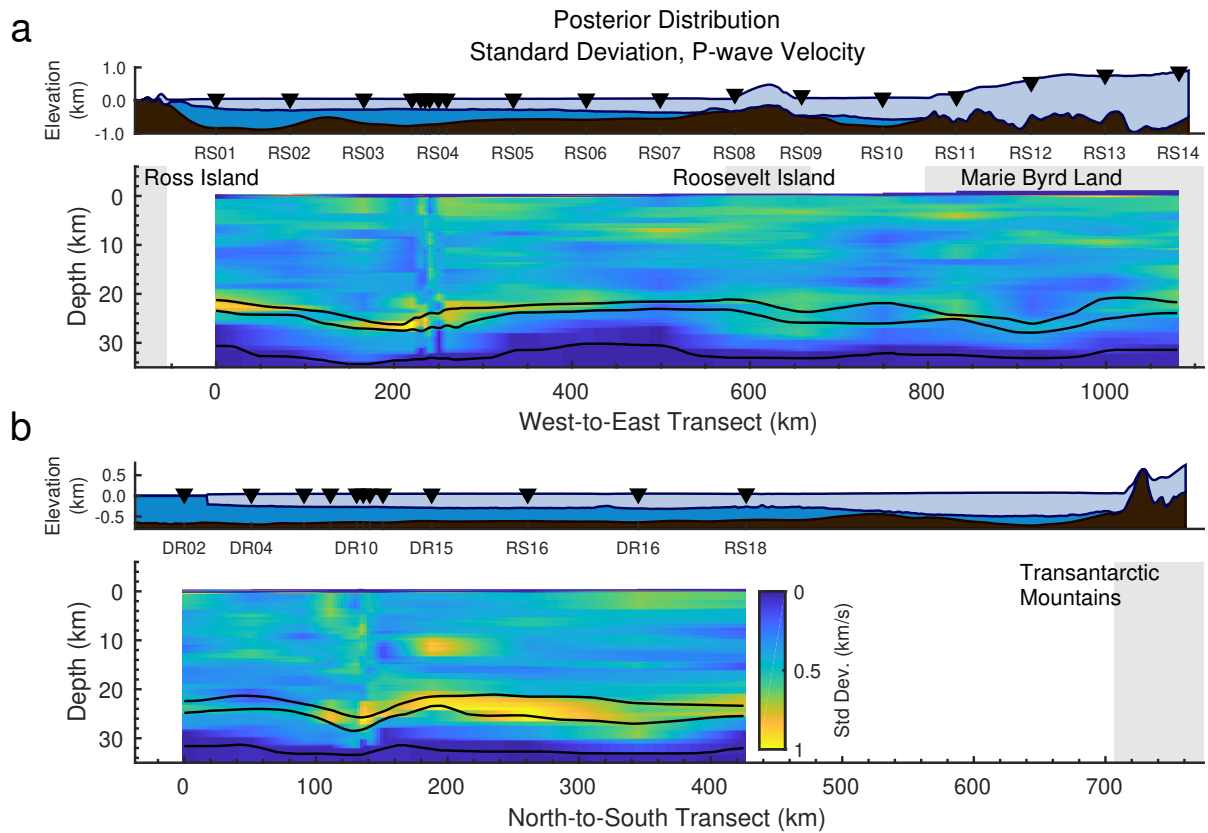


Figure 4.10: P-wave velocity standard deviation with depth for the posterior distribution shown in Figure 4.9.

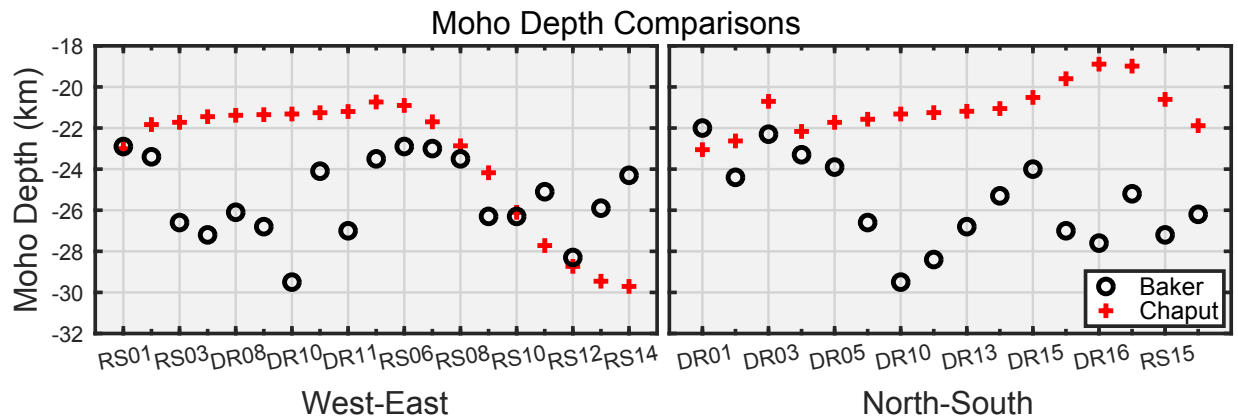


Figure 4.11: Moho depth estimates from this study (“Baker”) in comparison to Moho depth estimates interpolated from PRF inversions of West Antarctica-sited stations (“Chaput”) (Chaput et al., 2014). The West-East transect includes stations DR01 and DR03 (prefixed) and RS15 and RS17 (appended).

Bibliography

- Abdolali, A., Kadri, U., Parsons, W., and Kirby, J. T. (2018). On the propagation of acoustic-gravity waves under elastic ice sheets. *Journal of Fluid Mechanics*, 837:640–656.
- Aderhold, K., Anderson, K. E., Reusch, A. M., Pfeifer, M. C., Aster, R. C., and Parker, T. (2015). Data quality of collocated portable broadband seismometers using direct burial and vault emplacement. *Bulletin of the Seismological Society of America*, 105(5):2420–2432.
- Aki, K. and Richards, P. G. (2002). *Quantitative seismology*. University Science Books.
- Anthony, R. E., Aster, R. C., and McGrath, D. (2017). Links between atmosphere, ocean, and cryosphere from two decades of microseism observations on the Antarctic Peninsula. *Journal of Geophysical Research: Earth Surface*, 122(1):153–166.
- Anthony, R. E., Aster, R. C., Wiens, D. A., Anandkrishan, S., Huerta, A. D., Winberry, J. P., Wilson, T., and Rowe, C. (2015). The Seismic Noise Environment of Antarctica. *Seismological Research Letters*, 86(1):89–100.
- Anthony, R. E., Ringler, A., and Wilson, D. C. (2018). The widespread influence of great lakes microseisms across the midwestern united states revealed by the 2014 polar vortex. *Geophysical Research Letters*, 45(8):3436–3444.
- Apel, J. R. (1987). *Principles of Ocean Physics*, volume 38. Academic Press.
- Ardhuin, F. and Herbers, T. H. C. (2013). Noise generation in the solid earth, oceans and atmosphere, from nonlinear interacting surface gravity waves in finite depth. *Journal of Fluid Mechanics*, 716:316–348.
- Aster, R. C., Baker, M. G., Bromirski, P. D., Wiens, D., Nyblade, A., Gerstoft, P., Stephen, R. A., and Chen, Z. (2019). Large swell events impacting the Ross Ice Shelf and the harmonic excitation of ice shelf seismic waves. *proc. AGU, Fall Meeting, San Francisco*.
- Aster, R. C., Borchers, B., and Thurber, C. H. (2018). *Parameter estimation and inverse problems*. Elsevier.
- Aster, R. C., McNamara, D. E., and Bromirski, P. D. (2008). Multidecadal climate-induced variability in microseisms. *Seismological Research Letters*, 79(2):194–202.
- Aster, R. C., McNamara, D. E., and Bromirski, P. D. (2010). Global trends in extremal microseism intensity. *Geophysical Research Letters*, 37.
- Aster, R. C. and Winberry, J. P. (2017). Glacial seismology. *Reports On Progress in Physics*, 80.
- Baker, M. G., Aster, R. C., Anthony, R. E., Chaput, J., Wiens, D. A., Nyblade, A., Bromirski, P. D., Gerstoft, P., and Stephen, R. A. (2019). Seasonal and spatial variations in the ocean-coupled ambient wavefield of the Ross Ice Shelf. *Journal of Glaciology*, 65(254):912–925.

- Barklage, M., Wiens, D. A., Nyblade, A., and Anandakrishnan, S. (2009). Upper mantle seismic anisotropy of South Victoria Land and the Ross Sea coast, Antarctica from SKS and SKKS splitting analysis. *Geophysical Journal International*, 178(2):729–741.
- Barletta, V. R., Bevis, M., Smith, B. E., Wilson, T., Brown, A., Bordoni, A., Willis, M., Khan, S. A., Rovira-Navarro, M., Dalziel, I., Smalley, R., Kendrick, E., Konfal, S., Caccamise, D. J., Aster, R. C., Nyblade, A., and Wiens, D. A. (2018). Observed rapid bedrock uplift in amundsen sea embayment promotes ice-sheet stability. *Science*, 360(6395):1335.
- Beaudoin, B. C., ten Brink, U. S., and Stern, T. A. (1992). Characteristics and processing of seismic data collected on thick, floating ice: Results from the Ross Ice Shelf, Antarctica. *Geophysics*, 57(10):1359–1372.
- Borstad, C., McGrath, D., and Pope, A. (2017). Fracture propagation and stability of ice shelves governed by ice shelf heterogeneity. *Geophysical Research Letters*, 44(9):4186–4194.
- Bromirski, P. D., Chen, Z., Stephen, R. A., Gerstoft, P., Arcas, D., Diez, A., Aster, R. C., Wiens, D. A., and Nyblade, A. (2017). Tsunami and infragravity waves impacting Antarctic ice shelves. *Journal of Geophysical Research: Oceans*, 122(7):5786–5801.
- Bromirski, P. D., Diez, A., Gerstoft, P., Stephen, R. A., Bolmer, T., Wiens, D., Aster, R., and Nyblade, A. (2015). Ross Ice Shelf vibrations. *Geop Res. Lett.*, 42:7589–7597.
- Bromirski, P. D., Sergienko, O. V., and MacAyeal, D. R. (2010). Transoceanic infragravity waves impacting Antarctic ice shelves. *Geophysical Research Letters*, 37(2).
- Bromirski, P. D. and Stephen, R. A. (2012). Response of the Ross Ice Shelf, Antarctica, to ocean gravity-wave forcing. *Annals of Glaciology*, 53(60).
- Butler, R., Lay, T., Creager, K., Earle, P. S., Fischer, K., Gaherty, J., Ladke, G., Leith, W., Park, J., Ritzwoller, M., Tromp, J., and Wen, L. (2004). The global seismographic network surpasses its design goal. *Eos*, 85(23).
- Cathles, L. M., Okal, E. A., and MacAyeal, D. R. (2009). Seismic observations of sea swell on the floating Ross Ice Shelf, Antarctica. *Journal of Geophysical Research: Earth Surface*, 114(F2).
- Cavalieri, D. J., Parkinson, C. L., Gloersen, P., and Zwally, H. J. (1996). Sea Ice Concentrations from Nimbus-7 SMMR and DMSP SSM/I-SSMIS Passive Microwave Data, Version 1. updated yearly; subset accessed: 2014–17.
- Chaput, J., Aster, R. C., Huerta, A., Sun, X., Lloyd, A., Wiens, D., Nyblade, A., Anandakrishnan, S., Winberry, J. P., and Wilson, T. (2014). The crustal thickness of West Antarctica. *Journal of Geophysical Research: Solid Earth*, 119(1):378–395.
- Chaput, J., Aster, R. C., McGrath, D., Baker, M. G., Anthony, R. E., Gerstoft, P., Bromirski, P., Nyblade, A., Stephen, R. A. and Wiens, D., Das, S. B., and Stevens, L. A. (2018). Near-surface environmentally forced changes in the Ross Ice Shelf observed with ambient seismic noise. *Geophysical Research Letters*, 45(20):11–187.

- Chen, Z., Bromirski, P., Gerstoft, P., Stephen, R., Wiens, D., Aster, R. C., and Nyblade, A. (2018). Ocean-excited plate waves in the Ross and Pine Island Glacier ice shelves. *Journal of Glaciology*, 64(247):730–744.
- Crary, A. P. (1954). Seismic studies on Fletcher’s Ice Island, T-3. *Eos, Transactions American Geophysical Union*, 35(2):293–300.
- Diez, A., Bromirski, P. D., Gerstoft, P., Stephen, R. A., Anthony, R., Aster, R. C., Cai, C., Nyblade, A., and Wiens, D. (2016). Ice shelf structure derived from dispersion curve analysis of ambient seismic noise, Ross Ice Shelf, Antarctica. *Geophysical Journal International*, 205:785–795.
- DMC, I. (2014). Data Services Products: The IRIS DMC Noise Toolkit.
- Dowdeswell, J. and Bamber, J. L. (2007). Keel depths of modern Antarctic icebergs and implications for sea-floor scouring in the geological record. *Marine Geology*, 243:120–131.
- Dziak, R. P., Bohnenstiehl, D. R., Stafford, K. M., Matsumoto, H., Park, M., Lee, W. S., Fowler, M. J., Lau, T.-K., Haxel, J. H., and Mellinger, D. K. (2015). Sources and levels of ambient ocean sound near the antarctic peninsula. *PLoS one*, 10(4):e0123425.
- Dziewonski, A., Bloch, S., and Landisman, M. (1969). A technique for the analysis of transient seismic signals. *Bulletin of the Seismological Society of America*, 59(1):427–444.
- Ewing, W. M., Jardetzky, W. S., and Press, F. (1957). *Elastic Waves in Layered Media*. McGraw-Hill Series in the Geological Sciences. McGraw-Hill.
- Fofonoff, N. P. and Millard Jr, R. C. (1983). Algorithms for the computation of fundamental properties of seawater.
- Fretwell, P., Pritchard, H. D., Vaughan, D. G., Bamber, J. L., Barrand, N. E., Bell, R., Bianchi, C., Bingham, R. G., Blankenship, D. D., Casassa, G., Catania, G., Callens, D., Conway, H., Cook, A. J., Corr, H. F. J., Damaske, D., Damm, V., Ferraccioli, F., Forsberg, R., Fujita, S., Gim, Y., Gogineni, P., Griggs, J. A., Hindmarsh, R. C. A., Holmlund, P., Holt, J. W., Jacobel, R. W., Jenkins, A., Jokat, W., Jordan, T., King, E. C., Kohler, J., Krabill, W., Riger-Kusk, M., Langley, K. A., Leitchenkov, G., Leuschen, C., Luyendyk, B. P., Matsuoka, K., Mouginot, J., Nitsche, F. O., Nogi, Y., Nost, O. A., Popov, S. V., Rignot, E., Rippin, D. M., Rivera, A., Roberts, J., Ross, N., Siegert, M. J., Smith, A. M., Steinhage, D., Studinger, M., Sun, B., Tinto, B. K., Welch, B. C., Wilson, D., Young, D. A., Xiangbin, C., and Zirizzotti, A. (2013). Bedmap2: Improved ice bed, surface and thickness datasets for Antarctica. *The Cryosphere*, 7(1):375–393.
- Frigo, M. and Johnson, S. G. (1999). *FFTW user’s manual*. Massachusetts Institute of Technology.
- Furst, J., Durand, G., Gillet-Chaulet, G., Tvard, L., Rankl, M., Braun, M., and Gagliardini, O. (2016). The safety band of Antarctic ice shelves. *Nature Climate Change*.
- Glorieux, C., Van de Rostyne, K., Gusev, V., Gao, W., Lauriks, W., and Thoen, J. (2002). Non-linearity of acoustic waves at solid–liquid interfaces. *The Journal of the Acoustical Society of America*, 111(1):95–103.

- Godin, O. A. and Zabolin, N. A. (2016). Resonance vibrations of the Ross Ice Shelf and observations of persistent atmospheric waves. *Journal of Geophysical Research: Space Physics*, 121(10):10–157.
- Greene, C. A., Gwyther, D. E., and Blankenship, D. D. (2017). Antarctic mapping tools for MATLAB. *Computers & Geosciences*, 104:151–157.
- Griggs, J. A. and Bamber, J. L. (2011). Antarctic ice-shelf thickness from satellite radar altimetry. *Journal of Glaciology*, 57(203):485–498.
- Hasselmann, K. (1966). Feynman diagrams and interaction rules of wave-wave scattering processes. *Reviews of Geophysics*, 4(1):1–32.
- Heeszel, D., Fricker, H. A., Bassis, J. N., O’Neel, S., and Walter, F. (2014). Seismicity within a propagating ice shelf rift: The relationship between icequake locations and ice shelf structure. *J. Geophys. Res., Earth Surface*, 119:731–744.
- Helfrich, G. (2006). Extended-time multitaper frequency domain cross-correlation receiver-function estimation. *Bulletin of the Seismological Society of America*, 96(1):344–347.
- Hole, M. J. and LeMasurier, W. E. (1994). Tectonic controls on the geochemical composition of Cenozoic, mafic alkaline volcanic rocks from West Antarctica. *Contributions to Mineralogy and Petrology*, 117(2):187–202.
- Howat, I. M., Porter, C., Smith, B. E., Noh, M.-J., and Morin, P. (2019). The reference elevation model of Antarctica. *The Cryosphere*, 13(2):665–674.
- Jacobs, S. S., Giulivi, C. F., and Mele, P. A. (2002). Freshening of the ross sea during the late 20th century. *Science*, 297(5580):386–389.
- Joughin, I. and Alley, R. B. (2011). Stability of the West Antarctic ice sheet in a warming world. *Nature Geosci*, 4(8):506–513.
- Kadri, U. (2016). Generation of hydroacoustic waves by an oscillating ice block in arctic zones. *Advances in Acoustics and Vibration*, 2016.
- Kennett, B. L., Engdahl, E., and Buland, R. (1995). Constraints on seismic velocities in the Earth from traveltimes. *Geophysical Journal International*, 122(1):108–124.
- Kennett, B. L. N. (2013). *Seismic wave propagation in stratified media*. ANU Press.
- Kibblewhite, A. C. and Ewans, K. C. (1985). Wave–wave interactions, microseisms, and infrasonic ambient noise in the ocean. *The Journal of the Acoustical Society of America*, 78(3):981–994.
- King, E. C. and Jarvis, E. P. (2007). Use of shear waves to measure Poisson’s ratio in polar firn. *Journal of Environmental and Engineering Geophysics*, 12(1):15–21.
- Kirchner, J. and Bentley, C. (1979). Seismic short-refraction studies on the Ross Ice Shelf, Antarctica. *Journal of Glaciology*, 24(90):313–319.

- Kyle, P., Moore, J. A., and Thirlwall, M. F. (1992). Petrologic evolution of anorthoclase phonolite lavas at Mount Erebus, Ross Island, Antarctica. *Journal of Petrology*, 33(4):849–875.
- Langston, C. A. (1979). Structure under Mount Rainier, Washington, inferred from teleseismic body waves. *Journal of Geophysical Research: Solid Earth*, 84(B9):4749–4762.
- Langston, C. A. (2011). Wave-field continuation and decomposition for passive seismic imaging under deep unconsolidated sediments. *Bulletin of the Seismological Society of America*, 101(5):2176–2190.
- LeDoux, C. M., Hulbe, C. L., Forbes, M. P., Scambos, T. A., and Alley, K. (2017). Structural provinces of the Ross Ice Shelf, Antarctica. *Annals of Glaciology*, 58(75pt1):88–98.
- Lipovsky, B. P. (2018). Ice shelf rift propagation and the mechanics of wave-induced fracture. *Journal of Geophysical Research: Oceans*, 123(6):4014–4033.
- Longuet-Higgins, M. S. (1950). A theory of the origin of microseisms. *Phil. Trans. R. Soc. Lond. A*, 243(857):1–35.
- Lough, A. C., Wiens, D. A., Barcheck, C. G., Anandakrishnan, S., Aster, R. C., Blankenship, D. D., Huerta, A. D., Nyblade, A., Young, D. A., and Wilson, T. J. (2013). Seismic detection of an active subglacial magmatic complex in Marie Byrd Land, Antarctica. *Nature Geoscience*, 6(12):1031–1035.
- MacAyeal, D. R., Okal, E. A., Aster, R. C., and Bassis, J. N. (2008). Seismic and hydroacoustic tremor generated by colliding icebergs. *Journal of Geophysical Research: Earth Surface*, 113(F3):F03011.
- MacAyeal, D. R., Okal, E. A., Aster, R. C., and Bassis, J. N. (2009). Seismic observations of glaciogenic ocean waves (micro-tsunamis) on icebergs and ice shelves. *Journal of Glaciology*, 55(190):193–206.
- MacAyeal, D. R., Okal, E. A., Aster, R. C., Bassis, J. N., Brunt, K. M., Cathles, L. M., Drucker, R., Fricker, H. A., Kim, Y. J., Martin, S., Okal, M. H., Sergienko, O. V., Sponsler, M. P., and Thom, J. E. (2006). Transoceanic wave propagation links iceberg calving margins of Antarctica with storms in tropics and Northern Hemisphere. *Geophysical Research Letters*, 33(17):L17502.
- MacAyeal, D. R., Scambos, T. A., Hulbe, C. L., and Fahnestock, M. A. (2003). Catastrophic ice-shelf break-up by an ice-shelf-fragment-capsize mechanism. *Journal of Glaciology*, 49(164):22–36.
- Martin, S., Drucker, R., Aster, R., Davey, F. J., Okal, E., Scambos, T., and MacAyeal, D. R. (2010). Kinematic and seismic analysis of giant tabular iceberg breakup at Cape Adare, Antarctica. *Journal of Geophysical Research*, 115(B6):B06311.
- Massom, R. A., Scambos, T. A., Bennetts, L. G., Reid, P., Squire, V. A., and Stammerjohn, S. E. (2018). Antarctic ice shelf disintegration triggered by sea ice loss and ocean swell. *Nature*, 558(7710):383–389.

- McNamara, D. E. and Buland, R. P. (2004). Ambient Noise Levels in the continental United States. *Bulletin of the Seismological Society of America*, 94(4):1517–1527.
- Meier, T., Dietrich, K., Stöckhert, B., and Harjes, H.-P. (2004). One-dimensional models of shear wave velocity for the eastern Mediterranean obtained from the inversion of Rayleigh wave phase velocities and tectonic implications. *Geophysical Journal International*, 156(1):45–58.
- Mosegaard, K. and Tarantola, A. (1995). Monte Carlo sampling of solutions to inverse problems. *Journal of Geophysical Research: Solid Earth*, 100(B7):12431–12447.
- Nakata, K., Ohshima, K. I., Nihashi, S., Kimura, N., and Tamura, T. (2015). Variability and ice production budget in the Ross Ice Shelf Polynya based on a simplified polynya model and satellite observations. *Journal of Geophysical Research: Oceans*, 120(9).
- Nicolas, J. P., Vogelmann, A. M., Scott, R. C., Wilson, A. B., Cadetdu, M. P., Bromwich, D. H., Verlinde, J., Lubin, D., Russell, L. M., Jenkinson, C., et al. (2017). January 2016 extensive summer melt in West Antarctica favoured by strong El Niño. *Nature Communications*, 8.
- Nielsen, N.-P. V., Carstensen, J. M., and Smedsgaard, J. (1998). Aligning of single and multiple wavelength chromatographic profiles for chemometric data analysis using correlation optimised warping. *Journal of chromatography A*, 805(1-2):17–35.
- O'Donnell, J. P., Selway, K., Nyblade, A., Brazier, R., Wiens, D., Anandkrishan, S., Aster, R. C., Huerta, A., Wilson, T., and Winberry, J. P. (2017). The uppermost mantle seismic velocity and viscosity structure of central West Antarctica. *Earth and Planetary Science Letters*, 472:38 – 49.
- Okal, E. A. and MacAyeal, D. R. (2006). Seismic recording on drifting icebergs: Catching seismic waves, tsunamis and storms from Sumatra and elsewhere. *Seismological Research Letters*, 77(6):659–671.
- Olinger, S. D., Lipovsky, B. P., Wiens, D. A., Aster, R. C., Bromirski, P. D., Chen, Z., Gerstoft, P., Nyblade, A. A., and Stephen, R. A. (2019). Tidal and thermal stresses drive seismicity along a major Ross Ice Shelf rift. *Geophysical Research Letters*, 46(12):6644–6652.
- Paolo, F., Fricker, H. A., and Padman, L. (2015). Volume loss from Antarctic ice shelves is accelerating. *Science*, 348(6232):327–331.
- Peterson, J. (1993). Observations and Modeling of Seismic Background Noise. *Open File Report*, pages 93–322.
- Phạm, T.-S. and Tkalčić, H. (2017). On the feasibility and use of teleseismic p wave coda autocorrelation for mapping shallow seismic discontinuities. *Journal of Geophysical Research: Solid Earth*, 122(5):3776–3791.
- Phạm, T.-S. and Tkalčić, H. (2018). Antarctic ice properties revealed from teleseismic p wave coda autocorrelation. *Journal of Geophysical Research: Solid Earth*, 123(9):7896–7912.

- Phillips, E. H., Sims, K. W. W., Blichert-Toft, J., Aster, R. C., Gaetani, G., Kyle, P. R., Wallace, P. J., and Rasmussen, D. (2018). The nature and evolution of mantle upwelling at Ross Island, Antarctica, with implications for the source of HIMU lavas. *Earth and Planetary Science Letters*, 498:38–53.
- Podolskiy, E. A. and Walter, F. (2016). Cryoseismology. *Reviews of Geophysics*, 54(4):708–758.
- Press, F. and Ewing, M. (1951). Propagation of elastic waves in a floating ice sheet. *Eos, Transactions American Geophysical Union*, 32(5):673–678.
- Ramirez, C., Nyblade, A., Hansen, S. E., Wiens, D., Anandakrishan, S., Aster, R., Huerta, A., Shore, P. J., and Wilson, T. (2016). Crustal and upper-mantle structure beneath ice-covered regions in Antarctica from S-wave receiver functions and implications for heat flow. *Geophysical Journal International*, 204:1636–1648.
- Reguzzoni, M., Sampietro, D., and Sansò, F. (2013). Global moho from the combination of the crust2.0 model and goce data. *Geophysical Journal International*, 195(1):222–237.
- Reusch, A., Nyblade, A., Benoit, M., Wiens, D., Anandakrishnan, S., Voigt, D., and Shore, P. (2008). Mantle transition zone thickness beneath Ross Island, the Transantarctic Mountains, and East Antarctica. *Geophysical Research Letters*, 35(12).
- Rignot, E. and Jacobs, S. S. (2002). Rapid bottom melting widespread near Antarctic ice sheet grounding lines. *Science*, 296(5575):2020–2023.
- Robinson, E. S. (1983). Flexural–gravity waves on floating stratified ice. *Journal of Glaciology*, 29(101):133–141.
- Rose, J. L. (1999). *Ultrasonic Waves in Solid Media*. Cambridge University Press.
- Sanderson, C. (2010). Armadillo: An open source c++ linear algebra library for fast prototyping and computationally intensive experiments. Technical report, National ICT Australia Ltd.
- Schimmel, M. and Paulssen, H. (1997). Noise reduction and detection of weak, coherent signals through phase-weighted stacks. *Geophysical Journal International*, 130(2):497–505.
- Sergienko, O. V. (2017). Behavior of flexural gravity waves on ice shelves: Application to the Ross Ice Shelf. *Journal of Geophysical Research: Oceans*, 122(8):6147–6164.
- Seroussi, H., Ivins, E. R., Wiens, D. A., and Bondzio, J. (2017). Influence of a West Antarctic mantle plume on ice sheet basal conditions. *Journal of Geophysical Research: Solid Earth*, 122(9):7127–7155.
- Shen, W., Wiens, D., Stern, T., Anandakrishnan, S., Aster, R. C., Dalziel, I., Hansen, S., Heeszel, D., Huerta, A., Nyblade, A., Wilson, T., and Winberry, J. P. (2017). Seismic evidence for lithospheric foundering beneath the southern Transantarctic Mountains, Antarctica. *Geology*, 46(1):71–74.

- Shen, W., Wiens, D. A., Anandakrishnan, S., Aster, R. C., Gerstoft, P., Bromirski, P. D., Hansen, S. E., Dalziel, I. W. D., Heeszel, D. S., Huerta, A. D., Nyblade, A. A., Stephen, R., Wilson, T. J., and Winberry, J. P. (2018). The crust and upper mantle structure of central and West Antarctica from bayesian inversion of Rayleigh wave and receiver functions. *Journal of Geophysical Research: Solid Earth*, 123(9):7824–7849.
- Smalls, P. T., Sohn, R. A., and Collins, J. A. (2019). Lake-Bottom Seismograph Observations of Microseisms in Yellowstone Lake. *Seismological Research Letters*.
- Stein, S. and Wysession, M. (2009). *An introduction to seismology, earthquakes, and earth structure*. John Wiley & Sons.
- Sun, W. and Kennett, B. (2016). Receiver structure from teleseisms: Autocorrelation and cross correlation. *Geophysical Research Letters*, 43(12):6234–6242.
- Talandier, J., Hyvernaud, O., Reymond, D., and Okal, E. A. (2006). Hydroacoustic signals generated by parked and drifting icebergs in the Southern Indian and Pacific Oceans. *Geophysical Journal International*, 165(3):817–834.
- Tomasi, G., Van Den Berg, F., and Andersson, C. (2004). Correlation optimized warping and dynamic time warping as preprocessing methods for chromatographic data. *Journal of Chemometrics: A Journal of the Chemometrics Society*, 18(5):231–241.
- Traer, J. and Gerstoft, P. (2014). A unified theory of microseisms and hum. *Journal of Geophysical Research: Solid Earth*, 119(4):3317–3339.
- Tsai, V. C. and McNamara, D. E. (2011). Quantifying the influence of sea ice on ocean microseism using observations from the Bering Sea, Alaska. *Geophysical Research Letters*, 38(22).
- Viktorov, I. A. (1967). *Rayleigh and Lamb Waves: Physical Theory and Applications. Transl. from Russian. With a Foreword by Warren P. Mason*. Plenum press.
- Walter, F., Chaput, J., and Lüthi, M. P. (2014). Thick sediments beneath Greenland’s ablation zone and their potential role in future ice sheet dynamics. *Geology*, 42(6):487–490.
- Welch, P. (1967). The use of fast Fourier transform for the estimation of power spectra: A method based on time averaging over short, modified periodograms. *IEEE Transactions on audio and electroacoustics*, 15(2):70–73.
- Wessel, P. and Smith, W. H. (1998). New, improved version of generic mapping tools released. *Eos, Transactions American Geophysical Union*, 79(47):579–579.
- White-Gaynor, A. L., Nyblade, A. A., Aster, R. C., Wiens, D. A., Bromirski, P. D., Gerstoft, P., Stephen, R. A., Hansen, S. E., Wilson, T., Dalziel, I. W., Huerta, A. D., Paul Winberry, J., and Anandakrishnan, S. (2019). Heterogeneous upper mantle structure beneath the Ross Sea Embayment and Marie Byrd Land, West Antarctica, revealed by P-wave tomography. *Earth and Planetary Science Letters*, 513:40–50.

- Wiens, D. A., Aster, R. C., and Bromirski, P. D. (2014). Collaborative research: Dynamic response of the Ross Ice Shelf to wave-induced vibrations and collaborative research: Mantle structure and dynamics of the Ross Sea from a passive seismic deployment on the Ross Ice Shelf.
- Wiens, D. A., Pratt, M., Aster, R. C., Nyblade, A., Bromirski, P. D., Stephen, R. A., Gerstoft, P., Diez, A., Cai, C., and Anthony, R. (2015). Seismic excitation of the Ross Ice Shelf by Whillans Ice Stream slip events. *proc. AGU, Fall Meeting, San Francisco*.
- Wilson, D., Leon, J., Aster, R., Ni, J., Schlue, J., Grand, S., Semken, S., Baldrige, S., and Gao, W. (2002). Broadband seismic background noise at temporary seismic stations observed on a regional scale in the southwestern united states. *Bulletin of the Seismological Society of America*, 92(8):3335–3342.
- Xu, Y., Koper, K. D., and Burlacu, R. (2017). Lakes as a source of short-period (0.5–2 s) microseisms. *Journal of Geophysical Research: Solid Earth*, 122(10):8241–8256.
- Yamamoto, T. (1982). Gravity waves and acoustic waves generated by submarine earthquakes. *International Journal of Soil Dynamics and Earthquake Engineering*, 1(2):75–82.
- Zhan, Z., Tsai, V. C., Jackson, J. M., and Helmberger, D. (2014). Ambient noise correlation on the Amery Ice Shelf, East Antarctica. *Geophysical Journal International*, 196(3):1796–1802.

Appendices

A1 Chapter 2

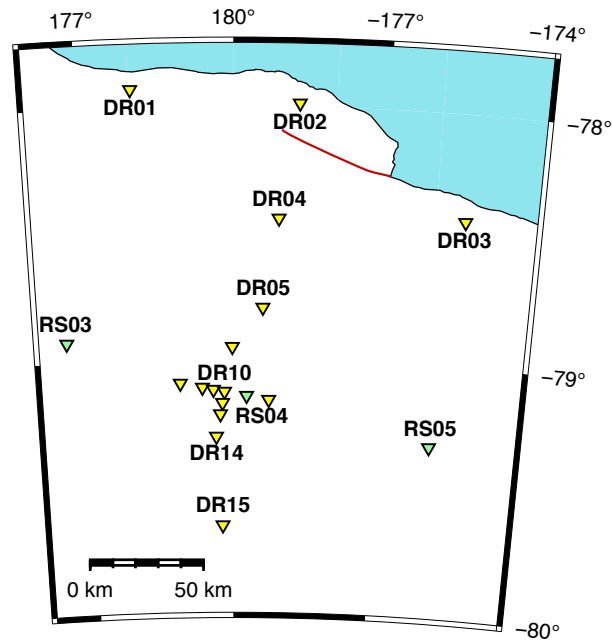


Figure A-2.1: Map of RIS ice front stations. The rift bounding the semi-detached Nascent Iceberg is denoted in red (adapted from LeDoux et al. (2017)). Station coordinates for DR01–DR03 have been manually shifted to accommodate the discrepancy between BEDMAP2 data and the current location of the RIS ice front and are presented for illustrative purposes only. DR stations (yellow) sampled at 200 Hz; RS stations (green) sampled at 100 Hz, except for RS04 which was also 200 Hz.

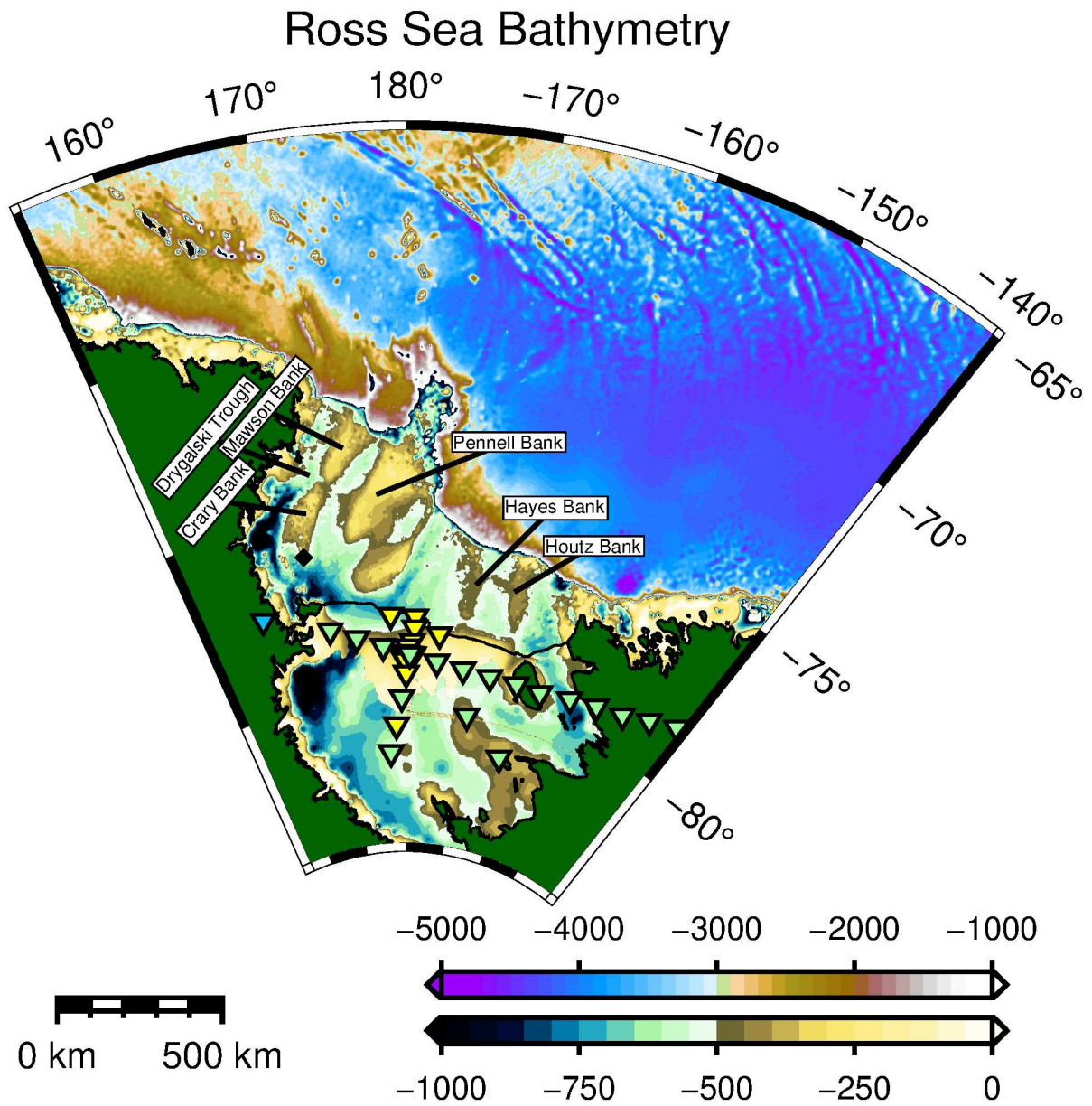


Figure A-2.2: High-contrast bathymetry for the Ross Sea Embayment (bottom color scale) and the adjacent continental slope and oceanic basin (top color scale). Depths are given in meters.

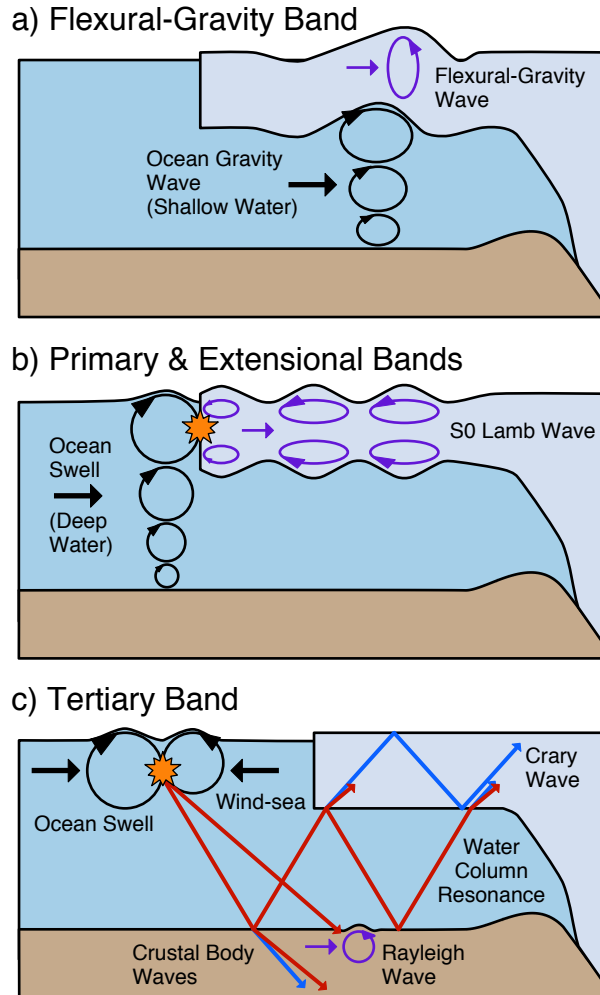


Figure A-2.3: Schematic of the ocean-forced wave modes endemic to the Ross Ice Shelf (Table 2.2), categorized by the period bands (Table 2.1) for which these modes are most dominant (but not necessarily exclusive). **a)** A long period (<150 s) flexural-gravity wave (i.e., a buoyancy-coupled asymmetric mode (A0) Lamb wave) propagating at a higher phase velocity than its progenating ocean gravity wave. At ultra long periods ($\gg 150$ s), the elastic properties of the ice shelf are negligible and particle motion is expected to become prograde and in-phase with the sub-shelf ocean waves. At short periods (<1 s for the RIS), buoyancy is insignificant in comparison to the elastic restoring force and this wavemode is entirely described by the A0 Lamb wave equation (Viktorov, 1967; Robinson, 1983; Chen et al., 2018). **b)** S0 Lamb waves in the Primary and Extensional bands are excited by the impact of ocean swell against the ice front; swell energy also propagates into the sub-shelf cavity and excites intermediate period (10–30 s) flexural-gravity waves. **c)** Potential mechanism for the generation of acoustic waves via nonlinear wave-wave interaction of ocean swell and opposing wind-sea (e.g., Ardhuin and Herbers, 2013). These acoustic phases can couple into crustal body and surface modes and may also propagate into the sub-shelf cavity, where high reflection coefficients at the ice/water and water/seafloor interfaces promote strong resonances within the ice shelf and water column. Rayleigh waves arising from this process may be responsible for similar lake-ice-modulated microseism signals (Xu et al., 2017; Anthony et al., 2018; Smalls et al., 2019).

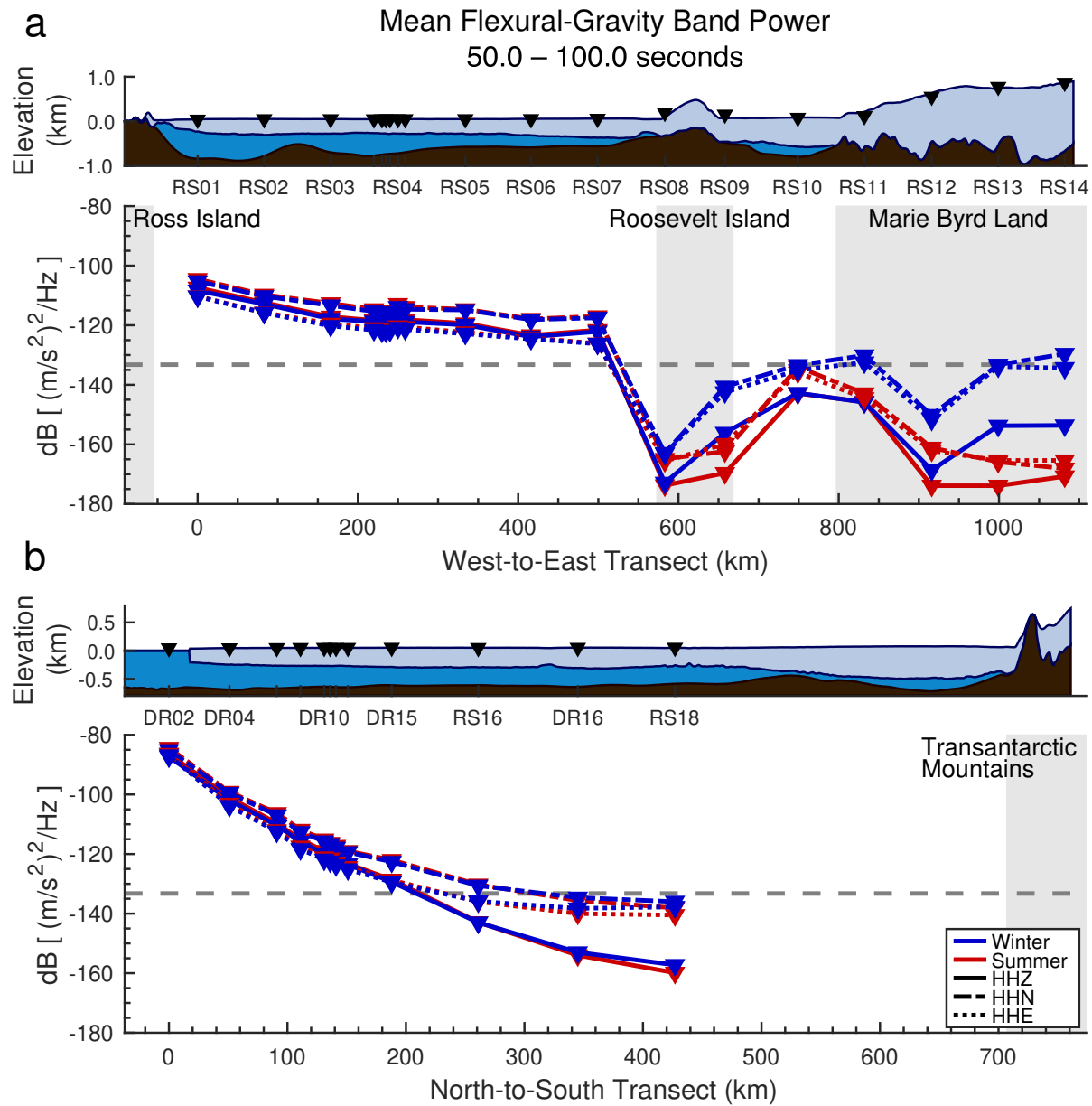


Figure A-2.4: Seasonal and geographic variations in the average ground acceleration power in the 50.0–100.0 second range. Energy in this bandpass is associated with flexural-gravity wave modes; i.e., a coupling of flexural A0 Lamb waves with water column buoyancy (Table 2.2). The faster decay of vertical power with distance from the ice front indicates the attenuation of infra-gravity waves within the sub-shelf cavity.

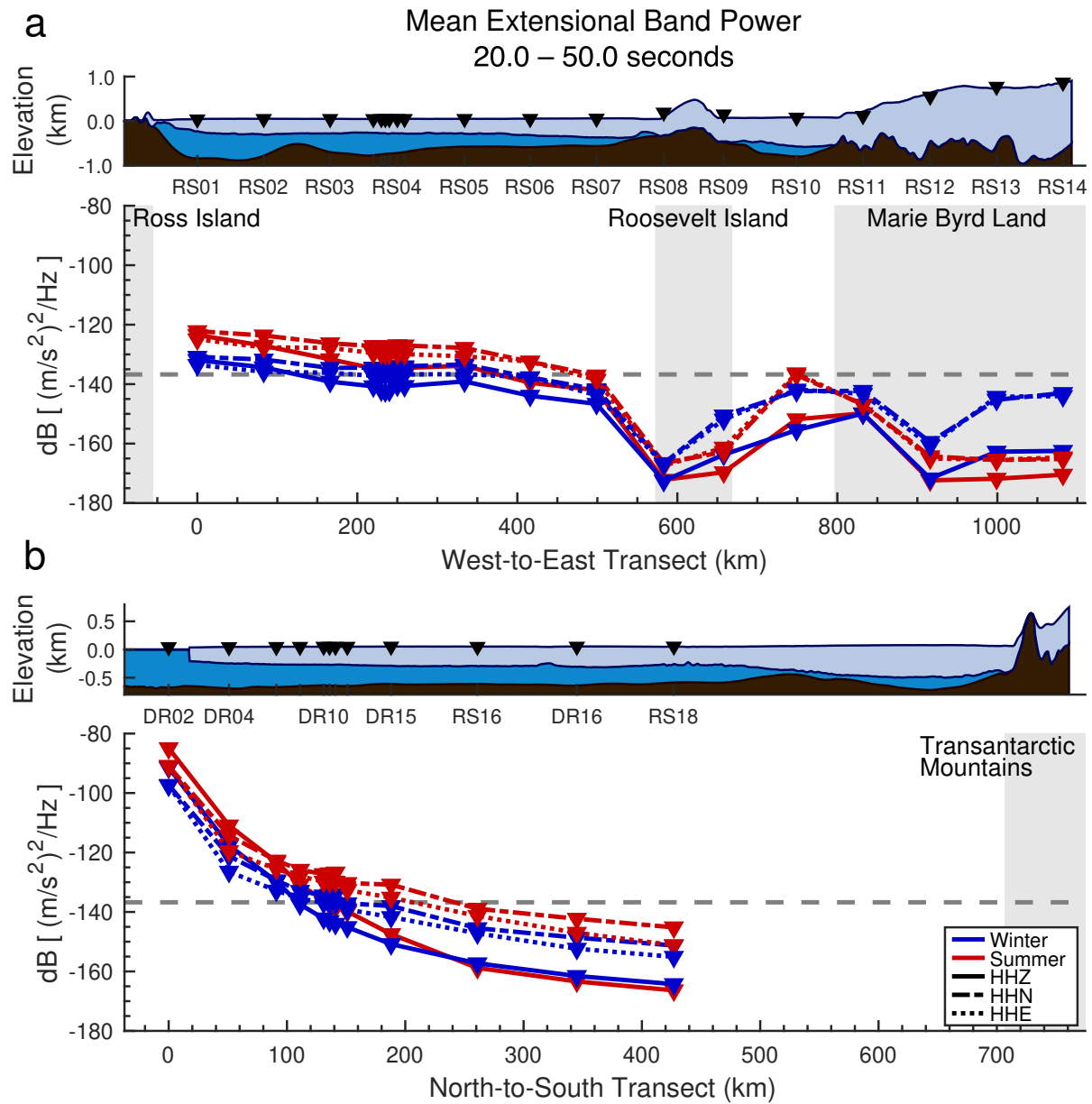


Figure A-2.5: Seasonal and geographic variations in the average ground acceleration power in the 20.0–50.0 second range. Energy in this bandpass is associated with longitudinally-polarized (+HOV) S0 Lamb wave modes (Table 2.2). See Figure 2.6 for details.

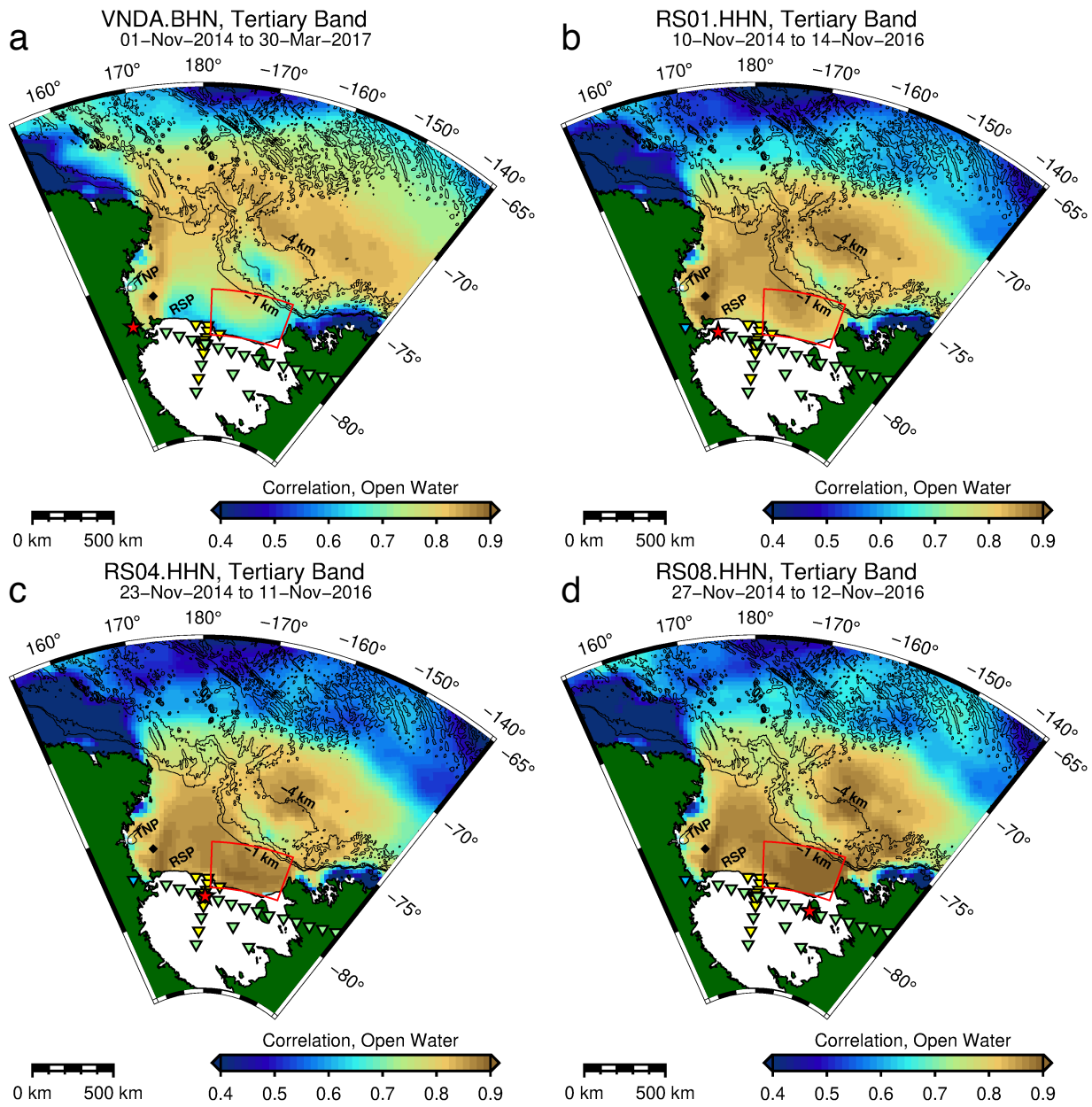


Figure A-2.6: North channel temporospatial correlations for the Tertiary band for an expanded selection of stations. Note the increasing correlations with proximity to the eastern Ross Sea. Vnda appears particularly insensitive to the Ross Sea state in comparison to the stations in the Ross Embayment. See also Figures 2.9, A-2.7.

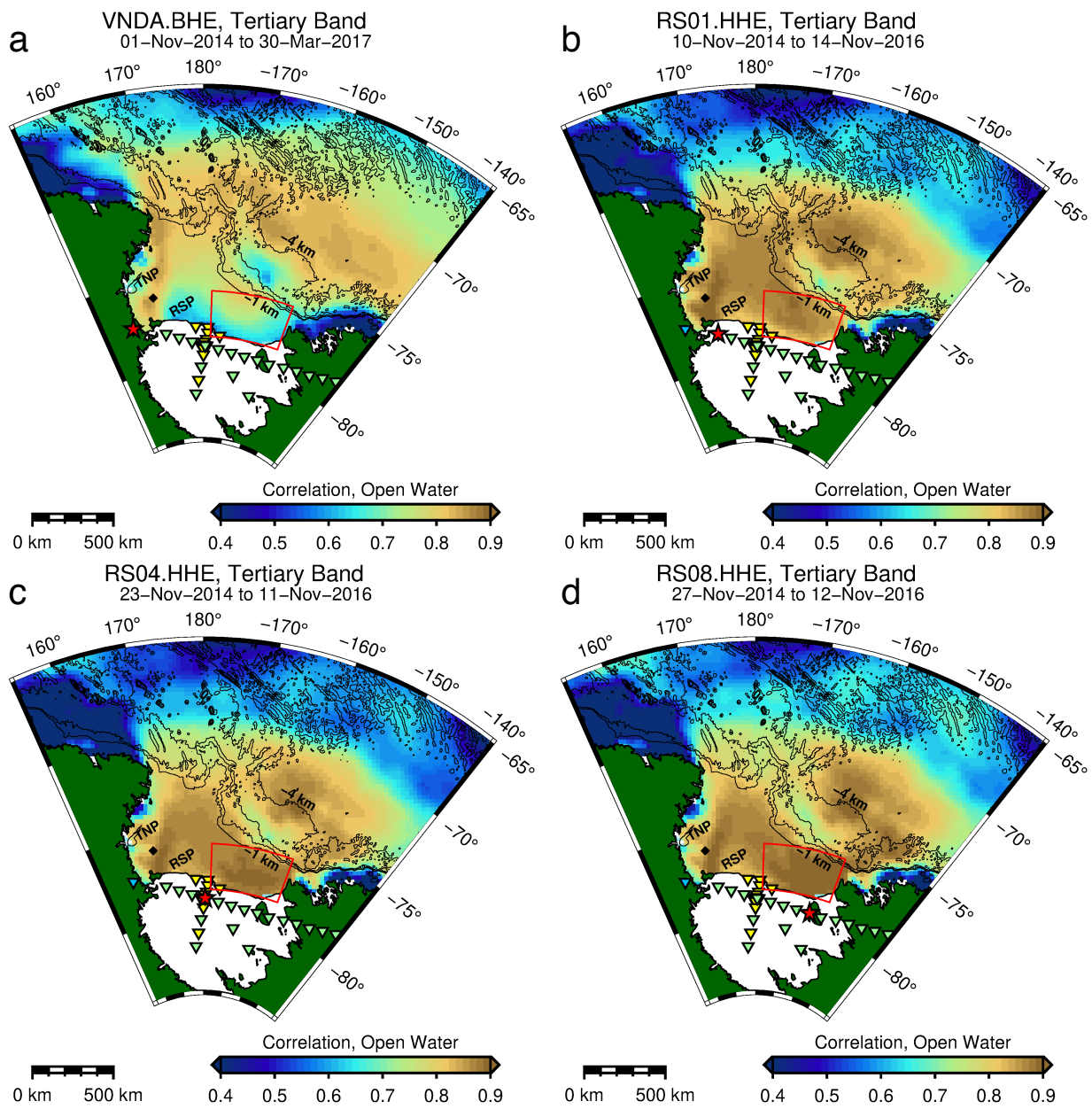


Figure A-2.7: East channel temporospatial correlations for the Tertiary band. See also Figure A-2.6.

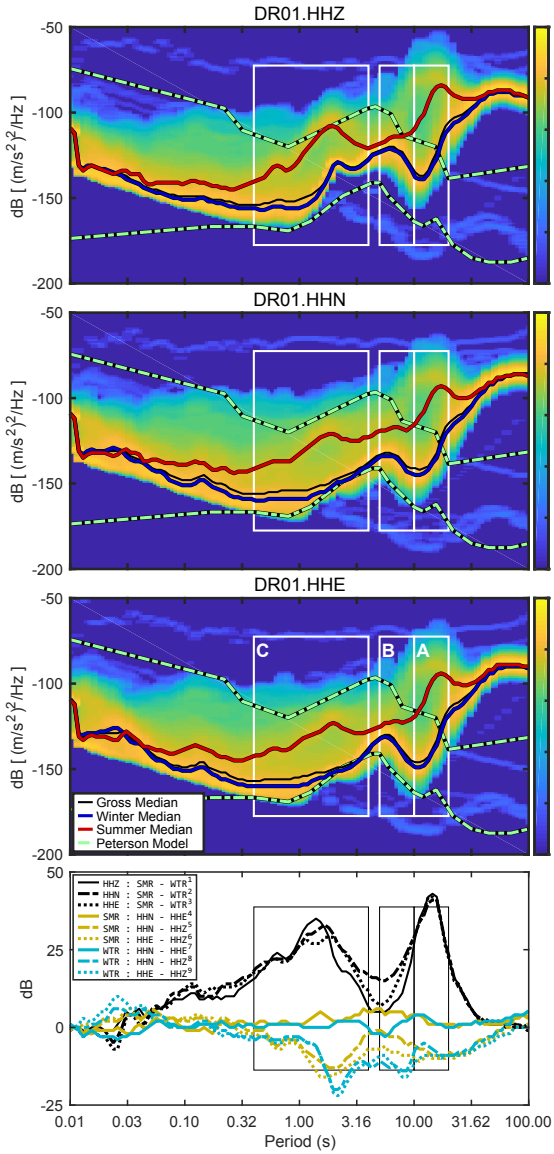


Figure A-2.8: DR01 PSD-PDF. Differential PSDs are shown in the bottom panel. Black traces (1, 2, 3) show seasonal changes for each component, with positive values indicating higher power during the summer months. Solid yellow (4) and teal (7) traces show the differences in North (HHN) versus East (HHE) components for summer and winter, respectively, with positive values indicating higher power observed on the North component. Chain-dashed yellow (5) and teal (8) traces indicate North versus Vertical HOV values; dotted yellow (6) and teal (9) traces indicate East versus Vertical HOV values.

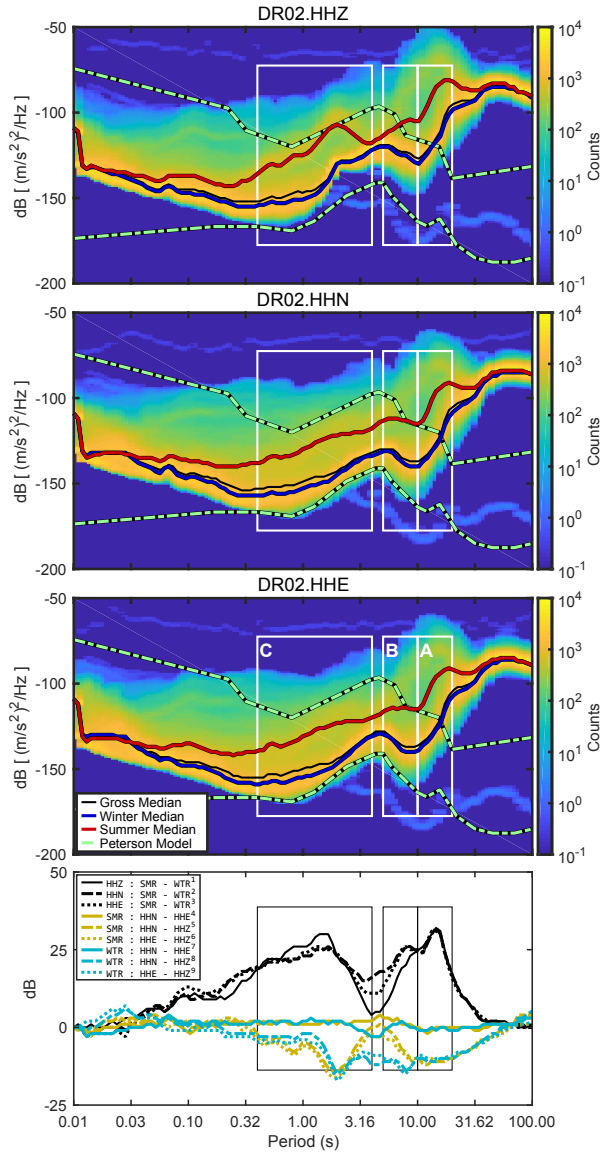


Figure A-2.9: DR02 PSD-PDF.

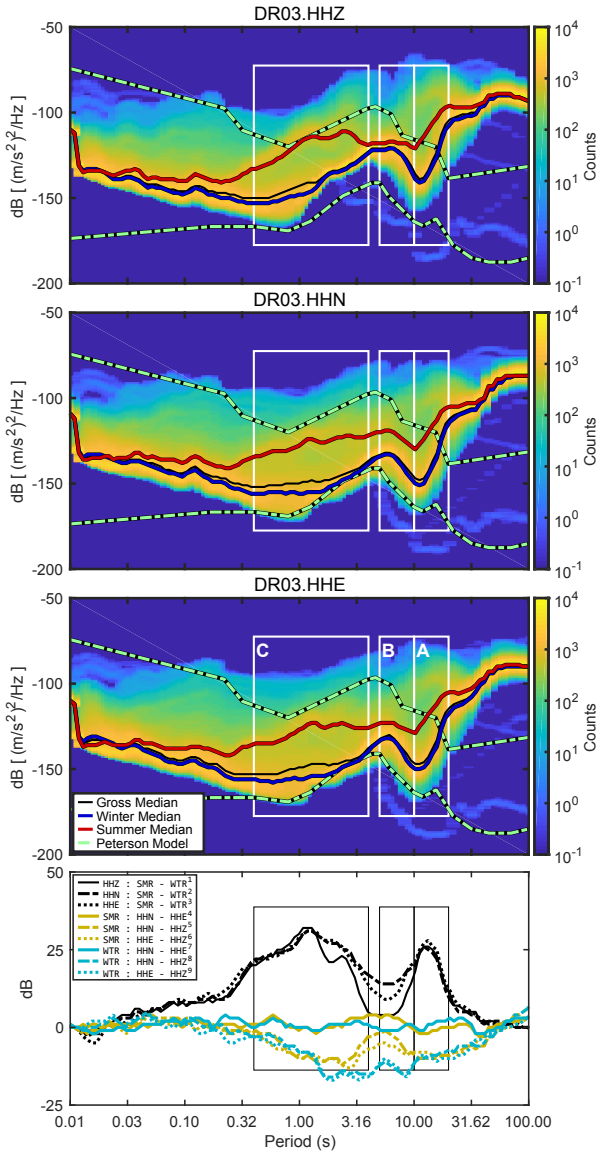


Figure A-2.10: DR03 PSD-PDF.

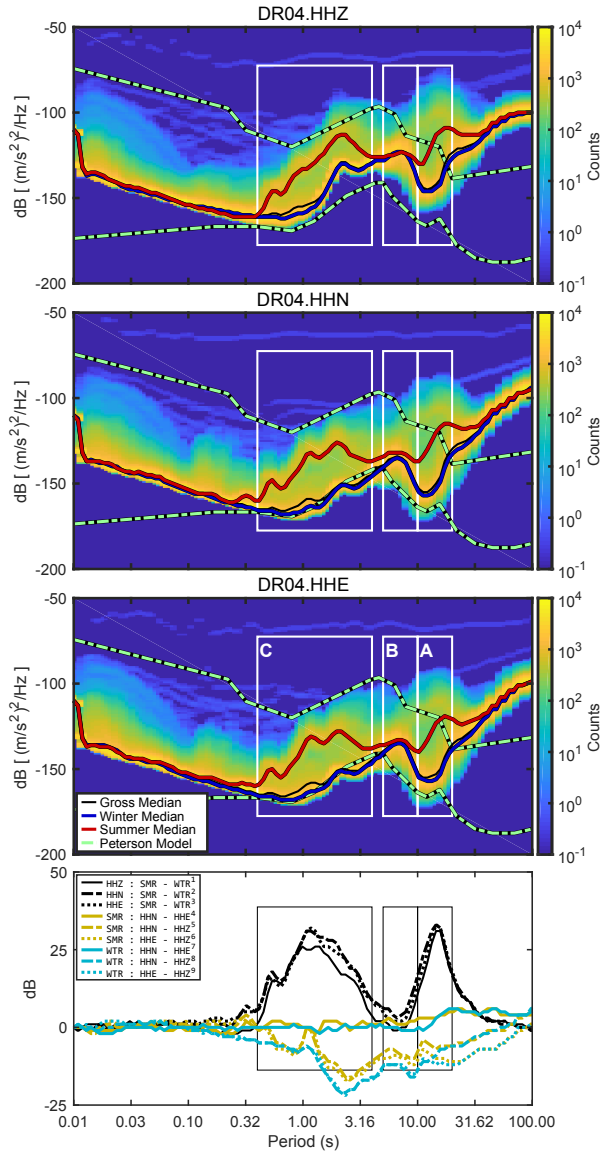


Figure A-2.11: DR04 PSD-PDF.

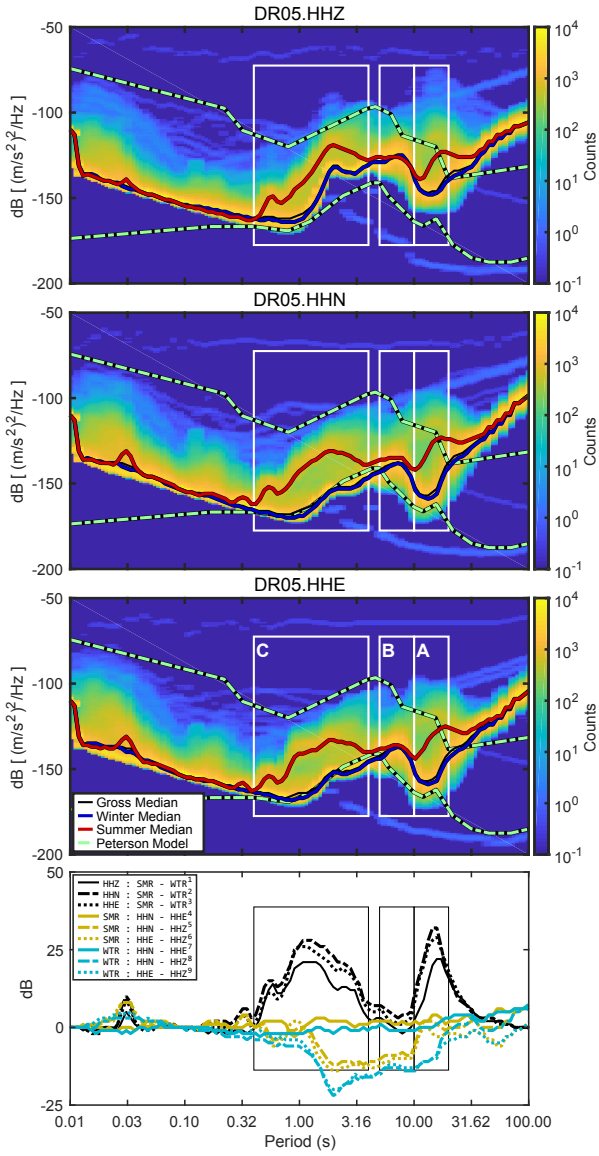


Figure A-2.12: DR05 PSD-PDF.

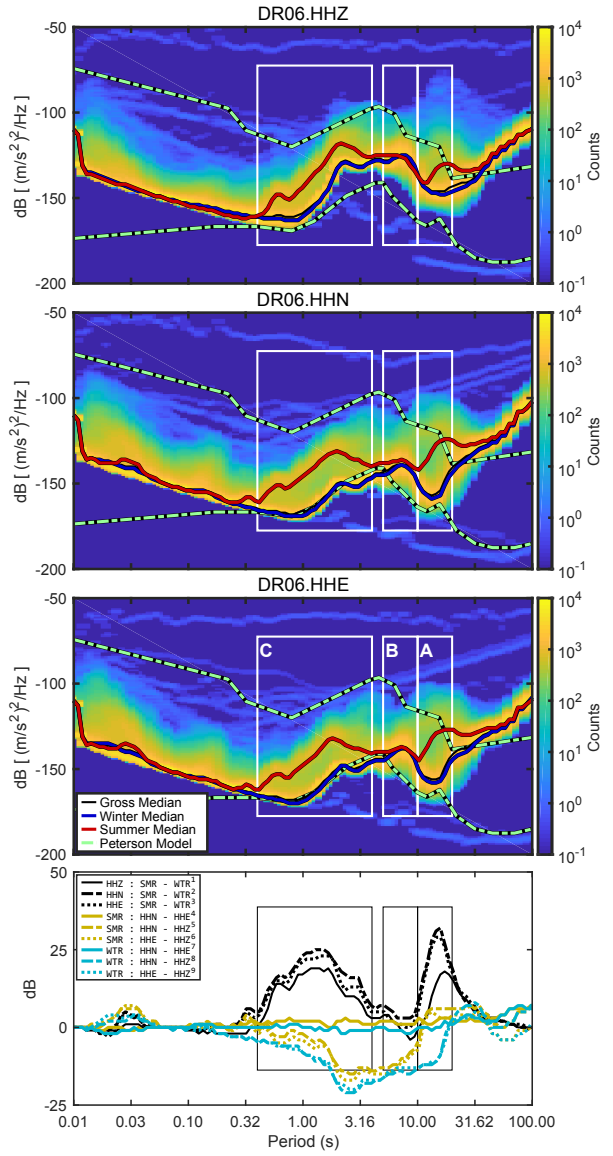


Figure A-2.13: DR06 PSD-PDF.

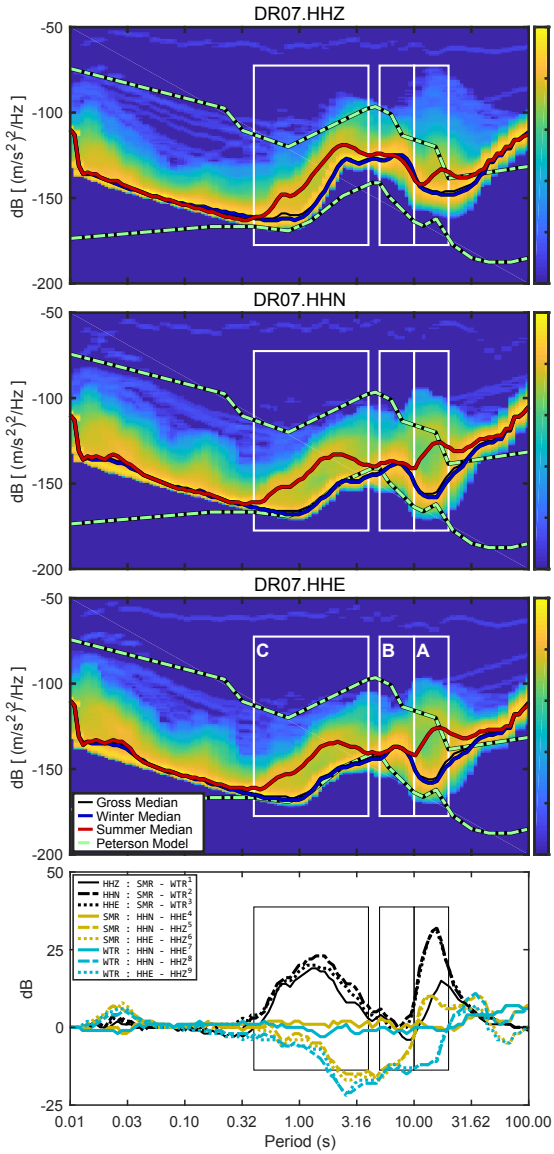


Figure A-2.14: DR07 PSD-PDF.

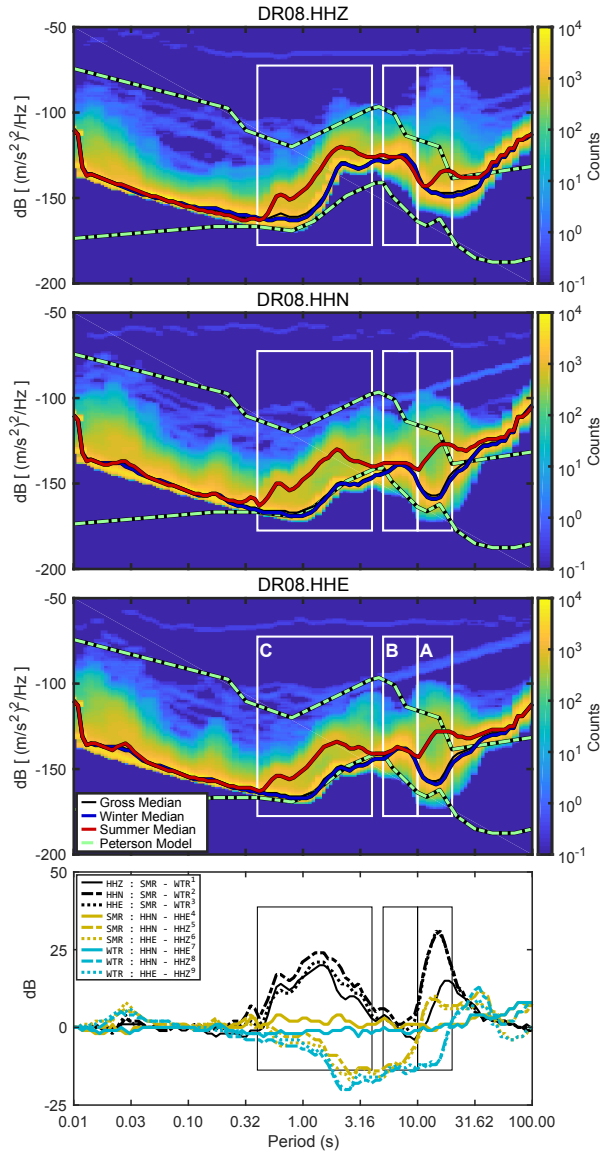


Figure A-2.15: DR08 PSD-PDF.

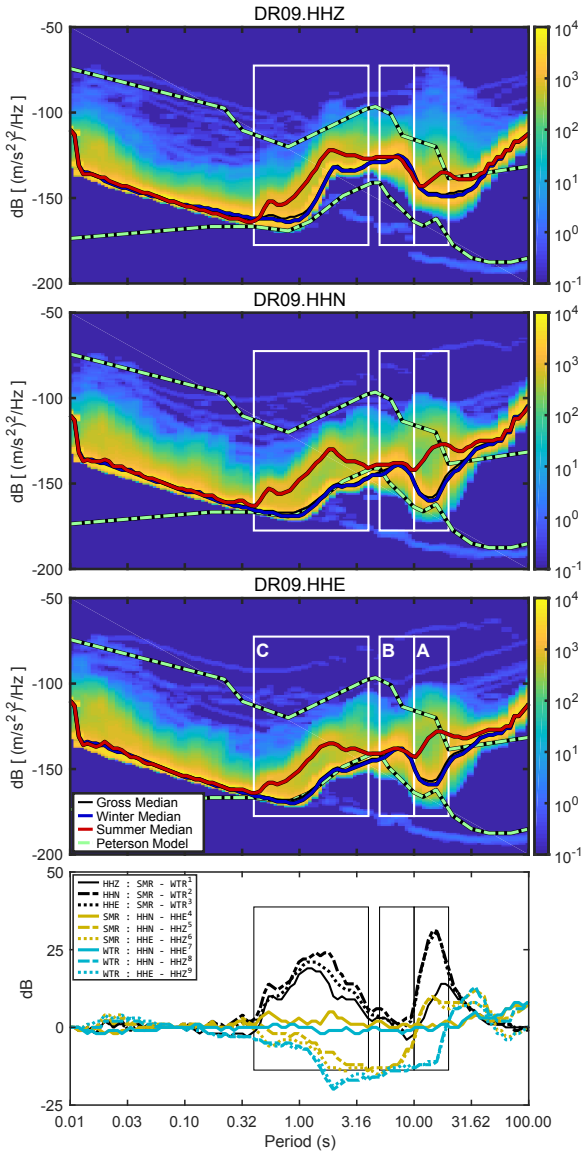


Figure A-2.16: DR09 PSD-PDF.

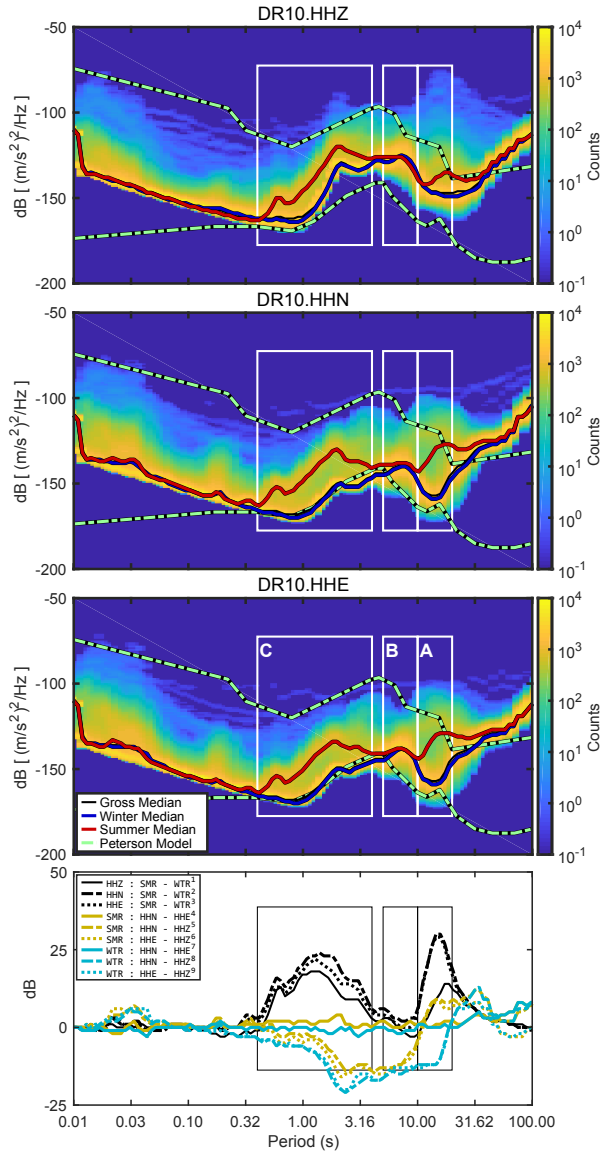


Figure A-2.17: DR10 PSD-PDF.

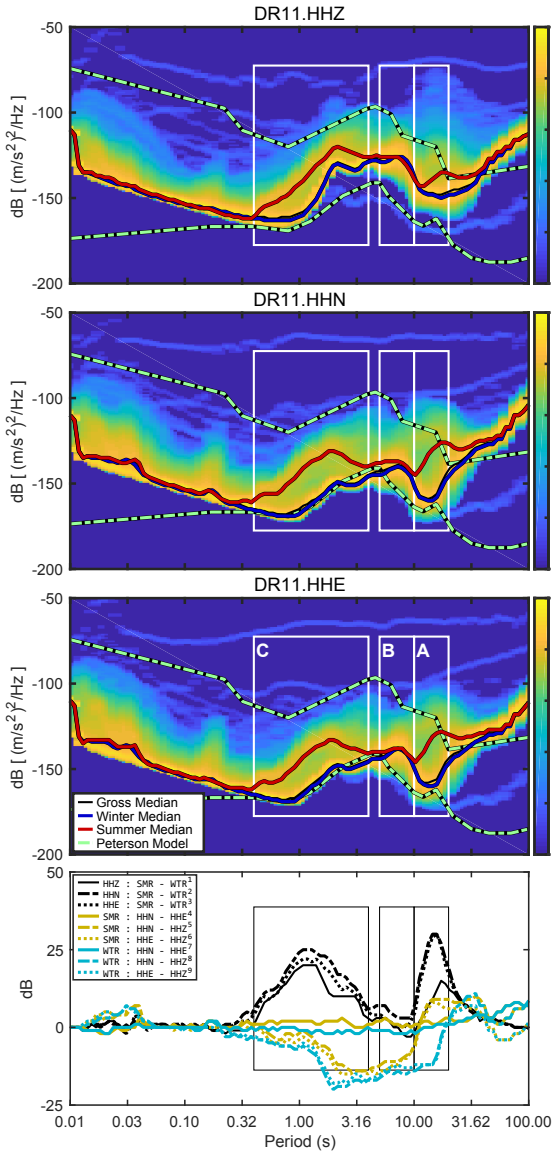


Figure A-2.18: DR11 PSD-PDF.

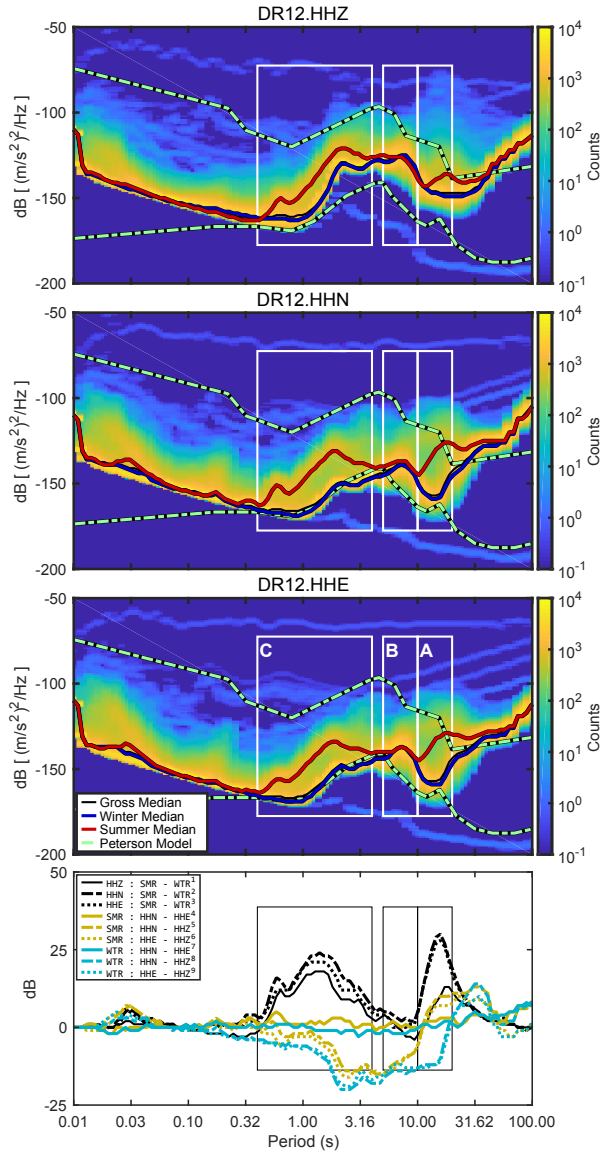


Figure A-2.19: DR12 PSD-PDF.

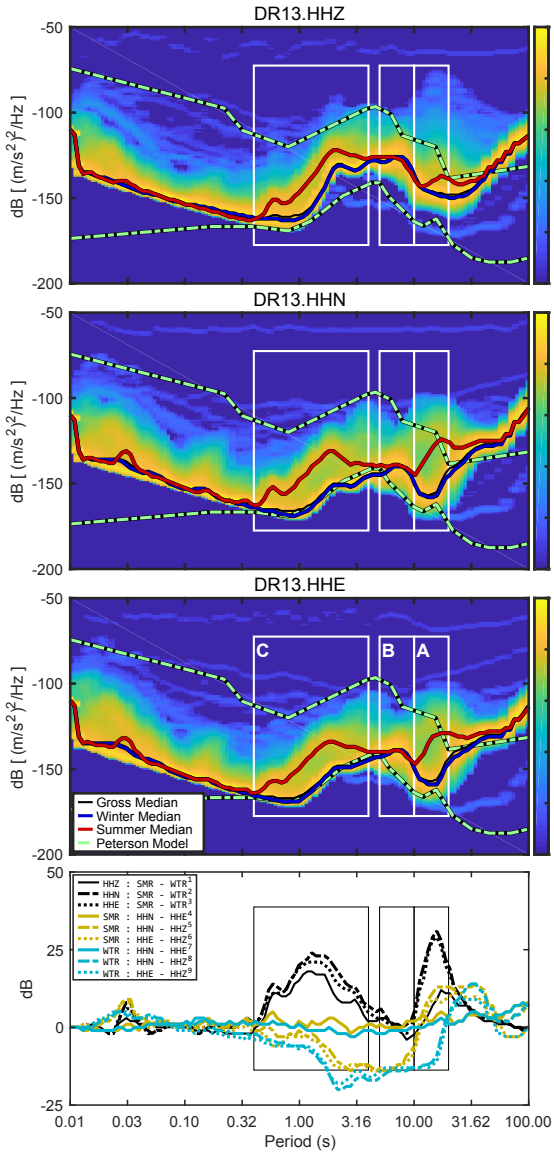


Figure A-2.20: DR13 PSD-PDF.

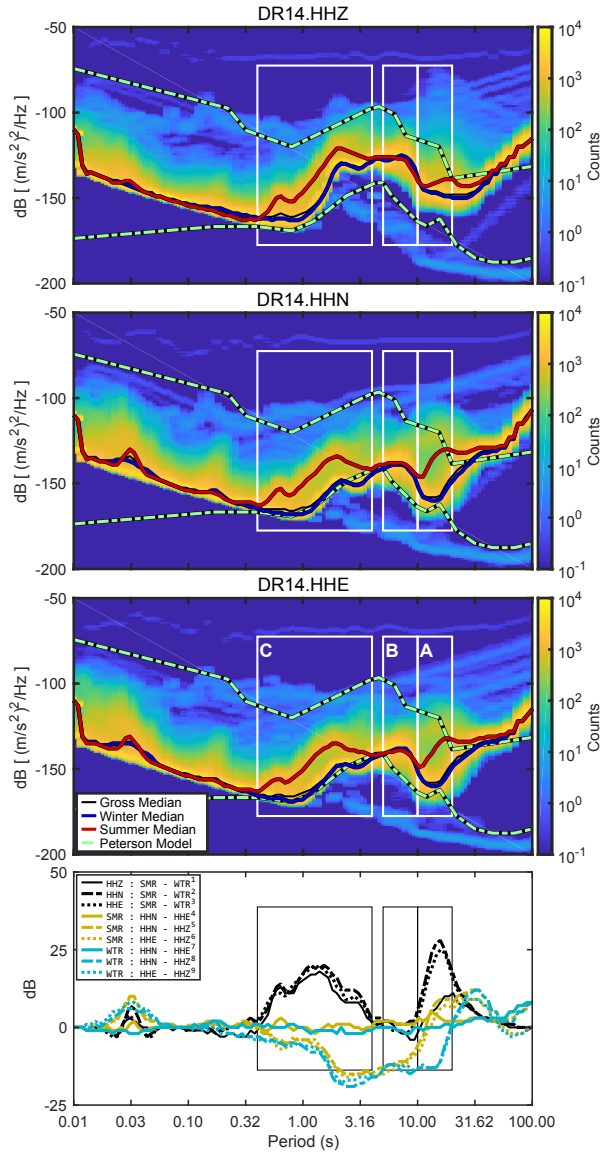


Figure A-2.21: DR14 PSD-PDF.

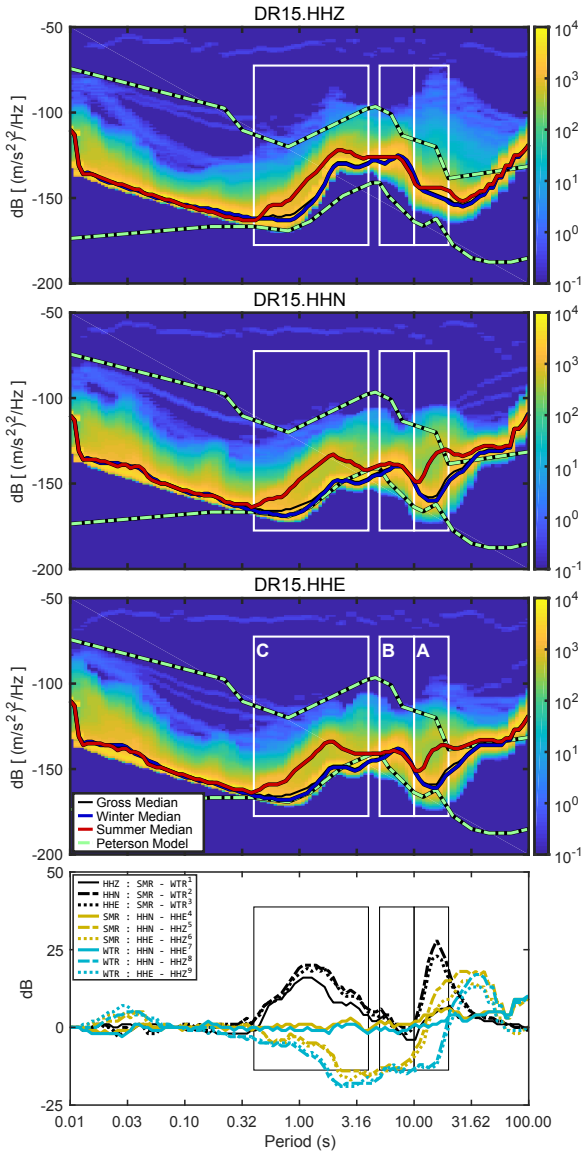


Figure A-2.22: DR15 PSD-PDF.

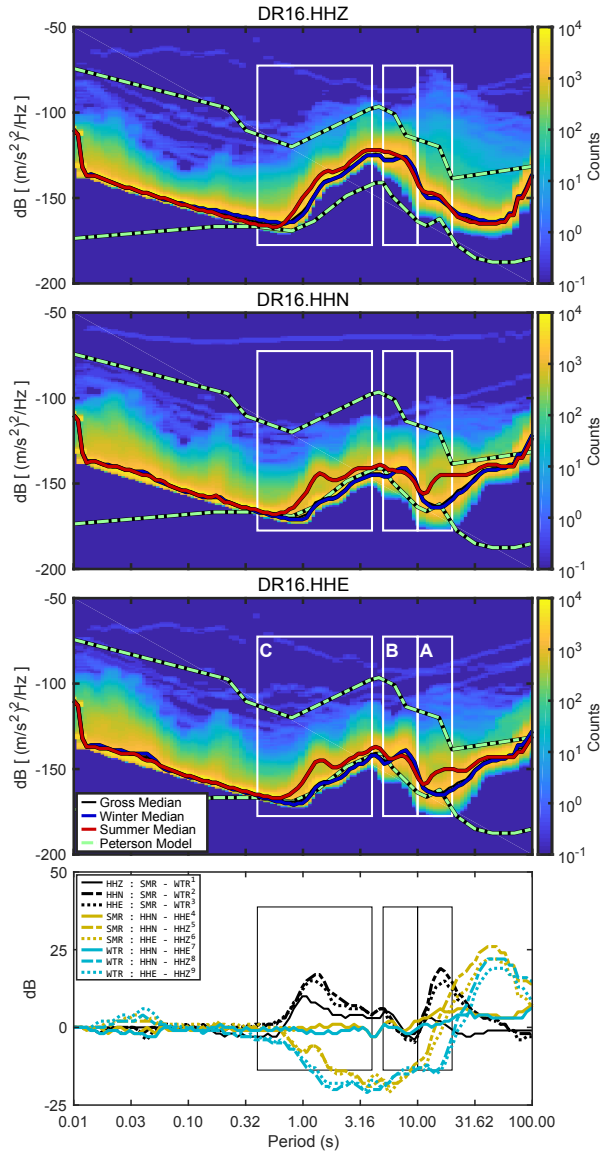


Figure A-2.23: DR16 PSD-PDF.

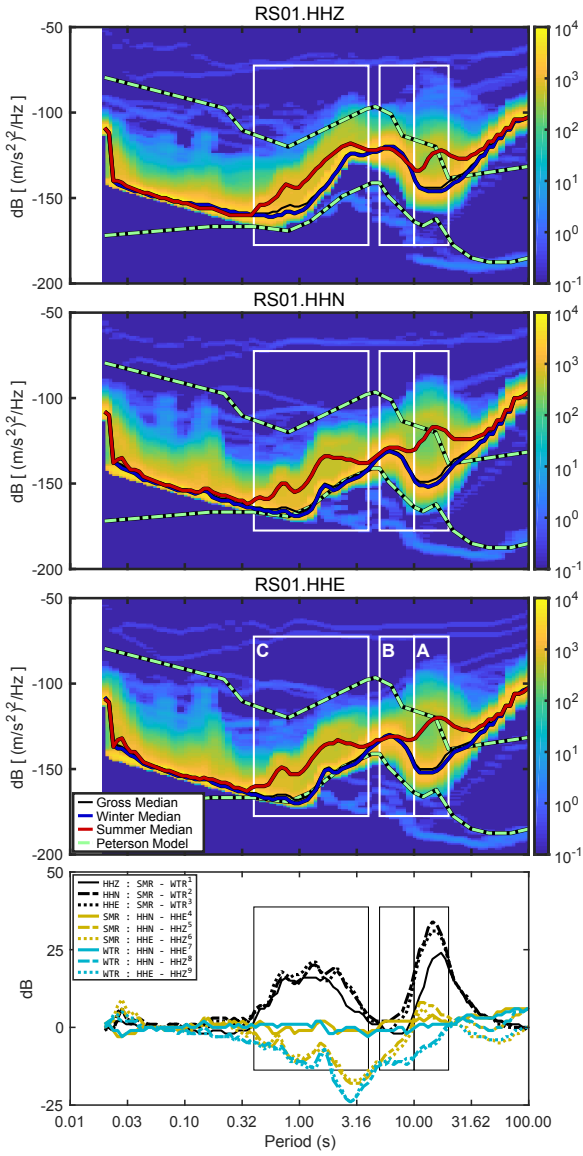


Figure A-2.24: RS01 PSD-PDF.

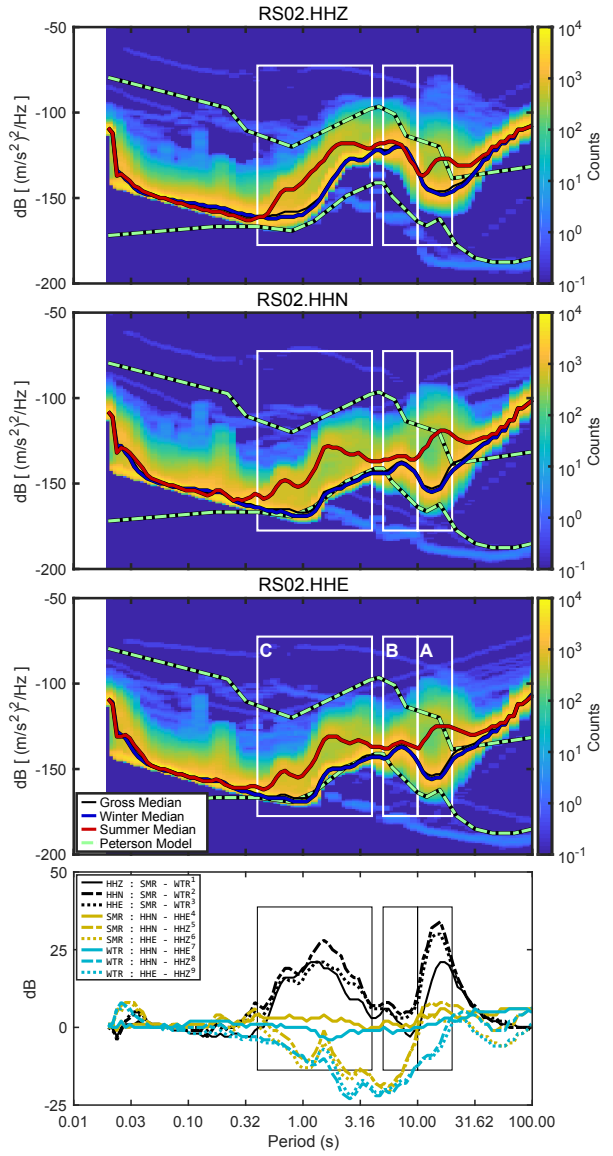


Figure A-2.25: RS02 PSD-PDF.

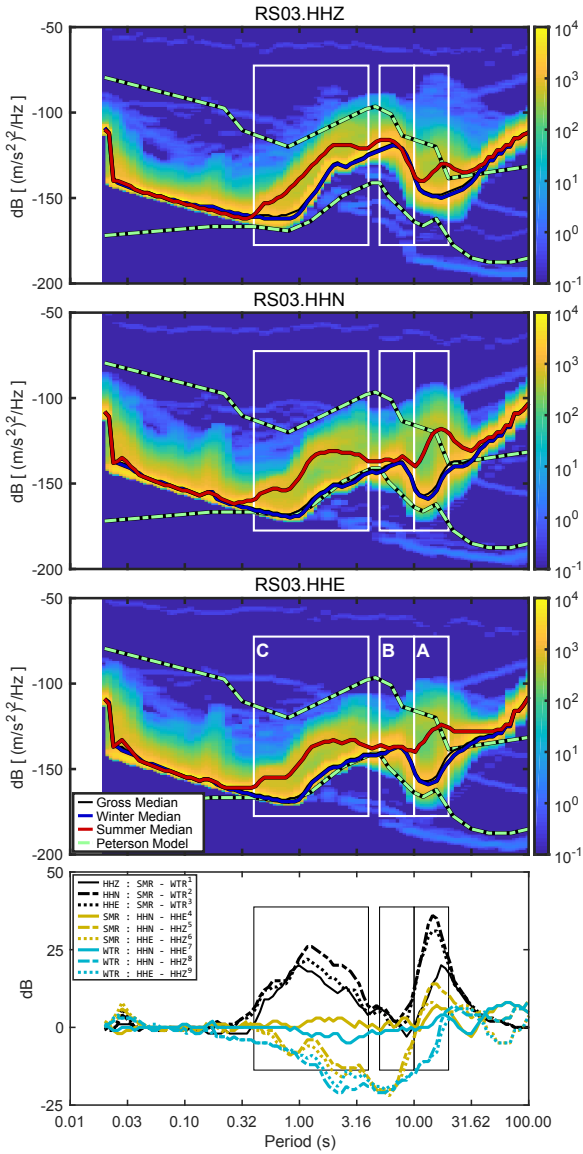


Figure A-2.26: RS03 PSD-PDF.

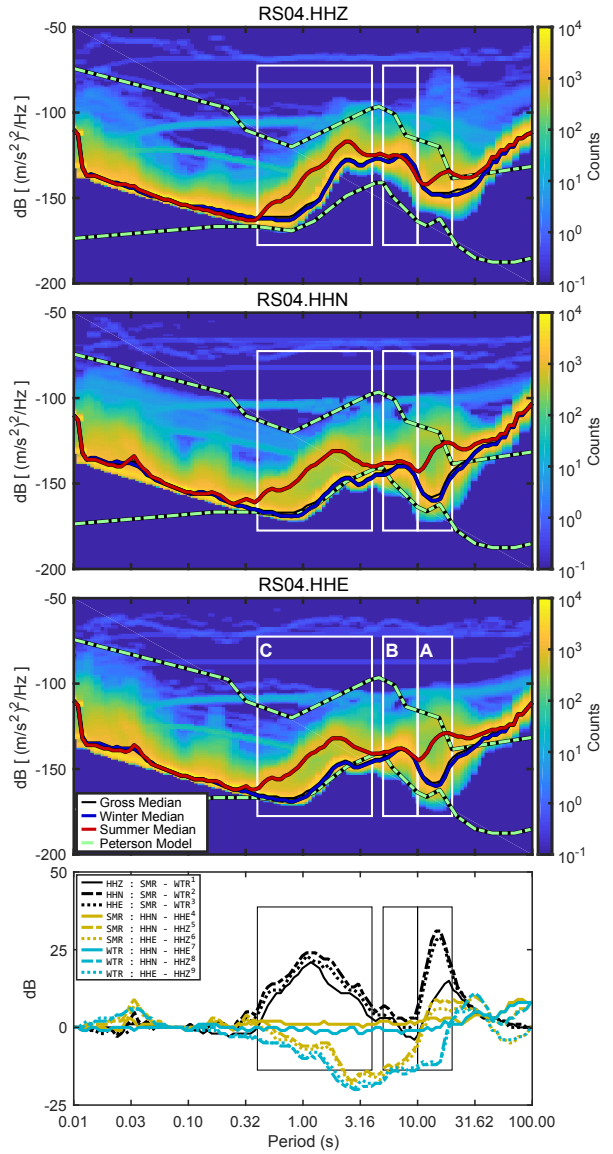


Figure A-2.27: RS04 PSD-PDF.

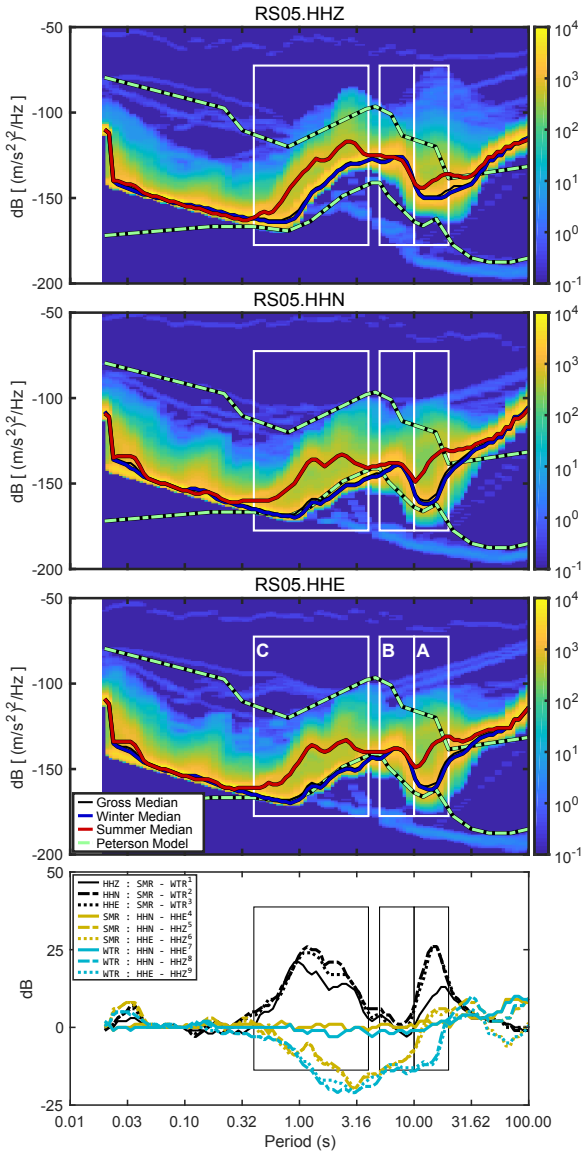


Figure A-2.28: RS05 PSD-PDF.

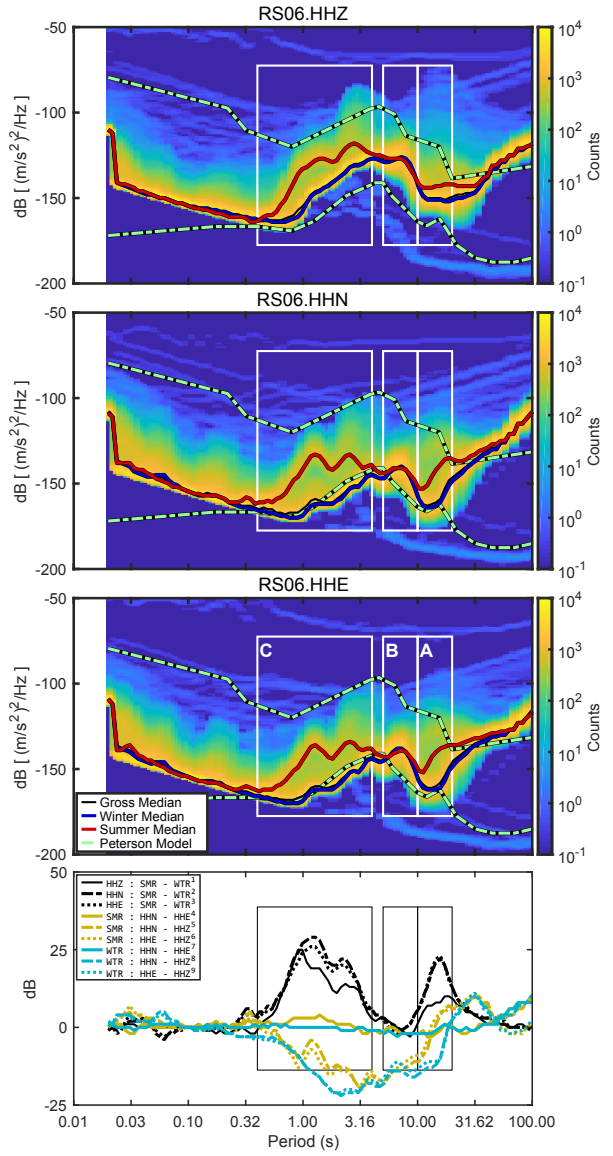


Figure A-2.29: RS06 PSD-PDF.

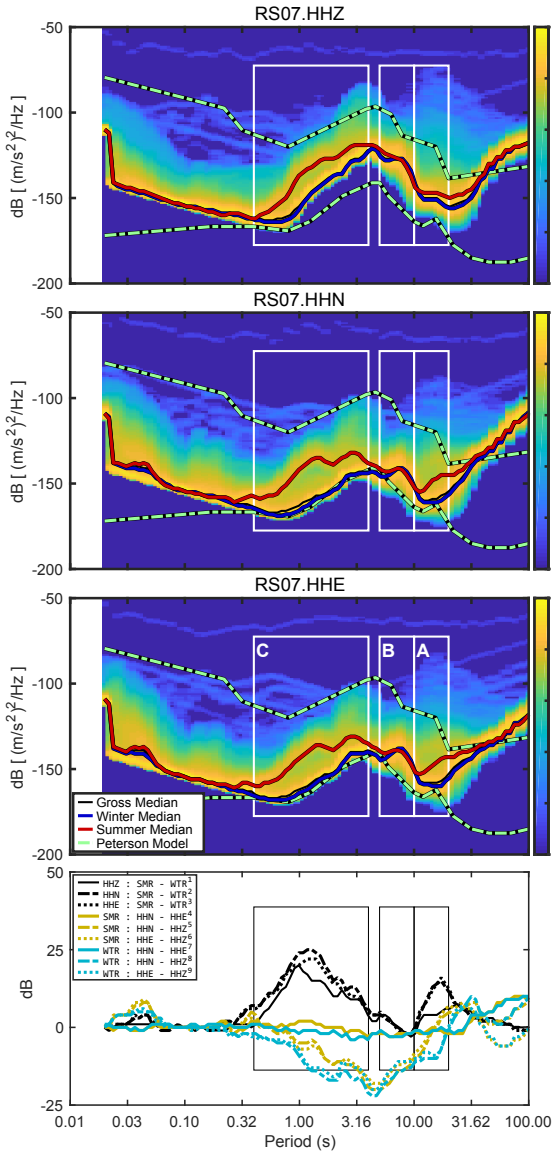


Figure A-2.30: RS07 PSD-PDF.

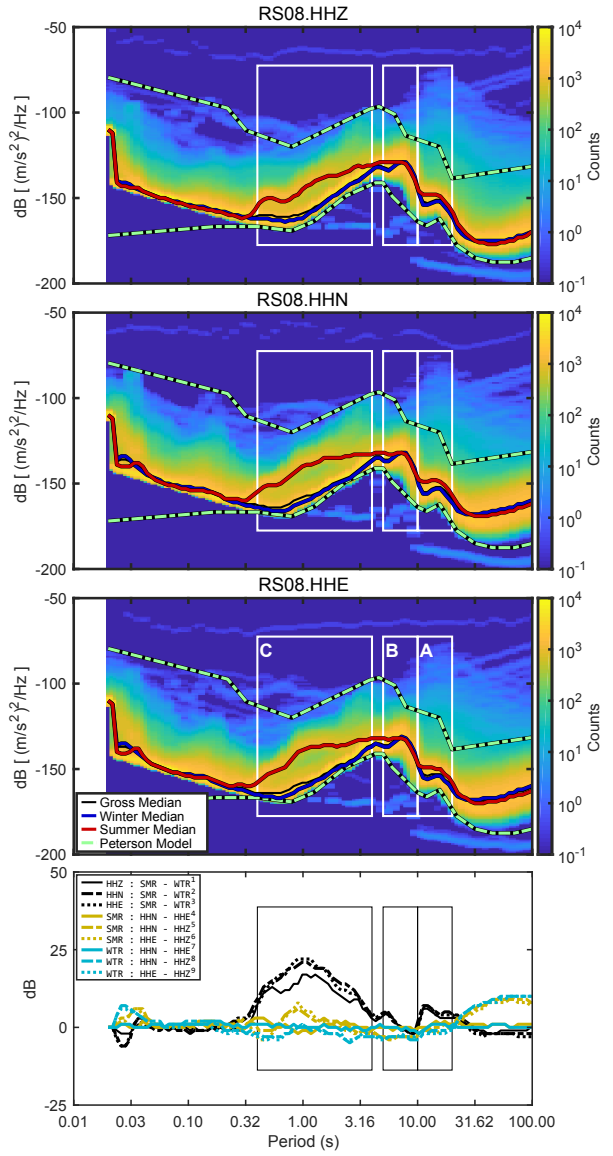


Figure A-2.31: RS08 PSD-PDF.

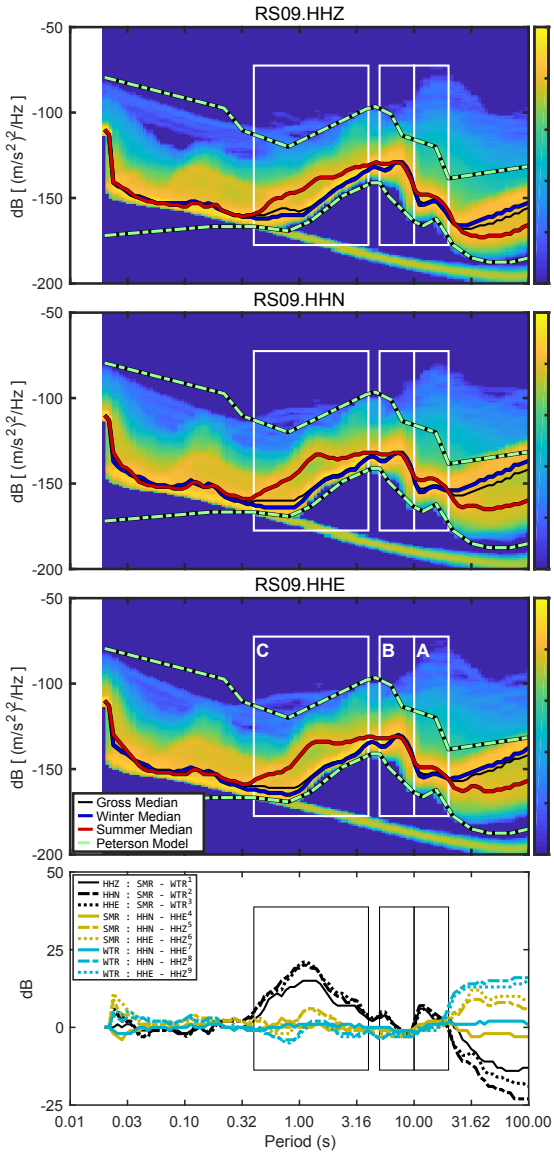


Figure A-2.32: RS09 PSD-PDF.

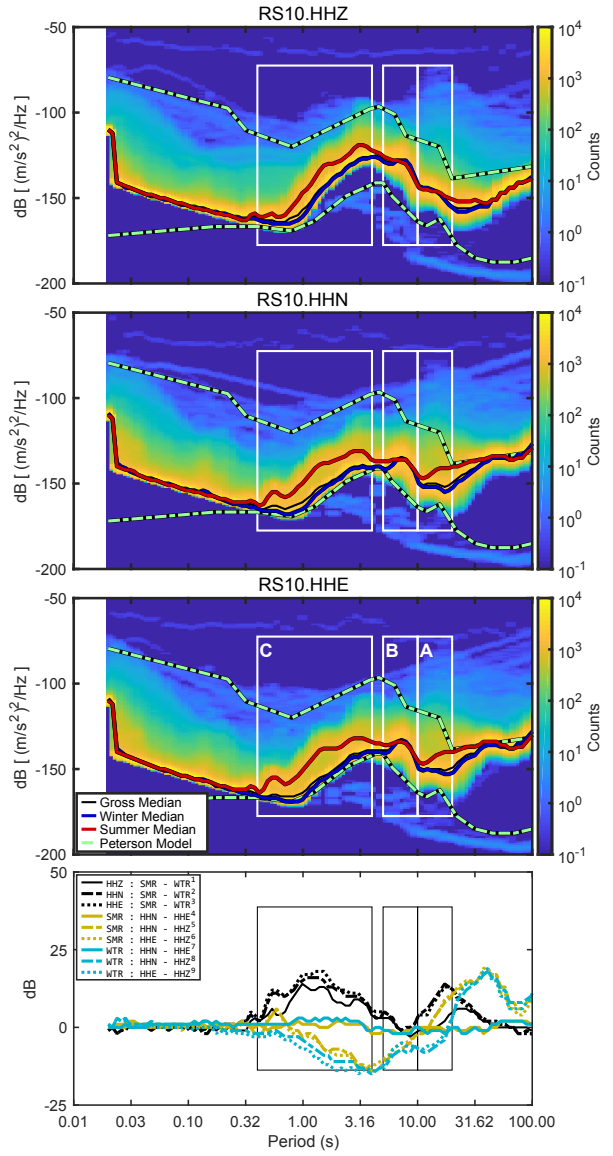


Figure A-2.33: RS10 PSD-PDF.

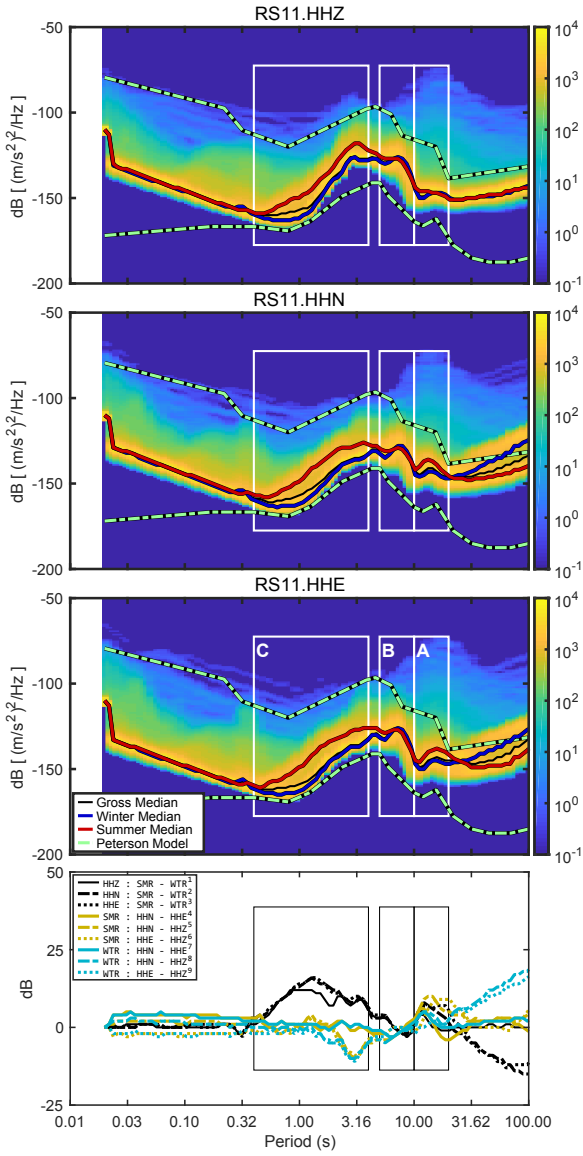


Figure A-2.34: RS11 PSD-PDF.

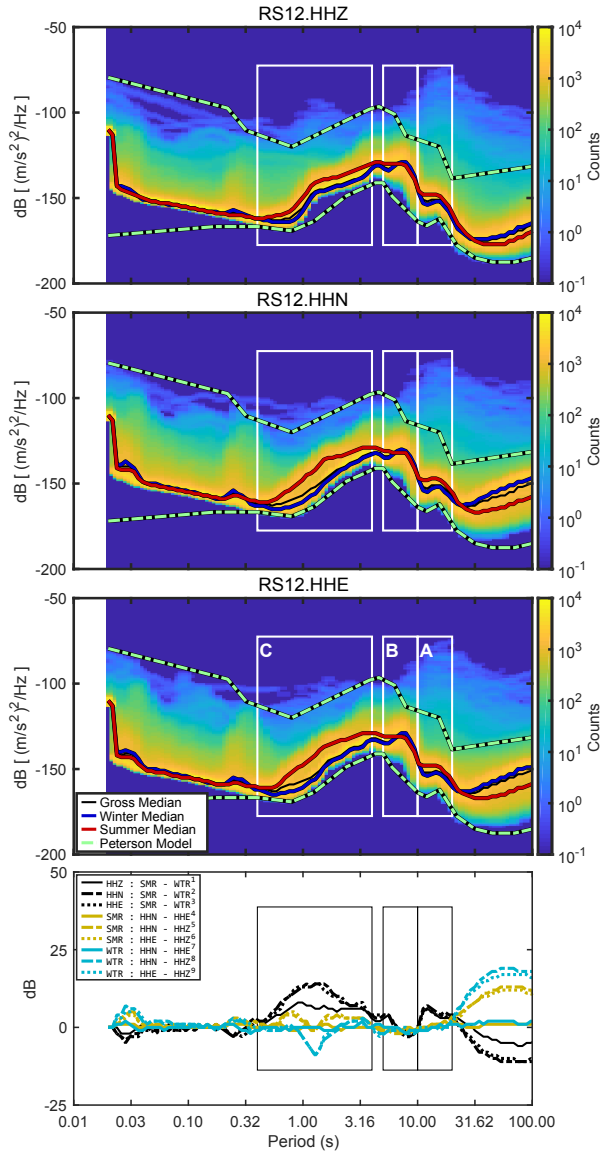


Figure A-2.35: RS12 PSD-PDF.

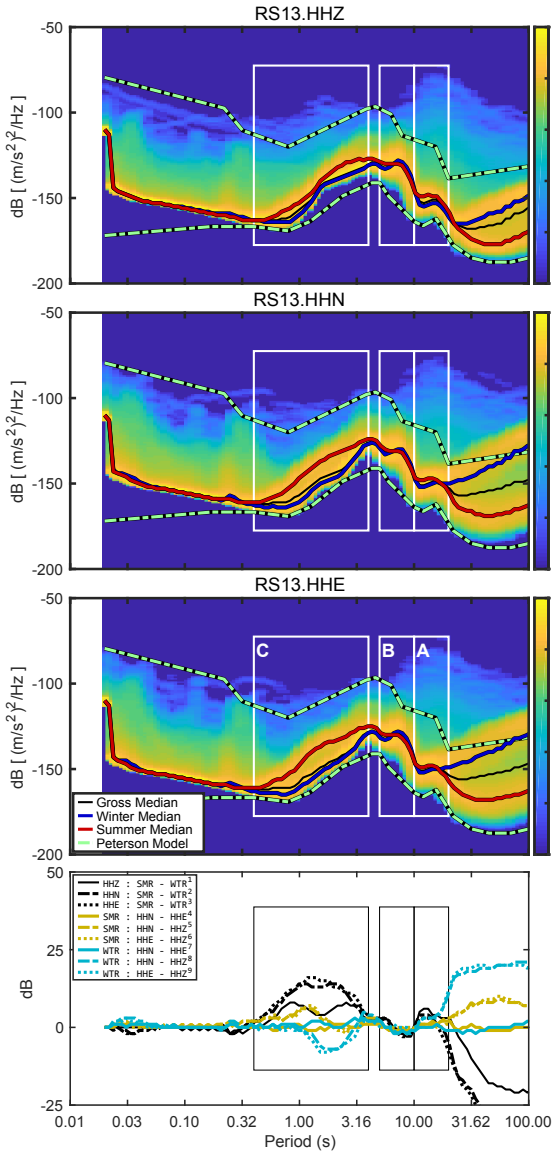


Figure A-2.36: RS13 PSD-PDF.

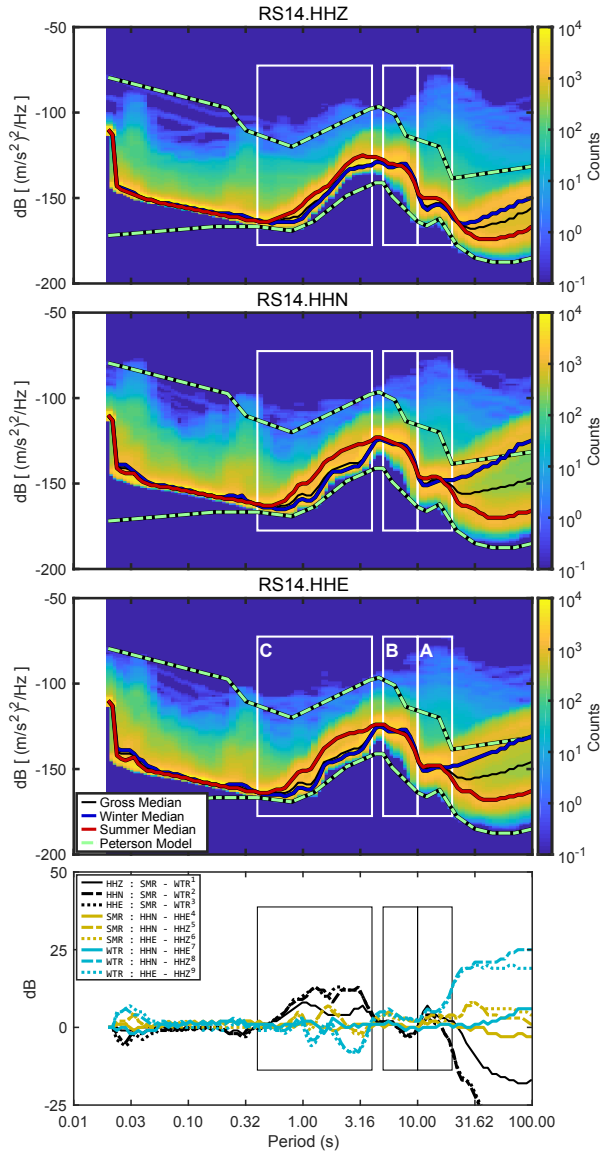


Figure A-2.37: RS14 PSD-PDF.

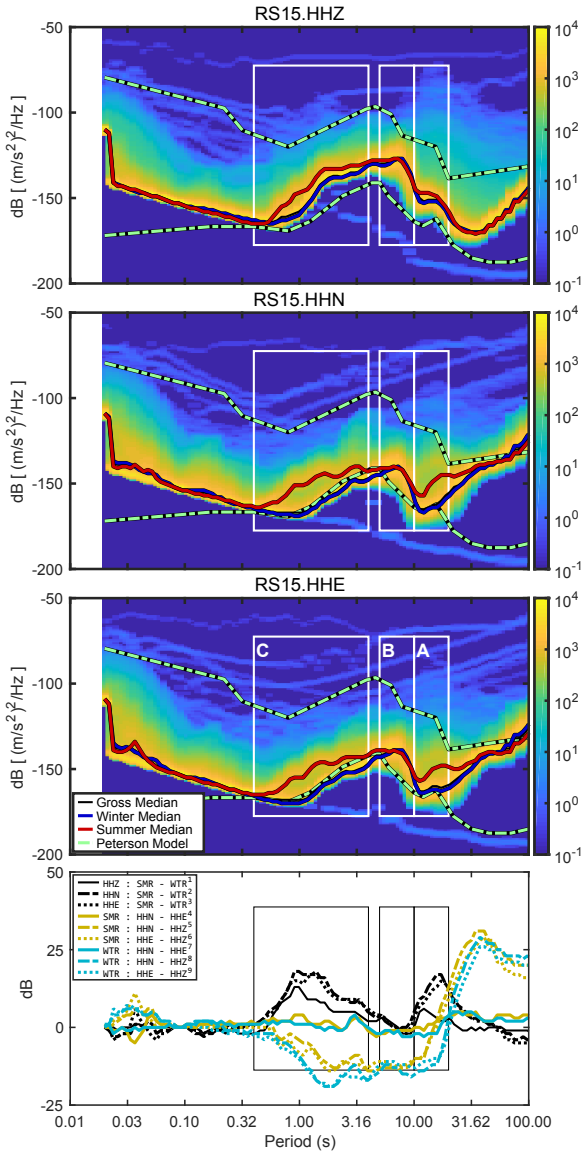


Figure A-2.38: RS15 PSD-PDF.

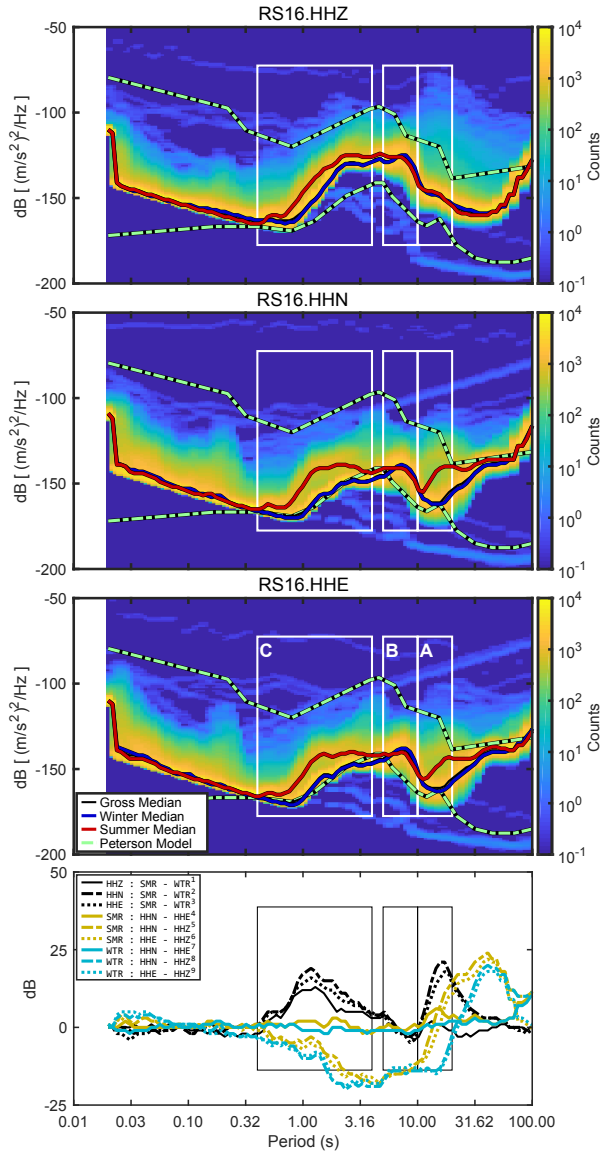


Figure A-2.39: RS16 PSD-PDF.

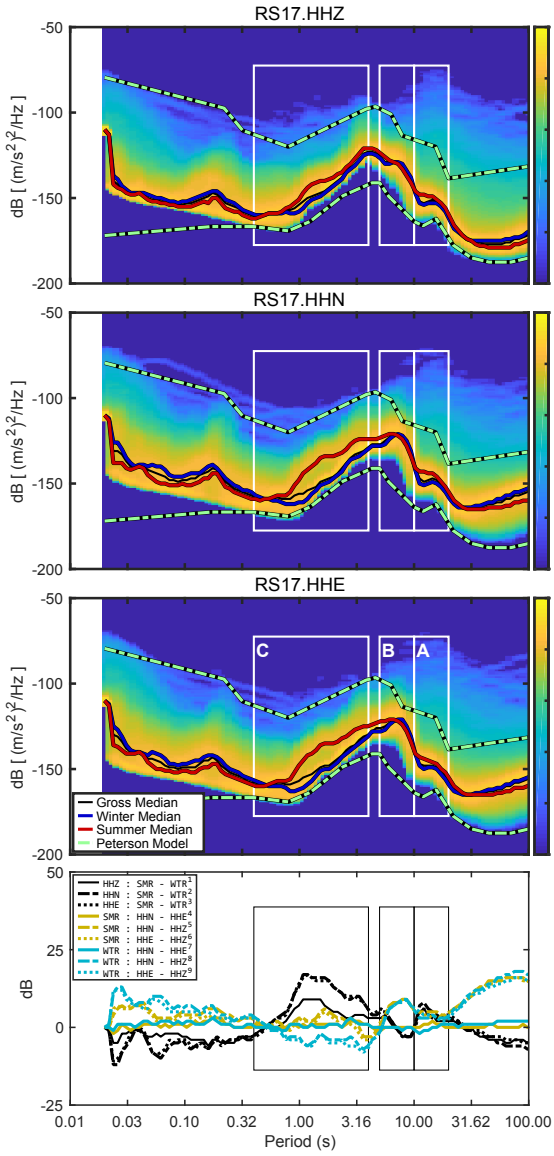


Figure A-2.40: RS17 PSD-PDF.

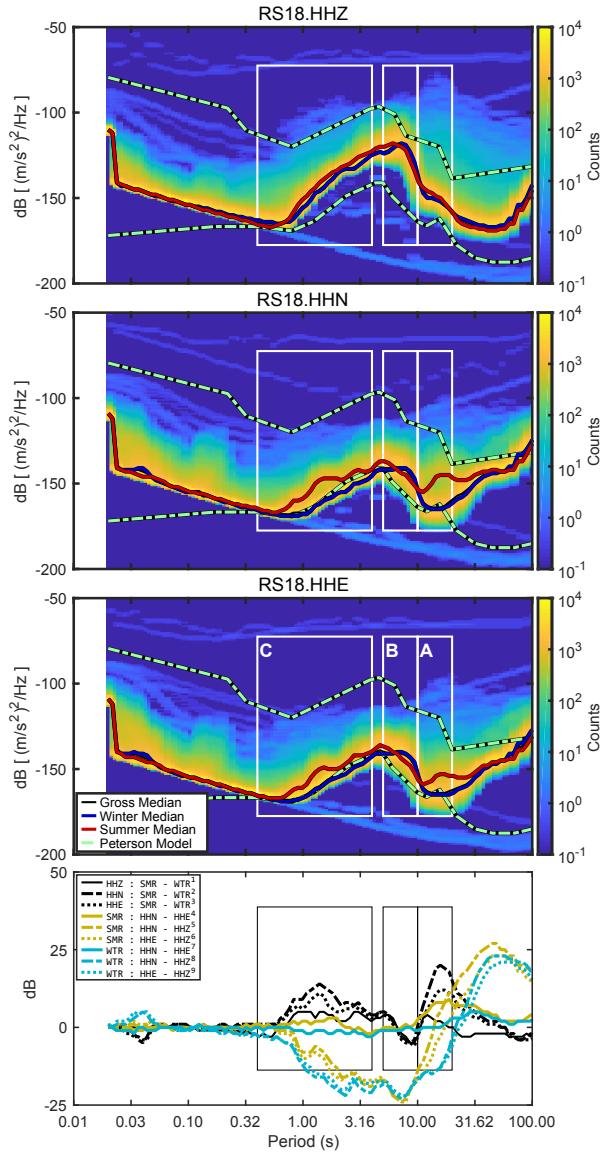


Figure A-2.41: RS18 PSD-PDF.

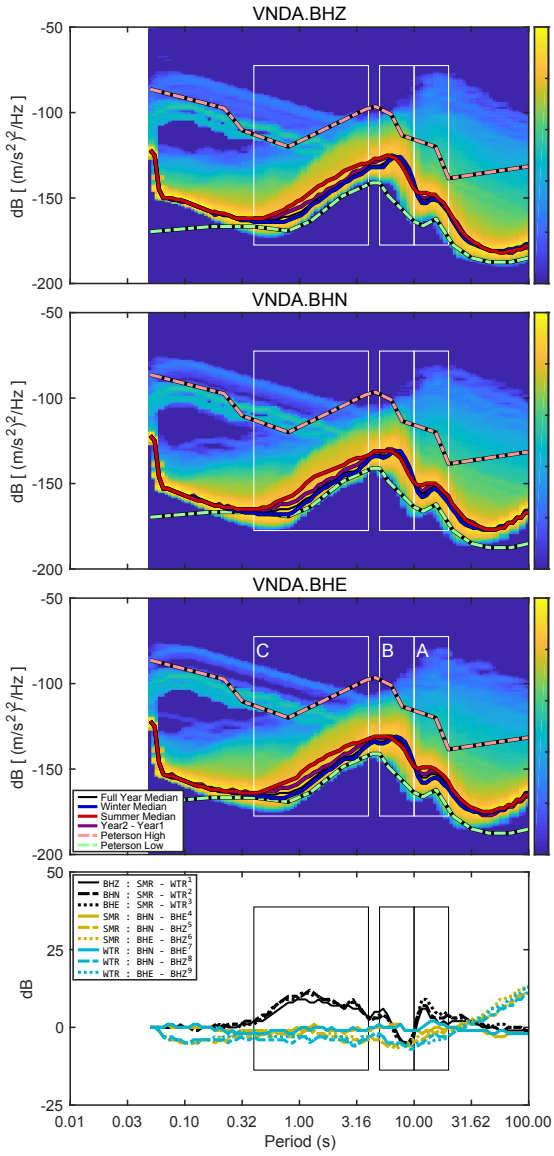


Figure A-2.42: VNDA PSD-PDF.

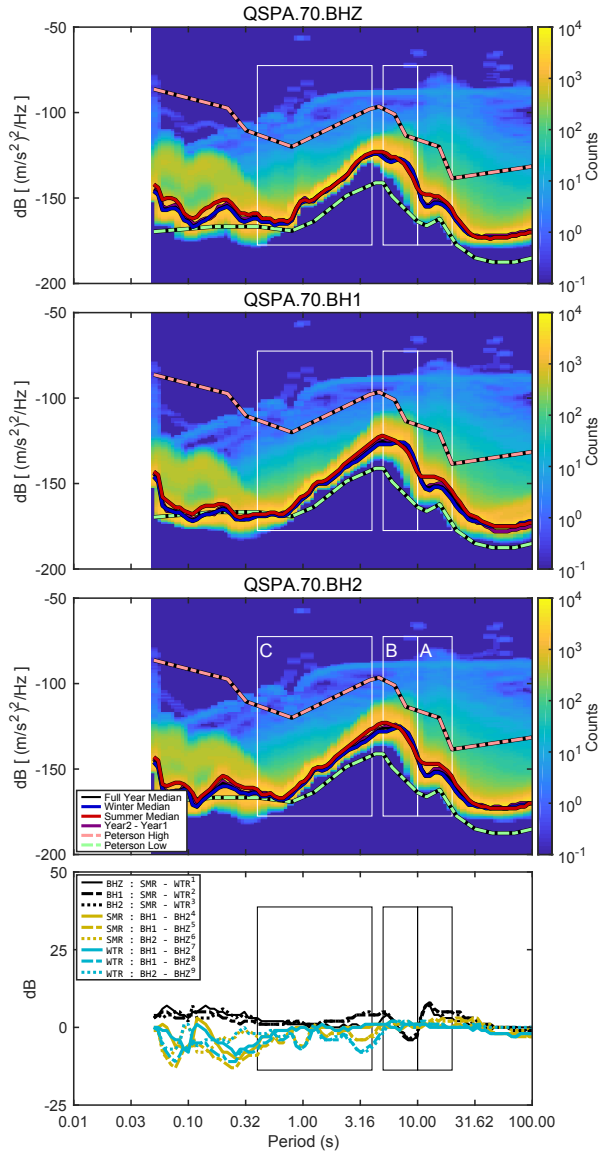


Figure A-2.43: QSPA Location 70 PSD-PDF.

A2 Chapter 3

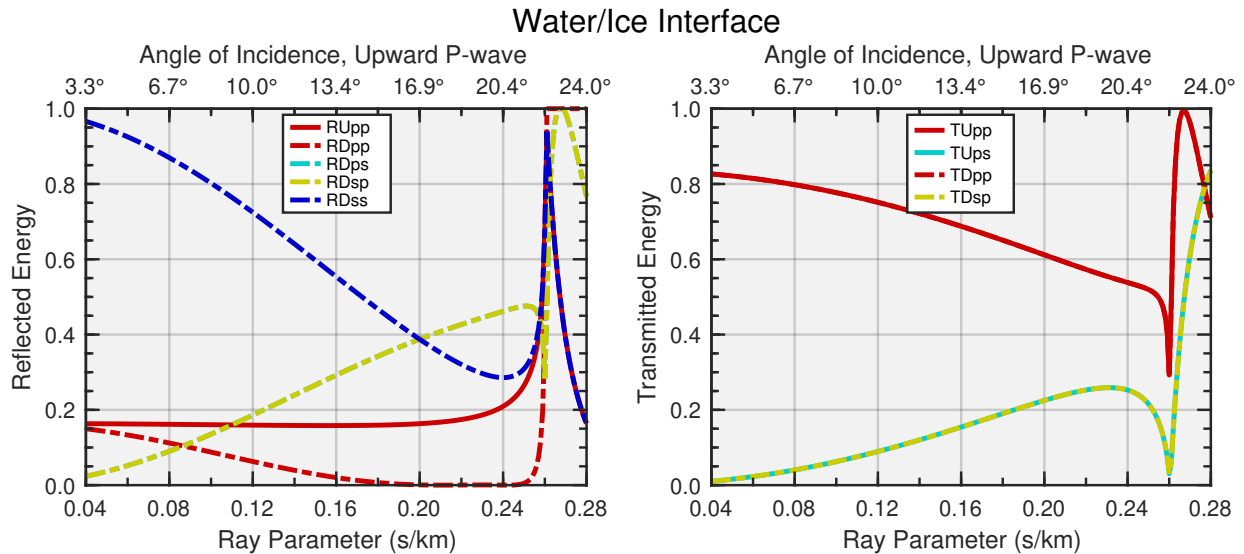


Figure A-3.1: Reflected and transmitted energy coefficients for the ice/water interface [Aki and Richards, 2002], using the values listed in Table 3.2. Coefficients read left-to-right; e.g., TDsp indicates the transmission coefficient for a downward propagating S-to-P conversion. RDps and RDsp overlap. TUpp and TDpp overlap.

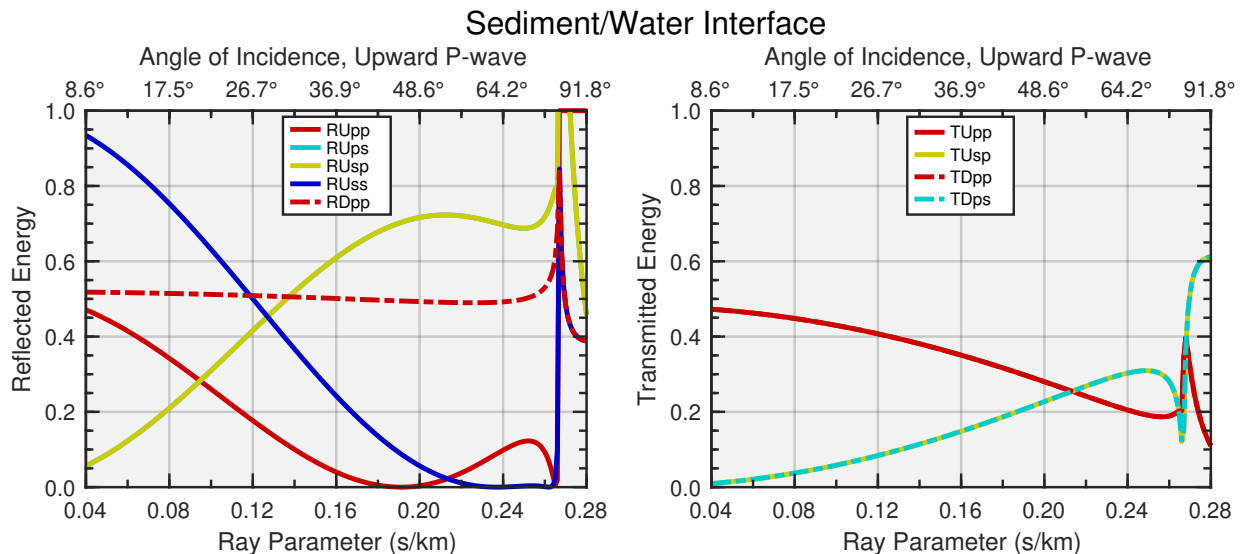


Figure A-3.2: Reflected and transmitted energy coefficients for the water/sediment interface [Aki and Richards, 2002], using the values listed in Table 3.2. Coefficients read left-to-right; e.g., TDps indicates the transmission coefficient for a downward propagating P-to-S conversion. RUps and RUsp overlap. TUpp and TDpp overlap.

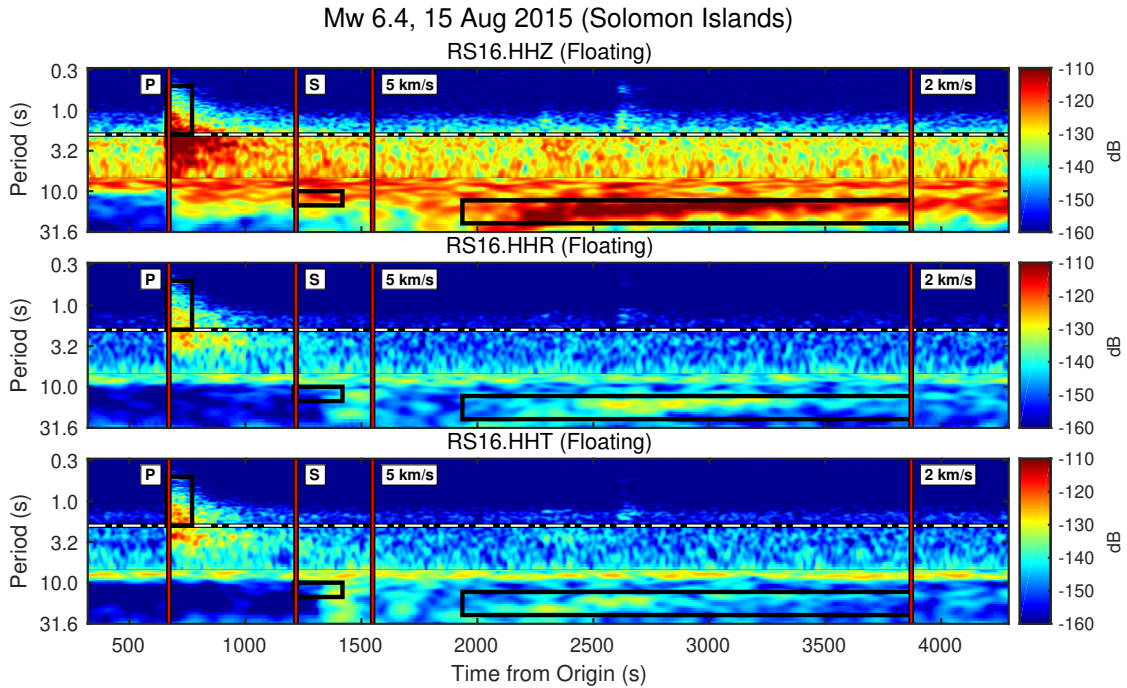


Figure A-3.3: Spectrogram (without background normalization) from floating station RS16 for the M_w 6.4 earthquake shown in Figure 3.3.

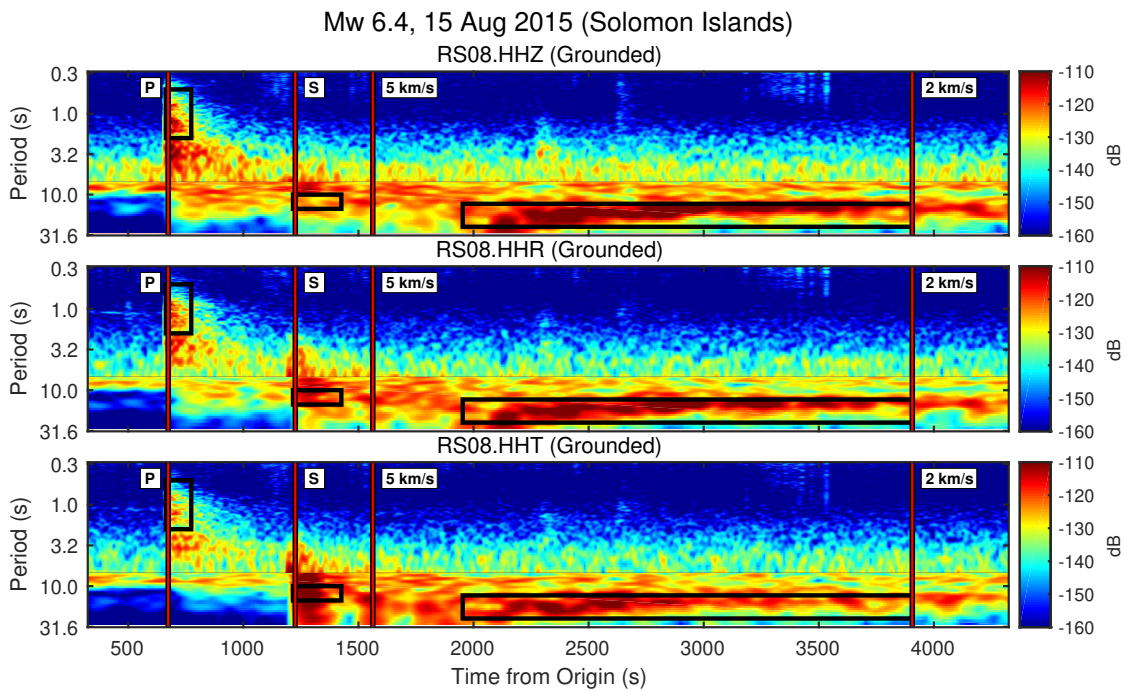


Figure A-3.4: Spectrogram (without background normalization) from grounded station RS08 for the M_w 6.4 earthquake shown in Figure 3.4.

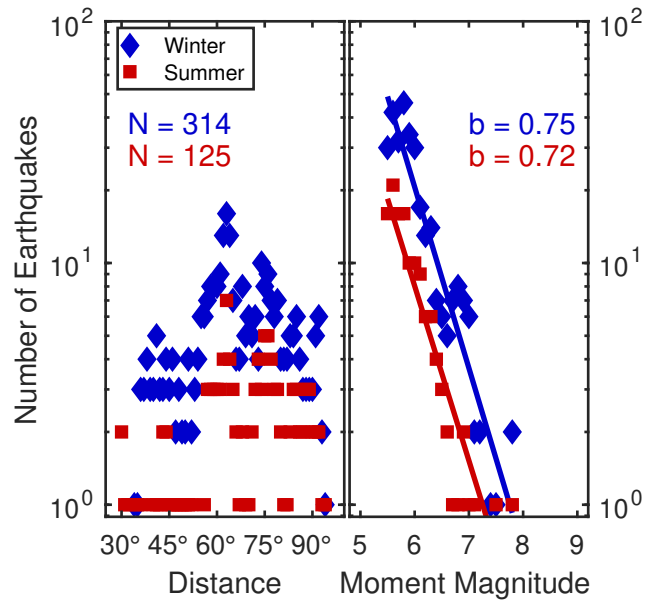


Figure A-3.5: Population metrics for all earthquakes used in this study. N-values indicate the number of earthquakes for Winter (blue) and Summer (red). b-values are the slopes of the Gutenberg-Richter relation, as determined with least squares regression. The P-wave analysis used all earthquakes shown here; the S- and surface wave analyses used the subsets defined in Table 2.1.

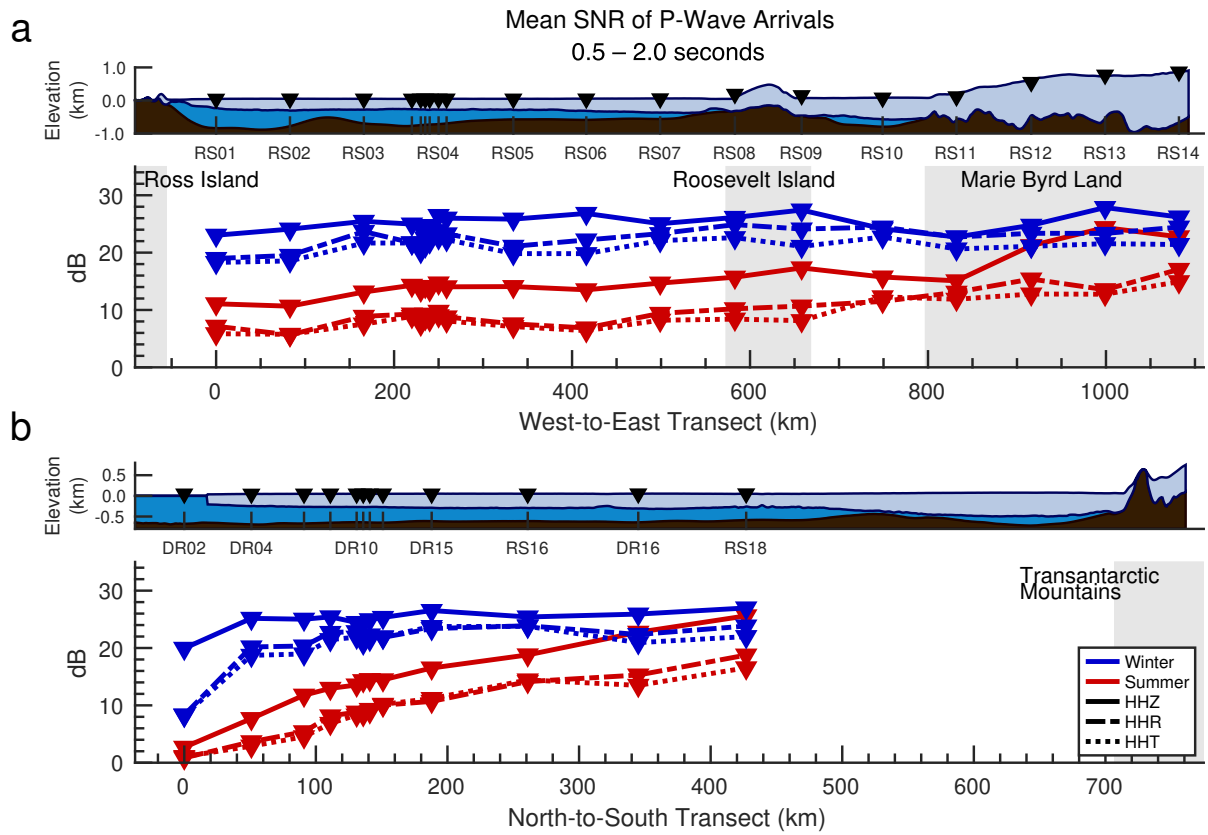


Figure A-3.6: Seasonal and geographic variations in average acceleration power for teleseismic P-wave arrivals, using data uncorrected with Equation 3.1. Compare to Figure 3.5.

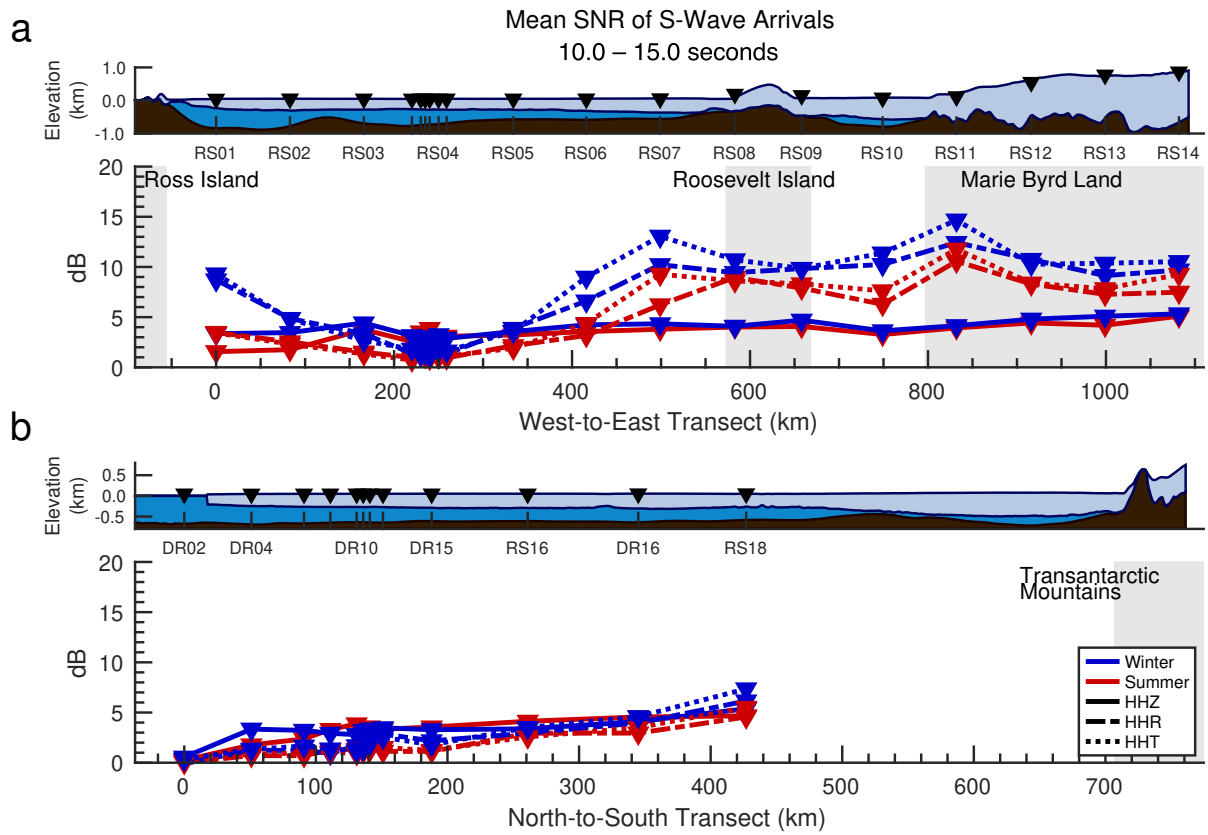


Figure A-3.7: Seasonal and geographic variations in average acceleration power for teleseismic S-wave arrivals, using data uncorrected with Equation 3.1. Compare to Figure 3.7.

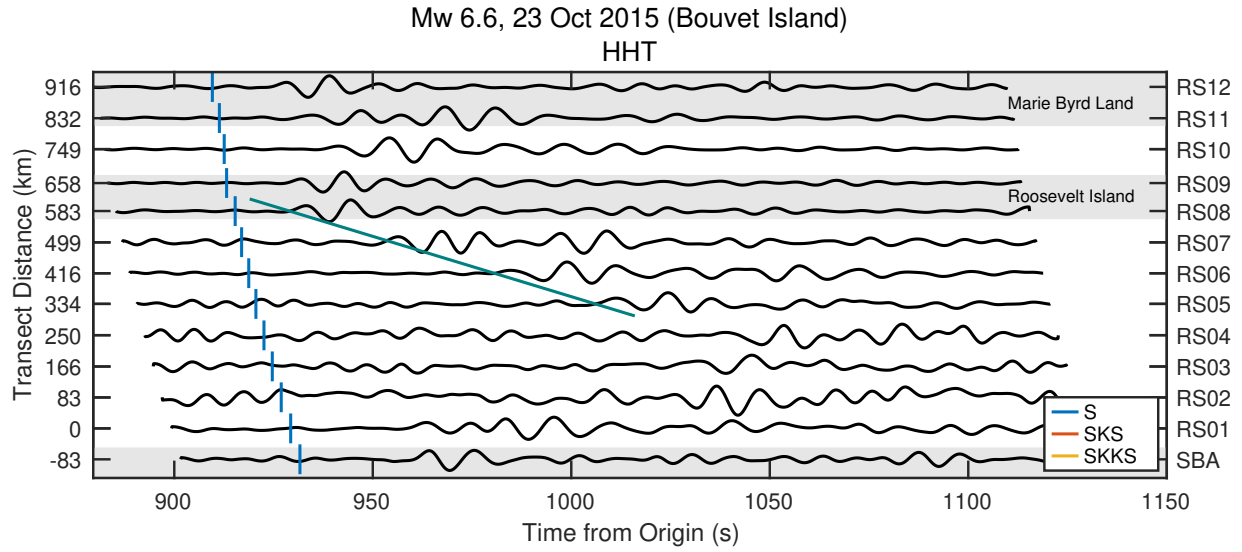


Figure A-3.8: Transverse component record section for teleseismic S-waves arriving from the 23 October 2016, 6.6 M_w Bouvet Island earthquake (hypocenter depth: 11 km). At RS08, the back azimuth for this event is -100° from the East-West transect great circle arc. The teal line marks the (manually fit) travel time curves for S_0 Lamb waves inferred to be generated by S_H -waves incident at the Roosevelt Island grounding line (Equation (3.7), $\varphi \approx 90^\circ$). S_0 Lamb wave propagation velocity was 3.23 km/s. See Figure 3.8 for more details.

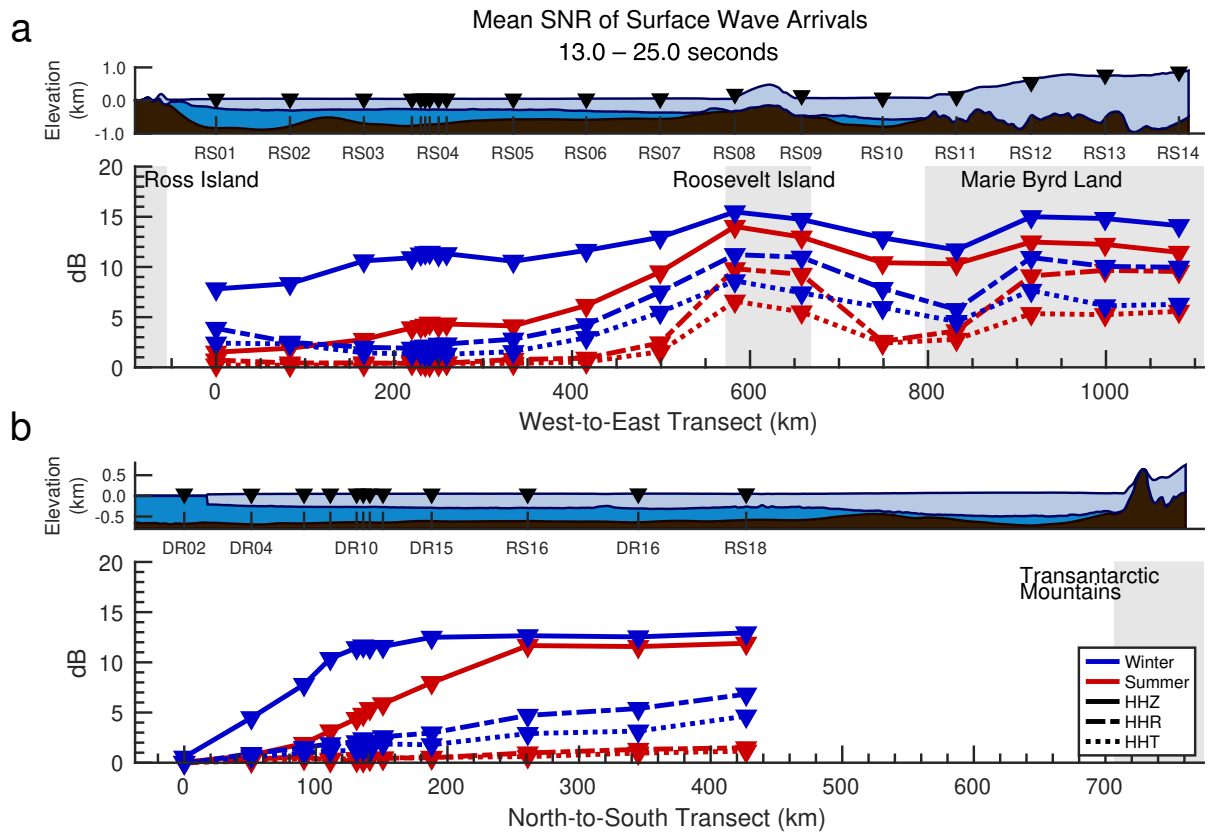


Figure A-3.9: Seasonal and geographic variations in average acceleration power for teleseismic surface wave arrivals, using data uncorrected with Equation 3.2. Compare to Figure 3.11.

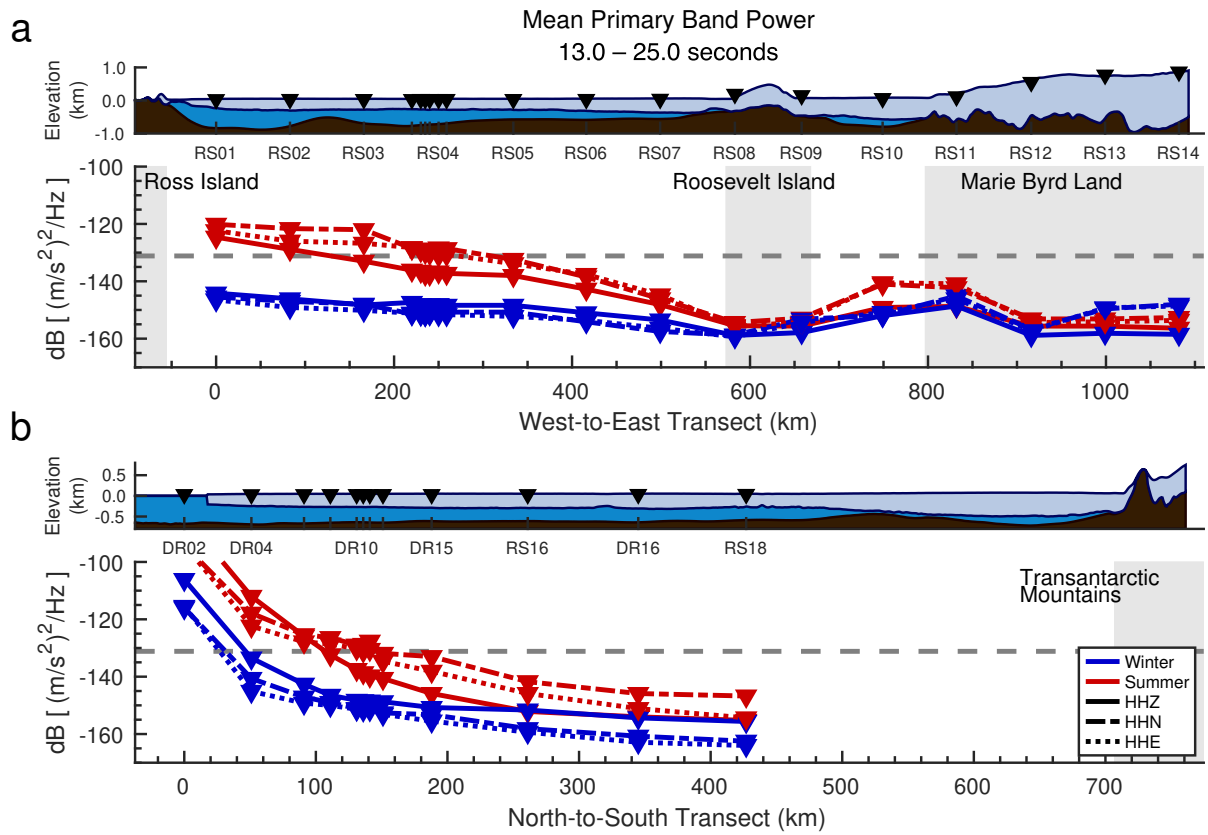


Figure A-3.10: Seasonal and geographic variations in average seismic acceleration power for ambient noise in the 13–25 s period band, adapted from the 10–20 s Primary band presented in Baker et al. (2019). The dashed gray lines indicates the mean Global Seismic Network high-noise model limit for this period band.